# Experimental and theoretical study on Fe-Cr-O thin films : from fine structure to macroscopic behavior

Pâmella Vasconcelos Borges Pinho

université
PARIS-SACLAY

# Experimental and theoretical study on Fe-Cr-O thin films: from fine structure to macroscopic behavior

*Étude expérimentale et théorique des films minces de composition Fe-Cr-O : de la structure fine aux propriétés macroscopiques*

**Thèse de doctorat de l'université Paris-Saclay**

École doctorale n° 564, École Doctorale Physique en Île de France (EDPIF)
Spécialité de doctorat : Physique
Graduate School : Physique. Référent : Faculté des sciences d'Orsay

Thèse préparée dans les unités de recherche **SCCME (Université Paris-Saclay, CEA)** et **SPEC (Université Paris-Saclay, CEA)**, sous la direction de **Jean-Baptiste MOUSSY**, directeur de recherche, la co-direction de **Alain CHARTIER**, directeur de recherche, le co-encadrement de **Frédéric MISERQUE**, chargé de recherche

**Thèse soutenue à Paris-Saclay, le 17 mars 2022, par**

**Pâmella VASCONCELOS BORGES PINHO**

## Composition du Jury

| | |
|---|---|
| **Nita DRAGOE**<br>Professeur, Université Paris-Saclay | Président |
| **Franck VIDAL**<br>Professeur, Sorbonne Université | Rapporteur & Examinateur |
| **Nathalie VIART**<br>Professeure, Université de Strasbourg | Rapporteuse & Examinatrice |
| **Laurence LATU-ROMAIN**<br>Directrice de recherche, Université Grenoble Alpes | Examinatrice |
| **Philippe SAINCTAVIT**<br>Directeur de recherche, Sorbonne Université | Examinateur |
| **Jean-Baptiste MOUSSY**<br>Directeur de recherche, CEA Saclay | Directeur de thèse |

THÈSE DE DOCTORAT

NNT : 2022UPASP028

université PARIS-SACLAY | ÉCOLE DOCTORALE Physique en Île-de-France (PIF)

**Titre :** Étude expérimentale et théorique des films minces de composition Fe-Cr-O : de la structure fine aux propriétés macroscopiques

**Mots clés :** films minces épitaxiés, spinelles, caractérisation de surface, ordre cationique, structures fines, théorie des multiplets

**Résumé :**

Les spinelles fer – chrome et la chromine sont des composés du système ternaire Fe-Cr-O qui sont présents aussi bien dans les couches de corrosion des aciers inoxydables que dans les dispositifs de stockage haute performance. L'enjeu de cette thèse est de lier des observations à l'échelle microscopique (par exemple, la structure électronique ou l'occupation des sites cationiques) à des grandeurs physiques macroscopiques (par exemple, la résistivité ou l'aimantation) sur ces matériaux sous forme de couches minces « modèle » épitaxiées. L'utilisation ciblée de calculs théoriques a permis d'apporter une interprétation fine de certaines mesures expérimentales.

La première partie de la thèse est dédiée à l'étude de l'effet de la déformation de films minces de chromine $\alpha$-$Cr_2O_3$ sur ses propriétés électroniques. Les couches minces de chromine $\alpha$-$Cr_2O_3$(0001) sont d'abord synthétisées par jets moléculaires (MBE) suivant trois états de contrainte : tension, compression dans le plan ou parfaitement relaxé. Pour chaque cas, les spectres des niveaux 2*p* du chrome ont été mesurés par photoémission de rayons X (XPS) et analysés à l'aide de calculs de multiplets (méthode CFM). Les résultats montrent que les distorsions de l'environnement local du chrome, lié à la déformation, lèvent la dégénérescence du triplet $t_{2g}$ des orbitales 3*d* en une orbitale et deux orbitales dégénérées $a_1$ + $e$. On remarque ainsi que la signature XPS de la chromine complètement relaxée correspond à une dégénérescence des orbitales $t_{2g}$. La tension (ou compression) dans le plan induit quant-à-elle une stabilisation (ou déstabilisation) de l'orbitale $a_1$ par rapport aux orbitales $e$. L'analyse des spectres XPS des niveaux 2*p* du chrome apparaît dès lors être un outil pour identifier l'état de contrainte de la chromine. Au-delà du cas des couches minces épitaxiées utilisées pour mettre au point la démarche, il a été ensuite possible de suivre l'évolution de l'état de contrainte de la couche de $\alpha$-$Cr_2O_3$ polycrystalline obtenue durant l'oxydation *in situ* d'un alliage commercial nickel-chrome.

La seconde partie de cette thèse est consacrée aux effets de composition, de désordre et de microstructure sur les propriétés physiques de films minces de spinelles $Fe_{3-x}Cr_xO_4$. A nouveau, la première étape a consisté à synthétiser par MBE des films minces épitaxiés de $Fe_{3-x}Cr_xO_4$(111) de haute qualité structurale et chimique. L'analyse des mesures obtenues par dichroisme magnétique circulaire (XMCD) à l'aide de calculs CFM a permis d'extraire l'environnement local (*i.e.* valence et occupation des sites cationiques) du fer et du chrome dans ces spinelles, en fonction de la teneur en chrome. Les résultats montrent (*i*) que le chrome est dans l'état $Cr^{3+}$ et se substitue au fer en position octaédrique (Oh) exclusivement, (*ii*) que les cations $Fe^{2+}$ et $Fe^{3+}$ sont redistribués dans les deux sites tétraédrique (Td) et octaédrique (Oh) et (*iii*) que l'évolution du taux d'inversion dans les films est plus faible que pour les composés massifs à mesure que la concentration en chrome augmente. La quantification de cette redistribution s'est révélée cruciale pour interpréter les mesures macroscopiques. Ainsi, il a été possible de relier l'évolution de l'aimantation en fonction de la concentration en chrome au taux d'inversion. De plus, l'augmentation de la résistivité avec la teneur en chrome a pu être associée à la disponibilité des chemins de sauts d'électrons Oh–Oh, c'est-à-dire à la concentration en fer dans les sites octaédriques.

université PARIS-SACLAY | ÉCOLE DOCTORALE Physique en Île-de-France (PIF)

**Title :** Experimental and theoretical study on Fe-Cr-O thin films: from fine structure to macroscopic behavior

**Keywords :** epitaxial thin films, spinel oxides, surface characterization, cationic ordering, fine structure, crystal-field multiplet theory

**Abstract :**

From corrosion layers to high-performance storage devices, the Fe-Cr-O ternary system contains typical "old" materials with widespread applications. In this PhD thesis, the macroscopic behavior of this multifaceted system is analyzed in the light of their microscopic properties. To do so, a comprehensive investigation of high-purity, epitaxial Fe-Cr-O thin films is performed in combination with theoretical calculations. Focus is placed on two stable structures of the Fe-Cr-O system: $\alpha$-$Cr_2O_3$ and $Fe_{3-x}Cr_xO_4$ series.

The first part of this thesis holds a discussion about the effects of lattice strain in the electronic structure of $\alpha$-$Cr_2O_3$ thin films. Here epitaxial $\alpha$-$Cr_2O_3$(0001) thin films were synthetized in three model strain scenarios: completely relaxed, under compressive or under tensile in-plane strain. For each scenario, Cr *2p* X-ray photoemission (XPS) spectra were recorded and their features were analyzed by crystal field multiplet (CFM) calculations. According to this approach, the lattice strains introduce distortions in the Cr local environment that split the *3d* valence orbitals triplet $t_{2g}$ into $a_1$ + $e$ orbitals. For relaxed thin films, the XPS spectroscopic signatures were well reproduced by CFM calculations when the $t_{2g}$ subset was fully degenerated. Meanwhile, spectra of films under tensile (or compression) in-plane strain were simulated properly when $a_1$ orbitals was stabilized (or destabilized) with respect to $e$ orbitals. Therefore, one proved that subtle changes observed in the lines-shape of the Cr *2p* XPS spectrum can be used to identify stress states on complex oxides. This convenient methodology (XPS+CFM), which was first optimized using model samples, was then used to successfully identify stress states on polycrystalline $\alpha$-$Cr_2O_3$ layers grown during the oxidation of a commercial chromia-forming alloy.

The second part of this thesis holds a discussion about the effects of composition, cation disorder and microstructure on the physical properties of $Fe_{3-x}Cr_xO_4$ thin films. Here stoichiometric series of epitaxial $Fe_{3-x}Cr_xO_4$(111) thin films were prepared by molecular beam epitaxy (MBE) and their structural, chemical and physical properties were studied by a number of characterization methods. These thin films are composed by $Cr^{3+}$ ions sitting exclusively at octahedral (Oh) interstices and $Fe^{2+}$ and $Fe^{3+}$ ions distributed at Oh and tetrahedral (Td) interstices of the spinel structure. Once again, spectroscopic signatures (here from X-ray magnetic circular dichroism or XMCD) of Cr and Fe were explored by CFM calculations in order to obtain their valence and local environment. More importantly, we were able to determine the cation site distribution, *i.e.* the relative concentration of each specie on each interstice of the spinel structure. This information is crucial in the analysis of physical properties. In general, we observed that increasing Cr content steadily decreases the magnetic moment and increases the resistivity of the $Fe_{3-x}Cr_xO_4$ thin films, which is consistent with previous studies in bulk samples. However, unlike bulk structures, the thin films kept an intermediate spinel structure (*i.e.* $Fe^{2+}$ and $Fe^{3+}$ ions in both Oh and Td-sites) for high Cr content. Because of that, all thin films presented Curie temperatures ($T_C$) above the room temperature, which is further proved using another theoretical model: the atomistic spin simulations. Furthermore, three possible conductive paths (involving electron hopping between $Fe^{2+}$ and $Fe^{3+}$ sites) were analyzed for the $Fe_{3-x}Cr_xO_4$ thin films. Because both $Fe^{2+}$ and $Fe^{3+}$ ions sit at Oh-sites (even at high Cr content), these films are less resistive than the bulk as the favored Oh-to-Oh electron-hopping path is still available. In conclusion, we showed that tuning the physical properties of the $Fe_{3-x}Cr_xO_4$ series can be achieved through the composition and size modulation.

À minha mãe, Cátia, com carinho e gratidão.

# Acknowledgments

Foremost, I would like to express my sincerest gratitude to the members of the jury committee: Pr. Nita Dragoe as jury's president, Pr. Franck Vidal and Pr. Nathalie Viart as reporters, Dr. Laurence Latu-Romain and Dr. Philippe Sainctavit as examiners, for taking the time out of their exceedingly busy schedules to read this thesis and participate in the thesis defense.

Next, my heartfelt thanks to all the colleagues, friends, and family members who contributed in any way to the realization of this project.

I would like to express my sincerest gratitude to my PhD advisor, Dr. Jean-Baptiste Moussy, and my CEA supervisors, Dr. Alain Chartier and Dr. Frédéric Miserque, for all the guidance and encouragement during the development of my thesis. Always available for discussions, all the time that they granted to me was a deep learning experience (and some very good laughs). All their insightful comments on my works have always been an invaluable source of inspiration. My thesis was a true teamwork. I would like to thank Jean-Baptiste for opening the door to the world of epitaxial thin films. Thanks to his great experience and refreshing ideas, I was able to synthesize and analyze beautiful samples that are the grounds of this work. I would like to thank Alain for the liveliest discussions around theoretical methods. Very empathetic and attentive, he has shared with me his enthusiasm for research work with the greatest sense of humor. I would like to thank Frédéric for the many insightful discussions beside the XPS apparatus and during Synchrotron weeks. With great pedagogy and fatherly patience, he has shared with me the world of spectroscopy and surface analysis. Together we have made a powerful team and I could not be happier for the three years we have shared.

I thank all the collaborators that I have worked with on various fascinating projects:

- Dr. Denis Menut and Dr. Myrtille Hunault for the fruitful collaboration with HRXRD and XAS studies performed at MARS beamline of synchrotron SOLEIL. In particular, Denis for the long hours spent on the beamline trying to unravel the mysteries of spinel structure and the analysis of very (and very) thin films. Also, Myrtille for the great tips on treating the XAS data using ATHENA and for kindly analyzing the EXAFS data.
- Dr. Bénédicte Warot, Dr. Cécile Marcelot and Robin Cours for the beautiful TEM images and the EELS and EDX studies carried out at CEMES-CNRS. They have always been very kind, helpful and open to discussion.
- Dr. Philippe Ohresser and Dr. Antoine Barbier for the fruitful collaboration with XAS and XMCD studies performed at DEIMOS beamline of synchrotron SOLEIL. They have shared with me not only their experience, but also some very good advices.
- Dr. Fabrice Charra for the UV-vis absorbance measurements. Our interaction was quick but very fruitful and definitely opened more perspectives to this work.

During my PhD thesis, I have been hosted by two laboratories in different institutions of CEA Saclay: *Laboratoire Nano-Magnétisme et Oxydes* (SPEC/LNO) and *Laboratoire de Modélisation, de Thermodynamique et de Thermochimie* (SCCME/LM2T). My warm thanks to all colleagues, young fellow lab-mates and administrative staff of both institutions, which I cannot exhaust the list here. Special thanks to Dr. Sylvie Chatain and Dr. Frantz Martin for being part of my thesis counselling committee and for the good advices. The "MBE team": Dr. Hélène Magnan, Dr. Antoine Barbier and Frederic Merlet for the advices and encouragements in difficult times of machine breakdown. Dr. Aurelie Solignac for the kind help with the XRR and AFM apparatuses. Dr. Christine Gueneau for the kind help with the software CALPHAD. Paul Foulquier – my fellow thin film expert – for giving some of his valuable time to help me with the XRD and transport measurements, especially having his own thesis to manage. Alan Brunel and Agustin Flores, with whom I have shared not only the office but also laughs, joys, beers and a few complaints.

I also would like to express my gratitude to the colleagues of the *Laboratoire de Physique des Solides* (*Université Paris-Saclay*), especially Z.Z. Li for the kind help with the XRD apparatus, and the colleagues of the *Laboratoire Léon Brillouin* (*CEA Saclay*), especially Josselin Dupont for the kind help with the VSM apparatus.

Finally, I would like to thank friends and family members for the care and emotional support. Especially my mother, sister and niece, whose confidence in my success exceeds my own expectations, and my old friends Pedro, Guilherme, Aurea e Lorena, with whom even from afar I share joy, anger, laughter, excitement, frustration and, most importantly, love.

# Thesis structure

From corrosion layers to high-performance storage devices, the Fe-Cr-O ternary system contains typical "old" materials with widespread applications. In this PhD thesis, the macroscopic behavior of this multifaceted system is analyzed in the light of their microscopic properties. Focus is placed on two stable structures of the Fe-Cr-O system: $\alpha$-$Cr_2O_3$ and $Fe_{3-x}Cr_xO_4$ series. It should be noted that this thesis is a transdisciplinary research work, so the results obtained for each studied compound are placed in two different contexts: (*i*) as key elements in the corrosion mechanism of Fe-Cr based alloys and (*ii*) as promising materials for spintronic and photocatalysis applications.

In the corrosion context, both $\alpha$-$Cr_2O_3$ and $Fe_{3-x}Cr_xO_4$ may appear on the surface of metallic materials (*e.g.,* Fe-Cr based alloys) during their corrosion process, playing a major role in their durability. The corundum $\alpha$-$Cr_2O_3$ phase constitutes protective layers that slow down the oxidation kinetic and extend the material lifetime. Meanwhile, the $Fe_{3-x}Cr_xO_4$ spinel series usually forms a continuous layer that governs the electronic and cationic transport between the alloy and the oxidizing medium. Many authors[1] have highlighted the importance of this spinel phase to the development and maintenance of the protective scales. Despite their key role in the corrosion mechanism of alloys, the study of these complex layers is far from easy. They are usually very thin (*i.e.,* nanoscale), poorly crystallized, with complex microstructure and, sometimes, variable composition (as for $Fe_{3-x}Cr_xO_4$ spinel series). In order to build up knowledge of physicochemical and structural properties of $\alpha$-$Cr_2O_3$ and $Fe_{3-x}Cr_xO_4$, this study proposes to synthetize and characterize "model" thin films, that is, of well-defined composition and single crystalline nature. The data collected here will aid the development of microscopic models and the improvement of mesoscopic models applied to corrosion.

Interestingly, these same high-purity and well-crystallized thin films have been subject of different studies due to their potential applications in spintronic devices and photocatalysis. For instance, $Cr_2O_3$-based systems are particularly promising for voltage control devices[2] as they have reversible, isothermal switching of the exchange-bias field at room temperature. Moreover, as multiferroic materials with adjustable band gap, the $Fe_{3-x}Cr_xO_4$ series can be also very interesting for modern applications, such as spintronics and photocatalysis[3]. Therefore, acquiring data on these compounds is of great scientific and technological interest. Particularly for the $Fe_{3-x}Cr_xO_4$ series, whose previous studies have mainly focused on structural and magnetic properties[4] and not much is known about the transport mechanisms. Moreover, these studies are mostly based on polycrystalline samples, while thin films have received little attention.

---

[1] I. Saeki *et al.*, *Corrosion Science*, vol. 38, no. 1, pp. 19–31, 1996.

[2] J.-L. Wang *et al.*, *Journal of Magnetism and Magnetic Materials*, vol. 486, p. 165262, Sep. 2019.

[3] S. A. Chambers *et al.*, *Advanced Functional Materials*, vol. 27, no. 9, p. 1605040, Mar. 2017.

[4] J. Ma *et al.*, *Physical Review B*, vol. 89, no. 13, Apr. 2014.

The main aim of this thesis was to analyze the macroscopic behavior of $\alpha$-$Cr_2O_3$ and $Fe_{3-x}Cr_xO_4$ thin films in the light of their microscopic properties. To do so, high-purity, epitaxial thin films are elaborated by molecular beam epitaxy (MBE) in order to de-convolute the effect of the fine structure from other types of defects. A comprehensive study is carried out coupling several characterization methods (*e.g.,* spectroscopy, diffraction and physical property measurements) with theoretical calculations. In fact, a global understanding of the macroscopic behavior of $\alpha$-$Cr_2O_3$ and $Fe_{3-x}Cr_xO_4$ thin films has been only possible thanks to this double expertise experiment/theory.

This PhD thesis consists of six chapters following the classical academic structure. The first two chapters are literature review of the Fe-Cr-O system (**Chapter 1**) and the experimental and computational methods (**Chapter 2**) applied. The remaining chapters are original research studies. For the sake of clarity, each chapter starts with a brief summary highlighting its main points and ends with its bibliographic references.

**Chapter 1** gives a general overview of the Fe-Cr-O system. In particular, it introduces the $\alpha$-$Cr_2O_3$ and $Fe_{3-x}Cr_xO_4$ structures, physicochemical properties and many applications. Here emphasis is placed on corrosion, spintronics and photocatalysis applications. Within these contexts, a particular area of concern is investigated for each compound in the Fe-Cr-O system and the thesis is divided into two parts. In general lines, a given macroscopic behavior of the Fe-Cr-O thin films is studied in the light of their microscopic properties. In the first part (**Chapter 3**), a bridge is built between lattice strain and the electronic structure of $\alpha$-$Cr_2O_3$ thin films. In the second part (**Chapter 4** and **Chapter 5**), the electronic transport and magnetic properties of $Fe_{3-x}Cr_xO_4$ thin films is unveiled in the light of their composition, cationic disorder and microstructure.

A brief introduction of the various experimental and computational methods applied in the development of this PhD thesis is presented in **Chapter 2**. It includes techniques for thin film growth (*i.e.* MBE), structural and chemical analysis, electrical transport and magnetic measurements. Theoretical simulations further explore some of these experimental results. In particular, **Chapter 2** shows the theoretical concepts behind the crystal field multiplet (CFM) calculations used to explore the results of core level spectroscopies. Moreover, it shows the fundamentals of atomistic spin model (ASM) used in the simulation of magnetic properties.

The first part of this thesis, **Chapter 3**, combines X-ray photoemission spectroscopy (XPS) and CFM calculations to quantify strain-induced changes in the electronic structure of high quality $\alpha$-$Cr_2O_3$(0001) epitaxial thin films. This methodology – which is first optimized using these "model" thin films – is subsequently used to identify stress states on polycrystalline $\alpha$-$Cr_2O_3$ layers grown during the oxidation of a commercial chromia-forming alloy. Additionally, **Chapter 3** discusses the main aspects and challenges of the MBE technique and CFM simulations that are reiterated in the study of $Fe_{3-x}Cr_xO_4$ series.

The second part of this thesis, **Chapter 4**, is a comprehensive study of the effects of substitutional Cr on the structural and chemical properties of high quality $Fe_{3-x}Cr_xO_4$(111) epitaxial thin films. In particular, it discusses in-depth the crystalline structure, epitaxial nature and stoichiometry of the films. Once again, spectroscopic signatures (here from X-ray absorption spectroscopy and X-ray magnetic circular dichroism) of Cr and Fe are explored by CFM calculations

in order to obtain their valence and local environment. Thanks to this detailed description of the microscopic properties of the $Fe_{3-x}Cr_xO_4$ thin films, their macroscopic behavior could be discussed in **Chapter 5**.

**Chapter 5** describes in detail the magnetism and electronic transport on $Fe_{3-x}Cr_xO_4$ thin films in the light of the cationic ordering. A close link is drawn between magnetic properties (*e.g.,* total magnetic moment and Curie temperature) and the spinel inversion ratio with the aid of ASM simulations. Furthermore, possible conductive mechanisms are discussed for these films considering the cationic ordering in the spinel structure. These results are compared with those available in the literature for bulk samples.

Finally, **Chapter 6** concludes about the most relevant results and gives the prospects of this research work.

# Articles and communications

## ❖ Articles:

**P.V.B Pinho**, A. Chartier, JB Moussy, D. Menut and F. Miserque (2020) Crystal field effects on the photoemission spectra in $Cr_2O_3$ thin films: From multiplet splitting features to the local structure, Materialia, 12, 100753.

**P.V.B Pinho**, A. Chartier, F. Miserque, D. Menut and JB Moussy (2021) Impact of epitaxial strain on crystal field splitting of $\alpha$-$Cr_2O_3$(0001) thin films quantified by X-ray photoemission spectroscopy, *Materials Research Letters*, 9:4, 163-168.

**P.V.B Pinho**, A. Chartier, F. Miserque, D. Menut, B. Warot-Fonrose, C. Marcelot, P. Ohresser, A. Barbier and JB Moussy. Chemical tuning of magnetic and electronic properties of $Fe_{3-x}Cr_xO_4$(111) epitaxial thin films. (*In progress*)

## ❖ Communications:

**P.V.B Pinho**, A. Chartier, JB Moussy and F. Miserque. XPS investigation on early oxidation stages of chromium: a theoretical and experimental account. *Workshop: Hands on Spectroscopy Calculations of Quantum Materials*. Heidelberg, October 7-11, 2019.

**P.V.B Pinho**, A. Chartier, JB Moussy and F. Miserque. Crystal field effects on the photoemission spectra in epitaxial ultrathin films of $\alpha$-$Cr_2O_3$(0001). *E-MRS Spring Meeting*. Virtual Conference, May 31 – June 3, 2021.

**P.V.B Pinho**, A. Chartier, F. Miserque, D. Menut, B. Warot-Fonrose, C. Marcelot, P. Ohresser, A. Barbier and JB Moussy. Synthesis, characterization and modeling of $Fe_{3-x}Cr_xO_4$(111) epitaxial thin films. *17ème Journées de la Matière Condensée*. Virtual Conference, August 24-27, 2021.

**P.V.B Pinho**, A. Chartier, F. Miserque, C. Marcelot, B. Warot-Fonrose, A. Barbier, P. Ohresser, D. Menut and Jean-Baptiste Moussy. Effect of chromium substitution on structural and chemical properties of $Fe_{3-x}Cr_xO_4$(111) epitaxial thin films. *EPIDOX.* Virtual conference, November 17-19, 2021.

# Contents

# List of figures

### Chapter 1: The Fe-Cr-O system and its many applications

## Chapter 2: Experimental and computational methods

### Chapter 3: Effect of strain on the crystal field of $Cr_2O_3$ thin films

### Chapter 4: Chemical and structural characterization of $Fe_{3-x}Cr_xO_4$ thin films

# List of tables

# Acronyms

| | |
|---|---|
| **AFM** | Atomic Force Microscopy |
| **APB** | AntiPhase Boundary |
| **ASM** | Atomistic Spin Model |
| **BE** | Binding Energy |
| **CCD** | Charge-Coupled Device |
| **CFM** | Crystal Field Multiplet |
| **EDX** | Energy Dispersive X-ray spectroscopy |
| **EELS** | Electron Energy-Loss Spectroscopy |
| **EXAFS** | Extended X-ray Absorption Fine Structure |
| **FWHM** | Full Width at Half Maximum |
| **HF** | Hartree-Fock theory |
| **HRTEM** | High-Resolution Transmission Electron Microscopy |
| **JT** | Jahn-Teller |
| **LLG** | Landau-Lifshitz-Gilbert method |
| **MBE** | Molecular Beam Epitaxy |
| **MC** | Monte Carlo method |
| **MCA** | MagnetoCrystalline Anisotropy |
| **NNH** | Nearest-Neighbor Hopping |
| **O-MBE** | Oxygen-plasma-assisted Molecular Beam Epitaxy |
| **PBC** | Periodic Boundary Conditions |
| **PLD** | Pulsed Laser Deposition |
| **PPMS** | Physical Properties Measurement System |
| **PVD** | Physical Vapor Deposition |
| **RC** | Rocking Curve |
| **RHEED** | Reflection High-Energy Electron Diffraction |
| **RSS** | Residual Sum of Squares |
| **TEM** | Transmission Electron Microscopy |
| **TEY** | Total Electron Yield |
| **TFY** | Total Fluorescence Yield |
| **UHV** | UltraHigh Vacuum |
| **VRH** | Variable Range Hopping |
| **VSM** | Vibrating Sample Magnetometer |
| **XANES** | X-ray Absorption Near-Edge Structure |
| **XAS** | X-ray Absorption Spectroscopy |
| **XMCD** | X-ray Magnetic Circular Dichroism |
| **XPS** | X-ray Photoemission Spectroscopy |
| **XRD** | X-Ray Diffraction |
| **XRR** | X-Ray Reflectivity |

« *A menor distância entre dois pontos pode ser a linha reta, mas é nos caminhos curvos que se encontram as melhores coisas.* »

Lygia Fagundes Telles

# Chapter 1:

# The Fe-Cr-O system and its many applications

This PhD thesis is a comprehensive study of the **physicochemical** and **structural properties** of epitaxial thin films in the Fe-Cr-O system. Over the last 50 decades, this system has been thoroughly studied, particularly with respect to the melting, refining and corrosion of Fe-Cr-based alloys. However, more recently, their different phases have been considered for modern electronic applications due to the inherent magnetic properties of Fe-Cr oxides. The following chapter is an overview of the different **crystalline structures** that can be found in this ternary system, their particular features and their **many applications**. Emphasis is placed on the **$Fe_{3-x}Cr_xO_4$ spinel** and **$Cr_2O_3$ corundum** compounds in the thin film form, which constitute the core of this study.

## 1.1 The Fe-Cr-O ternary system

The Fe-Cr-O ternary system contains typically "old" materials, which have been studied extensively since the mid-20th century due to their intervention in several fields, such as geology [1], metallurgy [2], corrosion [3], [4], and (more recently) electronics [5], [6]. In this system, solid oxide phases may appear in three different crystallographic structures: the halite (wüstite-based), the corundum and the spinel phases [7]–[9]. The wüstite (FeO) is a form of Fe(II) oxide that presents a defect NaCl-type structure, with generic name halite. The corundum phase ($Fe_{2-x}Cr_xO_3$) is formed by trivalent cations in the hexagonal $Al_2O_3$-type structure, while the spinel ($Fe_{3-x}Cr_xO_4$) is a mix of divalent and trivalent cations in the cubic $MgAl_2O_4$-type structure.

Among the oxides of the Fe-Cr-O ternary system, the corundum and the spinel are the most common phases. The wüstite is only thermodynamically stable above 843 K and under low partial pressure of oxygen (*e.g.* $p_{O_2}$ may range from $10^{-6}$ to $10^{-25}$ atm depending on temperature) [10]. Below 843 K, FeO decomposes into Fe and $Fe_3O_4$. **Figure 1.1** depicts an isothermal Fe-Cr-O phase diagram in function of the ratio between Cr molar fraction and Cr + Fe molar fractions ($n_{Cr}$ / $n_{Cr}$ + $n_{Fe}$). This diagram is based on the thermodynamic modeling proposed by Kjellqvist *et al.* [9] for the quaternary Fe-Cr-Ni-O system using the CALPHAD method[5] [11]. The solubility of Cr in wüstite is modeled with introduction of $Cr^{3+}$ on the cation lattice, for which deviation from stoichiometric and lack of electroneutrality are compensated by introducing vacancies to the cation sublattice. At temperature as high as 1073 K (**Figure 1.1**), the halite phase ($Fe_{1-x}Cr_xO$) is only stable at low oxygen partial pressure ($p_{O_2}$ from $10^{-18}$ to $10^{-19}$ atm) and over a very narrow range of $x$ ($x_{max}$ ~ 0.01). In contrast, the most common oxide phases of this ternary system, $Fe_{2-x}Cr_xO_3$ and $Fe_{3-x}Cr_xO_4$, are thermodynamically stable over a wide range of temperature (not shown), pressure and $x$-composition. The corundum phase forms a complete solid solution under $p_{O_2}$ from 1 to $10^{-9}$ atm, which can be intrinsically defect free over the complete $x$-range: from $Fe_2O_3$ (hematite) to $Cr_2O_3$ (eskolaïte). In turn, the spinel phase is stable under lower $p_{O_2}$ (*i.e.,* from $10^{-9}$ to $10^{-18}$ atm). However, because $Cr_3O_4$ is not stable under these conditions of temperature and pressure, the spinel phase does not form a continuous solid solution over the complete $x$-range. It extends from the binary $Fe_3O_4$ (magnetite) to $FeCr_2O_4$ (chromite).

The focus of this study is on two stable oxide structures in the Fe-Cr-O system: the corundum $\alpha$-$Cr_2O_3$ and the spinel $Fe_{3-x}Cr_xO_4$ series with $0 \leq x \leq 2$. These two materials play an active role in various research fields, particularly in the corrosion process of Fe-Cr-based alloys [12], [13] and, recently, they have been proposed for modern applications in electronic [14]–[16] and photocatalysis [17], [18]. The following sections outline the structural and physicochemical properties of $\alpha$-$Cr_2O_3$ and $Fe_{3-x}Cr_xO_4$ series, which are required for the proper understanding of this manuscript. Furthermore, the many facets of these materials are discussed in the light of their unique properties.

[5] The CAPHALD method performs thermodynamic calculations and modelling by minimizing the sum of the Gibb's free energy of the possible phases in a given system.

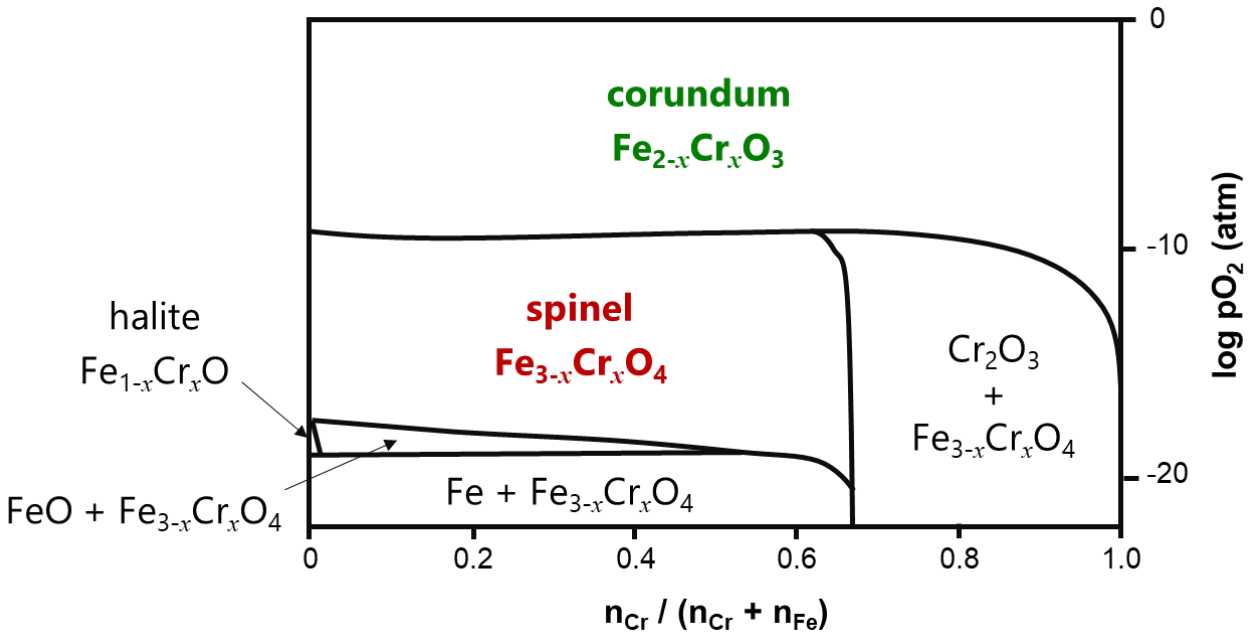


**Figure 1.1.** Chemical potential diagram of Fe-Cr-O system at 1073 K. Herein, the stable solid oxide phases are halite ($Fe_{1-x}Cr_xO$, space group $Fm\bar{3}m$), corundum ($Fe_{2-x}Cr_xO_3$, space group $R\bar{3}c$) and spinel ($Fe_{3-x}Cr_xO_4$, space group $Fd\bar{3}m$). These isotherms were calculated following the published thermodynamic modeling of the quaternary Fe-Cr-Ni-O system [9]. Figure adapted from Taylor and Dinsdale [8].

# 1.2 Structure, physicochemical properties and many applications of $Cr_2O_3$

## 1.2.1 The corundum structure

$\alpha$-$Cr_2O_3$ is the thermodynamically stable form of chromium oxide under standard conditions of temperature and pressure. It exhibits a corundum-type structure described by the $R\bar{3}c$ space group (No. 167 in the International Tables [19]). **Figure 1.2a** depicts the conventional hexagonal unit cell, which contains six formula units and has parameters $a$ = $b$ = 0.492 nm and $c$ = 1.37 nm [20]. The oxygen anions (Wyckoff position $18e$) form pseudo-hexagonal close-packed structure with $Cr^{3+}$ cations occupying two thirds of the octahedral interstices (Wyckoff position $12c$). The structure contains oxygen layers alternated with chromium bilayers along the $c$-axis of the hexagonal lattice. Each bilayer consists of two perfectly planar triangular lattices whose combined projections build an ideal honeycomb structure with one atom from each sublayer as the two-basis elements.

A close look in the local environment of $Cr^{3+}$ cations shows that $CrO_6$ is not a perfect octahedron. In fact, these cations lie in special positions along the threefold axis at ± [0 0 $z$, 0 0 ½+ $z$]. As shown in **Figure 1.2b**, they form with oxygen three Cr–O bonds of 0.197 nm length and three of 0.202 nm, and O–Cr–O angles of 81°24′ and 99°00′. The $Cr^{3+}$ cation is displaced (upward in **Figure 1.2b**) along the $C_3$ axis relative to the octahedral center, making two equilateral triangles formed by three oxygen ions each. Due to a slight rotation of the upper and lower oxygen ions triangles (dotted

lines in **Figure 1.2c**), the exact symmetry of the $Cr^{3+}$ cations in $\alpha$-$Cr_2O_3$ is $C_3$. In **Chapter 3**, the local Cr environment had to be dictated in order to exploit the $\alpha$-$Cr_2O_3$ spectroscopic data. For simplicity's sake, the system was approximated by the $C_{3v}$ point group[6], since the rotation angle between the oxygen ions triangles is very small (about 2°57′).

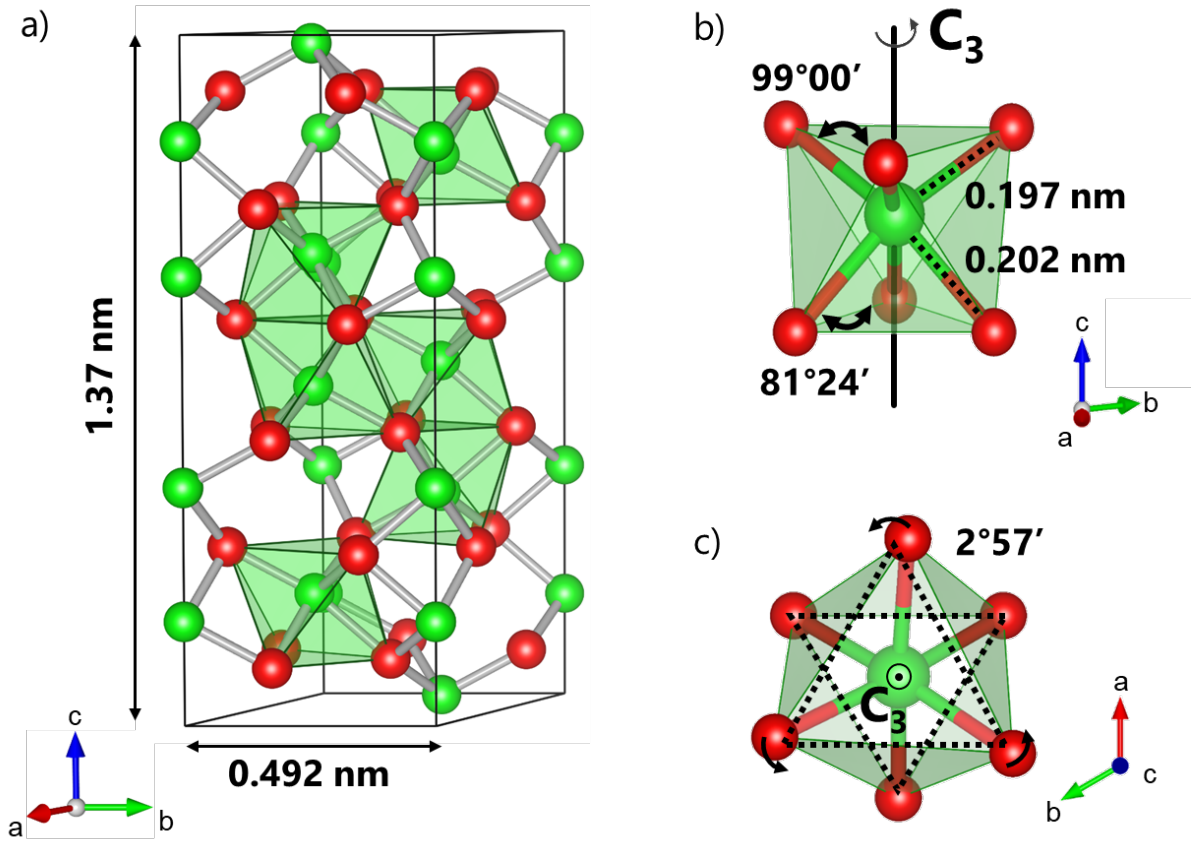


**Figure 1.2.** (a) Close-packed hexagonal unit cell of $\alpha$-$Cr_2O_3$, where trivalent Cr cations (green) bonded to six oxygen anions (red) form trigonal distorted octahedra. (b) The $Cr^{3+}$ ions lie along the threefold axis with Cr-O bond lengths of 0.197 nm and 0.202 nm, and O–Cr–O angles of 81°24′ and 99°00′. (c) A rotation angle of 2°57′ is observed between the upper and lower oxygen triangles (depicted in black dotted lines).

## 1.2.2 $Cr_2O_3$: an antiferromagnetic insulator with magnetoeletric effects

$Cr_2O_3$ is an archetype magnetoeletric antiferromagnetic material with Néel temperature[7] ($T_N$) of about 307 K [22]. Indeed, this material presents a rather interesting antiferromagnetic structure. Below $T_N$, $Cr^{3+}$ spins have not only an alternating order (↑↓↑↓) among nearest neighbors in each chromium bilayer, but also an interlayer order such that the (↑↓↑↓) sequence along the $c$-axis of the hexagonal setting is identical for each bilayer (**Figure 1.3**) [23], [24]. Because the material's magnetic

[6] The $C_{3v}$ point group of symmetry is characterized by three mirror planes containing a threefold rotation axis. It is a group of higher symmetry than $C_3$, which contains only the symmetry operations of identity and a threefold rotation axis [21].

[7] Néel temperature is the critical point temperature up to which an antiferromagnetic spin structure is stable.

moment prefers to align along a well-defined crystallographic axe (known as easy magnetization axe), an intrinsic property of $Cr_2O_3$ is the magnetocrystalline anisotropy ($K_{AF} \sim 2 \times 10^4$ J.m$^{-3}$) [25]. Due to the breaking of the space inversion and time reversal symmetries, $Cr_2O_3$ exhibits magnetoeletric effect [26], [27]. Such effect can be electrically and/or magnetically induced. For instance, when an electric field is applied parallel to the $c$-axis of $Cr_2O_3$, the inversion symmetry is destroyed and a difference in absolute magnitude between the up- and down-spin sublattices is created, producing a net magnetization. In addition, antiferromagnetic spin reversal can be observed by the simultaneous application of electric and magnetic field. **Figure 1.3** illustrates the magnetoeletric manipulation of two equivalent antiferromagnetic domains in $Cr_2O_3$ by changing the electric field direction.

In its antiferromagnetic phase, $Cr_2O_3$ has an intermediate behavior between charge transfer and Mott-Hubbard insulator with wide bandgap of 3.2-3.4 eV [28]–[30]. At high temperatures (above 1370 K), pure $Cr_2O_3$ exhibits intrinsic electrical conductivity that is independent of oxygen partial pressure ($p_{O_2}$). Below 1370 K, it has a defect-controlled conductivity that varies with $p_{O_2}$ (*i.e.* p-type semi-conductor behavior) [28]. The conductivity decreases with decrease in temperature. For temperatures higher than 500 K, conduction occurs by thermal excitation of holes and conductivity is about tens m$\Omega^{-1}$.cm$^{-1}$. For lower temperatures, conductivity follows the small polaron[8] hopping, assuming values of tens to few $\mu\Omega^{-1}$.cm$^{-1}$ [32], [33]. In addition to its large bandgap, $Cr_2O_3$ also shows excellent heat stability (melting temperature in air around 2550 K) and oxidation resistance, being an important refractory material [34].

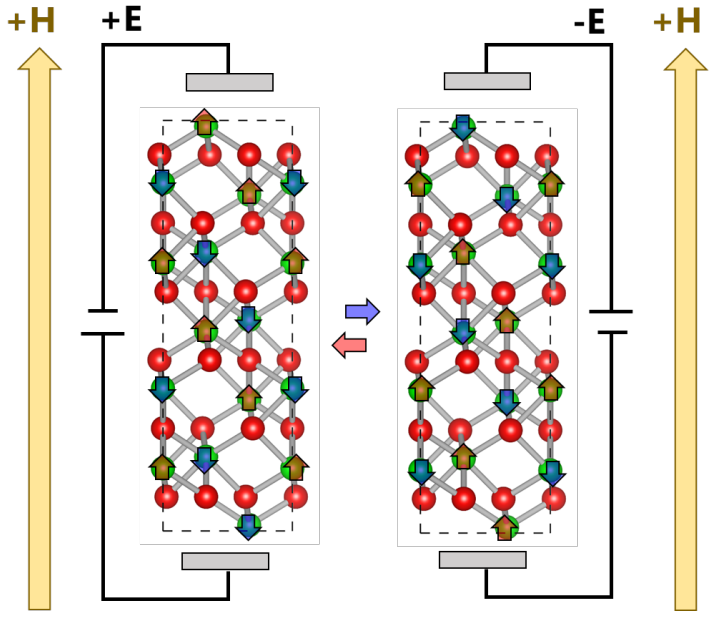


**Figure 1.3.** Scheme of magnetoeletric manipulation of equivalent antiferromagnetic domains in $Cr_2O_3$. Herein, different antiferromagnetic domain state (↑↓↑↓) or (↓↑↓↑) is stabilized by changing the electric field direction (only). Image adapted from Nozaki and Sahashi [35].

[8] Polarons are created when an electron (or hole) is coupled to a lattice distortion induced by its presence, which is a process known as 'self-trapping'. Depending on the spatial extension of the polaron, it can be small (spatial extension of the order of lattice constant) or large (spatial extension beyond the lattice constant) [31].

### 1.2.3 The different facets of $Cr_2O_3$

Owing particular electric, magnetic and refractory properties, $Cr_2O_3$ has been proposed for widespread applications in different scientific domains. As a magnetoeletric antiferromagnet oxide, $Cr_2O_3$ is often envisioned for use in future high-performance spintronic applications [15], [16], [36], *e.g.* storage, memory and logic use [37], [38]. As a refractory material with high-temperature oxidation resistance, $Cr_2O_3$ is suitable for wear and corrosion resistance materials [39]. Moreover, the $3d^3$ electronic configuration of $Cr^{3+}$ cations endows $Cr_2O_3$ with chlorophyll-like absorption in the visible region. Therefore, this material has been also commercialized as green pigment with outstanding tinting strength and migration resistance [40]. Other common application is in heterogeneous catalysis. For example, $Cr_2O_3$-based nanocomposites have been studied as promising catalysts for the oxidative dehydrogenation of ethane to ethylene with $CO_2$ [41], [42].

In this thesis, the growth of $Cr_2O_3$ thin films was investigated in two different roles: as a protective corrosion layer in chromia-forming alloys and as promising material for high-performance spintronic devices. How do these two research fields come together? The answer found in this manuscript to this question was strain. The first part of this study (**Chapter 3**) holds a discussion about the effects of strain in the electronic structure of growing $Cr_2O_3$ thin films. As discussed in detail below, accounting for strain evolution during oxide growth is of utmost importance for understanding the breakdown of the oxide scales in the corrosion context as well as for tuning their anisotropic properties in the spintronic context.

First, the motivation behind studying the growth of protective oxide layers is presented. Chromia-forming alloys are commonly encountered in high temperatures applications (*e.g.* in tubes and nozzles of nuclear reactor primary systems) due to their excellent mechanical properties and resistance to corrosion [43]–[45]. When exposed to oxidizing atmospheres, these alloys may develop $Cr_2O_3$ protective layers that slow down the oxidation kinetic and extend the material lifetime. A number of studies [46]–[48] have been performed to evaluate the growth kinetics and the microstructure of the oxide scales during alloy oxidation and, recently, focus has been placed on the early stages of this process [49], [50]. It has been shown that the initial reactions at the alloy-oxide interface control the continuous growth of the oxide coating and actively influence the performance of the metallic alloy. Because of volume changes (*i.e.,* ratio of oxide volume to that of the replaced metal is greater or smaller than unity), compressive or tensile growth stresses arise during formation of oxide. The alloy-oxide system accommodates strain by elastic deformations. However, if the elastic limit is exceeded, different mechanisms can take place to promote stress relief, which depends on the amount of residual strain [51]. For instance, compressive stresses may induce oxide whiskers or nanowires formation, [52] while tensile stresses may induce lateral oxide growth [53]. Both stress-induced growth processes relax strains and aid to maintain the integrity of the oxide scale. Other options for stress relief in oxide scales are plastic deformation and mechanical failure of the composite. Experimentally, it is difficult to assess the contributions of growth stresses towards oxide breakdown. Overall, this source of stress is not fully understood since it depends on the detailed mechanism of oxide growth [51]. Moreover, owing to the thinness of the oxide layers formed on

early stages of the alloy oxidation, the study of their chemical and microstructure evolutions can be very challenging.

In **Chapter 3**, strain-induced changes in the electronic structure of $Cr_2O_3$ during early oxidation stages of a commercial chromia-forming alloy (Ni30Cr) were investigated by combing a surface sensitive analytical technique (X-ray photoemission spectroscopy or XPS) and a multi-electronic semi-empirical method to simulate core-level spectra (crystal field multiplet calculations or CFM). To do so, first spectra from monocrystalline $Cr_2O_3$ thin films in different strain scenarios were acquired to evaluate the parameters used in the theoretical calculations. Since monocrystalline films generally depict a single local structure, geometric statements can be more easily made for the observed evolution of the photoemission spectra. Once the method calibrated, the problem was transposed to polycrystalline samples of $Cr_2O_3$ grown by exposing the Ni30Cr alloy to an oxygen-rich environment at high temperature.

Interestingly, this same monocrystalline $Cr_2O_3$ thin film has been subject of different studies due to its application in spintronic devices. Indeed, $Cr_2O_3$-based systems are particularly promising for voltage control devices as they have reversible, isothermal switching of the exchange-bias[9] field at room temperature [56], [57]. The interest in studying strains in such films is explained as follows. Even though promising, a crucial issue toward device application of $Cr_2O_3$-based systems is the enhancement of $Cr_2O_3$ operating temperature to assure enough stability for room temperature processes. To withstand the operating environment, two properties of $Cr_2O_3$ have to be enhanced: the Néel temperature ($T_N$ ~ 307 K) and the magnetic anisotropy ($K_{AF} \sim 2 \times 10^4$ J.m$^{-3}$). While increasing $T_N$ gives more stability of the antiferromagnetic phase and therefore more flexibility for practical applications, the magnetic anisotropy has the role of maintaining the thermal stability. Because of their small magnetic anisotropy, $Cr_2O_3$-based systems cannot sustain large exchange bias, which is observed only at significantly lower temperatures than $T_N$ [58], [59]. A propitious approach to overcome the operating temperature issue is strain engineering, because it can influence not only $T_N$, but also the magnetic anisotropy of the material [35], [60], [61]. In $Cr_2O_3$, the magnetic interaction is mainly controlled by the Cr-Cr direct exchange interaction. Therefore, any change in the Cr-Cr bond length affects the orbital overlap between these cations and, consequently, modifies the intra-layer antiferromagnetic exchange. In addition, strains induce distortions in the $CrO_6$ octahedron, which strongly affects the magnetocrystalline anisotropy through the modulation of the crystal field.

In **Chapter 3**, the line-shape differences of the Cr photoemission spectra are explored in order to quantify changes in the crystal field around the $Cr^{3+}$ cation induced by different epitaxial strains. To do so, monocrystalline ultrathin films of $\alpha$-$Cr_2O_3$(0001) were grown by molecular beam epitaxy (MBE) directly on $\alpha$-$Al_2O_3$(0001) substrate or on $\alpha$-$Fe_2O_3$(0001) buffer layer grown on the same sapphire substrate. These three oxides have a corundum-like crystal structure with $a$ parameters

[9] Exchange bias occurs when ferromagnetic (FM)-antiferromagnetic (AFM) interfaces of bilayers (or multilayers) materials are cooled in the presence of a static magnetic field from a temperature above $T_N$ of the AFM layer, but below Curie temperature of the FM layer, and a shift is induced in the magnetization curve of the FM layer. This phenomenon has several applications, including in read-heads, magnetic sensors and magnetoresistive memories [54], [55].

equal to 0.476, 0.492 and 0.503 nm for $\alpha$-$Al_2O_3$(0001), $\alpha$-$Cr_2O_3$(0001) and $\alpha$-$Fe_2O_3$(0001), respectively [62]. Due to the difference between the in-plane lattice parameters, the photoemission spectra of $Cr_2O_3$ thin films were analyzed under either compressive (for $\alpha$-$Cr_2O_3$ on $\alpha$-$Al_2O_3$ substrate) or tensile (for $\alpha$-$Cr_2O_3$ on $\alpha$-$Fe_2O_3$ buffer) in-plane strain. Besides providing different strain scenarios for this model system, the choice of substrate and buffer was made for two main reasons:

1. Because this three compounds have the same crystal structure, it has been shown [62] that epitaxial $\alpha$-$Cr_2O_3$ thin films grow nicely in this system with minimal defects. In addition, $\alpha$-$Al_2O_3$/$\alpha$-$Cr_2O_3$ and $\alpha$-$Al_2O_3$/$\alpha$-$Fe_2O_3$/$\alpha$-$Cr_2O_3$ configurations form nearly atomically abrupt interfaces with little cation diffusion between the firsts angstroms of the growing layers [63]. Therefore, changes in the photoemission spectra of $\alpha$-$Cr_2O_3$ were related exclusively to the deformation caused by the lattice mismatch, excluding the differences that could be produced by variation in chemical composition due to cation diffusion among interfaces.

2. Experimental [64], [65] and theoretical [66] studies have shown that growing $\alpha$-$Cr_2O_3$ layers strained by lattice mismatch using $\alpha$-$Al_2O_3$ substrate and $\alpha$-$Fe_2O_3$ buffer actually influences both $T_N$ and magnetocrystalline anisotropy energy (MAE) of $Cr_2O_3$. For example, for 20 nm thick $\alpha$-$Cr_2O_3$ grown on 20 nm $\alpha$-$Fe_2O_3$ buffer, Pati *et al.* [64] showed that the $\alpha$-$Cr_2O_3$ layer has high in-plane expansion and out-of-plane compression, decreasing $c/a$ ratio from 2.726 to 2.672. As consequence, they observed negative variation in $T_N$ of −12.37% from the bulk value. In this same system, Shimomura *et al.* [65] measured a high blocking temperature of 260 K for the films. The blocking temperature ($T_B$) is the one at which the perpendicular exchange bias disappears, thus it can be considered the upper limit of the operating temperature for $Cr_2O_3$-based devices. Typically, $T_B$ decreases with decreasing $Cr_2O_3$ thickness; *e.g.* the $T_B$ for non-strained 30-nm-thick $\alpha$-$Cr_2O_3$ films is as low as 80 K [67]. The higher $T_B$ value obtained using an $\alpha$-$Fe_2O_3$ buffer is most likely because of the lattice strain-induced increase in $Cr_2O_3$ magnetocrystalline anisotropy. Indeed, *ab initio* calculations [66] estimate a large increase in MAE (~$10^5$ J.m$^{-3}$) for such system. Therefore, in addition to providing an ideal model system to evaluate the parameters of crystal field multiplet (CFM) simulations, the $\alpha$-$Al_2O_3$/$\alpha$-$Cr_2O_3$ and $\alpha$-$Al_2O_3$/$\alpha$-$Fe_2O_3$/$\alpha$-$Cr_2O_3$ configurations are of real technological interest.

For each strain scenario, CFM calculations were performed to extract the crystal field parameters from the photoemission spectra of $\alpha$-$Cr_2O_3$ thin films. A quantitative relation was subsequently established between distortions of the $CrO_6$ octahedron and the crystal field splitting ($\delta$) of chromium $d$-orbitals. This relationship is crucial to predict changes in the magnetic and electronic properties of $\alpha$-$Cr_2O_3$ when a certain amount of internal strain is considered. For instance, according to *ab initio* calculations [68], even small changes of 30 meV in $\delta$ are enough to increase the MAE of $Cr_2O_3$.

After studying the corundum phase, attention was turned to the spinel oxide phase of the Fe-Cr-O system. The following sections discuss in detail the effect of chromium substitution on the structure and the physicochemical properties of $Fe_{3-x}Cr_xO_4$ series.

# 1.3 Structure, physicochemical properties and many applications of $Fe_{3-x}Cr_xO_4$ series

## 1.3.1 The spinel structure

The $Fe_{3-x}Cr_xO_4$ series exhibits a spinel-type structure described by the $Fd\bar{3}m$ space group (No. 227 in the International Tables [19]). The oxygen anion sublattice (Wyckoff position *32e*) is arranged in a pseudo-cubic close-packed spatial arrangement with multivalence cations occupying one eighth of the tetrahedral interstices (Wyckoff position *8a*) and half of the octahedral interstices (Wyckoff position *16d*) [69]. Throughout this manuscript, tetrahedral cation sites are called Td-sites, while octahedral cation sites are named Oh-sites. The conventional cubic unit cell of the spinel contains 8 formula units, each of which consist of 32 anions and 24 cations (8 in Td-sites and 16 in Oh-sites), for a total of 56 atoms. The Td-sites form a diamond cubic sublattice with a repeat unit equals to the lattice parameter ($a$), sharing corners with Oh-site cations. While all the tetrahedra on the same plane are isolated, the octahedra line up along the ⟨110⟩ axes of the cubic lattice sharing edges. Just like the Td-sites, the periodicity associated with Oh-sites is also equals to $a$. Description of the atomic positions in the spinel depends on the choice of setting for the origin in the $Fd\bar{3}m$ space group. **Figure 1.4** illustrates the conventional cubic unit cell (Td-sites in the origin) of a spinel structure with lattice parameter equals to $a$.

A major feature of the spinel compounds is that their structure can accommodate a significant amount of cation disorder [70]. Notably, the parent compounds of the $Fe_{3-x}Cr_xO_4$ series, $Fe_3O_4$ and $FeCr_2O_4$, arrange trivalent and divalent cations in an opposite way [71], [72]. The magnetite has trivalent $Fe^{3+}$ cations in Td-sites and both $Fe^{3+}$ and $Fe^{2+}$ cations randomly distribute in Oh-sites, as described by the general formula: $[Fe^{3+}]_{Td}[Fe^{2+}Fe^{3+}]_{Oh}O_4$. It presents a so-called inverse spinel structure with $a$ equals to 0.8396 nm. In contrast, the chromite has divalent $Fe^{2+}$ cations in Td-sites and $Cr^{3+}$ cations in Oh-sites, that is: $[Fe^{2+}]_{Td}[Cr^{3+}Cr^{3+}]_{Oh}O_4$. It exhibits thus a so-called normal spinel structure with $a$ equals to 0.8377 nm. The oxygen-parameters ($u$) are 0.253 for $Fe_3O_4$ and 0.263 for $FeCr_2O_4$, [73] which are comparable to the ideal ($u$ = 0.25) for perfect cubic close packing of the anionic framework. Note that the presence of $Fe^{2+}$ cations in Td-sites introduces small distortions in the spinel structure. At room temperature, the Fe cations in $Fe_3O_4$ (top right **Figure 1.4**) display almost perfect tetrahedron and octahedron local environments. In Td-sites, $Fe^{3+}$ cations form with oxygen Fe–O bonds of 0.1912 nm length and O–Fe–O angles of 109°28′, whereas $Fe^{2+/3+}$ cations in Oh-sites form Fe–O bonds of 0.2097 nm length and O–Fe–O angles close to 90° (*i.e.,* 87°57′ and 92°03′). In parallel, the $Cr^{3+}$ cations in Oh-sites of $FeCr_2O_4$ (bottom right **Figure 1.4**) form a more distorted octahedron with Cr–O bonds of 0.1994 nm length and O–Cr–O angles of 83°45′ and 96°15′. However, the $Fe^{2+}$ cations in this compound keep an almost perfect tetrahedron local environment, with Fe–O bonds of 0.1997 nm length and O–Fe–O angles of 109°28′. In **Chapter 4**, the point symmetry of Fe and Cr had to be dictated in order to exploit the spectroscopic data of $Fe_{3-x}Cr_xO_4$ series. For simplicity's sake, the Oh and Td-sites of the entire series were approximated by the $O_h$ and $T_d$ point groups, respectively.

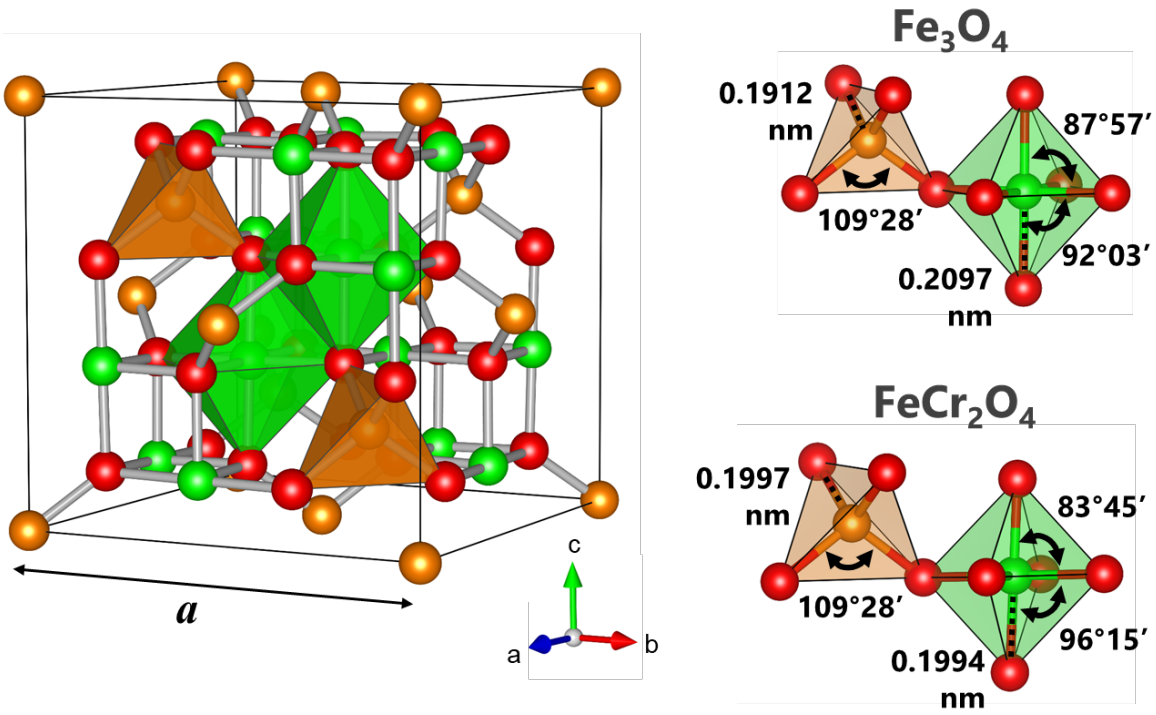


**Figure 1.4.** Close-packed cubic unit cell of $Fe_{3-x}Cr_xO_4$ series with Td-sites highlighted in orange and Oh-sites in green. At top right, the local structure of Fe cations in Oh and Td-sites of magnetite. In Td-sites, $Fe^{3+}$ cations form Fe–O bonds of 0.1912 nm length and O–Fe–O angles of 109°28′, whereas $Fe^{2+/3+}$ cations in Oh-sites form with oxygen Fe–O bonds of 0.2097 nm length and O–Fe–O angles of 87°57′ and 92°03′. At bottom right, the local structure of Cr and Fe cations in Oh and Td-sites of chromite, respectively. In Oh-sites, $Cr^{3+}$ cations form a more distorted octahedron with Cr–O bonds of 0.1994 nm length and O–Cr–O angles of 83°45′ and 96°15′, while the $Fe^{2+}$ cations constitute almost perfect tetrahedron with Fe–O bonds of 0.1997 nm length and O–Fe–O angles of 109°28′.

A key point in studying the $Fe_{3-x}Cr_xO_4$ series is to comprehend how the structure of these spinel oxides evolves from the inverse $Fe_3O_4$ to the normal $FeCr_2O_4$. Herein, cation distribution is described by the general formula: $[Fe^{3+}_{y}Fe^{2+}_{1-y}]_{Td}[Fe^{2+}_{y}Fe^{3+}_{2-x-y}Cr^{3+}_{x}]_{Oh}O_4$, where $y$ accounts for cation disorder and is commonly named as inversion parameter or inversion ratio. As abovementioned, the limiting compositions in this series present the two completely ordered configurations: inverse ($y$ = 1) and normal ($y$ = 0). Disorder occurs for intermediate compositions, since $Fe^{2+}$ cations can be displaced from Oh to Td-sites. The first evidence of cation disorder for intermediate compounds was observed in the unit cell parameter, which exhibits a non-linear variation with composition. **Figure 1.5** shows the evolution of lattice parameters determined from X-ray diffraction investigations [71], [72], [74], [75] of synthetic powder samples of well-known $x$ composition. According to these results, $Fe_{3-x}Cr_xO_4$ bulk samples can be divided (crystallographically) into three distinct regions: (I) $0 < x < 0.5$, (II) $0.6 < x < 1.3$ and (III) $1.4 < x < 2.0$. In summary, the cell parameter decreases for $x$ up to 0.5, increases for values between 0.6 and 1.3 and then decreases again for $x$ greater than 1.4. This behavior is associated to changes in the cation distribution among Td and Oh sublattices. Small reductions of $a$ parameter for $x < 0.5$ result from the replacement of $Fe^{3+}$ cations by slightly smaller $Cr^{3+}$ cations in Oh-sites, whereas the enhancement of $a$ parameter for $0.6 < x < 1.3$ can be understood

by the displacement of larger $Fe^{2+}$ into Td-sites. [10] Compositions with $x$ over 1.4 are assumed to have the normal type of spinel structure, so $a$ parameter decreases again because $Fe^{3+}$ cations are replaced by smaller $Cr^{3+}$ in Oh-sites.

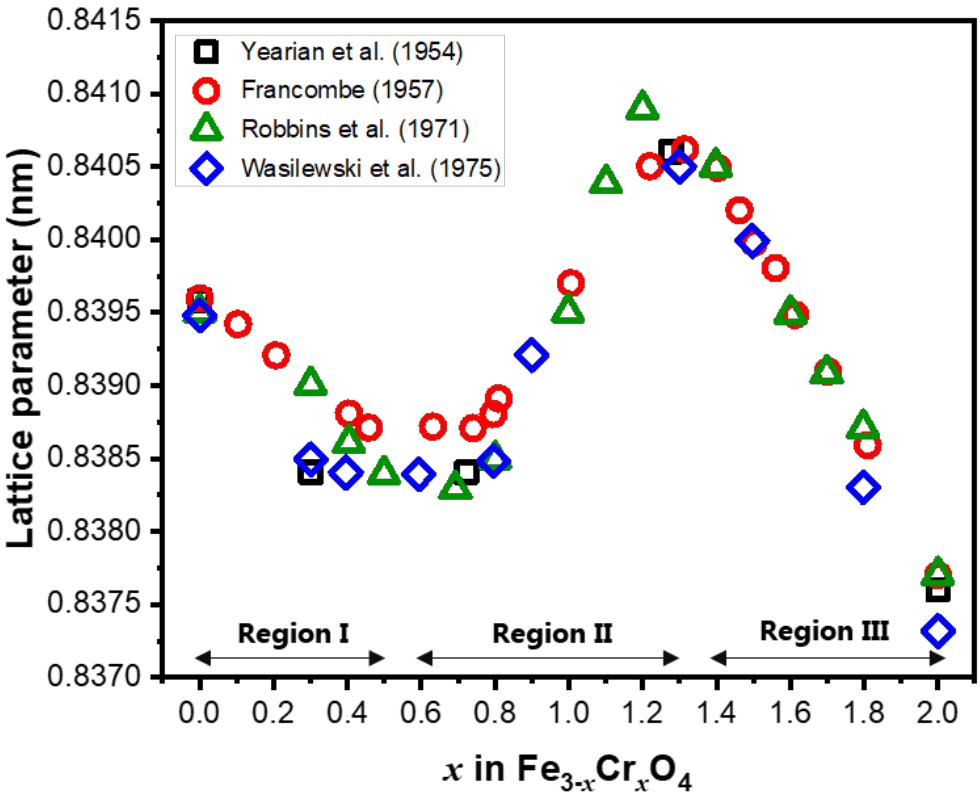


**Figure 1.5.** Room temperature lattice parameter (nm) evolution for $Fe_{3-x}Cr_xO_4$ bulk series. The experimental data were taken from the literature: Yearian *et al.* [71] (black squares), Francombe [72] (red circles), Robbins *et al.* [74] (green triangles) and Wasilewski *et al.* [75] (blue diamonds).

The physical and chemical properties of the $Fe_{3-x}Cr_xO_4$ series relate closely to the distribution of the Fe and Cr cations among the Td and Oh-sites, as discussed more in detail in the next section. Hence, much effort has been made to determine the cation distribution of intermediate compositions and disagreements are often found in the literature. **Figure 1.6** compares the inversion parameter deduced by Yearian *et al.* [71], Francombe [72] and Robbins *et al.* [74] for the $Fe_{3-x}Cr_xO_4$ bulk series ($0 \leq x \leq 2$).

In their study, Yearian *et al.* [71] proposed an empirical linear relation between lattice parameter ($a$) and inversion parameter ($y$) for a given $x$ composition:

$$a\ (nm) = 0.8460 - 0.0042x - 0.0064y \qquad (1.1)$$

To do so, few assumptions had to be made about the cation distribution. First, following empirical rules of ion distribution proposed by Verwey and Heilmann [70], they supposed that none of the $Cr^{3+}$

[10] Ionic radii for high spin $Cr^{3+}$, $Fe^{3+}$ and $Fe^{2+}$ species are 75.5 pm, 78.5 pm and 92.0 pm, respectively [76].

ions goes in Td-sites. Then, they performed a linear regression between the different crystallographic regions shown in **Figure 1.5**. They observed that the slope of the lattice parameter *vs.* composition curve of region I is the same within the experimental error as in region III. According to them, this would be expected if replacement of $Fe^{3+}$ by $Cr^{3+}$ were taking place in Oh-sites only. Hence, they assigned completely ordered configurations for the extreme compositional regions of this solid solution, which means inverse for $0 \leq x \leq 0.3$ and normal for $1.3 \leq x \leq 2$. The rate of change of the degree of inversion, $dy/dx$, is therefore zero in both regions. Based on these assignments, the intermediate region (II) was represented by two stages of reversion from the inverse to the normal form with $dy/dx$ equals to -0.65 (~2/3) and -1.31 (~4/3). The $y$ values at the limits of each of the four stages are depicted in **Figure 1.6**.

In the late 1950's, Francombe [72] retook the lines suggested by Yearian *et al.* [71] to calculate the approximated cation distribution for the $Fe_{3-x}Cr_xO_4$ series with $1 \leq x \leq 2$. For lower Cr-content ($x < 0.5$), they also assumed that the solid solution retained a complete inverse structure. For region II, they considered two steps over which the cation distribution gradually changes to the normal type, this process being fulfilled at $x \sim 1.3$ (end of region II). Beyond this value, all compositions were assumed to have normal configuration. For comparison sake, few $y$ values obtained by Francombe [72] are shown in **Figure 1.6**.

A decade later, Robbins *et al.* [74] constructed a diagram of site distribution as a function of composition for the $Fe_{3-x}Cr_xO_4$ series using Mössbauer spectroscopy[11] and magnetic measurements. The extrapolation of this diagram is depicted in green dashed lines in **Figure 1.6**. In region III ($x > 1.3$), their results were in agreement with the distribution proposed by Francombe [72], which stated that $Fe^{3+}$ cations substituted for $Cr^{3+}$ occupy Oh-sites exclusively. For $1.5 \leq x \leq 2.0$, the $Fe_{3-x}Cr_xO_4$ series was described by the general formula: $[Fe^{2+}]_{Td}[Fe^{3+}{}_{2-x}Cr^{3+}{}_x]_{Oh}O_4$ where $y = 0$. For intermediate compositions (region II), Robbins *et al.* [74] also agreed with Francombe [72] that $Fe^{2+}$ cations are displaced from Oh to Td-sites. According to Mössbauer and magnetic measurements, each added $Cr^{3+}$ displaces one $Fe^{2+}$ from the Oh-sites. Hence, in this region, the $Fe_{3-x}Cr_xO_4$ series assumes an intermediate configuration described by the general formula: $[Fe^{3+}{}_yFe^{2+}{}_{1-y}]_{Td}[Fe^{2+}{}_yFe^{3+}{}_{2-x-y}Cr^{3+}{}_x]_{Oh}O_4$ with $0.62 \leq x \leq 1.25$ and $y$ gradually decreasing from 0.7 to 0. On the other hand, with regard to the lower Cr-content region ($x < 0.5$), Robbins *et al.* [74] differed significantly from Francombe [72]. According to the former, even small amounts of $Cr^{3+}$ cations in the magnetite structure can displace both $Fe^{3+}$ and $Fe^{2+}$ from the Oh-sites. Therefore, the solid solution was no longer taken as a complete inverse spinel, but rather as an intermediate configuration. For $0 \leq x \leq 0.5$, Robbins *et al.* [74] described the series using the general formula: $[Fe^{3+}{}_{1-x/2}Fe^{2+}{}_{x/2}]_{Td}[Fe^{2+}{}_{1-x/2}Fe^{3+}{}_{1-x/2}Cr^{3+}{}_x]_{Oh}O_4$.

Whether or not there are $Fe^{2+}$ ions occupying Td-sites for chromium-doped magnetite is a common issue in the literature. Few years after Robbins's work, Ok *et al.* [78] revised the $^{57}Fe$

[11] Mössbauer spectroscopy [77] is an analytical technique based on the nearly recoil-free emission and absorption of nuclear gamma rays in solids. This method is sensitive to small changes in the chemical environment of certain nuclei. For instance, for Fe isomer shift occurs due to differences in nearby electron densities, which enables to differentiate $Fe^{2+}$ from $Fe^{3+}$ species. Hyperfine structure due to interactions between the nuclei and a surrounding magnetic field enables to distinguish Oh and Td-sites.

Mössbauer data at room temperature for $Fe_{3-x}Cr_xO_4$ with $0 \leq x \leq 0.5$. They observed that the ratio of the total area of the Oh subspectrum to that of the Td subspectrum steadily decreases to $x$ up to 0.3, as if no $Fe^{2+}$ ions occupy Td-sites. For $x$ near 0.5, the ratio changes and $Fe^{2+}$ ions apparently occupy the Td-sites; however, their Mössbauer parameters are similar to those of the Oh-site Fe ions. Hence, according to them, when $Cr^{3+}$ replaces $Fe^{3+}$ at Oh-sites of magnetite, no $Fe^{2+}$ ions are displaced from Oh to Td-sites until $x = 0.3$. For $x > 0.3$, small but increasing numbers of $Fe^{2+}$ ions move to Td-sites.

In addition to different assumptions and data treatments, another explanation for divergent results in the cation distribution is the presence of point defects, such as interstitial cations and vacancies. As perceived by Yearian *et al.* [71], the presence of vacancies can stabilize the inverse structure to a remarkable degree. In the same vein, Viart *et al.* [79] observed no $Fe^{2+}$ in Td Mössbauer subspectrum for lacunar Fe/Cr-substituted ferrite compounds with Cr/Fe ratio of 0.2 and 0.3.

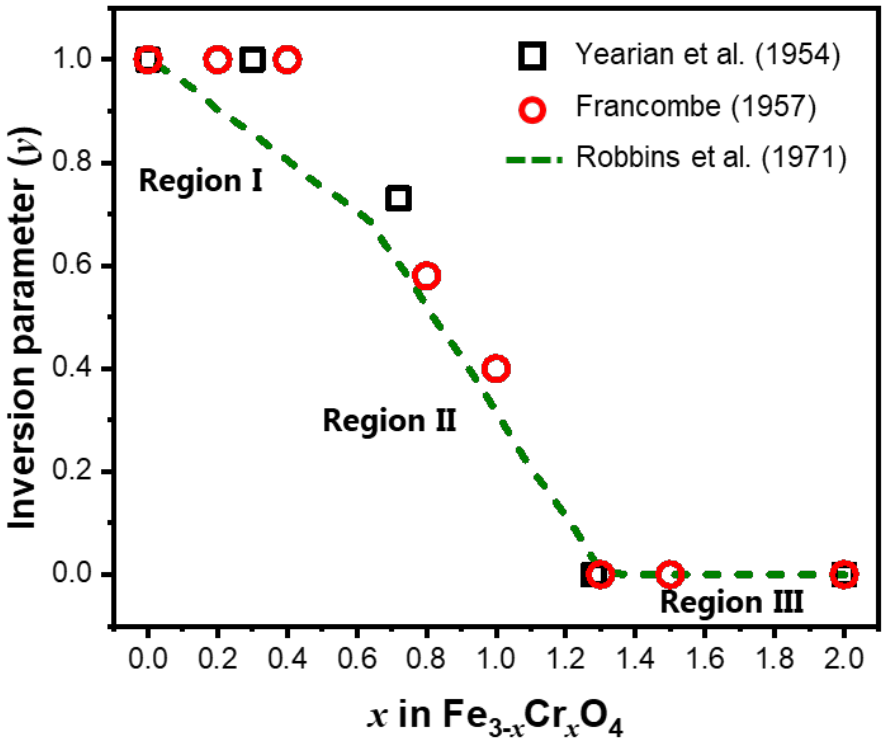


**Figure 1.6.** Inversion parameter ($y$) deduced for the $Fe_{3-x}Cr_xO_4$ series, as described by the general formula: $[Fe^{3+}_yFe^{2+}_{1-y}]_{Td}[Fe^{2+}_yFe^{3+}_{2-x-y}Cr^{3+}_x]_{Oh}O_4$. Herein, $y$ values range from 0 for normal ordering to 1 for a complete inverse spinel structure. Data from the literature: Yearian *et al.* [71] (black squares), Francombe [72] (red circles), Robbins *et al.* [74] (dashed green lines).

## 1.3.2 Structural and physicochemical properties of $Fe_{3-x}Cr_xO_4$ series

Besides an interesting evolution of cation disorder, the members of the $Fe_3O_4$-$FeCr_2O_4$ solid solution exhibit composition-dependent magnetic ordering, structural phase transitions, and different conduction mechanisms. The present section discusses in detail the structural, magnetic and electronic properties of $Fe_{3-x}Cr_xO_4$ bulk samples, starting by the magnetic ordering of the parent compound $Fe_3O_4$.

### 1.3.2.1 The magnetic structure

Since Néel [80] exposed his theory of ferrimagnetism and antiferromagnetism for ferrites in 1948, $Fe_3O_4$ has been classified as a typical ferrimagnetic material. In this landmark paper, Néel proposed that the magnetic interaction between cations in Td and Oh-sites (Td-Oh interaction) is strongly negative, while the interactions between cations of the same sublattice (Td-Td and Oh-Oh interactions) are weak. The sum of these magnetic interactions favor antiparallel arrangement of spins in Td and Oh-sites, the so-called collinear Néel configuration. Hence, the net magnetic moment ($\mu_{total}$) is written as the difference between the Oh ($\mu_{Oh}$) and Td ($\mu_{Td}$) lattice magnetizations:

$$\mu_{\mathrm{total}} = \sum \mu_{\mathrm{Oh}} - \sum \mu_{\mathrm{Td}} \tag{1.2}$$

This magnetic ordering justifies the magnetic moment of about 4 $\mu_B$ per formula unit (f.u.) prior measured for $Fe_3O_4$, since the contributions of $Fe^{3+}$ ions ($3d^5$, S = 5/2) on each sublattice cancel out and the net magnetic moment comes mostly from the remaining $Fe^{2+}$ cations ($3d^6$, S = 2).

The mechanism that makes the Fe ions cooperate to produce an ordered array of magnetic vectors throughout the spinel lattice is the exchange interaction, which results from the overlap of the orbitals of nearest neighbor atoms or ions. In spinel oxides, the predominant magnetic interactions are super-exchange interactions. This indirect exchange occurs because non-magnetic oxygen ions provide a link between nearest neighbor magnetic cations that are otherwise too far apart to direct overlap their $3d$ lobes [81]. The theory of super-exchange was first introduced by Kramers [82] in 1934 and then essentially developed in the 1950's by Anderson [83], [84], Goodenough [85], [86] and Kanamori [87]. Determining the value or even the sign of the magnetic coupling between two cations can be a very complex task, since one must consider all orbitals involved, cations and ligands, and their symmetries. According to Goodenough-Kanamori rule, antiferromagnetic interactions occur where the virtual electron transfer is between overlapping orbitals that are each half-filled, whereas virtual electron transfer from half-filled to an empty orbital or from a filled to a half-filled orbital produces ferromagnetic interactions. Without dwelling on the quantum description of the super-exchange mechanism, the efficiency of these interactions depends globally on the degree of overlap of the orbitals and, therefore, on the metal-oxygen distance and the metal-oxygen-metal angle ($\alpha$). If the orbital of the cations and that of the anions overlap each other considerably, the coupling is strong. For instance, the Td-Td interactions are very weak because of the larger distance between these cations. They do not affect the magnetic order as far as there are enough magnetic ions on the Oh-sites.

**Figure 1.7** shows a simplified scheme of possible magnetic interactions between the $p$ orbitals of $O^{2-}$ ions and the $3d$ orbitals of $Fe^{2+}$ and $Fe^{3+}$ ions. As discussed by Anderson [83], [84], the theory of superexchange estimates a maximum antiferromagnetic interaction for $\alpha$ = 180° and a weak interaction for $\alpha$ = 90°. Although $\alpha$ = 180° does not occur in the spinel structure, the 125° angle in the Td-Oh configuration still yields a significant strong antiferromagnetic interaction for the $Fe^{3+}$ ions in $Fe_3O_4$, as depicted in bottom right **Figure 1.7**. For the Oh-Oh configuration ($\alpha$ = 90°), there

are two exchange mechanisms in competition: the super-exchange, which includes an antiferromagnetic and a ferromagnetic component, and the Zener double-exchange [88]. As shown in top left **Figure 1.7**, the double exchange occurs due to the transfer of an electron from $Fe^{2+}$ ions towards the half-filled $d$-levels of $Fe^{3+}$ ions. This interaction is weak and often confused or masked by super-exchange interactions. For clarity's sake, **Figure 1.7** (bottom left) illustrates one possible combination of these exchange mechanisms in a 3D spinel structure.

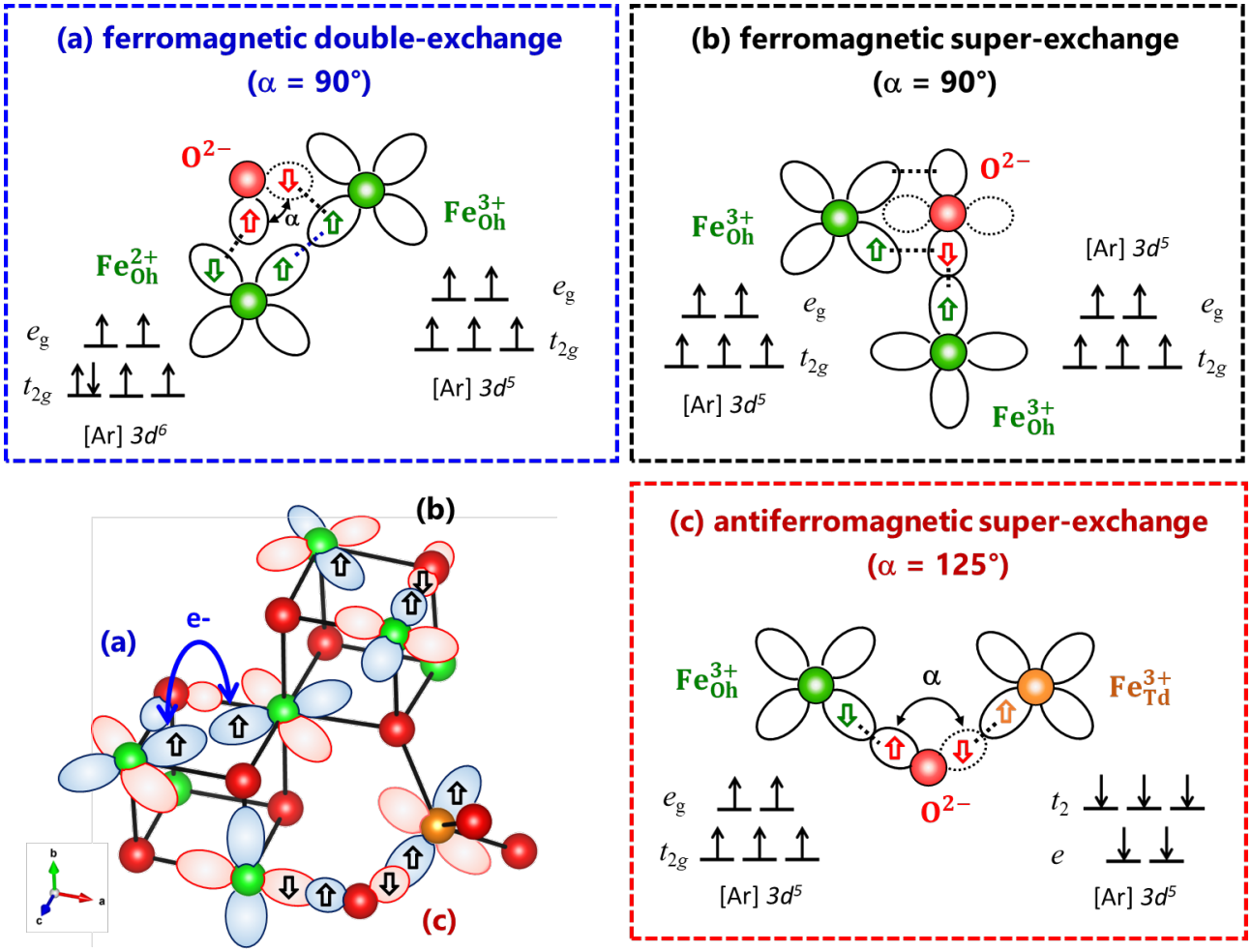


**Figure 1.7.** Scheme of magnetic exchange interactions in ferrites for overlapping angles α of 90° (top) and 125° (bottom). Below the overlapping orbitals, the magnetic configuration of the 3$d$ orbitals on Oh and Td-sites are shown. Because of the crystal field, 3$d$ orbitals of the Oh-site cations split into the triply degenerate high-energy $t_{2g}$ states and doubly degenerated $e_g$ states, whereas the Td-site cations exhibit two low energy $e$ states and three high energy $t_2$ states. Color code: Td-site (orange), Oh-site (green) and oxygen (red).

In the $Fe_{3-x}Cr_xO_4$ series ($0 \leq x \leq 2$), Cr substitutes Fe exclusively in Oh-sites of the spinel lattice, assuming a 3+ valence ($3d^3$, S = 3/2). Hence, a primary effect of increasing Cr content in this system would be to change the average magnetic moment on the Oh-sites and the competition between Td-Oh and Oh-Oh exchange interactions. **Figure 1.8a** shows the magnetic moment as a function of the composition ($x$) at temperatures of T = 1.5 K [74] and T = 300 K [75], measured for bulk samples in saturated magnetic field. In general, one observes that the magnetic moment decreases as $x$

increases at both temperatures, since $Fe^{3+}$ cations ($\mu$ = 5 $\mu_B$) are replaced by $Cr^{3+}$ cations ($\mu$ = 3 $\mu_B$). Note that at T = 1.5 K, $Fe_3O_4$ exhibits magnetic moment of 4.1 $\mu_B$ per f.u., as predicted using the collinear model presented by Néel (Equation 1.2, top **Figure 1.8b**). However, the moment of 0.8 $\mu_B$ for $FeCr_2O_4$ is considerably lower than the 2 $\mu_B$ predicted using the same model (Equation 1.2, bottom **Figure 1.8b**). Why is the Néel model not applicable for chromite at low temperature?

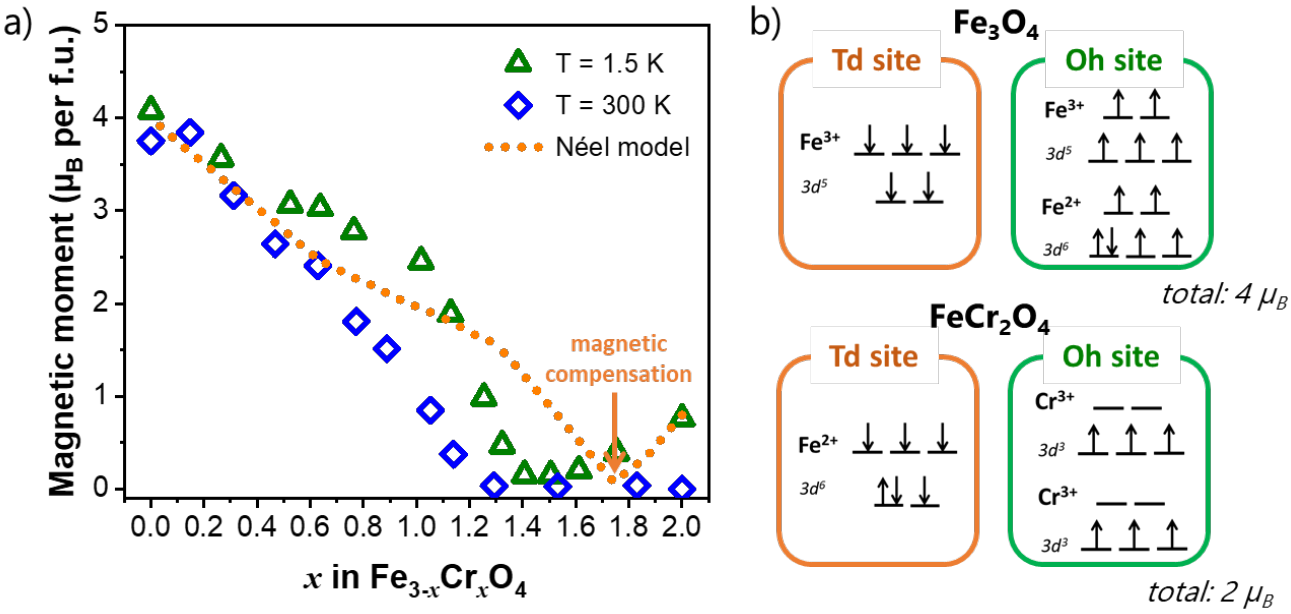


**Figure 1.8.** (a) Magnetic moment ($\mu_B$ per f.u.) evolution for $Fe_{3-x}Cr_xO_4$ bulk series at different temperatures. Experimental data taken from the literature: T = 1.5 K is from Robbins *et al.* [74] (green triangles) and T = 300 K is from Wasilewski *et al.* [75] (blue diamonds). These values were collected at magnetic induction equals to 1.6 T. The orange dots represent the net magnetic moment ($\mu_{total}$) calculated using Equation 1.2, the inversion parameter ($y$) determined by Robbins *et al.* [74], and resultant moment of 1.6 $\mu_B$ per $Cr^{3+}$ atoms: $\mu_{total} = 2 * (3 - y - 1.7x)$. (b) Magnetic configurations in inverse $Fe_3O_4$ (top) and normal $FeCr_2O_4$ (bottom) spinel structure, following the ideal Néel collinear configuration.

Very soon after Néel introduced his collinear model, it was shown that other magnetic structures could exist in spinel compounds when the magnetic cations is replaced by various magnetic or non-magnetic ions [81], [89]. In particular, this is the case when Td-Oh interaction is weakened by dilution of one of the sublattices and antiferromagnetic Oh-Oh interaction is no longer negligible. These competing interactions may break up the Oh-site into two sublattices whose moments make an angle between each other and the Td-site moment. This triangular uniform canting configuration was first introduced by Yafet and Kittel [90] in 1952. Such canted spin structure is thought to be the origin of low moments in Cr-containing spinels. Indeed, magnetic and neutron diffraction studies [91], [92] showed that the next-near neighbor $Cr^{3+}$-$Cr^{3+}$ magnetic interactions are antiferromagnetic in these spinel compounds. They compete with both near-neighbor Oh-Oh and Td-Oh interactions, since each Oh-site has 30 nearly equivalent next-near neighbors but only 6 near neighbors [74]. These opposing interactions split the Oh-site into two sublattices, whose canting angle with respect to the Td-site moment depends on the relative strength of the various

interactions. The canting of Oh-site moment decreases its net value. Hence, the resultant moment of 0.8 $\mu_B$ for $FeCr_2O_4$ at 1.5 K is the difference of 4 $\mu_B$ (due to $Fe^{2+}$ in Td-sites) and 3.2 $\mu_B$ (instead of 6 $\mu_B$) due to canting of $Cr^{3+}$ spin moments in Oh-sites.

Introducing small amounts of $Fe^{3+}$ ions ($\mu$ = 5 $\mu_B$) into the Oh-sites of $FeCr_2O_4$ should therefore lead to an increase in the Oh-site moment, which in turn should cause an initial decrease in the net moment. With further decrease in Cr-content, magnetic compensation ($\mu_{total}$ = 0) should be reached when Td and Oh-site moments are equal, followed by compositions in which $\mu_{Oh}$ exceeds $\mu_{Td}$. This is exactly the behavior seen at T = 1.5 K in **Figure 1.8a**. Even though a perfectly compensated composition was not found (*i.e.,* $\mu_{total} > 0$ for all samples), the measured magnetic moment does reach a minimum at $1.4 < x < 1.5$. If the moment of $Fe^{3+}{}_{Oh}$ was aligned completely parallel, magnetic compensation would occur at $x \sim 1.75$. The minimum between 1.4 and 1.5 suggest that $Fe^{3+}$ moments are also canted in these compounds. Because of the canted spin moments of $Fe^{3+}$ and $Cr^{3+}$, the Néel model (Equation 1.2) is no longer valid for compositions with $x > 0.5$, as shown by the trend drawn in orange dots in **Figure 1.8a**.

Unlike T = 1.5 K, the magnetic moment at T = 300 K steadily decreases as $x$ increases, reaching null values for $x$ greater than 1.3. This occurs because the disordering effects caused by the thermal energy dominates over the ordering force of the exchange [89]. Spins can only be perfectly parallel or antiparallel at the absolute zero of temperature. At finite temperature ($T \neq 0$ K), magnons are thermally excited so the spin vectors may rotate against each other, leading to disorder. The temperature at which the ferro- or ferrimagnetic spin structure is destroyed is the Curie temperature ($T_C$). **Figure 1.9** shows the evolution of Curie temperatures as a function of composition for the $Fe_{3-x}Cr_xO_4$ series. In general, one observes that $T_C$ decreases as $x$ increases, so that compounds having $x > 1.2$ become ferrimagnetic only below room temperature. Note that $T_C$ decreases slightly for limiting compositions ($x < 0.5$ and $x > 1.5$), while for intermediate compositions ($0.6 < x < 1.2$) $T_C$ decreases rapidly with increasing values of $x$. The sharp decrease in Curie temperature is probably related to the decrease in the inversion parameter from 0.7 to 0 (*i.e.,* the replacement of $Fe^{3+}$ on Td-sites by $Fe^{2+}$) in this same compositional range. According to Néel [80], in spinel oxides each ion experiences a field due to the ions on both spinel sublattices, so the Curie temperature of this ferrimagnet depends on the strength of inter (Td-Oh) and intra (Td-Td and Oh-Oh) sublattice exchange interactions. The presence of $Fe^{3+}$ on both Td and Oh-sites leads to strong Td-Oh antiferromagnetic interactions that are responsible for the high Curie temperatures of inverse ferrite spinels. For example, $T_C$ values for $Fe_3O_4$, $NiFe_2O_4$ and $CoFe_2O_4$ are 860 K, 865 K and 790 K, respectively [81]. Another factor contributing to the higher $T_C$ values for lower Cr-content is the occurrence of electron transfer from $Fe^{2+}{}_{Oh}$ to $Fe^{3+}{}_{Oh}$ ions. The charge hopping provides an additional ferromagnetic interaction through double exchange (**Figure 1.7b**), which helps to overcome the antiferromagnetic Oh-Oh interactions.

In spinel oxides, the magnetic transitions are usually accompanied by complicated structural phase transitions thanks to strong interactions among the spin, orbital and lattice degrees of freedom. The following section discusses the magnetic and structural phase transitions encountered in the spinel compounds of the $Fe_{3-x}Cr_xO_4$ series.

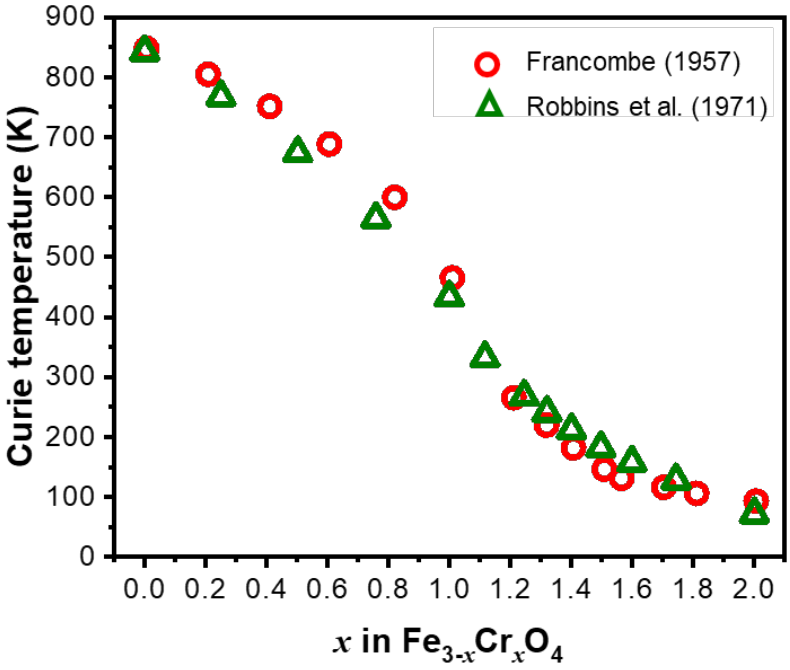


**Figure 1.9.** Curie temperature for $Fe_{3-x}Cr_xO_4$ bulk series with $0 \leq x \leq 2$. Experimental data taken from the literature: Francombe [72] (red circles) and Robbins *et al.* [74] (green triangles).

### 1.3.2.2 Magnetic and structural phase transitions

One possible cause of structural phase transitions in spinel oxides is the ordering of Jahn-Teller (JT) deformations, originating from orbitally active transition metals. Among the species in the $Fe_{3-x}Cr_xO_4$, the high-spin $Fe^{2+}$ cations ($3d^6$, S = 2) are the only JT active, which means that they can lower their energy by spontaneously deforming their Oh or Td environment. Briefly, the Jahn–Teller theorem [93] states that any non-linear system with a spatially degenerate electronic ground state may undergo a geometric distortion in order to remove that degeneracy, if this process lowers the overall energy of the species. In Oh (or Td) symmetry, the distortions cause further splitting of the $t_{2g}$ and $e_g$ (or $t_2$ and $e$) orbitals. JT effects are expected only if these orbitals are unevenly occupied, otherwise, there is no net change in energy. Thus, no JT effect is expected for $3d^3$ and high-spin $3d^5$ cations, like $Cr^{3+}$ and $Fe^{3+}$ in the $Fe_{3-x}Cr_xO_4$ system. However, strong JT effect is expected for high-spin $Fe^{2+}$ cations ($3d^6$) in Td environment, since they have an odd number of electrons occupying the high-energy $t_2$ orbitals, that is $(e)^3(t_2)^3$ electronic configuration. Therefore, the presence of $Fe^{2+}$ cations in Td-sites introduces phase transitions in the $Fe_{3-x}Cr_xO_4$ series, which are usually followed by magnetic order. The magnetic ordering is stabilized by reducing the lattice symmetry through a spin-lattice coupling (cooperative JT effect). For instance, at room temperature, $FeCr_2O_4$ is paramagnetic and presents a normal cubic spinel structure with $Fe^{2+}{}_{Td}$ only. Upon cooling from room temperature, JT effect leads to a cubic-to-tetragonal phase transition at 135 K, which is followed by a paramagnetic-to-collinear ferrimagnetic phase transition at 80 K. Then, another structural transition[12], tetragonal-to-orthorhombic, is observed for $FeCr_2O_4$ at 75 K, which is also followed by a

[12] The characteristic temperature of this transition slightly differs from one report to another.

magnetic transition towards a conical spiral magnetic at 40 K [94]–[96]. The magnetic ordering induced by JT effect distortions was assimilated to the origin of low moments in Cr-containing spinels. According to Baltzer and Wojtowicz [97], canted spin structures are not stable in the cubic spinel symmetry, but can be stabilized by trigonal or tetragonal distortions that are sufficient in number to alter the symmetry about at least a fraction of the $Cr^{3+}$ ions.

Much effort has been done to uncover the origin of the orbital ordering effect on the structural transition of spinel oxides since Verwey and Heilmann [70] first discussed their structure in 1947. Even though the observed complexity of the crystal distortions in the spinel $Fe_{3-x}Cr_xO_4$ system is usually attributed to the electronic state and the ionic arrangement of the cations placed on Oh-sites, the detailed features of the phase transitions are still under debate [94], [98], [99]. **Figure 1.10** shows the structural and magnetic phase diagram drawn by Ma *et al.* [94] for $Fe_{3-x}Cr_xO_4$ compounds ($1 \leq x \leq 2$), using magnetization, specific heat, X-ray, and neutron scattering measurements. As expected, this phase diagram is rather complex and clearly reflects the impact of increasing Cr-content on the JT distortions, $Fe^{2+}$-$Fe^{3+}$ electron hopping, cation disordering ($y$), spin-lattice and orbital-lattice interactions. Three major composition regions were discussed by Ma *et al.* [94]:

1. **Region I: $x \geq 1.7$.** In this region, Ma *et al.* state that compounds with $x \geq 1.7$ have the normal type of spinel structure ($y = 0$), which is in agreement with other authors (**Figure 1.6**). As for the magnetic transitions, they observed paramagnetic-to-collinear ferrimagnetic and collinear-to-conical ferrimagnetic phase transitions at $T_C$ and $T_N$, respectively. Cubic, tetragonal, and orthorhombic structures are observed in sequence upon cooling from room temperature. The cubic-to-tetragonal and the tetragonal-to-orthorhombic phase transitions are observed at $T_{S1}$ and $T_{S2}$, respectively. With increasing Cr-content, $T_C$ and $T_{S2}$ decreases, while $T_N$ and $T_{S1}$ increases. As aforementioned, $T_C$ decreases because the replacement of $Fe^{3+}$ by $Cr^{3+}$ decreases not only the Td-Oh exchange interactions but also the total moment of Oh-site ions. The decrease of $T_C$ drives $T_{S2}$ to decrease. Meanwhile, $T_N$ and $T_{S1}$ increases because of geometrical magnetic frustration. The presence of $Cr^{3+}$ cations in Oh-sites stabilizes JT distortion of $Fe^{2+}$ ions, which in turn favors a conical magnetic state.

2. **Region II: $1.3 \leq x < 1.7$.** As in $x \geq 1.7$, compounds with $1.3 \leq x < 1.7$ also have the normal type of spinel structure ($y = 0$). Even though Ma *et al.* observed upon cooling a cubic-to-tetragonal followed by a tetragonal-to-orthorhombic phase transitions in this region, the driving force of these structural transitions are the opposite of those in region I. That is, the spin-orbital coupling effect on JT distortion leads to the first structural transition ($T_{S1}$), while the second one ($T_{S2}$) is due to the Oh-site disorders of $Fe^{3+}$ and $Cr^{3+}$ ions. Hence, $T_C$ accompanies $T_{S1}$, which decreases linearly with increasing $x$, whereas the spin reorientation transition, occurring at $T_N$, increases with $x$. No conical spin structure is observed for $x < 1.4$, because the $Fe^{3+}$ Oh-Oh antiferromagnetic exchange interactions are weaker than the ones of $Cr^{3+}$ and, consequently, they compete less with the strong Td-Oh interactions. The moments of $Fe^{3+}{}_{Oh}$ ions are then less canted than the ones of $Cr^{3+}{}_{Oh}$. In fact, according to Lyons et *al.* [100], the conical state is only stable if the factor $u$, which is tightly related with

both spin moments ($S_i$) and exchange interactions ($J_{ij}$) between Td and Oh-site cations, has values between $8/9 \leq u \leq 1.298$. This factor was described as:

$$u = 4J_{Oh\text{-}Oh}S_{Oh} / 3J_{Td\text{-}Oh}S_{Td} \quad (1.3)$$

Although it is hard to obtain quantitatively the value of $u$ due to the lack of information on the individual exchange energies ($J_{ij}$), one can expect from magnetic measurements that $S_{Oh}$ and $J_{Td\text{-}Oh}$ decrease with increasing Cr-content, as explained in **Section 1.3.2.1**.

3. **Region III: $1.0 \leq x < 1.3$.** Unlike region I and II, Ma *et al.* state that compounds with $1.0 \leq x < 1.3$ have an intermediate spinel configuration, which makes the system even more complicated. In this region, $T_C$ increases more sharply with decreasing Cr-content than in region II due to electron hopping between $Fe^{2+}$ and $Fe^{3+}$ ions in Oh-sites, as aforementioned. Magnetic ordering and structural distortion temperature are disconnected and the temperatures $T_{S1}$ and $T_{S2}$ disappear. Nonetheless, some structural distortions seem to persist. Ma *et al.* suggested that, at lower temperature, there are possible orthorhombic/monoclinic distortions related to JT active $Fe^{2+}$ ions on Oh-sites, as found in the inverse spinel $Fe_3O_4$. They are presented as the shaded blue region in **Figure 1.10**.

In addition to cooperative Jahn-Teller effects, changes in the spinel structure can be also due to redistribution of the cations between the spinel sublattices. Notably, the parent compound $Fe_3O_4$ suffers first order transition near 120 K driven by $Fe^{2+}/Fe^{3+}$ charge ordering on Oh-sites. This characteristic temperature is known as the Verwey transition temperature ($T_V$), since Verwey *et al.* [101]–[103] in a pioneer study proposed a simple charge order model that led to an orthorhombic symmetry for the low temperature phase. According to them, the rather high electrical conductivity of $Fe_3O_4$ at room temperature is due to rapid transfer of the "extra" electron between equivalent Oh-sites. The formal charge distribution in magnetite is then described as $[Fe^{3+}]_{Td}[Fe^{2.5+}]_{Oh}O_4$ and the $d$-orbital occupation at Oh-sites represented as $(t_{2g}\downarrow)^3(e_g\downarrow)^2(t_{2g}\uparrow)^{0.5}$. Cooling below $T_V$ freezes the "extra" electron at $Fe^{2+}{}_{Oh}$ sites. Consequently, a configuration of (001) planes alternatively occupied by $Fe^{2+}{}_{Oh}$ and $Fe^{3+}{}_{Oh}$ ions is observed. Such charge localization effect has been probed by Mössbauer measurements [104], which detects a 2.5+ charge on the iron atoms above $T_V$ and 2+ and 3+ charges below $T_V$.

After almost 80 years since Verwey *et al.* [101], [102] proposed their charge order model, the crystallographic structure of the low-temperature phase remains controversial. Few decades after Verwey's work, neutron-scattering experiments [105] showed the symmetry of the low temperature unit cell to be monoclinic and, more recently, deviations from the monoclinic cell have also been reported [106]. In order to understand the Verwey transition, many theoretical models for charge ordering have been proposed [107], [108], including purely electronic, electron–phonon coupled, and bond dimerized ground states. However, the nature of the Verwey transition in magnetite has not yet been clarified.

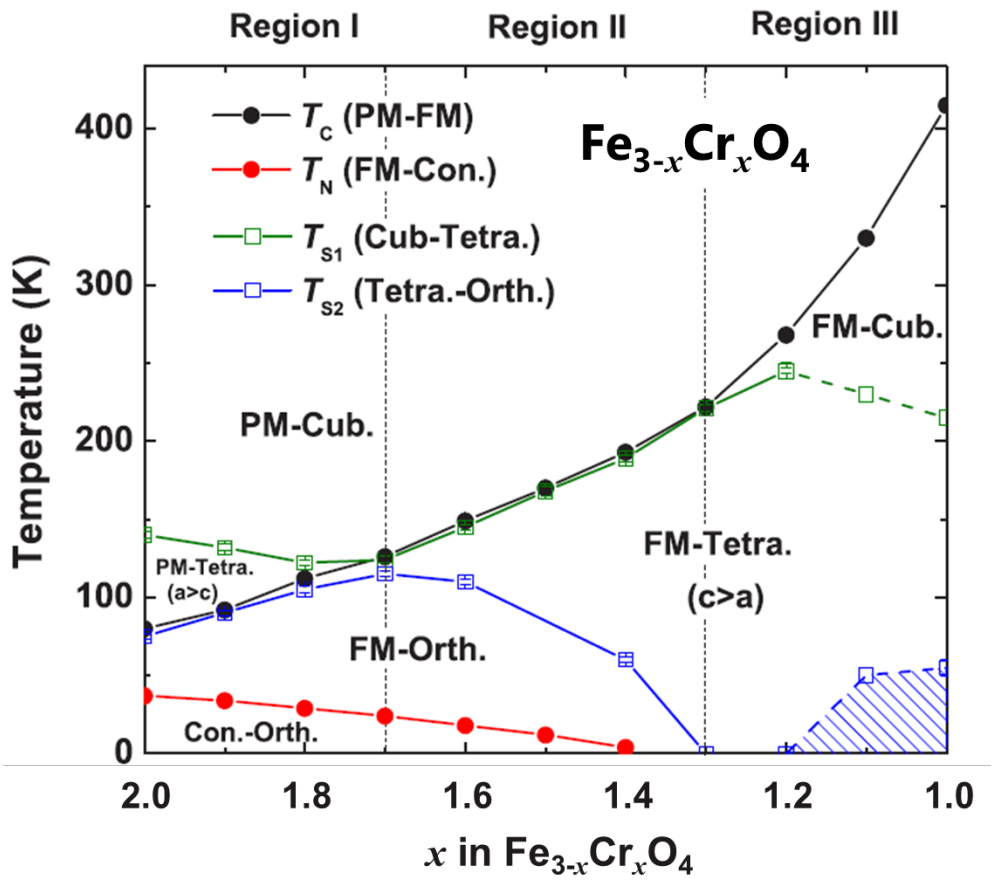


**Figure 1.10.** The temperature versus Cr content ($x$) phase diagram of $Fe_{3-x}Cr_xO_4$. $T_C$ is the paramagnetic-to-collinear ferrimagnetic phase transition temperature (black lines and dots), $T_N$ is the collinear-to-conical ferrimagnetic phase transition temperature (red lines and dots), $T_{S1}$ is the cubic-to-tetragonal lattice transition temperature (green line with open squares), and $T_{S2}$ is the tetragonal-to-orthorhombic lattice transition temperature (blue line with open squares). The solid lines show the structural and magnetic transitions, while the dashed lines display the possible structural distortions. Figure adapted from Ma *et al.* [94].

It is important to highlight that the structural transition at $T_V$ modifies a number of physical properties of $Fe_3O_4$. Above $T_V$ (and below $T_C$), $Fe_3O_4$ is a known half-metal ferrimagnetic spinel with hard, intermediate and easy magnetization axes along the cubic <001>, <110> and <111> directions, respectively. Below $T_V$, the electrons on the Oh-sites form a polaronic charge-ordered state inducing a monoclinic distortion. A sharp drop in the conductivity is therefore observed[13] and the hard, intermediate and easy magnetization axes change to coincide with the monoclinic $a$ (cubic $[1\bar{1}0]$), $b$ (cubic [110]) and $c$ (cubic [001]) directions [81], [109].

The Verwey transition temperature is very sensitive for impurities and non-stoichiometry. It can decrease to about 80 K for impurity levels as low as 0.3% [81], [110]. Hence, a decrease in $T_V$ or even vanishing of this transition is expected for Cr-doped magnetite. Indeed, according to Robbins *et al.* [74], the presence of $Cr^{3+}$ on Oh-sites apparently prevents the formation of a crystallographically ordered $Fe^{2+}/Fe^{3+}$ structure, which presumably induces the phase transition.

[13] The Verwey transition is often considered as a metal-insulator transition, which strictly speaking is not correct since magnetite does not fit into either of these two categories.

### 1.3.2.3 The electronic transport

Another important result of substitutional Cr in $Fe_{3-x}Cr_xO_4$ series is the modification in the conduction mechanism. First, a brief description of the conduction behavior of the parent compound $Fe_3O_4$ is given. Bulk magnetite is a reasonably good n-type conductor with an unusual evolution of the conductivity with temperature, as depicted in **Figure 1.11**. At elevated temperatures, this material shows a rather flat temperature dependence of conductivity such that the conductivity near the melting point (~1870 K) is almost the same as at room temperature (~200 $\Omega^{-1}.cm^{-1}$). At $T_C$ (860 K), a change of the slope is observed in temperature dependence conductivity curve (**Figure 1.11a**). Above $T_C$, the slight increase of conductivity is often related to the appearance of carriers in, or migration of $Fe^{2+}$ ions to, the Td-sites. Below $T_C$, the conductivity also increases and a maximum of 250 $\Omega^{-1}.cm^{-1}$ appears at about 350 K, which is usually attributed to the correlation and/or polaron effect of carriers. Then, an abrupt drop of the conductivity by several orders of magnitude (**Figure 1.11b**) is observed upon cooling through Verwey transition ($T_V$) [111], [112]. This unusual conduction behavior has confounded the interpretation of possible conduction mechanisms over the years, especially at low temperatures where the results are more ambiguous [113]–[116]. Hence, no unified model has yet emerged for $Fe_3O_4$.

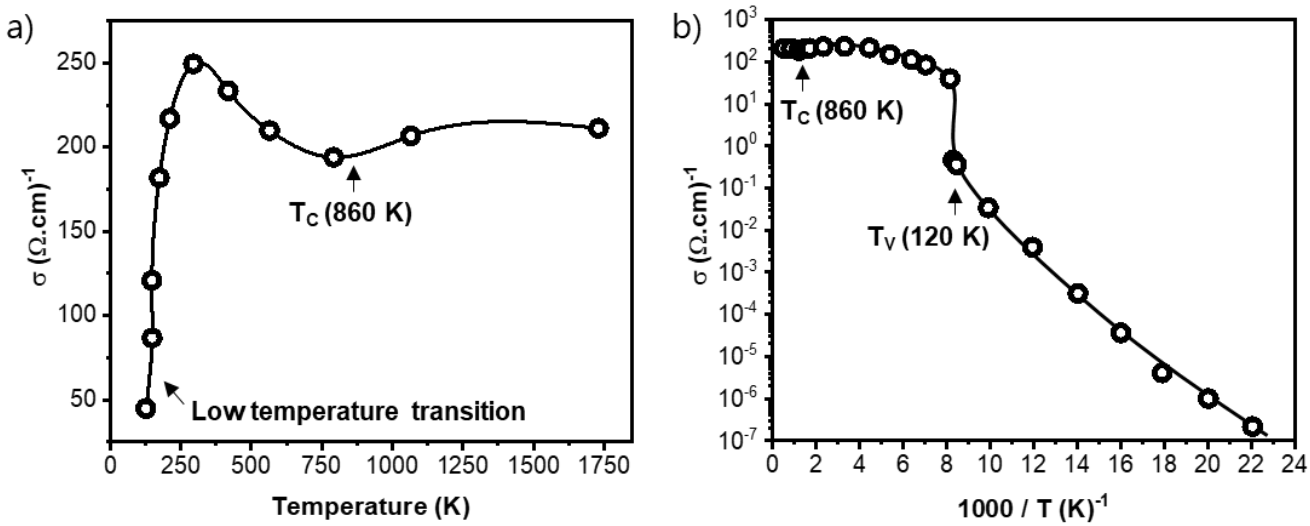


**Figure 1.11.** Temperature (T) dependence on the dc conductivity (σ) of $Fe_3O_4$ single crystal. The magnetite has several conduction regimes depending on the temperature, as highlighted in (a). The conductivity passes through a maximum at about 350 K and then shows a drop of two orders of magnitude at about 120 K ($T_V$), as verified in (b). Experimental data from Miles *et al.* [111].

The most common types of transport mechanisms in semiconductors are band and polaron-hopping [31]. Band-like carrier transport occurs when electron or hole carriers are thermally activated and transported to delocalized states. This mechanism is usually taken for granted in conventional semiconductor systems. However, transition metal oxides are prone to localize charge carries due to the strong electron correlation within the valence $d$-orbitals. In this case, transport occurs via polaron-hopping through localized states in the vicinity of the Fermi energy instead of band conduction

mechanism. The creation of polarons is generally induced by lattice distortions in a process known as self-trapping. In small polaron conductors, localized self-trapped state is energetically favorable over the delocalized band-like state, while in band-conductors, the delocalized state is stable.

Polarons can be small or large. In small polaron conductors, the carrier (electron or hole) in the self-trapped state is localized at one or few atoms. Its formation can often be attributed to a change of the oxidation state of a particular ion. On the other hand, large-polaron has higher length scale of polarization. It can directly and quickly equilibrate with the lattice upon carrier generation and it still maintains band-like transport properties. In fact, both band and hopping conduction mechanism can co-exist in a system, since a certain amount of self-trapped carriers can be thermally excited into the respective band-state at finite temperature. Recently, experimental results are often combined with theoretical approaches (*e.g.* DFT calculations) [31], [117], [118] in order to confirm whether the transport mechanism of a semiconductor is band or small polaron conduction.

For later use, a brief review of some elementary concepts pertaining to electrical phenomena will be helpful. The general expression of electron conductivity σ [119], [120] (which is the inverse of resistivity, ρ) may be stated in terms of the number of charge carriers ($n$), charge on an electron ($e$) and charge mobility ($\zeta$):

$$\sigma = \frac{1}{\rho} = ne\zeta \tag{1.4}$$

Whereas $n$ is governed solely by the impurity content or by the sample stoichiometric, $\zeta$ exhibits dependence on temperature. For semiconductors, the temperature dependent conductivity, $\sigma(T)$, is usually given by the relation:

$$\sigma(T) = \sigma_0 \times e^{-(E_t/k_B T)^p} \tag{1.5}$$

where the pre-factor $\sigma_0$ is the conductivity at infinite temperature ($T \rightarrow \infty$), $E_t$ is the transition energy, $k_B$ is the Boltzmann's constant. The formula of the pre-factor and the power-law dependence ($p$) are related to the type of conduction mechanism. For instance, considering the simplest possible description of electrical transport between localized states, the conductivity can be modeled in the small polaron approximation. Thus, Equation 1.4 is written as the probability that a given cationic site will contain an extra charge carrier. In such case, the mobility is derived from three governing equations: the Einstein diffusion model, the random walk model and the effective number of jumps [120]. According to the Einstein model, $\zeta$ is:

$$\zeta = \frac{eD}{k_B T} \tag{1.6}$$

Hence, the number of charge carriers ($n$) is given by the total charge carrier density (N) times the fraction of conducting sites occupied by charge carriers (c') and the diffusion constant (D) is related to the effective number of jumps per unit of time ($\Gamma_{eff}$). Based on the random walk model, after $j$ jumps of distance $a$, the total distance ($\langle R_j^2 \rangle$) travelled by the hopping electron is:

$$\langle R_j^2 \rangle = ja^2 = (t\Gamma_{\text{eff}})a^2 = \left(\frac{1}{\text{g}}\right)\text{D}t \tag{1.7}$$

where $\Gamma_{\text{eff}}$ is effective number of jumps per unit of time ($t$) and g is a geometric factor that is constant for a given system[14]. Hence, the diffusion constant is given by:

$$\text{D} = \text{g}a^2\Gamma_{\text{eff}} \tag{1.8}$$

The effective number of jumps is proportional to the fraction of available jump sites, (1- c'), and it depends on the activation barrier ($e^{-(E_t/k_BT)}$). At its limit, $\Gamma_{\text{eff,max}}$ is equals to the lattice vibration frequency ($\nu_0$) due to coupling of electrons to phonons. Combining these relations, the effective number of jumps is written as:

$$\Gamma_{\text{eff}} = \nu_0(1 - \text{c}') \times \text{e}^{-(\text{E}_t/\text{k}_\text{B}\text{T})} \tag{1.9}$$

and the mobility assumes the following form:

$$\zeta = \frac{ega^2\nu_0(1 - \text{c}')}{\text{k}_\text{B}\text{T}} \times \text{e}^{-(\text{E}_t/\text{k}_\text{B}\text{T})} \tag{1.10}$$

The final form of the conductivity equation for the small polaron approximation is then derived by merging Equation 1.4 and Equation 1.10:

$$\sigma(\text{T}) = \frac{\text{Nc}'(1 - \text{c}')e^2\text{g}a^2\nu_0}{\text{k}_\text{B}\text{T}} \times \text{e}^{-(\text{E}_t/\text{k}_\text{B}\text{T})} \tag{1.11}$$

Therefore, at fixed temperature, $\sigma$ should be proportional to the product c'(1- c').

In the case of $Fe_3O_4$, the electron transport is ascribed to $Fe^{2+}$–$Fe^{3+}$ exchange between Oh-sites. Considering the cations randomly distributed on the interstices, the conductivity can be written as the probability that an electron from $Fe^{2+}{}_{Oh}$ performs a successful hop to $Fe^{3+}{}_{Oh}$. Hence, the fraction of conducting sites occupied by charge carriers (c') and the fraction of available jump sites (1 – c') take the following form:

$$\text{c}' = \frac{\text{Fe}_{\text{Oh}}^{2+}}{(\text{Fe}_{\text{Oh}}^{2+} + \text{Fe}_{\text{Oh}}^{3+})} \tag{1.12}$$

$$(1 - \text{c}') = \frac{\text{Fe}_{\text{Oh}}^{3+}}{(\text{Fe}_{\text{Oh}}^{2+} + \text{Fe}_{\text{Oh}}^{3+})} \tag{1.13}$$

and the total charge carrier density (N) becomes the total concentration of Fe cations in Oh-sites:

[14] Usually, g is 1/2, 1/4 and 1/6 for 1D, 2D and 3D materials, respectively.

$$N = Fe_{Oh}^{2+} + Fe_{Oh}^{3+} \quad (1.14)$$

Herein, one assumes that $Fe^{2+}$ ions do not occupy Td-sites. Otherwise, additional activation barrier ($E_D$) due to disorder should be introduced into the mobility, since the oxygen environment would be distorted [121].

It should be noted that when the conductivity is defined by electron hopping directly between localized states, two hopping mechanisms may take place: nearest-neighbor hopping (NNH), as described by Equation 1.11, and variable range hopping (VRH). As the name implies, the hopping conductivity occurs by transition between the nearest neighbors in the NNH mechanism. Therefore, it requires a large number of pairs of close neighbor states, with one of them being free. In relatively low disordered systems, the number of empty states among the nearest neighbor sites decreases as temperature decreases and the conduction mechanism can change from NNH to VRH. The VRH model was first prosed by Mott [121] to describe low-temperature conduction in strongly disordered systems with localized charge-carrier states. In the original paper, Mott showed that the probability ($P$) of hopping between two states is proportional to their spatial separation ($R$) and their energy separation ($W$):

$$P \propto e^{-(2\alpha R + \frac{W}{k_B T})} \quad (1.15)$$

where $\alpha^{-1}$ is the attenuation length for a hydrogen-like localized wave-function. The exponents in Equation 1.15 can be combined into a single parameter ($\mathcal{R}$), namely the range between two sites: $\mathcal{R} = 2\alpha R + \frac{W}{k_B T}$.

As the result of many series of short-range hops, the overall conductivity is then determined by the average nearest-neighbor distance between states ($\bar{\mathcal{R}}$). Thus, the conductivity has the form:

$$\sigma \propto e^{-\bar{\mathcal{R}}} \quad (1.16)$$

Considering $\bar{\mathcal{R}}$ less than the bandwidth and much bigger than the interatomic spacing, Mott showed that the hopping energy depends inversely on the cube of the hopping distance (in the three-dimensional case), so $\sigma$ is written as:

$$\sigma(T) = \sigma_0 \times e^{-(E_t/k_B T)^{1/4}} \quad (1.17)$$

Therefore, by fitting the $\ln(\sigma)$ curves[15] versus $T^{-p}$, the power-law dependence ($p$) gives the type of electron hopping in each case, where $p$ = 1 corresponds to NNH and $p$ = 0.25 to Mott-VRH.

[15] According to Equation 1.11, the temperature dependent conductivity is roughly determined by the product $T^{-1} \times e^{-(E_t/k_B T)}$; however, for electron-transfer materials, the variation of $T^{-1}$ is small relative to that of $e^{-(E_t/k_B T)}$. Hence, plots of $\ln(\sigma)$ versus $T^{-1}$ yield slopes that are proportional to the free energy of activation ($E_t$), rather than to energy gaps, as would be the case for conventional semiconductors [120].

Different mechanisms can be proposed for a material as a function of its temperature dependent conduction behavior. For $Fe_3O_4$, there is a lot of controversy about the conduction mechanism in the literature, although substantial support is found for NNH model (Equation 1.11) at temperatures above $T_V$. For instance, Aragon and Honig [122] showed that the main aspects of the electrical conductivity and thermoelectric power curves at temperatures above and below $T_V$ can be described with a small polaron model if the thermal dependence of the density of states is considered. Whereas Chakraverty proposed bipolaron formation as a result of ordering between neighboring $Fe^{2+}$-$Fe^{3+}$ pairs, Ihle and Lorenz [123] interpreted the conductivity of $Fe_3O_4$ in terms of the superposition of small polaron band and small polaron hopping conduction. The latter signaled however, that above 350 K, the hopping mechanism is rapidly favored over the band conduction. Other mechanism that has been proposed includes itinerant electrons as charge carriers and formation of intermediate polarons where long-range ordered $Fe^{2+}$-$Fe^{3+}$ are responsible for conduction [124]. Again, in this mechanism, the increasing temperature leads to gradual loss of long-range order and at $T > 405$ K conduction is dominated by small polaron hopping.

At temperatures below $T_V$, even more disagreements are found about the conduction mechanism. Herein, most conclusions were drawn by analyzing the plots of $\ln(\sigma)$ versus $1/T$. Graener et al. [113] showed that $\ln(\sigma)$ is proportional to $T^{-1/4}$, indicating VRH mechanism below $T_V$, whereas Pai and Honig [116] stated that $\ln(\sigma)$ is proportional to $T^{-1}$ (NNH). In contrast, Hurd *et al.* [114] proposed that $\ln(\sigma)$ is proportional to $T$ rather than $T^{-1}$ in the temperature range of $T_V/2 < T < T_V$, which indicates incoherent tunneling of electrons induced by thermal motion of atoms. One possible explanation for such a contrast is the different microstructures and crystallinity of the specimens. Experiments by Graener et al. [113] were performed in polycrystalline samples, while Pai and Honig [116] worked with single crystals. It should be noted that Pai and Honig [116] only found $\ln(\sigma) \propto T^{-1}$ after annealing to make the sample stoichiometric, but the proportionality is lost after an aging of ten months in air at room temperature. Therefore, it follows that Verwey transition and thus electrical conductivity below $T_V$ is structure sensitive.

Disregarding the controversies in the literature, the very high conductivity of magnetite below $T_C$ is without a doubt associated to the easy electron transfer in Oh-sites. In the $Fe_{3-x}Cr_xO_4$ series, as the $Cr^{2+}$ energy level lies well above the $Fe^{2+/3+}$ energy level, the electron transfer should occur in this system only between $Fe^{2+}$ and $Fe^{3+}$ ions. Hence, when $Cr^{3+}$ ions substitute $Fe^{3+}$ in the Oh-sites of the magnetite structure, the transfer between conducting Oh-sites is expected to be disrupted, resulting in more resistive materials. Indeed, Nell and Wood [125] showed that the electrical conductivity at high temperatures ($T > 800$ K) in the $Fe_{3-x}Cr_xO_4$ series globally decreases as $x$ increases. They demonstrated that for low Cr-concentration ($x < 1.2$) the conduction mechanism is consistent with the $Fe^{2+}$–$Fe^{3+}$ pairwise electron hopping in the same way as $Fe_3O_4$. This corroborates with Mössbauer findings [74], which indicated charge hopping for $x < 1.3$ at room temperature. For compositions with $x > 1.2$, however, Nell and Wood [125] found a nearly stepwise increase in activation barrier for electron hopping. Since the nearest neighbors of most $Fe^{2+}$ ions on Oh-sites are now $Cr^{3+}$ ions, they interpreted the increased activation energy as a mixed $Fe^{2+}$–$Fe^{3+}$–$Cr^{3+}$ electron transfer. In such case, a new conduction mechanism involving hopping between Td and Oh-sites [126] could also be considered. Regarding the parent compound $FeCr_2O_4$, not much is known about its transport

properties. Boudjemma *et al.* [127] analyzed the photoelectrochemical properties of $FeCr_2O_4$, measuring an optical band gap of 1.3 eV and a conductivity as low as $10^{-9}$ $\Omega^{-1}.cm^{-1}$ at room temperature. According to them, this material has p-type semi-conductor behavior due to metal deficiency and the conduction mechanism occurs through mixed valence states $Cr^{3+/4+}$ with a density thermally activated.

### 1.3.3 The different facets of $Fe_{3-x}Cr_xO_4$ series

As said in **Section 1.1**, the oxides in the Fe-Cr-O system intervene in several fields. Starting from geology and metallurgy [1], [2]. While magnetite represents one of the most abundant Fe-containing minerals on our planet and the oldest known magnetic material, chromite is the main source of chromium, an essential metal to stainless steel as it provides corrosion-resistant properties to these materials. As multiferroics, namely materials that simultaneously exhibit ferroelectric and magnetic order, these oxides are interesting for modern electronic applications. Particularly $Fe_3O_4$, which is predicted to be a half-metallic ferromagnet (*i.e.* the conduction electrons are 100% spin polarized) at room temperature, making it attractive for spintronic applications such as magnetic memories and spin field-effect transistors [5], [6], [14]. $FeCr_2O_4$ shows multiferroic ordering and dielectric response induced by magnetic field up to $T_C$ [128], [129], also attracting attention as a material with magnetoeletric effects. As semiconductor materials, the $Fe_{3-x}Cr_xO_4$ series can be of considerable interest for photocatalysis, particularly for the compositions whose band gap remains small, enabling visible light harvesting [18]. For instance, Boudjemma *et al.* [127] studied the photocatalytic $H_2$-production over $FeCr_2O_4$ and stated that the conduction band of this material lies below the $H_2O/H_2$ level yielding a thermodynamically favorable $H_2$-photoevolution. Other common field of application is heterogeneous catalysis. A novel and promising catalytic application of iron oxides is the decomposition of organic pollutants in wastewaters using $H_2O_2$ in a heterogeneous Fenton system [130]. Magalhães *et al.* [17] examined the reactivity of $Fe_{3-x}Cr_xO_4$ series for oxidation of the dye methylene blue using $H_2O_2$. They claimed that presence of small concentration of Cr ($x$ = 0.07 and 0.21) led to significant increase on the activity in the oxidation process with complete discoloration of the dyes and high degree of mineralization. Other application areas include medicine and biology, where they can be used for mechanical manipulation of cells and drug deliver [131]. In this thesis, similarly to the $Cr_2O_3$ study (**Section 1.2.3**), the motivation behind studying the structural and physicochemical properties of $Fe_{3-x}Cr_xO_4$ series also lies in two main contexts: as corrosion products of Fe-Cr alloys and as promising materials for spintronics and photocatalysis.

First, the corrosion context is portrayed. Fe-Cr based alloys, as in stainless steel, are generally good candidates for industrial applications whenever high erosion-corrosion resistance is required [132]. When Fe-Cr alloys are exposed to oxidizing environments, a complex multiphasic oxide layer – containing Fe-Cr mixed corundum and spinel oxides – can be formed depending on the oxidation conditions [133]. The oxidation resistance of these alloys is primarily governed by the presence of sufficient Cr content at the oxide-alloy interface to develop a protective $Cr_2O_3$ layer [134]. The spinel phase, however, is considerably less protective and it was even identified [13] as one of the main

reasons for the accelerated oxidation of high Cr ferritic steels in the presence of steam. When studying the early stages of oxidation Fe-Cr alloys (≥ 9 wt. % Cr) at elevate temperatures (T > 800 K), Kuroda *et al.* [135] pointed out the $Fe_{3-x}Cr_xO_4$ spinel oxide layer as the precursor to the formation of the protective $Cr_2O_3$ layer. They claimed that the defect structure in spinel oxides favors inward oxygen diffusion instead of outward cation diffusion, thus an inward growing oxide phase is formed at the oxide-alloy interface. Many other authors [133], [136] have also emphasized the importance of the spinel layer to the development and maintenance of protective scales as it governs the electronic and cationic transport between the alloy and the aqueous medium.

Despite its key role in the corrosion mechanism of Fe-Cr alloys, not much is known about the transport properties of spinel oxides in corrosion layers because of their variable composition, poor crystallinity, complex microstructure and nanometer thickness. For instance, **Figure 1.12a** depicts the oxide layers formed by the exposure of a commercial ferritic-martensitic Fe9Cr steel (T91) to water vapor at 823 K. In such environment, Fe-9Cr steels exhibit a duplex oxide layer containing an upper layer of iron oxides composed of $Fe_3O_4$ topped by $Fe_2O_3$ and an inner $Fe_{3-x}Cr_xO_4$ spinel layer. The microstructure of $Fe_3O_4$ and $Fe_2O_3$ layers is well known. The former is composed of columnar magnetite grains, while the latter is made of small equiaxed grains [137]. The inner layer microstructure, however, is more complex and less described in literature. It is composed of equiaxed grains of Fe–Cr spinel whose stoichiometry is between $Fe_3O_4$ and $FeCr_2O_4$. According to **Figure 1.12b**, the Fe–Cr spinel stoichiometry is uneven throughout the layer, where Fe-rich spinel grains alternate with Cr-rich spinel grains [138]. The stacking order and physicochemical properties of these compounds have great importance in oxidation kinetics, since the protective oxide scale for T91 is the inner Fe–Cr spinel layer. Therefore, in order to building up knowledge of structure and transport of this spinel layer, the second part of this thesis was devoted to study $Fe_{3-x}Cr_xO_4$ spinel models.

The main idea of this thesis is to use model systems to aid the understanding of complex systems. To do so, first $Fe_{3-x}Cr_xO_4$ thin films of high-crystallinity and well-known composition $x$ were prepared. Then, a complete characterization (structural, chemical, magnetic and electronic transport) of each sample was performed. Note that it is very important to draw a whole picture of this system since the structural and physicochemical properties of spinels are closely related. As explained in **Section 1.3.2**, composition-dependent cationic disorder strongly affects the transport and magnetic properties of these compounds and vice-versa. Finally, numerical tools were used to aid the treatment of experimental data and thus comprehend at atomic scale the evolution of the physicochemical properties of the oxides due to the insertion of Cr in the spinel structure. Although this work did not go as far as comparing the model systems and the corrosion layers, the experimental data collected here will ultimately help in the development of microscopic models and the improvement of mesoscopic models applied to corrosion. Thus, the results obtained will provide a solid database for the analysis of real corrosion layers (see Perspectives section).

Remarkably, these same high-crystallinity thin films can be very interesting in the search for novel materials. As previously mentioned, oxides with spinel structure are very attractive due to their unique physicochemical properties. The complexity of the spinel structure opens way for tailoring the functional properties of these materials by incorporating different metal cations into the host matrix [81]. New functionality will depend mainly on the local structure of these substituents, that is

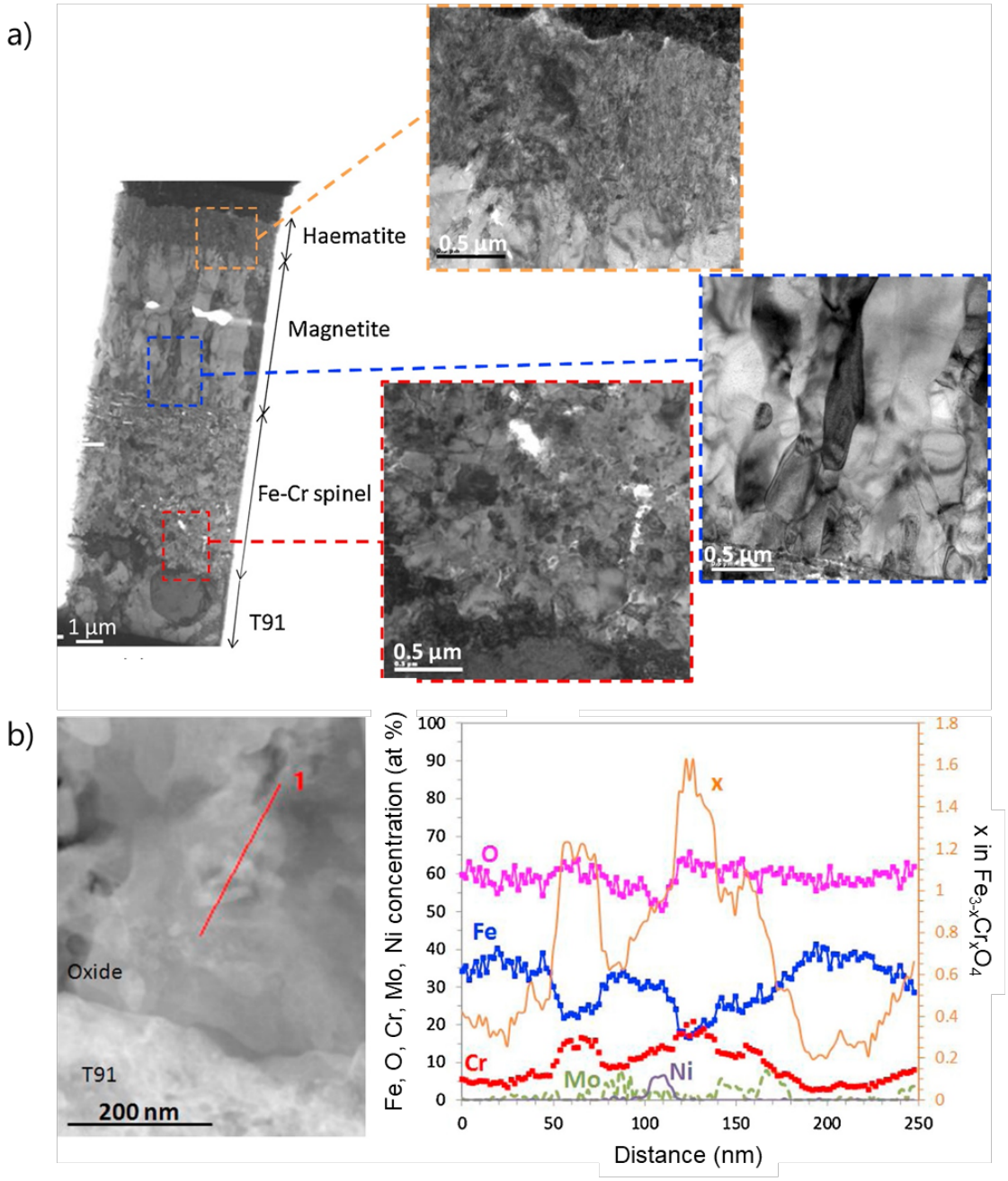


**Figure 1.12.** (a) Cross-sectional transmission electron micrograph (TEM) of Fe9Cr oxidized for 48 h in water vapor. Highlighted the interfaces between the hematite ($Fe_2O_3$), magnetite ($Fe_3O_4$), $Fe_{3-x}Cr_xO_4$ spinel and Fe9Cr steel. (b) At left, high-angle annular dark-field image (STEM-HAADF) of T91/Fe-Cr spinel interface. At right, the composition profile near T91/Fe–Cr spinel interface recorded through the red line (1) by energy dispersive X-ray analysis (TEM-EDX). The stoichiometry ($x$) of the $Fe_{3-x}Cr_xO_4$ spinel is given on the second axis of the graph. Figure adapted from Martinelli *et al.* [138].

valences, distribution among the cation sublattices and relative strength of competing effects. In this regard, the $Fe_{3-x}Cr_xO_4$ spinels are of considerable interest. This series forms a complete solid solution intrinsically defect free for a wide compositional range ($0 \leq x \leq 2$), in which the two limiting compositions have highly distinct functional properties. Whereas $Fe_3O_4$ is a typical half-metal ferrimagnetic material with high Curie temperature ($T_C$ = 850 K), $FeCr_2O_4$ is a p-type semiconductor with an interesting conical spiral spin structure and low Curie temperature ($T_C$ = 80 K). Owing to these

unique physicochemical properties, as abovementioned both materials have been suggested for modern applications like spintronics and photocatalysis. Despite the potential of the $Fe_3O_4$-$FeCr_2O_4$ system as multiferroic materials with adjustable band gap, previous studies have mainly focused on structural and magnetic properties [71], [72], [74], [75], [94] and not much is known about the transport mechanisms [125], [127]. Moreover, these studies are mostly based on polycrystalline samples, while epitaxial thin films [18], [139], [140] have received little attention.

The growth of thin films of optical and magnetic functional materials is a key technology for modern applications. Numerous studies have shown that the magnetic and transport properties of those films strongly deviate from the bulk, depending on the growth method [141], film thickness [142], and surface and interface effects [143]. Hence, the second part of this work (**Chapter 4 and 5**) is a systematic study of the effect of substitutional Cr on the structural and physicochemical properties of high quality $Fe_{3-x}Cr_xO_4$ epitaxial thin films. The main aim is to dissociate the compositional effect from other types of defects in order to fully comprehend the electronic, magnetic and conductive properties of these materials. To do so, high-purity, single-crystalline films of $Fe_{3-x}Cr_xO_4$ with $0 \leq x \leq 2$ supported on single-crystalline $\alpha$-$Al_2O_3$(0001) substrate were prepared using oxygen assisted molecular beam epitaxy (O-MBE). The choice of substrate was made for two main reasons:

1. It has been shown [144] that epitaxial $Fe_3O_4$ thin films oriented (111) grow nicely on $\alpha$-$Al_2O_3$(0001), exhibiting nearly atomically abrupt interfaces with minimal cation diffusion from substrate to film.

2. The few studies on epitaxial films of the $Fe_{3-x}Cr_xO_4$ series [18], [139], [140], [145] were done exclusively using MgO or $MgAl_2O_4$ substrates both oriented (001). To the best of my knowledge, no study so far has been performed on sapphire substrates, which brings to this thesis an extra originality. Briefly, the main difference between these substrates is that the cubic crystal structure of MgO or $MgAl_2O_4$ favors the epitaxial growth of spinel scales, but imposes low deposition temperatures due to cationic substrate-film diffusion. On sapphire, the heteroepitaxy is less favored due to the corundum structure; however, it enables higher deposition temperatures and then higher crystalline quality. These growth issues are discussed in more detail in **Section 2.1**.

After growth, several experimental techniques – such as spectroscopies, electron or X-ray diffraction, microscopies, electronic transport and magnetometry – were required in order to draw a comprehensive link between composition, electronic and magnetic properties, and distortions of the lattice. By means of crystal field multiplet (CFM) calculations, X-ray absorption spectra were explored to obtain the cation distribution among Td and Oh-sites of the spinel structure, as well as to investigate the Cr doping effect on the element magnetic properties at temperatures of 4 K and 300 K. As stated in **Section 1.3.2**, the cation distribution is a crucial point in understanding electronic and magnetic properties of films. The electronic properties of $Fe_{3-x}Cr_xO_4$ series are dictated by the relative energies of Fe and Cr $t_{2g}$ and $e_g$ band edges and the corresponding charge and spin distributions. For

instance, $Fe_2CrO_4$ ($x$ = 1) is a n-type semiconductor [18], but it could be a half metallic ferrimagnet if only the Cr cations occupy Td-sites, as predicted by Liu *et al.* [146] using crystal field theory. Likewise, the magnetic properties of the $Fe_{3-x}Cr_xO_4$ series are also directly related to charge and spin distributions among the spinel sublattices. As explained by the Néel's collinear model [80] and the Yafet and Kittel's canting spin configuration [90], the total magnetic moment and the Curie temperature of spinels depend on the competition between antiferromagnetic and ferromagnetic interactions of Td and Oh-site cations, which in turn depend on the effectiveness of spin coupling among nearest-neighbor atoms. In this regard, some anomalies were observed while studying the magnetic hysteresis properties of the $Fe_{3-x}Cr_xO_4$ thin films. These issues were addressed here using atomistic simulations (**Section 2.6**), whose first results and hypotheses are shown in **Chapter 5**.

## 1.4 Conclusions & thesis statement

The study of oxides in the Fe-Cr-O system does not come without difficulties. Even nowadays, these materials continue to receive fundamental interest due to their complex and intriguing electronic and magnetic properties (*e.g.,* Verwey transition in $Fe_3O_4$). Complications in the interpretation of experimental data is even more flagrant for intermediate spinel configuration, which has mixed cations distributed among Td and Oh slightly distorted sublattices. Especially for the spectroscopic data, where the relation between chemical composition, redox, local environment (*i.e.,* structure), and spectroscopic properties remains in general poorly understood. For simplicity's sake, this work started by the "textbook case" $\alpha$-$Cr_2O_3$. Compared to the $Fe_{3-x}Cr_xO_4$ series, $\alpha$-$Cr_2O_3$ is much simpler to study because it has Cr in one oxidation state and one cationic site, while the $Fe_{3-x}Cr_xO_4$ series has mixed valence Fe distributed among the different spinel sublattices. Hence, this first step enabled not only to master the technique of growing thin films on sapphire substrates (*i.e.,* O-MBE), but also to understand the theory behind core-level spectra simulation (*i.e.,* CFM) that would be used later in the study of $Fe_{3-x}Cr_xO_4$ series. Moreover, the results obtained through the $\alpha$-$Cr_2O_3$ study illustrate well how model films can be used to interpret data from more complex polycrystalline scales, which is the overall philosophy of this thesis.

As abovementioned, the method chosen to perform the epitaxial growth of the single-crystalline thin films is named oxygen assisted molecular beam epitaxy (O-MBE). In the O-MBE process (see **Section 2.1**), co-evaporated metals are oxidized by an oxygen plasma to form a single crystal oxide film, which condenses on a template created by the substrate. This method is the most suitable for the growth of a series of films with variable composition (*e.g.* $Fe_{3-x}Cr_xO_4$ with $0 \leq x \leq 2$), since the metal ratio (Fe:Cr) can be fixed by adjusting their atomic flux. In addition, O-MBE has atomic-layer control, which enabled the growth of multilayers such as the $\alpha$-$Cr_2O_3$ on $\alpha$-$Fe_2O_3$ buffer used in the study of epitaxial strain in $\alpha$-$Cr_2O_3$ growing layers. Other physical vapor deposition (PVD) methods that also can perform epitaxial growth are pulsed laser deposition (PLD) and sputtering [147]. Both of these PVD methods require a target of the material that is to be deposited, which would involve synthetizing in advance each of the various compositions proposed here. This "extra"

synthesis step would definitely add complexity to the study, which is why O-MBE was chosen over PLD or sputtering.

After growth, several characterization methods were proposed, each tailored expressly to the problem being worked on, as discussed in detail in **Chapter 2**. In summary, the experiments performed in this thesis can be divided in three major steps, as depicted in **Figure 1.13**. **Step 1** was to obtain chemical (*i.e.,* composition and redox) and structural information (*i.e.,* phase and dimensions) from the thin films. Purity, stoichiometry and cation redox were initially verified using X-ray photoemission spectroscopy (XPS). Whereas structural information was acquired with X-ray and electron diffractions (XRD and RHEED), X-ray reflection (XRR) experiments verified the thickness and surface roughness. After this first step, both composition and structure of the films are completely known. For the investigation of $\alpha$-$Cr_2O_3$ films (**Chapter 3**) only this first step was performed. The main asset of this study is that it further exploits the techniques routinely used in the analysis of thin films to draw satisfactory conclusions about the electronic structure of strained $Cr_2O_3$ films. For the investigation of $Fe_{3-x}Cr_xO_4$ films (**Chapter 4** and **Chapter 5**), whose main aim is to comprehend macroscopic properties of the films from the fine structure perspective, two further steps are required. **Step 2** was to analyze the microstructure and the fine structure of the films. To do so, collaborations were established with research groups belonging to the *Centre d'Elaboration des Matériaux et d'Etudes Structurales* (CEMES-CNRS) and the Synchrotron SOLEIL. Thanks to these partnerships, the structural defects, the film structure and interface were probed using high-resolution transmission electron microscopy (HRTEM), while the local atomic environment (*i.e.*, valence, coordination, and distortions in geometry due to nearest-neighbor atoms) were explored using X-ray absorption spectroscopy (XAS) and X-ray magnetic circular dichroism (XMCD) measurements. The macroscopy properties of the films were obtained in **Step 3**, where magnetic and resistivity measurements were carried out using magnetometry (VSM) and a standard four-probe method in a quantum design physical properties measurement system (PPMS).

Throughout this manuscript, special attention is given to cross-referencing and comparing the results of the different methods. For instance, the surface roughness given by XRR measurement was also verified using atomic force microscopy (AFM), whereas the structural information obtained by XRD and RHEED was compared with TEM results. Moreover, the chemical information obtained using XPS was compared with XAS data as well as with electron energy loss spectroscopy (EELS) and energy-dispersive X-ray spectroscopy (EDX) performed during the acquisition of HRTEM images. Note that these methods do not probe the same volume or the same depth. While XPS and XMCD mostly probe the first nanometers of the film surface, XAS measures its entire volume. Likewise, RHEED, AFM and TEM are local measurements, whereas XRD and XRR investigate the whole sample. Therefore, the comparison of results issue from different methods is very important as it frankly questions the homogeneity and coherence of the films.

Another interesting feature of this work is the use of simulation methods as powerful complementary tools to interpret experimental data. Two methods were proposed: CFM to simulate core level spectra (XPS, XAS and XMCD) and atomistic spin model (ASM) to simulate magnetic properties. The CFM model is explained in detail in **Section 2.4**. Briefly, this semi-empirical method was chosen because it is particularly adapted to the study of localized final states (*e.g.,* $3d$ orbitals)

with multielectronic interactions. By means of CFM simulations, indirect structural information is extracted from the core level spectra, since this method is intimately related to the point group symmetry of the cations. This aspect is very interesting for this study as it aims to discriminate Td from Oh-sites in the spinel samples and the distortions in $CrO_6$ local environment of the $Cr_2O_3$ samples. Emphasis is placed on finding a unique set of parameters that enables all spectroscopic data to be calculated. The other simulation method used in this work is the atomistic spin model (see **Section 2.6**). The main feature of ASM is that it bridges the gap between *ab initio* electronic structure simulations and micromagnetics by using a multiscale model. Within this model, the effective properties (*e.g.,* anisotropy and exchange constants) can be treated with a classical approximation, while the quantum mechanical properties are mapped onto atomic cores in a manner similar to molecular dynamics. Because it naturally deals with atomic ordering and variation of local properties seen in real materials (*e.g.,* interfaces, defects and roughness), ASM is particularly useful for simulation of magnetic properties of nanomaterials. Indeed, this point is a great advantage for the study of the $Fe_{3-x}Cr_xO_4$ series, since it aims to evaluate the effect of disorder and microstructure on the magnetic properties of the thin films.

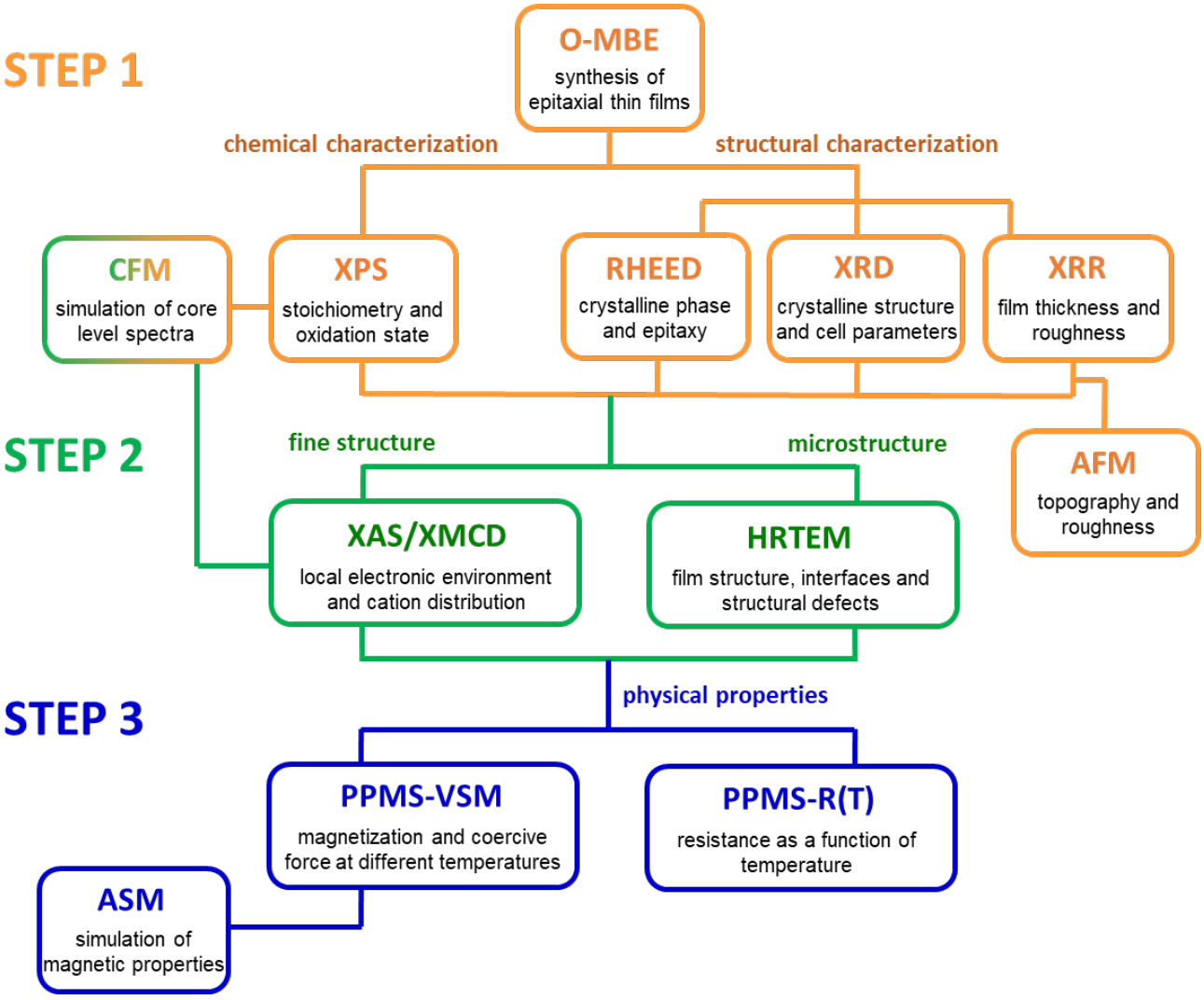


**Figure 1.13.** Scheme of experimental and computational methods used in each step of this thesis.

The following chapter gives an overview of the experimental and computational methods used in this thesis.

## 1.5 References

[1] J. F. W. Bowles, "Oxides - Chromite," in *Encyclopedia of Geology (Second Edition)*, Second Edition., vol. 1, D. Alderton and S. A. Elias, Eds. Oxford: Academic Press, 2021, pp. 438–441.

[2] N. McEwan, T. Courtney, R. A. Parry, and P. Knupfer, "Chromite-A cost-effective refractory raw material for refractories in various metallurgical applications," *Southern African Pyrometallurgy*, pp. 359–372, 2011.

[3] C. A. C. Sequeira, *High temperature corrosion: fundamentals and engineering*, First edition. Hoboken, NJ: Wiley, 2019.

[4] T. Jonsson *et al.*, "High-Temperature Oxidation of FeCr(Ni) Alloys: The Behaviour After Breakaway," *Oxidation of Metals*, vol. 87, no. 3–4, pp. 333–341, Apr. 2017.

[5] I. Žutić, J. Fabian, and S. Das Sarma, "Spintronics: Fundamentals and applications," *Reviews of Modern Physics*, vol. 76, no. 2, pp. 323–410, Apr. 2004.

[6] M. Bibes and A. Barthelemy, "Oxide Spintronics," *IEEE Transactions on Electron Devices*, vol. 54, no. 5, pp. 1003–1023, May 2007.

[7] A. U. Seybolt, "Observations on the Fe-Cr-O System," vol. 107, no. 3, p. 147, 1960.

[8] J. R. Taylor and A. T. Dinsdale, "A Thermodynamic Assessment of the Cr - Fe - O System," *International Journal of Materials Research*, vol. 84, no. 5, pp. 335–345, 1993.

[9] L. Kjellqvist, M. Selleby, and B. Sundman, "Thermodynamic modelling of the Cr–Fe–Ni–O system," *Calphad*, vol. 32, no. 3, pp. 577–592, Sep. 2008.

[10] J. Berthon, A. Revcolevschi, H. Morikawa, and B. Touzelin, "Growth of wustite ($Fe_{1-x}O$) crystals of various stoichiometries," *Journal of Crystal Growth*, vol. 47, no. 5–6, pp. 736–738, 1979.

[11] L. Kaufman and H. Bernstein, *Computer Calculation of Phase Diagrams with Special Reference to Refractory Metals*. Academic Press, 1970.

[12] T. Jonsson *et al.*, "Oxidation of Fe–10Cr in $O_2$ and in $O_2$+$H_2O$ environment at 600°C: A microstructural investigation," *Corrosion Science*, vol. 75, pp. 326–336, 2013.

[13] Y. Murata, H. Minai, K. Nagai, A. Shiraki, and M. Morinaga, "$(Fe, Cr)_3O_4$ Spinel Layer as the Key to Solving the Accelerated Oxidation of High Cr Iron Alloy in High-temperature Steam," *ISIJ International*, vol. 48, no. 10, pp. 1434–1437, 2008.

[14] M. Alexe *et al.*, "Ferroelectric Switching in Multiferroic Magnetite ($Fe_3O_4$) Thin Films," *Advanced Materials*, vol. 21, no. 44, pp. 4452–4455, Nov. 2009.

[15] J.-M. Hu and C.-W. Nan, "Opportunities and challenges for magnetoelectric devices," *APL Materials*, vol. 7, no. 8, p. 080905, Aug. 2019.

[16] S.-W. Cheong, M. Fiebig, W. Wu, L. Chapon, and V. Kiryukhin, "Seeing is believing: visualization of antiferromagnetic domains," *npj Quantum Materials*, vol. 5, no. 1, Dec. 2020.

[17] F. Magalhães *et al.*, "Cr-containing magnetites $Fe_{3-x}Cr_xO_4$: The role of $Cr^{3+}$ and $Fe^{2+}$ on the stability and reactivity towards $H_2O_2$ reactions," *Applied Catalysis A: General*, vol. 332, no. 1, pp. 115–123, Nov. 2007.

[18] S. A. Chambers *et al.*, "Electronic and Optical Properties of a Semiconducting Spinel ($Fe_2CrO_4$)," *Advanced Functional Materials*, vol. 27, no. 9, p. 1605040, Mar. 2017.

[19] P. P. Ewald, "International Tables for X-Ray Crystallography," *Nature*, vol. 171, pp. 944–946, 1953.

[20] R. E. Newnham and Y. M. Haan, "Refinement of the α-$Al_2O_3$, $Ti_2O_3$, $V_2O_3$ and $Cr_2O_3$ structures," *Zeitschrift für Kristallographie*, no. 117, pp. 235–237, 1962.

[21] P. H. Butler, *Point Group Symmetry Applications: Methods and Tables*. Boston, MA: Springer US, 1981.

[22] B. N. Brockhouse, "Antiferromagnetic Structure in $Cr_2O_3$," *The Journal of Chemical Physics*, vol. 21, no. 5, pp. 961–962, 1953.

[23] P. J. Brown, J. B. Forsyth, E. Lelièvre-Berna, and F. Tasset, "Determination of the magnetization distribution in $Cr_2O_3$ using spherical neutron polarimetry," vol. 14, no. 8, pp. 1957–1966, Feb. 2002.

[24] J. A. Cline, A. A. Rigos, and T. A. Arias, "Ab Initio Study of Magnetic Structure and Chemical Reactivity of $Cr_2O_3$ and its (0001) Surface," *The Journal of Physical Chemistry B*, vol. 104, no. 26, pp. 6195–6201, Jul. 2000.

[25] J. O. Artman, J. C. Murphy, and S. Foner, "Magnetic Anisotropy in Antiferromagnetic Corundum-Type Sesquioxides," *Physical Review*, vol. 138, no. 3A, pp. A912–A917, May 1965.

[26] G. T. Rado and V. J. Folen, "Observation of the Magnetically Induced Magnetoelectric Effect and Evidence for Antiferromagnetic Domains," *Physical Review Letters*, vol. 7, no. 8, pp. 310–311, Oct. 1961.

[27] E. Kita, A. Tasaki, and K. Siratori, "Application of SQUID Magnetometer to the Measurement of Magnetoelectric Effect in $Cr_2O_3$," vol. 18, no. 7, pp. 1361–1366, Jul. 1979.

[28] J. A. Crawford and R. W. Vest, "Electrical Conductivity of Single-Crystal $Cr_2O_3$," *Journal of Applied Physics*, vol. 35, no. 8, pp. 2413–2418, 1964.

[29] R. Cheng *et al.*, "Characterization of the native $Cr_2O_3$ oxide surface of $CrO_2$," *Applied Physics Letters*, vol. 79, no. 19, pp. 3122–3124, 2001.

[30] Y. Guo, S. J. Clark, and J. Robertson, "Electronic and magnetic properties of $Ti_2O_3$, $Cr_2O_3$, and $Fe_2O_3$ calculated by the screened exchange hybrid density functional," vol. 24, no. 32, p. 325504, Jul. 2012.

[31] S. Lany, "Semiconducting transition metal oxides," vol. 27, no. 28, p. 283203, Jun. 2015.

[32] C.-S. Cheng, H. Gomi, and H. Sakata, "Electrical and Optical Properties of $Cr_2O_3$ Films Prepared by Chemical Vapour Deposition," *Physica Status Solidi (a)*, vol. 155, no. 2, pp. 417–425, Jun. 1996.

[33] N. Iordanova, M. Dupuis, and K. M. Rosso, "Theoretical characterization of charge transport in chromia (α-$Cr_2O_3$)," *The Journal of Chemical Physics*, vol. 123, no. 7, p. 074710, 2005.

[34] D. Chen, A. Huang, H. Gu, M. Zhang, and Z. Shao, "Corrosion of $Al_2O_3$–$Cr_2O_3$ refractory lining for high-temperature solid waste incinerator," *Ceramics International*, vol. 41, no. 10, Part B, pp. 14748–14753, 2015.

[35] T. Nozaki and M. Sahashi, "Magnetoelectric manipulation and enhanced operating temperature in antiferromagnetic $Cr_2O_3$ thin film," *Japanese Journal of Applied Physics*, vol. 57, no. 9, p. 0902A2, Sep. 2018.

[36] A. Hashmi, K. Nakanishi, M. U. Farooq, and T. Ono, "Ising ferromagnetism and robust half-metallicity in two-dimensional honeycomb-kagome $Cr_2O_3$ layer," *npj 2D Materials and Applications*, vol. 4, no. 1, p. 39, Dec. 2020.

[37] T. Kosub, M. Kopte, F. Radu, O. G. Schmidt, and D. Makarov, "All-Electric Access to the Magnetic-Field-Invariant Magnetization of Antiferromagnets," *Physical Review Letters*, vol. 115, no. 9, Aug. 2015.

[38] T. Kosub *et al.*, "Purely antiferromagnetic magnetoelectric random access memory," *Nature Communications*, vol. 8, no. 1, Apr. 2017.

[39] Z. Pei, X. Zheng, and Z. Li, "Progress on Synthesis and Applications of $Cr_2O_3$ Nanoparticles," *Journal of Nanoscience and Nanotechnology*, vol. 16, no. 5, pp. 4655–4671, 2016.

[40] D. Xie, Q. Luo, S. Zhou, M. Zu, and H. Cheng, "One-step preparation of $Cr_2O_3$-based inks with long-term dispersion stability for inkjet applications," *Nanoscale Advances*, vol. 3, no. 21, pp. 6048–6055, 2021.

[41] S. Deng, H. Li, S. Li, and Y. Zhang, "Activity and characterization of modified $Cr_2O_3/ZrO_2$ nano-composite catalysts for oxidative dehydrogenation of ethane to ethylene with $CO_2$," *Journal of Molecular Catalysis A: Chemical*, vol. 268, no. 1, pp. 169–175, 2007.

[42] M. Hoang, J. F. Mathews, K. C. Pratt, and Z. Xie, "A kinetic study of oxidative dehydrogenation of isobutane to isobutylene over chromium oxide supported on lanthanum carbonate," *Kinetics and Catalysis*, vol. 51, no. 3, pp. 398–403, Jun. 2010.

[43] S. Fyfitch, "Corrosion and Stress Corrosion Cracking of Ni-Base Alloys," in *Comprehensive Nuclear Materials*, Elsevier, 2012, pp. 69–92.

[44] W. Kuang, M. Song, and G. S. Was, "Insights into the stress corrosion cracking of solution annealed alloy 690 in simulated pressurized water reactor primary water under dynamic straining," *Acta Materialia*, vol. 151, pp. 321–333, Jun. 2018.

[45] A. H. Heuer *et al.*, "Enhanced corrosion resistance of interstitially hardened stainless steel: Implications of a critical passive layer thickness for breakdown," *Acta Materialia*, vol. 60, no. 2, pp. 716–725, Jan. 2012.

[46] M. Kemdehoundja, J. F. Dinhut, J. L. Grosseau-Poussard, and M. Jeannin, "High temperature oxidation of Ni70Cr30 alloy: Determination of oxidation kinetics and stress evolution in chromia layers by Raman spectroscopy," *Materials Science and Engineering: A*, vol. 435–436, pp. 666–671, Nov. 2006.

[47] E. Schmucker, C. Petitjean, L. Martinelli, P.-J. Panteix, S. Ben Lagha, and M. Vilasi, "Oxidation of Ni-Cr alloy at intermediate oxygen pressures. I. Diffusion mechanisms through the oxide layer," *Corrosion Science*, vol. 111, pp. 474–485, Oct. 2016.

[48] L. Bataillou *et al.*, "Growth Kinetics and Characterization of Chromia Scales Formed on Ni–30Cr Alloy in Impure Argon at 700 °C," *Oxidation of Metals*, Feb. 2020.

[49] W. H. Blades and P. Reinke, "From Alloy to Oxide: Capturing the Early Stages of Oxidation on Ni–Cr(100) Alloys," *ACS Applied Materials & Interfaces*, vol. 10, no. 49, pp. 43219–43229, Dec. 2018.

[50] L. Luo *et al.*, "In situ atomic scale visualization of surface kinetics driven dynamics of oxide growth on a Ni–Cr surface," *Chemical Communications*, vol. 52, no. 16, pp. 3300–3303, 2016.

[51] M. M. Nagl and W. T. Evans, "The mechanical failure of oxide scales under tensile or compressive load," *Journal of Materials Science*, vol. 28, no. 23, pp. 6247–6260, Dec. 1993.

[52] A. Kumar, A. K. Srivastava, P. Tiwari, and R. V. Nandedkar, "The effect of growth parameters on the aspect ratio and number density of CuO nanorods," vol. 16, no. 47, pp. 8531–8543, Nov. 2004.

[53] M. Schütze, "Mechanical properties of oxide scales," *Oxidation of Metals*, vol. 44, no. 1, pp. 29–61, Aug. 1995.

[54] W. H. Meiklejohn and C. P. Bean, "New Magnetic Anisotropy," *Physical Review*, vol. 105, no. 3, pp. 904–913, Feb. 1957.

[55] J. Nogués and I. K. Schuller, "Exchange bias," *Journal of Magnetism and Magnetic Materials*, vol. 192, no. 2, pp. 203–232, Feb. 1999.

[56] X. He *et al.*, "Robust isothermal electric control of exchange bias at room temperature," *Nature Materials*, vol. 9, no. 7, pp. 579–585, Jul. 2010.

[57] J.-L. Wang, W. Echtenkamp, A. Mahmood, and C. Binek, "Voltage controlled magnetism in $Cr_2O_3$ based all-thin-film systems," *Journal of Magnetism and Magnetic Materials*, vol. 486, p. 165262, Sep. 2019.

[58] Y. Shiratsuchi, T. Fujita, H. Noutomi, H. Oikawa, and R. Nakatani, "Control of the Interfacial Exchange Coupling Energy in Pt/Co/α-$Cr_2O_3$ Films by Inserting a Pt Spacer Layer at the Co/α-$Cr_2O_3$ Interface," *IEEE Transactions on Magnetics*, vol. 47, no. 10, pp. 3909–3912, 2011.

[59] Y. Shiratsuchi, T. Fujita, H. Oikawa, H. Noutomi, and R. Nakatani, "High Perpendicular Exchange Bias with a Unique Temperature Dependence in Pt/Co/α-$Cr_2O_3$ (0001) Thin Films," vol. 3, no. 11, p. 113001, Oct. 2010.

[60] G. Gorodetsky, R. M. Hornreich, and S. Shtrikman, "Magnetoelectric Determination of the Pressure-Induced $T_N$ Shift in $Cr_2O_3$," *Physical Review Letters*, vol. 31, no. 15, pp. 938–940, Oct. 1973.

[61] Y. Kota, H. Imamura, and M. Sasaki, "Strain-Induced Néel Temperature Enhancement in Corundum-Type $Cr_2O_3$ and $Fe_2O_3$," *Applied Physics Express*, vol. 6, no. 11, p. 113007, Nov. 2013.

[62] S. A. Chambers, Y. Liang, and Y. Gao, "Noncommutative Band Offset at α-$Cr_2O_3$/α-$Fe_2O_3$(0001) Heterojunctions," *Physical Review B*, vol. 61, pp. 13223–13229, 2000.

[63] T. C. Kaspar *et al.*, "Built-In Potential in $Fe_2O_3$-$Cr_2O_3$ Superlattices for Improved Photoexcited Carrier Separation," *Advanced Materials*, vol. 28, no. 8, pp. 1616–1622, 2016.

[64] S. P. Pati, N. Shimomura, T. Nozaki, T. Shibata, and M. Sahashi, "Néel temperature of $Cr_2O_3$ in $Cr_2O_3$/Co exchange-coupled system: Effect of buffer layer," *Journal of Applied Physics*, vol. 117, no. 17, p. 17D137, 2015.

[65] N. Shimomura, S. P. Pati, T. Nozaki, T. Shibata, and M. Sahashi, "Enhancing the blocking temperature of perpendicular-exchange biased $Cr_2O_3$ thin films using buffer layers," *AIP Advances*, vol. 7, no. 2, p. 025212, Feb. 2017.

[66] T. Nozaki *et al.*, "Large perpendicular exchange bias and high blocking temperature in Al-doped $Cr_2O_3$/Co thin film systems," *Applied Physics Express*, vol. 10, no. 7, p. 073003, Jul. 2017.

[67] Y. Shiratsuchi, H. Noutomi, H. Oikawa, T. Fujita, and R. Nakatani, "Competition of perpendicular magnetic anisotropy and exchange magnetic anisotropy in a Pt/Co/α-$Cr_2O_3$(0001) thin film," *Journal of Applied Physics*, vol. 109, no. 7, p. 07C101, 2011.

[68] S. Mu and K. D. Belashchenko, "Influence of strain and chemical substitution on the magnetic anisotropy of antiferromagnetic $Cr_2O_3$: An *ab-initio* study," *Physical Review Materials*, vol. 3, no. 3, Mar. 2019.

[69] K. E. Sickafus, J. M. Wills, and N. W. Grimes, "Structure of Spinel," *Journal of the American Ceramic Society*, vol. 82, no. 12, pp. 3279–3292, Dec. 2004.

[70] E. J. W. Verwey and E. L. Heilmann, "Physical Properties and Cation Arrangement of Oxides with Spinel Structures I. Cation Arrangement in Spinels," *The Journal of Chemical Physics*, vol. 15, no. 4, pp. 174–180, Apr. 1947.

[71] H. J. Yearian, J. M. Kortright, and R. H. Langenheim, "Lattice Parameters of the $FeFe_{(2-x)}Cr_xO_4$ Spinel System," *The Journal of Chemical Physics*, vol. 22, no. 7, pp. 1196–1198, 1954.

[72] M. H. Francombe, "Lattice changes in spinel-type iron chromites," *Journal of Physics and Chemistry of Solids*, vol. 3, pp. 37–43, 1957.

[73] R. J. Hill, J. R. Craig, and G. V. Gibbs, "Systematics of the spinel structure type," *Physics and Chemistry of Minerals*, vol. 4, no. 4, pp. 317–339, 1979.

[74] M. Robbins, G. K. Wertheim, R. C. Sherwood, and D. N. E. Buchanan, "Magnetic properties and site distributions in the system $FeCr_2O_4$-$Fe_3O_4$($Fe^{2+}Cr_{2-x}Fe_x^{3+}O_4$)," *Journal of Physics and Chemistry of Solids*, vol. 32, no. 3, pp. 717–729, Jan. 1971.

[75] P. Wasilewski, D. Virgo, G. C. Ulmer, and F. C. Schwerer, "Magnetochemical characterization of $Fe(Fe_xCr_{2-x})O_4$ spinels," *Geochimica et Cosmochimica Acta*, vol. 39, pp. 889–902, 1975.

[76] R. D. Shannon, "Revised effective ionic radii and systematic studies of interatomic distances in halides and chalcogenides," *Acta Crystallographica Section A*, vol. 32, no. 5, pp. 751–767, Sep. 1976.

[77] G. J. Long, "Basic Concepts of Mössbauer Spectroscopy," in *Mössbauer Spectroscopy Applied to Inorganic Chemistry*, G. J. Long, Ed. Boston, MA: Springer US, 1984, pp. 7–26.

[78] H. N. Ok, L. S. Pan, and B. J. Evans, "$Fe^{57}$ Mössbauer study of chromium-doped magnetite, $Fe_{3-x}Cr_xO_4$ ($0 \leq x \leq 0.5$) above the Verwey transition," *Physical Review B*, vol. 17, no. 1, pp. 85–90, Jan. 1978.

[79] N. Viart, G. Pourroy, J.-M. Grenèche, D. Niznansky, and J. Hommet, "Microstructural and magnetic properties of Fe/Cr-substituted ferrite composites," *Eur. Phys. J. AP*, vol. 12, no. 1, pp. 37–46, Oct. 2000.

[80] Néel, M. Louis, "Propriétés magnétiques des ferrites: ferrimagnétisme et antiferromagnétisme," *Annales de Physique*, vol. 12, no. 3, pp. 137–198, 1948.

[81] V. A. M. Brabers, "Chapter 3 Progress in spinel ferrite research," in *Handbook of Magnetic Materials*, vol. 8, Elsevier, 1995, pp. 189–324.

[82] H. A. Kramers, "L'interaction Entre les Atomes Magnétogènes dans un Cristal Paramagnétique," *Physica*, vol. 1, no. 1, pp. 182–192, 1934.

[83] P. W. Anderson, "Antiferromagnetism. Theory of Superexchange Interaction," *Physical Review*, vol. 79, no. 2, pp. 350–356, Jul. 1950.

[84] P. W. Anderson, "Ordering and Antiferromagnetism in Ferrites," *Physical Review*, vol. 102, no. 4, pp. 1008–1013, May 1956.

[85] J. B. Goodenough, "Theory of the Role of Covalence in the Perovskite-Type Manganites [La,M(II)]$MnO_3$," *Physical Review*, vol. 100, no. 2, pp. 564–573, Oct. 1955.

[86] J. B. Goodenough, "An interpretation of the magnetic properties of the perovskite-type mixed crystals $La_{1-x}Sr_xCoO_{3-\lambda}$," *Journal of Physics and Chemistry of Solids*, vol. 6, no. 2, pp. 287–297, 1958.

[87] J. Kanamori, "Superexchange interaction and symmetry properties of electron orbitals," *Journal of Physics and Chemistry of Solids*, vol. 10, no. 2, pp. 87–98, 1959.

[88] C. Zener, "Interaction Between the d Shells in the Transition Metals," *Physical Review*, vol. 81, no. 3, pp. 440–444, Feb. 1951.

[89] W. O'Reilly, "The atomic basis of magnetism," in *Rock and Mineral Magnetism*, Boston, MA: Springer US, 1984, pp. 30–57.

[90] Y. Yafet and C. Kittel, "Antiferromagnetic Arrangements in Ferrites," *Physical Review*, vol. 87, no. 2, pp. 290–294, Jul. 1952.

[91] M. Robbins, "Magnetic properties of chromium chalcogenide spinels," *Geochimica et Cosmochimica Acta*, vol. 39, pp. 883–888, 1975.

[92] S. Nakamura and A. Fuwa, "Spin Order in $FeCr_2O_4$ Observed by Mössbauer Spectroscopy," *Physics Procedia*, vol. 75, pp. 747–754, 2015.

[93] H. A. Jahn, E. Teller, and F. G. Donnan, "Stability of polyatomic molecules in degenerate electronic states - I. Orbital degeneracy," *Proceedings of the Royal Society of London. Series A - Mathematical and Physical Sciences*, vol. 161, no. 905, pp. 220–235, 1937.

[94] J. Ma *et al.*, "Magnetic and structural phase transitions in the spinel compound $Fe_{1+x}Cr_{2-x}O_4$," *Physical Review B*, vol. 89, no. 13, Apr. 2014.

[95] W. M. Xu *et al.*, "$FeCr_2O_4$ spinel to near megabar pressures: Orbital moment collapse and site-inversion facilitated spin crossover," *Physical Review B*, vol. 95, no. 4, Jan. 2017.

[96] M. Younis, M. Saleem, S. Atiq, and S. Naseem, "Magnetic phase transition and magneto-dielectric analysis of spinel chromites: $MCr_2O_4$ (M = Fe, Co and Ni)," *Ceramics International*, vol. 44, no. 9, pp. 10229–10235, Jun. 2018.

[97] P. K. Baltzer and P. J. Wojtowicz, "On the Origin of Low Moments in Chromium-Containing Spinels," *Journal of Applied Physics*, vol. 30, no. 4, pp. S27–S29, 1959.

[98] K. Kose and S. Iida, "Interacting phase transitions in $Fe_{1+x}Cr_{2-x}O_4$ ($0 \leq x \leq 0.4$)," *Journal of Applied Physics*, vol. 55, no. 6, pp. 2321–2323, Mar. 1984.

[99] H. J. Levinstein, M. Robbins, C. Capio, B. Laboratories, and M. Hill, "A crystallographic study of the system $FeCr_2O_4$-$Fe_3O_4$ ($Fe^{2+}Fe^{3+}{}_xCr_{2-x}O_4$)," *Materials Research Bulletin*, vol. 7, no. 1, pp. 27–34, 1972.

[100] D. H. Lyons, T. A. Kaplan, K. Dwight, and N. Menyuk, "Classical Theory of the Ground Spin-State in Cubic Spinels," *Physical Review*, vol. 126, no. 2, pp. 540–555, Apr. 1962.

[101] E. J. W. Verwey, "Electronic Conduction of Magnetite ($Fe_3O_4$) and its Transition Point at Low Temperatures," *Nature*, vol. 144, no. 3642, pp. 327–328, Aug. 1939.

[102] E. J. W. Verwey and P. W. Haayman, "Electronic conductivity and transition point of magnetite ('$Fe_3O_4$')," *Physica*, vol. 8, no. 9, pp. 979–987, Nov. 1941.

[103] E. J. Verwey, P. W. Haayman, and F. C. Romeijn, "Physical Properties and Cation Arrangement of Oxides with Spinel Structures II. Electronic Conductivity," *The Journal of Chemical Physics*, vol. 15, no. 4, pp. 181–187, Apr. 1947.

[104] F. Walz, "The Verwey transition - a topical review," *Journal of Physics: Condensed Matter*, vol. 14, no. 12, pp. R285–R340, Mar. 2002.

[105] E. J. Samuelsen, E. J. Bleeker, L. Dobrzynski, and T. Riste, "Neutron Scattering from Magnetite below 119°K," *Journal of Applied Physics*, vol. 39, no. 2, pp. 1114–1115, 1968.

[106] C. Medrano, M. Schlenker, J. Baruchel, J. Espeso, and Y. Miyamoto, "Domains in the low-temperature phase of magnetite from synchrotron-radiation x-ray topographs," *Phys. Rev. B*, vol. 59, no. 2, pp. 1185–1195, Jan. 1999.

[107] M. Fonin, Y. S. Dedkov, R. Pentcheva, U. Rüdiger, and G. Güntherodt, "Magnetite: a search for the half-metallic state," *Journal of Physics: Condensed Matter*, vol. 19, no. 31, p. 315217, Aug. 2007.

[108] H. Seo, M. Ogata, and H. Fukuyama, "Aspects of the Verwey transition in magnetite," *Physical Review B*, vol. 65, no. 8, p. 085107, Feb. 2002.

[109] M. S. Senn, I. Loa, J. P. Wright, and J. P. Attfield, "Electronic orders in the Verwey structure of magnetite," *Physical Review B*, vol. 85, no. 12, p. 125119, Mar. 2012.

[110] Z. Kakol and J. M. Honig, "Influence of deviations from ideal stoichiometry on the anisotropy parameters of magnetite," *Physical Review B*, vol. 40, no. 13, pp. 9090–9097, Nov. 1989.

[111] P. A. Miles, W. B. Westphal, and A. Von Hippel, "Dielectric Spectroscopy of Ferromagnetic Semiconductors," *Review Modern Physics*, vol. 29, no. 3, pp. 279–307, Jul. 1957.

[112] C. C. WU and T. O. MASON, "Thermopower Measurement of Cation Distribution in Magnetite," *Journal of the American Ceramic Society*, vol. 64, no. 9, pp. 520–522, 1981.

[113] H. Graener, M. Rosenberg, T. E. Whall, and M. R. B. Jones, "The low-temperature resistivity and Seebeck coefficient of fluorine-substituted magnetite," *Philosophical Magazine B*, vol. 40, no. 5, pp. 389–399, 1979.

[114] C. M. Hurd, S. P. McAlister, N. Savvides, I. Shiozaki, W. R. McKinnon, and P. Strobel, "Conductivity of some mixed-valence oxides below Tv," *Journal of Applied Physics*, vol. 53, no. 3, pp. 2161–2163, 1982.

[115] A. J. M. Kuipers and V. A. M. Brabers, "Electrical transport in magnetite near the Verwey transition," *Physical Review B*, vol. 20, no. 2, pp. 594–600, Jul. 1979.

[116] M. Pai and J. M. Honig, "Comments on the temperature dependence of the resistivity of magnetite below the Verwey transition," vol. 16, no. 2, pp. L35–L38, Jan. 1983.

[117] A. R. Nagaraja *et al.*, "Band or Polaron: The Hole Conduction Mechanism in the p-Type Spinel $Rh_2ZnO_4$," *Journal of the American Ceramic Society*, vol. 95, no. 1, pp. 269–274, 2012.

[118] A. Bhargava *et al.*, "Breakdown of the Small-Polaron Hopping Model in Higher-Order Spinels," *Advanced Materials*, vol. 32, no. 49, p. 2004490, Dec. 2020.

[119] R. R. Heikes, R. W. Ure, S. J. Angello, and J. E. Bauerle, *Thermoelectricity: Science and Engineering*. Interscience Publishers, 1961.

[120] J. M. Honig, "Electrical properties of metal oxides which have 'hopping' charge carriers," *Journal of Chemical Education*, vol. 43, no. 2, p. 76, Feb. 1966.

[121] I. G. Austin and N. F. Mott, "Polarons in crystalline and non-crystalline materials," *Advances in Physics*, vol. 18, no. 71, pp. 41–102, Jan. 1969.

[122] R. Aragón and J. M. Honig, "Mean-field model of the Verwey transition in magnetite," *Physical Review B*, vol. 37, no. 1, pp. 209–218, Jan. 1988.

[123] D. Ihle and B. Lorenz, "Small-polaron conduction and short-range order in $Fe_3O_4$," vol. 19, no. 26, pp. 5239–5251, Sep. 1986.

[124] J. B. Goodenough, "The Verwey Transition Revisited," in *Mixed-Valence Compounds: Theory and Applications in Chemistry, Physics, Geology, and Biology*, D. B. Brown, Ed. Dordrecht: Springer Netherlands, 1980, pp. 413–425.

[125] J. Nell and B. Wood, "High temperature electrical measurements and thermodynamic properties of $Fe_3O_4$-$FeCr_2O_4$-$MgCr_2O_4$-$FeAl_2O_4$ spinels," *American Mineralogist*, vol. 76, pp. 405–426, 1991.

[126] B. Gillot, F. Jemmali, and A. Rousset, "Kinetics and mechanism of ferrous spinel oxidation studied by electrical conductivity and thermogravimetry," *Journal of Materials Science*, vol. 21, no. 12, pp. 4436–4442, Dec. 1986.

[127] A. Boudjemaa, R. Bouarab, S. Saadi, A. Bouguelia, and M. Trari, "Photoelectrochemical $H_2$-generation over Spinel $FeCr_2O_4$ in $X^{-2}$ solutions ($X^{-2}$ = $S^{-2}$ and $SO_3^{-2}$)," *Applied Energy*, vol. 86, no. 7, pp. 1080–1086, Jul. 2009.

[128] K. Singh, A. Maignan, C. Simon, and C. Martin, "$FeCr_2O_4$ and $CoCr_2O_4$ spinels: Multiferroicity in the collinear magnetic state?," *Applied Physics Letters*, vol. 99, no. 17, p. 172903, Oct. 2011.

[129] K. V. Vasin and M. V. Eremin, "Magnetoelectric coupling and spin-canting in $FeCr_2O_4$ ferrimagnet," *Journal of Magnetism and Magnetic Materials*, vol. 537, p. 168185, 2021.

[130] L. Zhao, Z.-R. Lin, X. Ma, and Y.-H. Dong, "Catalytic activity of different iron oxides: Insight from pollutant degradation and hydroxyl radical formation in heterogeneous Fenton-like systems," *Chemical Engineering Journal*, vol. 352, pp. 343–351, 2018.

[131] P. Tartaj, M. P. Morales, T. Gonzalez-Carreño, S. Veintemillas-Verdaguer, and C. J. Serna, "The Iron Oxides Strike Back: From Biomedical Applications to Energy Storage Devices and Photoelectrochemical Water Splitting," *Advanced Materials*, vol. 23, no. 44, pp. 5243–5249, 2011.

[132] C. A. C. Souza, D. V. Ribeiro, and C. S. Kiminami, "Corrosion resistance of Fe-Cr-based amorphous alloys: An overview," *Journal of Non-Crystalline Solids*, vol. 442, pp. 56–66, 2016.

[133] G. C. Wood, "High-temperature oxidation of alloys," *Oxidation of Metals*, vol. 2, p. 47, 1970.

[134] B. V. Mahesh, R. K. Singh Raman, and C. C. Koch, "Resistance of Nanostructured Fe-Cr Alloys to Oxidative Degradation: Role of Zr and Cr Contents," *Metallurgical and Materials Transactions A*, vol. 46, no. 4, pp. 1814–1824, Apr. 2015.

[135] K. Kuroda, P. A. Labun, G. Welsch, and T. E. Mitchell, "Oxide-formation characteristics in the early stages of oxidation of Fe and Fe-Cr alloys," *Oxidation of Metals*, vol. 19, no. 3–4, pp. 117–127, Apr. 1983.

[136] I. Saeki, H. Konno, and R. Furuichi, "The initial oxidation of type 430 stainless steel in O2-H2O-N2 atmospheres at 1273 K," *Corrosion Science*, vol. 38, no. 1, pp. 19–31, 1996.

[137] I. G. Wright and R. B. Dooley, "A review of the oxidation behaviour of structural alloys in steam," *International Materials Reviews*, vol. 55, no. 3, pp. 129–167, 2010.

[138] L. Martinelli, C. Desgranges, F. Rouillard, K. Ginestar, M. Tabarant, and K. Rousseau, "Comparative oxidation behaviour of Fe-9Cr steel in $CO_2$ and $H_2O$ at 550°C: Detailed analysis of the inner oxide layer," *Corrosion Science*, vol. 100, pp. 253–266, 2015.

[139] D. S. Lee and G. Chern, "Electrical transport properties of $Fe_{3-x}Cr_xO_4$ ferrite films on MgO (001) grown by molecular beam epitaxy," *Physica B: Condensed Matter*, vol. 407, no. 3, pp. 297–301, Feb. 2012.

[140] C.-L. Chen, C.-L. Dong, K. Asokan, G. Chern, and C. L. Chang, "Electronic structure of Cr doped $Fe_3O_4$ thin films by X-ray absorption near-edge structure spectroscopy," *Solid State Communications*, vol. 272, pp. 48–52, Apr. 2018.

[141] J. A. Moyer, R. Gao, P. Schiffer, and L. W. Martin, "Epitaxial growth of highly-crystalline spinel ferrite thin films on perovskite substrates for all-oxide devices," *Scientific Reports*, vol. 5, no. 1, Sep. 2015.

[142] A. V. Ramos *et al.*, "Magnetotransport properties of $Fe_3O_4$ epitaxial thin films: Thickness effects driven by antiphase boundaries," *Journal of Applied Physics*, vol. 100, no. 10, p. 103902, Nov. 2006.

[143] X. Wang, Y. Liao, D. Zhang, T. Wen, and Z. Zhong, "A review of $Fe_3O_4$ thin films: Synthesis, modification and applications," *Journal of Materials Science & Technology*, vol. 34, no. 8, pp. 1259–1272, Aug. 2018.

[144] S. Gota, J.-B. Moussy, M. Henriot, M.-J. Guittet, and M. Gautier-Soyer, "Atomic-oxygen-assisted MBE growth of $Fe_3O_4$ (111) on $\alpha$-$Al_2O_3$ (0001)," *Surface Science*, vol. 482–485, pp. 809–816, 2001.

[145] M. D. Scafetta, T. C. Kaspar, M. E. Bowden, S. R. Spurgeon, B. Matthews, and S. A. Chambers, "Reversible Oxidation Quantified by Optical Properties in Epitaxial $Fe_2CrO_4{}^{+\delta}$ Films on (001) $MgAl_2O_4$," *ACS Omega*, vol. 5, no. 7, pp. 3240–3249, Feb. 2020.

[146] L. J. L. Y. C. X.-M. D. Hui-Ning, "Electronic Structures of New Half-Metal Material $CrFe_2O_4$," *Acta Physico-Chimica Sinica*, vol. 25, no. 01, p. 107, 2009.

[147] M. Ohring, "Chapter 3 - Thin-Film Evaporation Processes," in *Materials Science of Thin Films (Second Edition)*, Second Edition., M. Ohring, Ed. San Diego: Academic Press, 2002, pp. 95–144.

# Chapter 2:

# Experimental and computational methods

The characterization of nanoscale films requires specific methods, which may be complemented and further explored by theoretical simulations. The following chapter is a brief introduction to the experimental methods applied in the development of this thesis, which includes a description of the **O-MBE method** and the growth conditions, as well as the **structural**, **physicochemical** and **fine structure investigations** performed on the films. Theoretical concepts used to explore the experimental data are highlighted in each section. In particular, the theory behind the **simulation of core level spectra** and the **simulation of magnetic properties**.

## 2.1 Epitaxial growth of thin films: the O-MBE setup

All epitaxial films studied in this thesis (*i.e.,* $\alpha$-$Cr_2O_3$ and $Fe_{3-x}Cr_xO_4$ series) were grown by molecular beam epitaxy (MBE), as sketched in **Figure 2.1**. The MBE technique was developed in the late 1960s for the growth of III-V semiconductor surfaces with high crystalline quality [1]. This versatile technique underwent many upgrades in the 1980s and, in the past two decades, it has been widely applied to the growth of thin epitaxial structures made of semiconductors, metals or insulators [2], [3]. In MBE, one generates thermal-energy molecular and/or atomic beams of the required elements, which crystallize following the substrate template. Indeed, the term epitaxy is employed because there is a coherence between the crystalline structure of the film and the substrate. Low growth rate is required to ensure the surface migration of the impinging species and thereby to reduce the surface defects. Optimal growth rates typically range from a few to tens of $Å.min^{-1}$. Thus, the chemical composition of the film is controlled at atomic scale by adjusting the beam flux. In addition, mechanical shutters in front of the beam sources are used to control the start and end-point of the deposition, enabling the synthesis of multilayer materials. This versatility is exactly the reason why this growth method was chosen for this thesis.

The MBE growth of thin films is performed under ultra-high vacuum (UHV) conditions, which grants to this technique some advantages. The first one is to reduce surface contaminations. One estimates that pressures as low as $10^{-6}$ mbar are already sufficient for a pollution layer to deposit on the surface. In this work, a pump system – containing turbomolecular, ionic and titanium sublimation pumps – is used to maintain the base pressure inside the deposition chamber of about $10^{-10}$ mbar. Another advantage of working under UHV conditions is that film growth can be followed *in situ* using surface-sensitive diagnostic methods. For instance, a reflection high-energy electron diffraction (RHEED) gun is connected to the deposition chamber used in this work. The RHEED gun is used to follow in real time the diffraction patterns of the growing film in order to monitor surface crystallographic and morphological properties, as discussed in detail in **Section 2.2**.

Two strategies could be used in the case of growing oxide films by MBE. The first one is to evaporate directly the desired material. However, UHV conditions often lead to oxygen losses that hinder the growth of oxide films with the correct stoichiometry. The other one is to create a flux of metallic elements and react them with a source of oxygen, which can be atomic (O) or molecular oxygen ($O_2$), ozone ($O_3$), or nitrogen oxides (NO or $NO_2$). In this PhD thesis, co-evaporated Fe and/or Cr metals are oxidized by an *oxygen plasma* to form a single crystal oxide film, which condenses on a template created by the $\alpha$-$Al_2O_3$(0001) substrate. This specific technique is addressed by the name *oxygen-plasma-assisted* MBE or O-MBE. The advantage of this approach is that atomic oxygen is more reactive than molecular $O_2$ or $NO_x$, so the metal oxidation on the surface occurs at higher rate than that of film growth, avoiding formation of undesirable suboxides. The O-MBE setup used in this work is equipped with a water-cooled radio-frequency (rf) plasma source. In this system, a constant oxygen pressure ($P_{O_2,plasma}$ from 0.1 to 0.5 Torr) is injected in a quartz cavity where an electric discharge (rf power from 250 to 450 W) creates the oxygen plasma. The oxidizing species in the

plasma is mostly atomic oxygen created via electronic dissociation. They are introduced in the deposition chamber through a conical effusion hole of 200 µm diameter, which increases the pressure inside the chamber to around $10^{-7}$ mbar during deposition. The amount of atomic oxygen introduced into the MBE chamber determines the oxidation conditions during growth and, therefore, the oxidation state of the cations and the crystalline phase. For instance, one approach for finding the optimal growth conditions for $Fe_3O_4$ is to mimic the growth conditions for $\alpha$-$Fe_2O_3$, except for the amount of oxygen that is decreased in order to have mixed Fe (II) and Fe (III) species. Another approach could be to increase the Fe evaporation rate in order to force a 3:4 stoichiometry. In this work, the O-MBE system is equipped with Fe and Cr Knudsen effusion cells whose temperatures control the evaporation rates of these metals. A quartz balance is placed in the same position as the sample during deposition in order to precisely determine the evaporation rates, which were smaller than one Å.min$^{-1}$ in this study. Therefore, the stoichiometry of the final product in this work could be controlled properly by adjusting the beam flux and the oxygen amount.

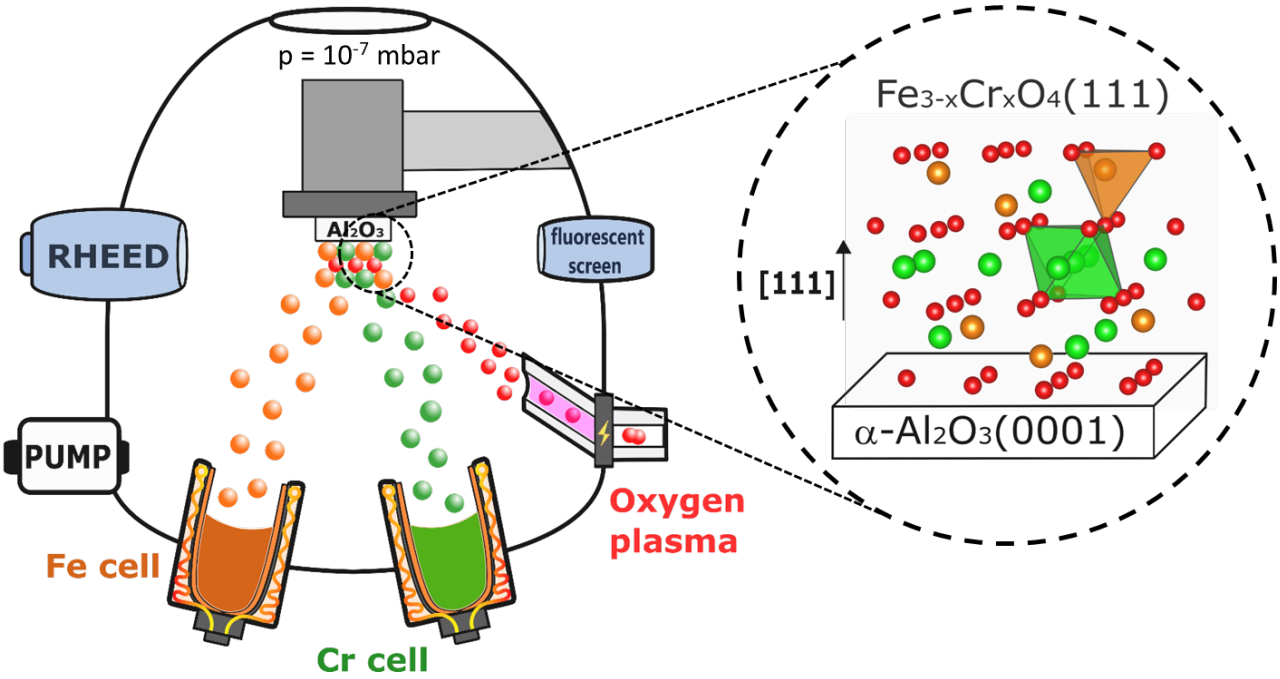


**Figure 2.1.** Schematic representation of the O-MBE setup for the growth of $Fe_{3-x}Cr_xO_4$ series on sapphire substrate.

The MBE is very powerful technique as it offers not only perfect control of the stoichiometry of the film, but also of its crystalline structure. However, it requires extremely precise control of beam fluxes and growth conditions. Because of UHV conditions, MBE growth is performed out of thermodynamic equilibrium. Four main consecutive surface processes are involved in the O-MBE growth [1]. First, the constituent atoms impinging on the substrate are adsorbed in its crystal surface. These species usually interact with the so-called crystal sites of the surface. Each crystal site is a small part of the surface characterized by its individual chemical activity. They may be created by a dangling bond, vacancy, step edge, *etc*. After adsorbed, the atoms migrate and assimilate into the crystal

lattice of the substrate or the epilayer already grown. Then, the species that are not incorporated into the crystal lattice undergo thermal desorption.

The growth mechanisms are governed mainly by the kinetics of the surface reactions between the impinging beams and the outermost atomic layers of the substrate crystal. Three general modes of crystal growth on surfaces may be distinguished [1]:

1. **The layer-by-layer (Frank-van der Merwe mode).** The atoms (or molecules) are strongly bounded to the substrate and form a complete monolayer on the surface.

2. **The island (Volmer-Weber mode).** The atoms (or molecules) are more strongly bounded to each other than to the substrate. Hence, small clusters nucleate directly on the substrate surface and then grow into islands of the condensed phase.

3. **The layer plus island (Stranski-Krastanov mode).** After forming the first few monolayers, subsequent layer growth is unfavorable and islands are formed.

Due to the kinetic character of the MBE growth, the substrate is usually submitted to elevate temperatures during deposition in order to obtain the desired crystalline phase. In the MBE setup, the sample holders are attached to a furnace that radiatively heats the substrate in the deposition chamber. The substrate temperature is thus controlled by the power delivered by the furnace, whose radiation environment is monitored by a thermocouple.

In this thesis, the goal is to synthetize model 2D materials with low surface roughness. The optimal growth is the result of a delicate compromise between substrate temperature, metal evaporation rate, atomic oxygen flux, UHV conditions, system size, and deposition time. The experimental conditions optimized in this work for the growth of $\alpha$-$Cr_2O_3$(0001), $\alpha$-$Fe_2O_3$(0001) and $Fe_{3-x}Cr_xO_4$(111) thin films on $\alpha$-$Al_2O_3$(0001) substrate are presented in detail in **Section 3.2** and **Section 4.1**. Following growth, several characterization techniques were employed to probe the structural, chemical and physical properties of the thin films. The following sections of this chapter provide a general outline of these techniques and briefly describe their particular features.

## 2.2 Structural characterization of thin films

### 2.2.1 *In situ* RHEED diffraction

Reflection high-energy electron diffraction (RHEED) is one of the most common diffraction methods used to real-time monitor surface crystallographic and morphological properties during thin film growths [4], [5]. In RHEED, a beam of high-energy electrons (here, E = 30 keV) are incident on the substrate/film surface at small incident angle ($\theta \leq 4°$), as depicted in **Figure 2.2**. Hence, only the outermost atomic layers are probed (~0.5 nm deep). The electrons coherent diffracted from the

surface give rise to semicircular zones of scattered beams, which are collected on a fluorescent screen and then digitized by a CCD camera. The RHEED images represent the reciprocal lattice of the surface along the direction perpendicular to the incident beam.

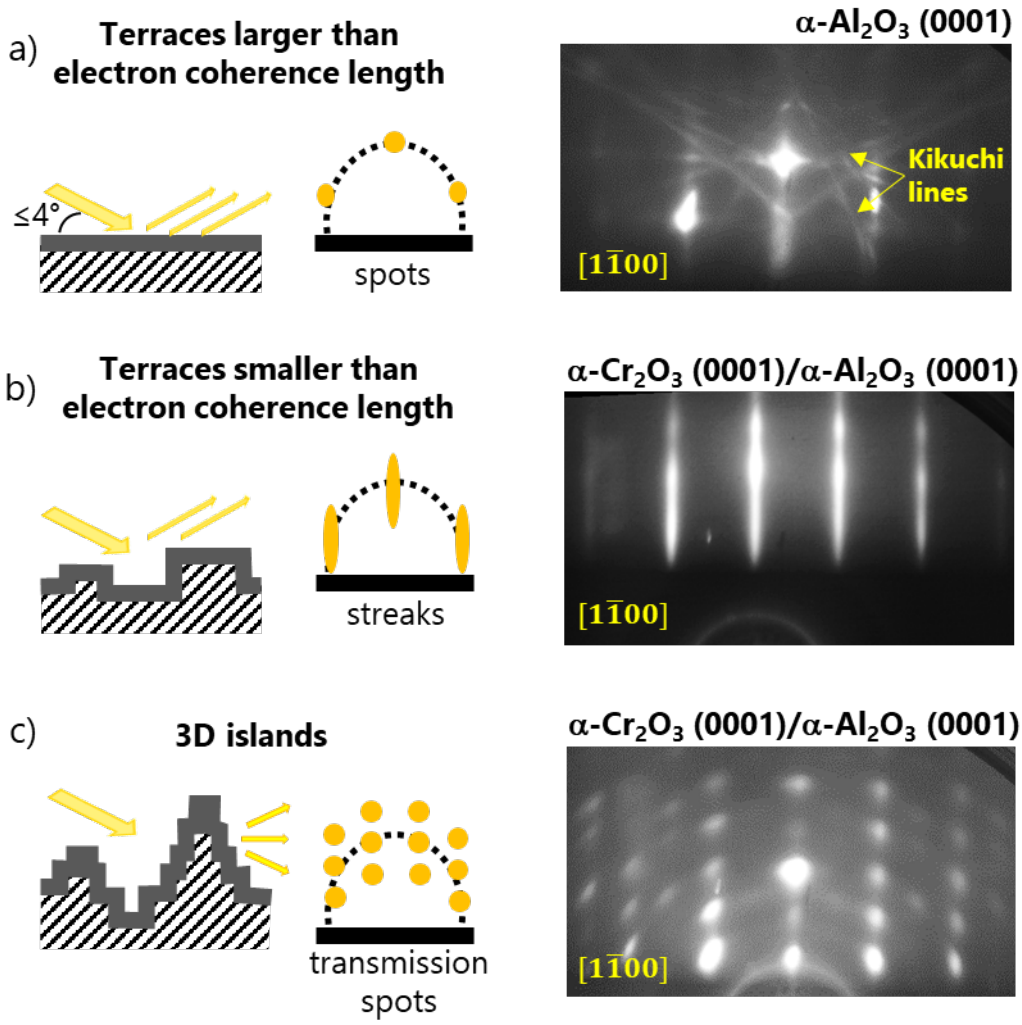


**Figure 2.2.** Schematic diagram of RHEED patterns for different surface morphologies. (a) RHEED patterns for $\alpha$-$Al_2O_3$ surface with terrace widths that are larger than the electron beam coherence length. (b) RHEED patterns for $\alpha$-$Cr_2O_3$ layers slowly grown on $\alpha$-$Al_2O_3$, for which the terrace widths that are comparable to the electron beam coherence length. (c) RHEED patterns for $\alpha$-$Cr_2O_3$ layers rapidly grown on $\alpha$-$Al_2O_3$. In this case, the high growth rate favored the formation of 3D islands through which significant transmission occurs.

The spatial resolution in RHEED structure analysis is determined by the coherence length of electron beam used, which is typically around 100 nm for a well-collimated beam. For 2D materials, the diffraction pattern is given by the intersection of the rods of the reciprocal lattice with the Ewald sphere. The scattered beams result in an image with spots for a perfect single-crystalline surface whose terrace widths are greater than or equal to the electron coherence length. For example, **Figure 2.2a** depicts the typical RHEED image for a single-crystalline $\alpha$-$Al_2O_3$ substrate, where one observes three diffraction spots with different intensities due to interference among scattered beams from

different atomic layers. One can also notice bright straight line features, referred to as Kikuchi lines [6], which are originated from inelastic scattering process.

The diffraction spots in the RHEED pattern will elongate and broaden when the surface is composed of small out-of-phase domains whose size is smaller than the coherence length of electron beam. The width of the streaky spots is inversely proportional to the average size of the domains. The broadening of the RHEED patterns is further accentuated when the surface is rough with multilevel terraces of different widths. In this case, the reciprocal rods are modulated because of superposition of constructive interference of the scattered electrons under the on-Bragg conditions with various spacing of split rods at the off-Brag conditions. Hence, the RHEED patterns show elongated streaks with intensity modulation in the perpendicular direction.

**Figure 2.2b** shows the RHEED image of $\alpha$-$Cr_2O_3$(0001) grown $\alpha$-$Al_2O_3$(0001) substrate, in which the sharp diffraction streaks prove the high crystalline quality of the layer and the existence of a bidimensional layer-by-layer growth mode. Very small elongations of the streaks are observed on the perpendicular direction, depicting a surface with low roughness. When the surface is very rough with three-dimensional islands, the electron beam transmits through the protruded parts of islands, producing a transmission diffraction pattern instead of a reflection pattern. In this case, one observes diffraction spots rotated around the direction of electron beam. **Figure 2.2c** shows the RHEED image of $\alpha$-$Cr_2O_3$(0001) grown $\alpha$-$Al_2O_3$(0001) substrate, for which the high growth rate hindered the surface migration of the impinging species and favored island growth-mode. Herein, the presence of spots in the RHEED image indicates poor surface quality.

In this work, the RHEED patterns were systematically recorded with the 30 keV primary beam aligned parallel to $[1\bar{1}00]$ and $[10\bar{1}0]$ azimuths of sapphire. Three main information were extracted from these images:

1. **The crystalline quality of the growing layers.** As explained above, singular RHEED patterns are obtained from different surface morphologies. However, it is important to note that obtaining a good RHEED image does not exclude larger scale inhomogeneity. Therefore, further structural characterization is required to confirm the crystalline quality of the film.

2. **The evolution of lattice parameter of the growing layers.** The evolution of the in-plane lattice parameter can be followed using the substrate as calibration point. The rod spacing of the reciprocal lattice is inversely proportional to the inter-reticular distance in the real space. In this work, IMAGEJ software [7] was used to obtain the pixel spacing between the RHEED streaks during deposition. For instance, **Figure 2.3** shows the $179 \pm 1$ pixel spacing between the $(\bar{1}\bar{1})$ and $(11)$ RHEED streaks of $\alpha$-$Cr_2O_3$ thin film obtained by integrating the image gray level within a rectangular selection of $500 \times 250$ pixels. The error bars were determined by the precision in the measurement of a pixel. The pixel lengths can be converted into metric units using the substrate lattice parameter in the starting point. Since the RHEED images are acquired successively during the entire film growth, this approach gives good insight into the relaxation of stresses with deposition time, as discussed in detail in **Section 3.3**.

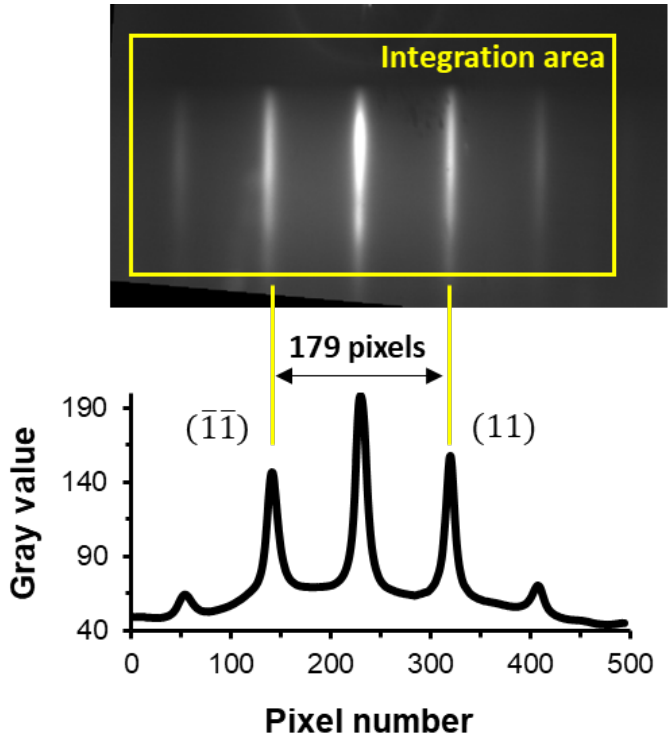


**Figure 2.3.** RHEED pattern (top) and extracted profile line (bottom) of 16 nm-thick $\alpha$-$Cr_2O_3$(0001) layer grown on $\alpha$-$Al_2O_3$. Herein, the 30 keV electron beam was aligned along the $[1\bar{1}00]$ hexagonal azimuth. The gray level was integrated using the IMAGEJ software.

3. **The crystalline phase of the growing layers.** The Fe-Cr-O system may crystallize in three forms: $\alpha$-$(Fe,Cr)_2O_3$ corundum, $(Fe,Cr)_3O_4$ spinel or (Fe,Cr)O halite. Compared to the RHEED patterns of the corundum substrate, the rods can appear, disappear or be enhanced in intensity depending on the growing phase. From the real-time monitoring of the RHEEDs images, the growth parameters can be adjusted to obtain the desired crystalline phase and the best film quality possible. However, it is important to note that this technique has no chemical sensitivity and cannot distinguish different systems that crystallizes within the same lattice (*e.g.,* $Fe_3O_4$ and $\gamma$-$Fe_2O_3$). Therefore, further structural and chemical characterization is required to confirm the film phase.

### 2.2.2 *Ex situ* X-ray diffraction and X-ray reflectivity

Following growth, the crystalline phase and quality of the films were confirmed by X-ray diffraction (XRD) using a standard diffractometer (Bruker D8 Advance) running in the Bragg–Brentano ($\theta$-$2\theta$) geometry and rocking curve. The measurements were performed on *Plateforme Matière Condensée et Matériaux* of *Université Paris-Saclay*. **Figure 2.4** illustrates the principle of the measurement. During $\theta$-$2\theta$ scans, the intensity of the diffraction peak is maximal for coherent scattering of the atomic arrangement, *i.e.,* under Bragg diffraction conditions:

$$n\lambda = 2d_{hkl}sin\theta \quad (2.1)$$

where $n$ is the diffraction order, $\lambda$ is the wavelength of the X-ray source (here, $\lambda_{Cu\ K\alpha}$ = 0.154 nm), $d$ is the distance between crystallographic ($hkl$) planes, and $\theta$ is the incident angle. Epitaxial thin films produce only one family of Bragg peaks in the θ-2θ diffraction pattern, *i.e.* {0001} for corundum and {111} for spinel structure in this study. The position of the diffraction lines on the XRD scan (here, 10° ≤ 2θ ≤ 90°) thus gives access to the out-of-plane lattice parameter of the material.

In addition to θ-2θ measurements, rocking curve (RC) scans were performed by tilting the sample around a specific Bragg angle. It probes planes that are not parallel. A perfect crystal will produce a very sharp RC peak. However, defects like mosaicity, dislocations, and curvature create disruptions in the perfect parallelism of atomic planes, broadening the RC peak. Hence, the full width at half maximum (FWHM) value of this peak (ΔΩ) gives valuable information on the crystalline quality of the epitaxial films. In general, high crystalline quality is associated to ΔΩ values around 0.1°-0.2°.

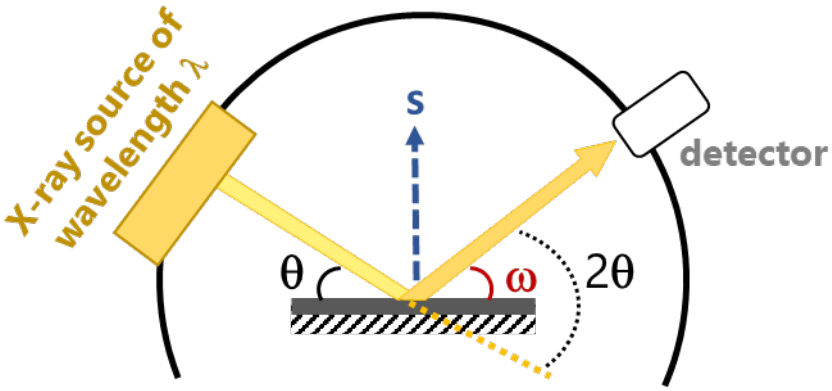


**Figure 2.4.** Schematic illustration of X-ray diffraction in θ-2θ Bragg–Brentano geometry. Diffraction patterns are produced by the coherent scattering of X-ray beam (λ) with incident angle (θ) by atoms in crystalline materials. The diffracted angle (ω) is equal to θ in this setup. The 2θ angle is then the angle defined between the incident beam and the detector angle.

Another interesting information obtained from θ-2θ scans is the out-of-plane domain size, which should correspond to the thickness of a single crystal thin film. According to the Debye-Scherrer equation [8], the Bragg peak width ($B$) of a particular reflection ($hkl$) is inversely proportional to the domain size ($D$):

$$D = K\lambda / B_{hkl} \cos(\theta_{hkl}) \quad (2.2)$$

where λ is the X-ray wavelength and $\theta_{hkl}$ the scattering angle. The constant $K$ takes different values depending on how the peak width is defined. For instance, $K$ = 0.9394 if $B$ is the FWHM of the Bragg peak (common value for cubic symmetries). However, if one considers the RC measurements (ΔΩ), $K$ = 0.3989. Either way, similar $D$ values were obtained in this study (see **Section 4.2**).

The film thickness, roughness and density were determined *ex situ* by X-ray reflection (XRR) using a diffractometer equipped with Cu Kα source (λ = 0.154 nm) in my host laboratory (SPEC/LNO). This measurement corresponds to θ-2θ scans with grazing incident angles (θ < 7°). Reflectivity curves are produced by the interference between the X-ray waves reflected from the film-substrate

interface. It appears as interference fringes, the spacing of which is inversely proportional to the thickness of the layer. **Figure 2.5** shows reflectivity curves simulated in a reflectivity software package (SimulReflec) [9] based on the Parratt's formulism [10]. These theoretical calculations were performed considering a multilayered film formed by a sapphire substrate, a $Fe_3O_4$ thin layer and a vacuum phase on the top of the film. The parameters used to simulate each layer is thickness ($t$), atomic density ($\rho$), scattering lengths ($f$ and $f'$), and roughness ($\sigma$). For the sapphire substrate, one used the theoretical values within the software database: $t$ = 0 nm, $\rho$ = 2.3×10$^{28}$ m$^{-3}$, $f$ = 51.9 fm, $f'$ = 0.57 fm and $\sigma$ = 0 nm. Likewise, the $Fe_3O_4$ thin layer (black line) has: $t$ = 15 nm, $\rho$ = 1.4×10$^{28}$ m$^{-3}$, $f$ = 108.0 fm, $f'$ = 9.7 fm and $\sigma$ = 0.1 nm. As depicted in **Figure 2.5a**, the spacing between two maxima of the interference fringes is halved by doubling the thickness from 15 nm (black line) to 30 nm (red line). The $\theta$ values for the maxima and minima of are related to the thickness ($t$) as follows [11]:

$$sin^2\theta_i = \theta_C^2 + (n_i + \Delta n)^2\lambda^2/4t^2 \tag{2.3}$$

where $\theta_i$ is the observed position of the maximum or minimum of the i$^{th}$ interference fringe, $n$ is an integer and $\Delta n$ is equal to 0.5 and 0 for the maximum and minimum, respectively. The $\theta_C$ is the critical angle below which the X-ray beam is completely reflected. Hence, before the oscillations begin ($\theta$ smaller than ~0.3°), one observes a reflectivity plateau in the XRR data. The critical angle ($\theta_C$) is a function of the density ($\rho$) and composition of the layer:

$$\theta_C^2 = 5.402 \times 10^{-6}\rho\lambda^2(Z + f)/A \tag{2.4}$$

where $Z$ is the atomic number, $A$ the atomic mass and $f$ the real part of the anomalous dispersion term (atomic scattering factor). As shown in **Figure 2.5b**, both $\theta_C$ value and amplitude of the oscillations increase as the density increases from 1.4×10$^{28}$ m$^{-3}$ (black line) to 2.8×10$^{28}$ m$^{-3}$ (blue line).

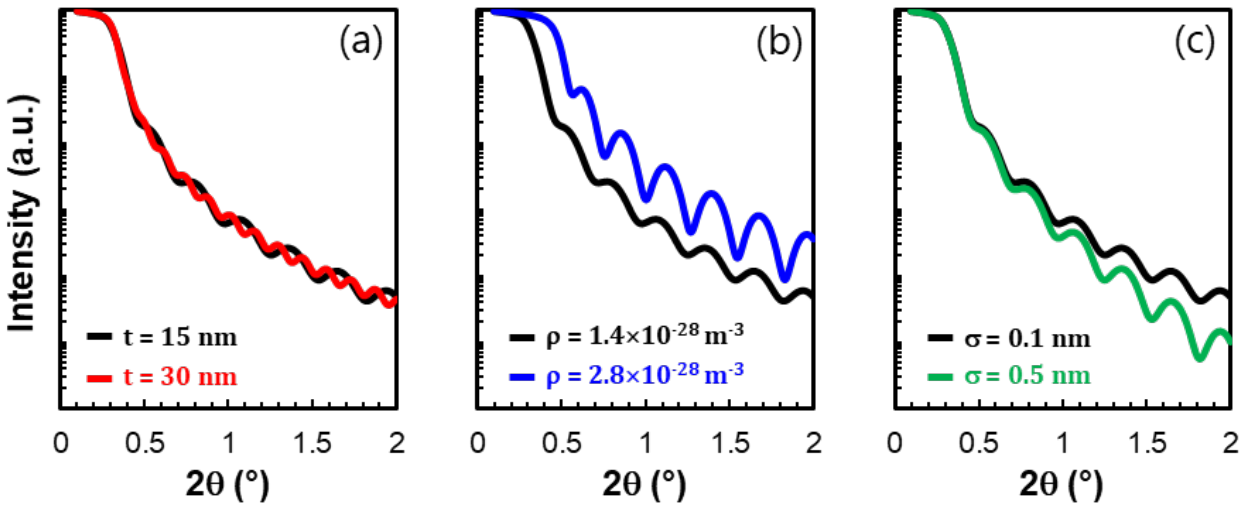


**Figure 2.5.** Simulated XRR pattern for a multilayered film formed by a sapphire substrate, a $Fe_3O_4$ thin layer and a vacuum phase on the top of the film. The shape of the interference fringes depends on the film (a) thickness, (b) density and (c) roughness.

The surface roughness (σ) determines how quickly the reflected signal decays, as shown in **Figure 2.5c**. A rougher surface produces more diffuse scatter than reflected, causing the reflected beam intensity to decay quicker with θ. Hence, thickness and roughness are two of the parameters that can be determined directly from the position and spacing of the interference fringes observed in a reflectivity curve. Herein, the XRR data were normalized and then analyzed in the SimulReflec package. As abovementioned, this software simulates the reflectivity curve of a multilayer model, parametrized by the thickness, density and roughness of each layer. These parameters are determined by a non-linear least-squares fitting of the experimental data compared to the calculated one. According to the literature [11], the precision for the values of t and ρ were reportedly about 1% and 3%, respectively.

For selected $Fe_{3-x}Cr_xO_4$(111) samples, high-resolution XRD (HRXRD) were performed in collaboration with Denis Menut on MARS beam line of SOLEIL synchrotron [12]. These measurements showed a close-up view of the (222) Bragg peak where the appearance of Laue oscillations reflects the structural homogeneity of the film and low density of defects (see **Section 4.2**). Thickness and the lattice parameter were determined by the fit of the oscillations with a Laue function:

$$sin^2(\frac{Qt}{2})/sin^2(\frac{Qd}{2}) \quad (2.5)$$

where $Q$ is the length of the scattering vector, $t$ is the crystal thickness and $d$ is the interplanar spacing in the direction of the scattering vector. These parameters were compared with the ones obtained by laboratory instruments.

### 2.2.3 Structural and chemical characterization electron microscopies

The microstructure of selected $Cr_2O_3$(0001) and $Fe_{3-x}Cr_xO_4$(111) samples were investigated by high-resolution transmission electron microscopy (HRTEM) on CEMES-CNRS laboratory in Toulouse. This work was done in collaboration with Robin Cours (preparation of microscope slides in focused ion beam), Cécile Marcelot and Bénédicte Warot (acquisition and analysis of micrographs). Succinctly, HRTEM images are formed by a process known as *phase contrast*. The contrast is defined by constructive or destructive interference between the electron waves passing through the crystal. If all electron waves are in phase (*i.e.,* perfect focus), there is no contrast. By altering the focus (either under or over focus), the waves move out of phase given rise to interference patterns that form the actual image. The HRTEM image is not a simple function of the position of individual atoms in the crystal. Yet, in many cases, atomic columns appear as nearly Gaussian shaped regions of contrast, which are either dark or bright depending on the crystal thickness and the objective lens defocus. Hence, such images can be used to determine local distortions of the lattice and analyze local variations in structural parameters [13].

In this work, HRTEM images were recorded using I2TEM microscope operating at 300 kV and fitted with an objective lens aberration corrector (point resolution of 80 pm). Cross-sectional samples were prepared by cutting along the $[1\bar{1}00]$ and/or $[\bar{1}2\bar{1}0]$ crystallographic directions before thinning

by mechanical grinding and ion milling (using a precision ionic polish system) in order to achieve electron transparency. Three main information were obtained within this technique:

1. **Film structure and interfaces.** In **Chapter 3 and 4**, low magnification TEM micrographs probed the homogeneity and thickness of the films (**Figure 2.6a**), whereas HRTEM micrographs (**Figure 2.6b**) checked the presence of parasites phases at atomic scale and confirmed the epitaxial nature of the films.

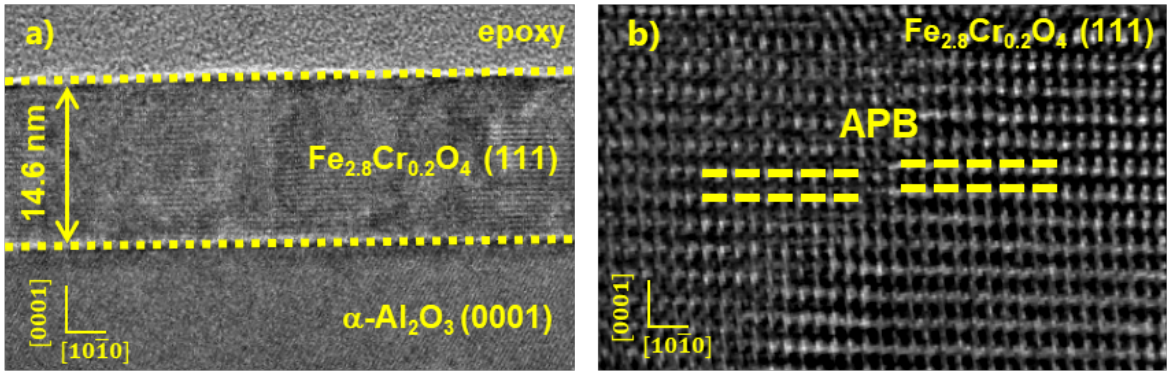


**Figure 2.6.** Cross-sectional TEM images of $Fe_{2.8}Cr_{0.2}O_4$ thin film recorded along the $[\bar{1}2\bar{1}0]$ direction at increasing magnification. Low magnification TEM (a) shows the homogeneity in thickness and structure of the 14.6 nm thick film. HRTEM images (b) depict the epitaxial nature of the film and the presence of an antiphase boundary (APB).

2. **Structural defects.** HRTEM micrographs probed structural defects such as misfit dislocations (**Chapter 3**) and antiphase boundaries (**Chapter 4**). **Figure 2.6b** shows an example of HRTEM micrograph obtained for an iron chromite thin film, for which a vertical half-lattice translation of the cationic sublattice is highlighted (*i.e.,* antiphase boundary). These results were key to understand the epitaxial growth of the film, as well as the observed deviations of the film physical properties from the bulk, as detailed in **Section 4.3**.

3. **Chemical characterization.** The I2TEM microscope is equipped with electron energy loss spectroscopy (EELS) detector, which enables chemical maps of the samples to be drawn [14], [15]. This spectroscopic method measures the energy loss of the electrons traversing a specimen due to inelastic interactions. These interactions include core level excitations, which yield a unique energy losses spectrum for each element of the periodic table. By detecting the losses corresponding to a specific element absorption edge (here, O-K edge and Cr and/or Fe $L_{2,3}$-edge), one obtains a map of the areas in the sample where that element can be found. This technique was especially useful to confirm the nominal composition and the homogeneity of the thin films. The quantitative elemental analysis is usually given as the concentration ratio between elements in the same spectrum. For instance, **Figure 2.7** shows a STEM-EELS spectrum for an iron chromite. Herein, the stoichiometric ratio between Fe and Cr ($N_{Fe}/N_{Cr}$) is determined by the relative intensities of the characteristic signals (I) between the Fe and Cr $L_{2,3}$-edge after background subtraction (shaded are in **Figure 2.7**):

$$\frac{N_{Fe}}{N_{Cr}} = \frac{I_{Fe}(\beta,\Delta)}{I_{Cr}(\beta,\Delta)} \times \frac{\sigma_{Fe}(\beta,\Delta)}{\sigma_{Cr}(\beta,\Delta)} \quad (2.6)$$

where N is the number of atoms per unit area in the analyzed volume, I is the area obtained after background subtraction[16] and integration over the energy loss window (Δ) and σ is the scattering cross-section partially integrated over the collection angle (β) and the energy loss window (Δ).

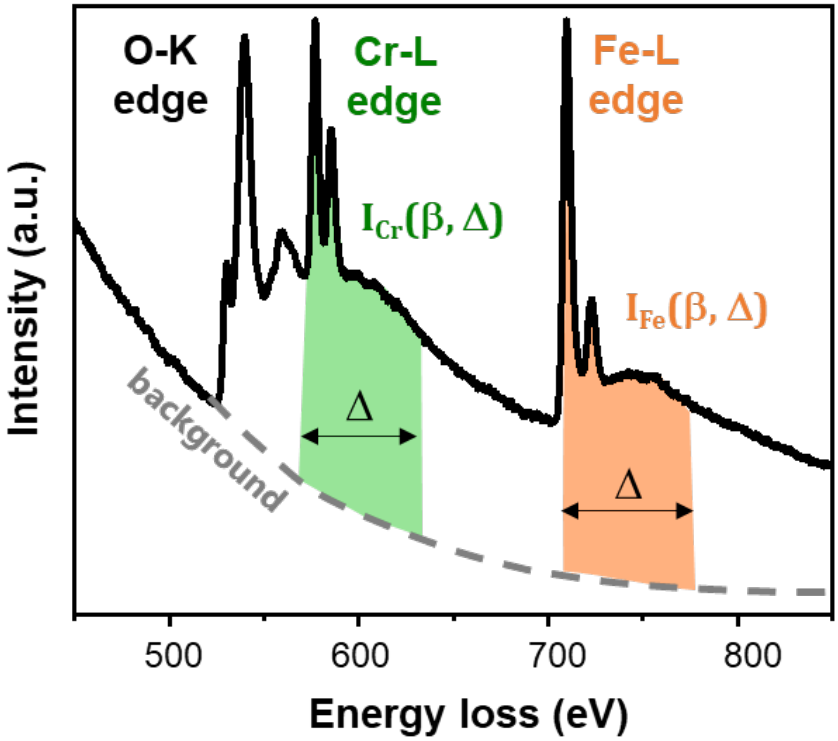


**Figure 2.7**. STEM-EELS spectrum of 15 nm-thick $Fe_{2.3}Cr_{0.7}O_4$ thin film highlighting the characteristic signals (I) of the Fe and Cr $L_{2,3}$-edge integrated over the energy loss window (Δ).

The elemental composition of the iron chromites was also investigated using CM20FEG microscope (200 kV), equipped with energy-dispersive X-ray spectroscopy (EDX) detector. This method measures the X-rays emitted due to transition of electrons located in high-energy outer shells to fill the core holes created by the impact of the incident electron beam on a low-energy inner shell. Herein, the quantitative analysis is also performed by the ratio of the element characteristic signals within the same spectra. EELS and EDX are complementary techniques and their results are discussed in detail in **Section 4.4.1**.

[16] The continuous background is due to scattering phenomena that precede the studied edges. They are usually represented by a power law of type $AE^{-r}$ (where E is the energy loss) but also sometimes by a polynomial function or a line. The parameters that describe this law (*e.g.*, A and r for the $AE^{-r}$ law) are determined by the simulation of the continuous background before the analyzed edges.

# 2.3 Chemical and fine structure investigations

## 2.3.1 X-ray photoemission spectroscopy: fundamentals and applications

X-ray photoemission spectroscopy (XPS) is a powerful tool to obtain elemental and chemical information of the surface of solids. The fundamentals of this technique is to measure the kinetic energy of photoelectrons ejected from the sample after hitting a core electron with soft x-rays [16], as depicted in **Figure 2.8**. The emitted electrons have measured kinetic energies ($\varepsilon$) given by:

$$\varepsilon = h\nu - (\varepsilon_F - \varepsilon_C) - \phi_S \tag{2.7}$$

where $h\nu$ is the incident photon energy, $\varepsilon_F$ the Fermi energy, $\varepsilon_C$ the core level, and $\phi_S$ the spectrometer work function. By definition, $\varepsilon_F$ corresponds to zero binding energy and the depth beneath the Fermi level indicates the binding energy of the electron (BE). Thus, BE is rigorously defined as the $A^0 \rightarrow A^+(\underline{k})$ transition from atoms in a neutral initial state $A^0$ with Z electrons to atoms in a excited final state $A^+$ with Z-1 electrons after the ejection of an electron from the $k$-level. Many final states with different probabilities (or cross-section) are possible for each type of atom, for which a variety of kinetic energies of the emitted electrons can be related. Because each element has a unique set of BEs, XPS can be used to identify and quantify elements in the surface. It should be noted that most of the XPS signal comes from the first nanometer of a sample.

Theoretically, $\varepsilon_C$ values can be obtained by the Hartree-Fock theory[17] (HF) [17] within the mono-electron approximation, and then Equation 2.7 represents the Koopmans' theorem. Experimentally, on the other hand, this value is deduced from the XPS spectrum if the other quantities ($\varepsilon$, $h\nu$, and $\phi_S$) in Equation 2.7 are known. In fact, the measured value of $\varepsilon_C$ does not diverge much from the corresponding value of the free atom. Small deviations, known as chemical shift, occur due to chemical bonding of valence electron states. Hence, XPS is also sensitive to the oxidation state of the transition metals and the iono-covalent character of the bonds.

For transition metals, Koopmans' theorem does not usually hold because of the many-body effect beyond the HF approximation. The excitation of a photoelectron by an X-ray photon creates a core-hole that is screened by the surroundings. The core-hole potential polarizes the valence electron states mainly by charge-transfer effects, which are reflected in the XPS spectrum as a spectral asymmetry and satellites. This effect is more drastic for transition metals with incompletely filled $d$ states. In these materials, charge transfer occurs from conduction (or valence) band states to the $d$ electron states in order to screen the core-hole potential, resulting in characteristic splitting of the XPS spectrum into well- and poorly-screened final states. Satellites originate from the charge transfer between the ligand $2p$ and metal $3d$ orbitals are commonly observed in metal oxide spectra [18]. The

[17] The Hartree-Fock theory is a simplification of the electronic Schrodinger equation introduced in the late 1920s, in which the $N$-electron wave function is approximated as a single Slater determinant constructed from the one-electron wave function.

number of charge transfer satellites is proportional to the number of possible initial state configurations: $3d^n$, $3d^{n+1}\underline{L}$, $3d^{n+2}\underline{L}\underline{L}'$, *etc.*, where $\underline{L}$ indicates an oxygen $2p$ hole. The position and intensity of these satellites structures are also element specific and are commonly used to identify different oxidation states of a given element in the material [19].

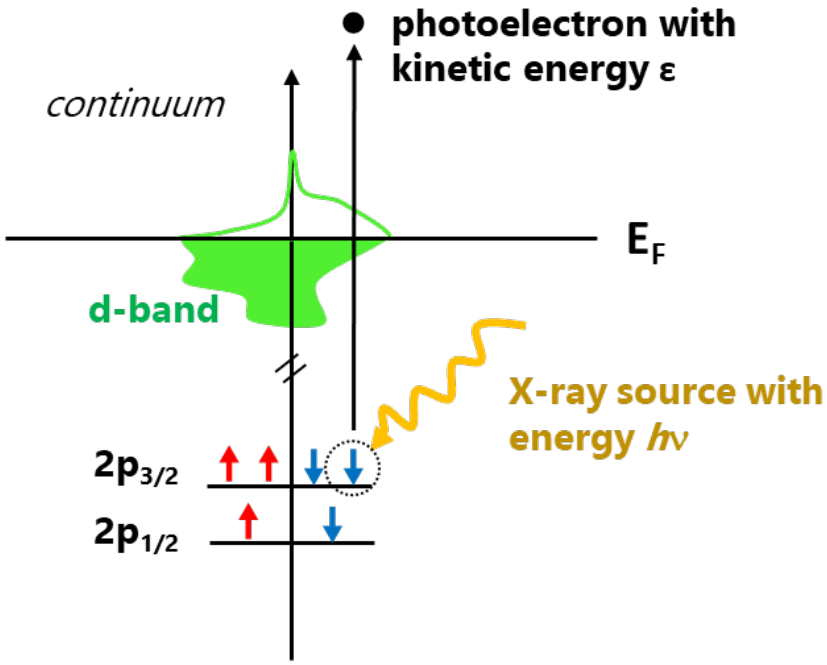


**Figure 2.8.** Two-step schema of the $2p$ XPS principle. Soft X-ray ($h\nu$) is absorbed inside the solid and excite a photoelectron of the $2p$ core level. The excited photoelectron is transported to the surface and escape with kinetic energy $\varepsilon$.

Spectral asymmetry and peak broadening are also observed in paramagnetic transition metals due to coupling between the core-hole and the unpaired electrons in the $3d$ outer shell [16]. This effect is referred as intra-atomic multiplet coupling. In order to understand it, let us analyze the simple theoretical case of photoemission of the lithium $1s$ core level. In this case, the excitation of lithium initial configuration ($1s^2\ 2s^1$) gives rise to two final states ($1s^1\ 2s^1$), in which the residual unpaired electron is parallel ↑↑ (*i.e.,* high spin $^3S_1$) or antiparallel ↑↓ (*i.e.,* low spin $^1S_0$) coupled to the $2s$ valence electron. Due to repulsive exchange interactions between electrons with same spin, the high spin final state ($^3S_1$) has potential energy higher than the low spin final state ($^1S_0$). Hence, two peaks with different BEs should appear in the XPS Li $1s$ spectra. The relative energy between these two peaks is given by the spin multiplicity $2s+1$ (*i.e.,* for Li $1s$, $^3S_1/^1S_0 = 3$). Moreover, the energy difference ($\Delta E$) between the final states is theoretically given by the Van Vleck relation [20] for a free atom:

$$\Delta E = \frac{2S+1}{2l+1}G \tag{2.8}$$

where $S$ is the total spin at initial state ($S$ = ½ for Li), $l$ the orbital moment of ionized orbital ($l$ = 0 for Li $1s$ orbital), and $G$ the repulsive exchange integral between the $1s$ residual electron and the unpaired

electron in the outer $2s$ shell. In solid systems, $\Delta E$ is smaller than the theoretical value because the exchange interactions are reduced due to the delocalization of valence electrons by chemical bond formation. Therefore, BE position and intensity of the spin multiplets are sensible to crystal field effects surrounding the transition metal. **Section 2.4** gives more details in the mathematical description of many body effects, while **Section 3.4** shows how they can be used to explore core level spectra.

In this work, *ex situ* XPS analyses were carried out for all samples using an *Escalab 250 XI* spectrometer placed in one of my host laboratories (SCCME/LECA). The instrument is equipped with a monochromatic Al Kα source ($h\nu$ = 1486.6 eV) and a dual-beam flood gun for charge compensation[18]. High-resolution spectra were acquired at room temperature using a 5 eV pass energy[19] and an analysis spot of 900 µm of diameter. For spinels with low Cr-content, there was no need for charge compensation. However, for spinels with high Cr-content and corundum samples, a low-energy electron flood gun was used during spectral acquisition to avoid charge effects. The binding energies were corrected by fixing the contamination $1s$ line of carbon at 285.0 eV. The data was treated using the commercial AVANTAGE software (*Thermo Fisher Scientific Inc.*). Three main information were extracted from these spectra:

1. **$Cr_2O_3$ local structure.** In **Chapter 3**, the position and intensity of the spin multiplets in the Cr $2p$ XPS spectra of $Cr_2O_3$ are used to quantify strain-induced changes in the crystal field around the $Cr^{3+}$ cation. In fact, core level spectra are sensitive not only to the oxidation state, but also to the cation local environment. For instance, **Figure 2.9a** shows XPS spectra for chromium oxides in the corundum ($Cr_2O_3$) and the spinel ($Fe_{1.8}Cr_{1.2}O_4$) phases. Both Cr $2p$ spectra present two main asymmetrical peaks for Cr $2p_{3/2}$ and Cr $2p_{1/2}$ envelopes, centered respectively at 576.5 eV and 586.5 eV. Although the Cr cations in these two samples have only oxidation state 3+, they do not have the same spectrum shape due to changes in their cation local symmetry. To aid interpretation of the complicated Cr $2p$ spectral shape, theoretical calculations were performed (see **Section 2.4**). The results of these calculations are discussed in detail in **Section 3.4** and **Section 4.4.2**.

[18] Charge effects [21] are artifacts that appear during XPS measurements of insulating samples. Due to the photoemission phenomenon, the surface of the sample becomes positively charged. These residual charges accumulate in electrically insulating surfaces, creating a surface potential that slows down the emitted photoelectrons. This artefact causes the peaks in the spectrum to shift to high BEs and become distorted. The charge effects are especially important for monochromatic X-ray sources and need to be neutralized by replenishing electrons from an external source.

[19] The XPS analyzer operates as an energy window (or pass energy) that accepts only electrons within the range of this window. Constant energy resolution is obtained by fixing the pass energy (*i.e.,* constant analyzer energy mode).

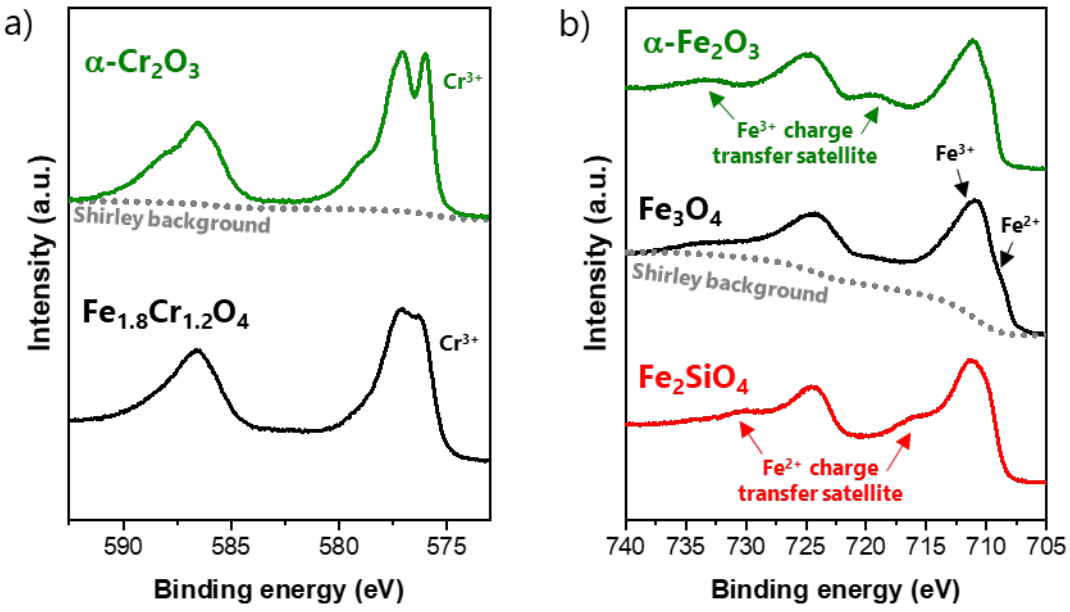


**Figure 2.9.** Reference (a) Cr and (b) Fe 2*p* XPS spectra for different chromium and iron oxides. For $\alpha$-$Fe_2O_3$ and $Fe_2SiO_4$, $Fe^{3+}$ and $Fe^{2+}$ charge transfer satellites are marked with green and red arrows, respectively. For $Fe_3O_4$, the $Fe^{2+}$ and $Fe^{3+}$ contributions are evidenced using black arrows. The Shirley-type background is depicted as dotted gray line.

2. **The stoichiometry of the $Fe_{3-x}Cr_xO_4$ films.** XPS is a semi-quantitative surface analysis technique with low matrix effect and great repeatability. Herein, the stoichiometric ratio between Fe and Cr ($N_{Fe}/N_{Cr}$) is determined by the relative intensities (I) between the Cr 2*p* and Fe 2*p* core level after Shirley background subtraction[20]:

$$\frac{N_{Fe}}{N_{Cr}} = \frac{3-x}{x} = \frac{\frac{I_{Fe}}{\sigma_{Fe}\lambda_{Fe}T(E_{Fe})}}{\frac{I_{Cr}}{\sigma_{Cr}\lambda_{Cr}T(E_{Cr})}} \quad (2.9)$$

where $\sigma$ is the photoelectric cross-section for the atomic orbital of interest, $\lambda$ the mean free path of the photoelectrons in the sample, $T(E)$ is the detection efficiency for electrons emitted from the sample. These physical parameters were evaluated and tabulated for many elements years ago [23]. In this work, the AVANTAGE software database was used. It is important to highlight that the path length of photoelectrons in a sample is limited to few nanometers. Because of the surface sensitive character of the XPS technique, complementary chemical analyses were performed to confirm the stoichiometric of the $Fe_{3-x}Cr_xO_4$ films (see **Section 4.4.1**).

[20] In the photoemission process, electrons undergoing inelastic collisions before emerging from the surface form the background in the spectrum. The Shirley function [22] is widely adopted to describe this inelastic background. It has an S shape and proposes a background intensity at a given energy proportional to that of the photoelectrons emitted at the next higher kinetic energies.

3. **Fe and Cr oxidation state in the Fe-Cr-O system.** As abovementioned, the XPS method is element specific. The value chemical shift and the satellites structures are commonly used to identify different oxidation states of a given element. **Figure 2.9b** depicts reference XPS spectra for different iron oxides. The Fe $2p$ spectra present two main asymmetrical peaks for Fe $2p_{3/2}$ and Fe $2p_{1/2}$ envelopes, centered respectively at 711 eV and 724 eV. While additional satellite peaks due to charge transfer appear 8 eV above the main peaks for pure $Fe^{3+}$ compounds ($\alpha$-$Fe_2O_3$), pure $Fe^{2+}$ compounds ($Fe_2SiO_4$) have satellite peaks 4 eV above the main peaks. No satellite peaks are observed in mixed iron oxides such as $Fe_3O_4$ and $Fe_{3-x}Cr_xO_4$. Herein, the oxidation state of the iron species was differentiated by XPS measurements due to the presence (or not) and the position of satellite peaks.

## 2.3.2 X-ray absorption spectroscopy: fundamentals and applications

In the study of $Fe_{3-x}Cr_xO_4$ thin films, X-ray absorption spectroscopy (XAS) measurements were performed to access the electronic structure and the local environment of the Fe and Cr atoms in the spinel structure. The fundamentals of this synchrotron-based characterization technique is to measure the energy-dependent fine structure of the X-ray absorption coefficient, μ(E), near the absorption edge of a particular element [24]. The probability of that X-rays will be absorbed is described by the Beer-Lambert's law:

$$I_{sample} = I_0 e^{-\mu t} \tag{2.10}$$

where $I_{sample}$ is the intensity transmitted through the sample, $I_0$ the X-ray intensity incident on a sample, and $t$ is the sample thickness. The value of μ depends strongly on both energy (E) and atomic number (Z): $\mu \approx \rho Z^4/AE^3$, where $\rho$ is the sample density and A the atomic mass.

In the XAS process, a core electron is excited to an empty state through the electric dipole transition (and quadrupole transitions for some hard X-ray regions). Hence, a sharp rise in absorption is observed when the incident X-ray has energy equal to that of the binding energy (BE) of a core level electron. This intense peak is referred as the *absorption edge*, more precisely: K-edge for excitation of $1s$ core level electrons, $L_1$-edge for $2s$, $L_{2,3}$-edge for $2p$, and $M_{4,5}$-edge for $3d$. Similar to the XPS technique, the position and shape of the XAS absorption edges depend on the electronic structure and the local environment of the transition metals. For instance, increasing the redox state of the cation shifts the absorption edge to higher energies. Moreover, since in XAS a core level electron is excited near to the excitation threshold, it probes empty states. That is, in K-edge $1s$ electrons are promoted to vacant $p$ levels ($1s \rightarrow 3d$, $4p$), while in $L_{2,3}$-edge $2p$ electrons are promoted to vacant $d$ or $s$ levels ($2p \rightarrow 3d$, $4s$). The shape of the peaks arising from electron excitation to $d$ localized orbitals is then very sensitive to the crystal field surrounding the absorbing transition metal. The chemical and orbital selectivity offered by this technique are essential to obtain spectral information on all cations contained in mixed spinels, such as $Fe_{3-x}Cr_xO_4$ series, since XAS spectral shape is a linear combination of all individual sites.

### 2.3.2.1 K-edge XANES and EXAFS for fine structure investigation

The XAS technique has different names depending on the energy resolution used and the spectral region studied. One refers this technique as XANES for near-edge spectra, typically within 50 eV of the main absorption edge and EXAFS for the extended fine structure, typically 50 eV above the edge energy [25]. Depending on the energy of the incident X-ray photon ($E_{in}$), different physical events lead to different structures in the measured absorption spectrum. **Figure 2.10** depicts the four different regions of the Fe K-edge XAS spectrum and the physical events occurring in each of them.

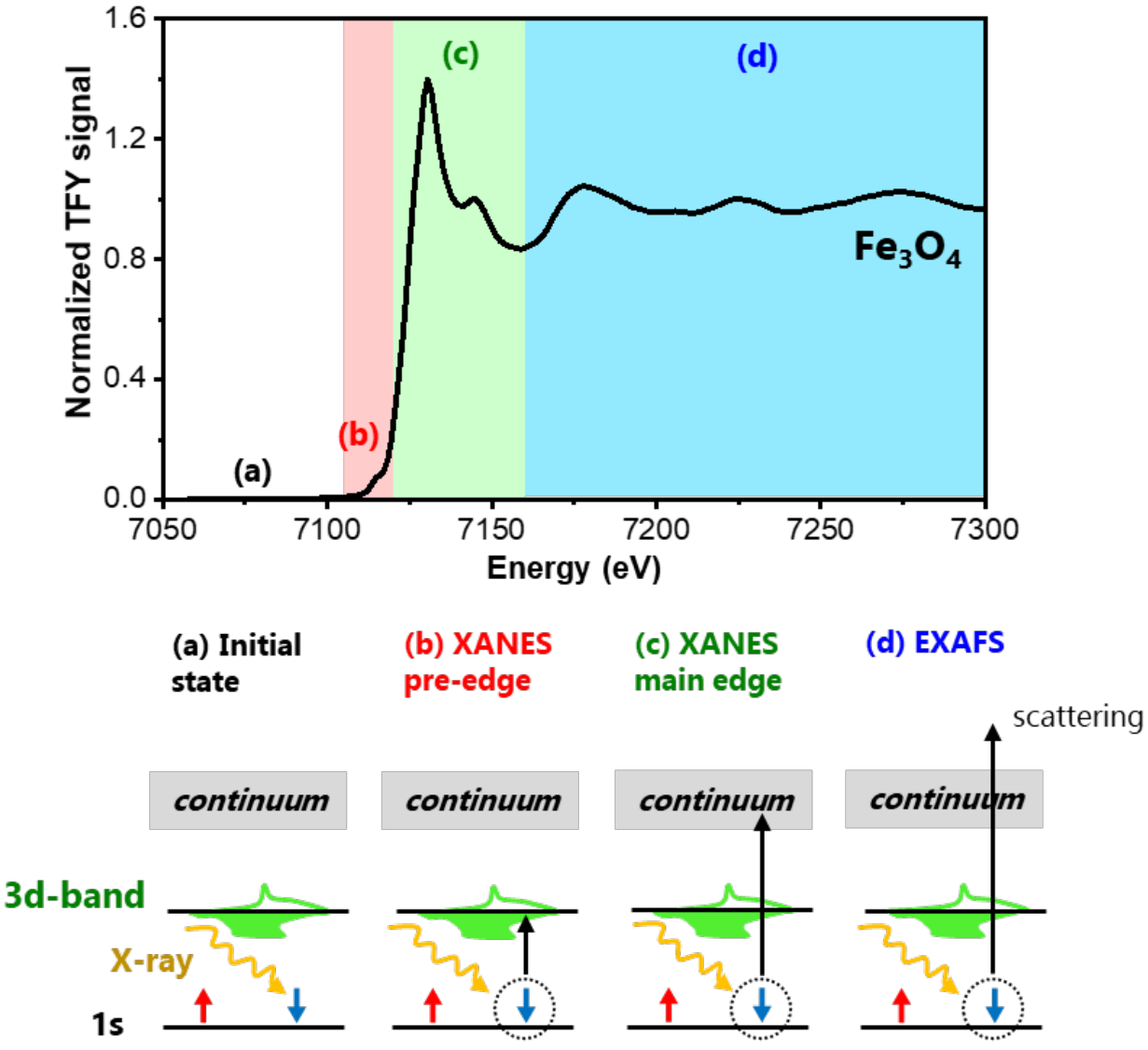


**Figure 2.10.** Different regions of the Fe K-edge XAS normalized spectrum of $Fe_3O_4$ and the physical events occurring in each of them.

First, $E_{in}$ is lower than the $1s$ BE and the electrons are not excited, leading to a flat region in the XAS spectra (**Figure 2.10a**). When $E_i$ becomes sufficient to transfer $1s$ core electrons to the first

open shells (**Figure 2.10b**), some unfavorable transitions may occur, such as local electric quadrupole transitions $1s \rightarrow 3d$. The quadrupole transitions are some hundred times weaker than the dipole transitions and results in small peaks in the XANES pre-edge region. A large jump in absorption is observed in the XANES region for the local electric dipole transitions $1s \rightarrow 4p$, where the $4p$ levels of the absorbing cation are hybridized with the empty $3d$ states [26] (**Figure 2.10c**). The further increasing in $E_{in}$ ejects the core electron to the continuum with a large kinetic energy. In the EXAFS region (**Figure 2.10d**), the electron is essentially involved in scattering processes with neighboring atoms, forming oscillations in the experimental data.

There are three basic modes for XAS signal collection, *i.e.,* transmission, fluorescence, and electron yield. The transmission mode measures the difference between incident and directly transmitted X-ray intensity. The fluorescence mode collects the emitted X-rays from the elements, whereas electron yield mode measures the emitted photoelectrons from the sample itself. In this thesis, K-edge XANES and EXAFS measurements were carried out on the MARS Beamline of synchrotron SOLEIL [27], together with Dr. Denis Menut and Dr. Myrtille Hunault. The spectra were recorded at the K-edge of Cr (5989 eV) and Fe (7112 eV) in total fluorescence yield (TFY) mode, which enables to probe the entire film. The XANES and EXAFS data presented here are an average of four spectra obtained successively. The pre-edge and post-edge background of the average spectra was removed followed by a normalization procedure (*i.e.* edge-step normalization) performed using the ATHENA software [28]. Whereas the pre-edge background was traced by an arctangent function used to fit the edge tail, the post-edge is determined by a quadratic polynomial beyond the edge. The difference between these two functions extrapolated to the edge energy ($E_0$) is used as the normalization constant in the definition of the edge-step normalization. The criteria for good pre- and post-edge lines can be a bit subjective. **Figure 2.11** shows the background used to normalize the $Fe_3O_4$ spectrum (**Figure 2.10**). Note that the parameters ($E_0$, pre-edge and post-edge range) were well chosen as both lines pass through the middle of the data in their respective energy ranges.

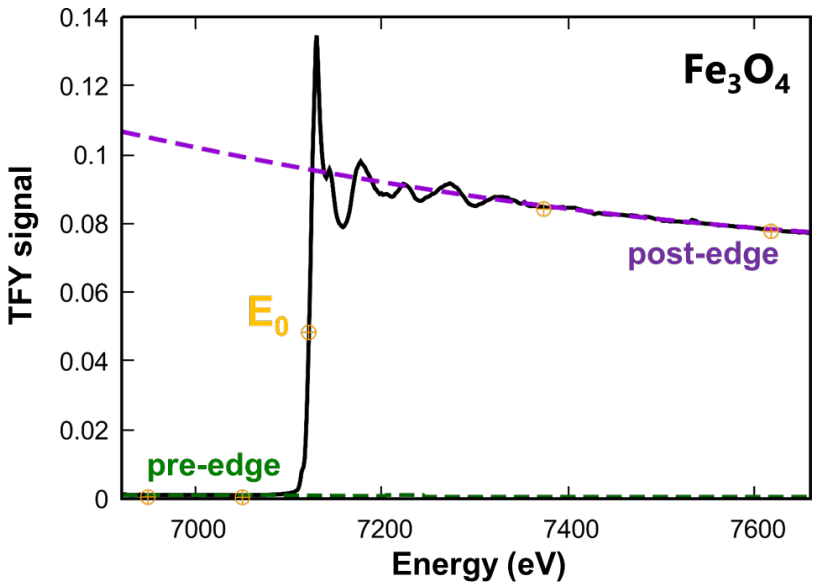


**Figure 2.11.** Fe-edge XAS spectrum of $Fe_3O_4$ with the pre (green line) and post-edge (purple line) backgrounds used to normalize the spectrum.

Two main information were extracted from the XANES and EXAFS data:

1. **Fe and Cr local electronic environment in the $Fe_{3-x}Cr_xO_4$ films.** The XANES region is sensitive to the oxidation state and electronic structure of the absorbing elements as it is affected by the electron distribution in the valence state. Although rich in information, this region is very complex due to multiple scattering processes and the support of calculations are often needed to interpret the spectra. In this thesis, XANES spectra above K-edge is interpreted using simple fingerprint analysis, as discussed in **Section 4.4.2**.

2. **Coordination number and bond distances.** In the EXAFS region, the interferences between the electronic wave from the absorber cation and the waves backscattered by neighboring atoms form oscillations in the experimental data. The analysis of these EXAFS oscillations was made in order to extract average information about the nature and number of neighbors, the first cation-neighbors bond distances and the structural disorder around the cations. The EXAFS was treated using the ARTEMIS software [28], in which the data are described as a summation of one or more scattering paths as computed by the code FEFF [29], [30]. The EXAFS equation for each path $\Gamma$ included in the fit is:

$$\chi^{\Gamma}(k) = -\sum_{\Gamma} \frac{S_0^2}{kR^2} |f_{eff}^{\Gamma}(k)| \sin\left[2kR + \phi^{\Gamma}(k) + 2\delta_c(k)\right] \times e^{-2\sigma_{\Gamma}^2 k^2} e^{-2R/\lambda(k)} \qquad (2.11)$$

where $k$ is the momentum of the photoelectron, $R$ the effective path length, $f_{eff}^{\Gamma}(k)$ is the effective scattering amplitude for that path, $S_0^2$ is an amplitude reduction factor to account for intrinsic losses and interference, $\phi^{\Gamma}(k)$ is the net scattering phase shift, $\delta_c(k)$ is the final state shift at the absorbing atom and $e^{-2\sigma_{\Gamma}^2 k^2}$ is the Debye-Waller factor. Herein, there are five potential adjustable parametric terms that must be specified for each path: the number of data points (N), the edge energy ($E_0$), $S_0^2$, $R$, and $\sigma^2$. These are too many parameters to be independently measured. Thus, **Section 4.4.2** discusses constrains and simplifications made in order to get physically meaningful measurements out of the XAFS analysis.

### 2.3.2.2 $L_{2,3}$-edge XAS and XMCD for fine structure investigation

The $L_{2,3}$-edge XAS signal is mainly built by excitation of $2p$ core electrons to $3d$ empty states ($2p^6 3d^n \rightarrow 2p^5 3d^{n+1}$) through the electric dipole transition. Dipole $2p \rightarrow 4s$ and quadrupole electron transitions are usually negligible in transition metals [31]. Just like XPS, many-body effects play a key role in the XAS process. In this process, the core-hole potential is mainly screened by the photo-excited electron itself, suppressing the screening effect because of the charge-transfer effect. Hence, XAS spectral shape is especially influenced by crystal field and intra-atomic multiplet coupling effects. These multiplet structures are element specific and can be used to obtain information on the local environment of the cations.

One of the most powerful applications of $L_{2,3}$-edge XAS to ferromagnetic or ferrimagnetic materials is to use polarized incident X-ray in order to assess their local magnetic properties. Detailed information about this technique can be found elsewhere [32]–[35]. Briefly, dichroic signal arises when the absorption depends on the relative orientation between the polarization of the light (right- and left-circularly-polarized, or even horizontal and vertical-linearly-polarized) and the electronic properties of the material. In the X-ray magnetic circular dichroism (XMCD) technique, a saturating magnetic field is applied in the same direction as the wave vector of the incident photons in order to align the spins in ferromagnetic or ferrimagnetic materials. Then, the difference in absorption between right ($\sigma^+$) and left ($\sigma^-$) circularly-polarized X-rays is measured:

$$I_{XMCD} = \sigma^+ - \sigma^- \tag{2.12}$$

**Figure 2.12** depicts the physical origin of XMCD signal at $L_{2,3}$-edge in a two-step model. The first step is the excitation of $2p$ core electrons by circularly-polarized X-ray photon, carrying angular momentum with helicity vector parallel (right) or antiparallel (left) to the propagation direction. Part of the angular momentum carried by the photon is converted into spin via spin-orbit coupling. The sign of the acquired spin moment depends on the helicity of the incident X-ray photon and on the spin-orbit coupling ($l+s$ at the $L_3$ and $l-s$ at the $L_2$). Since the transition is spin conservative (*i.e.,* an up electron is not allowed to land in the down valence band), the second step is driven by the magnetic properties of the sample. The polarized photoelectrons probe the spin-up or spin-down states of the $3d$-bands. If there is any imbalance in either spin or orbital momentum in the final states, the XMCD signal is non-zero. Therefore, in addition to chemical and orbital selectivity, the XMCD technique probes the magnetic moment of the elements.

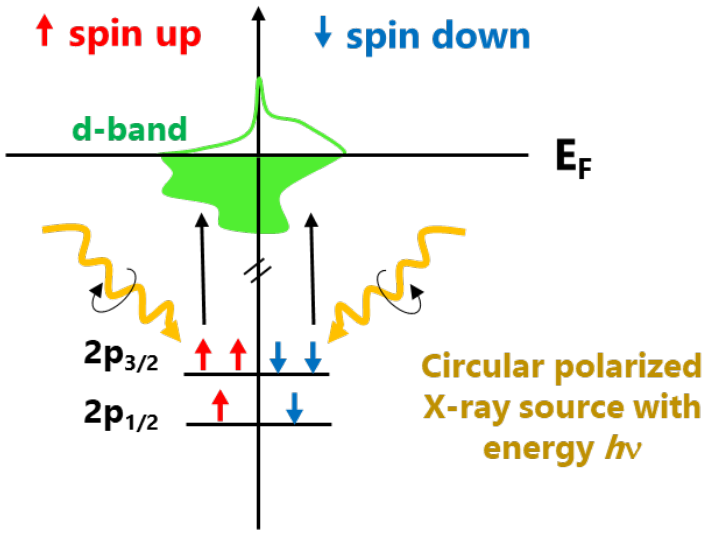


**Figure 2.12.** Two-step schema of the XMCD principle at $L_{2,3}$-edge. Left- (or right) circularly-polarized X-ray excites electrons from the $2p$ core level, which selectively probe spin-up or spin-down states of the $3d$-bands.

In this work, the $L_{2,3}$-edge XAS and XMCD measurements were performed at DEIMOS Beamline [36], [37] of synchrotron SOLEIL together with Dr. Philippe Ohresser and Dr. Antoine

Barbier. The samples were saturated with a magnetic induction[21] of ±2.0 T parallel to the wave vector of the incident photons. X-ray absorption spectra were acquired at temperatures of 4 K and 300 K, with an angle of 60° between the beam and the sample surface. The XAS spectrum (**Figure 2.13a**) is the average of the circular ($\sigma^+$ and $\sigma^-$) absorption cross section, while the XMCD spectrum (**Figure 2.13b**) is the difference between the circular right ($\sigma^+$) and left ($\sigma^-$) absorption cross section. The absorption signal was recorded in total electron yield (TEY) mode. The photocurrent of the electrons flowing from the sample was measured with electrometers connected to a counting card. Because electrons are emitted mostly from the first 2–5 nm of a sample, this approach is very sensitive to the surface. All measurements were performed in UHV conditions, *i.e.,* base pressure inside the chamber of about $10^{-10}$ mbar.

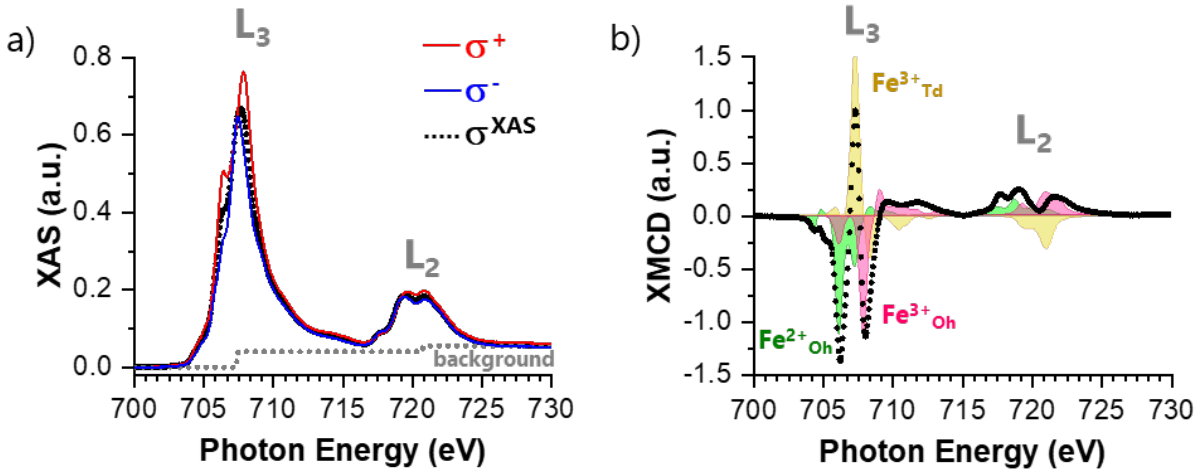


**Figure 2.13.** Fe $L_{2,3}$-edges (a) XAS and (b) XMCD spectra for $Fe_3O_4$ acquired at magnetic induction of 2.0 T and at room temperature. Here the raw spectra were normalized to the pre-edge and the background constant to 1 was subtracted. The contributions of each iron species – $Fe^{2+}_{Oh}$, $Fe^{3+}_{Oh}$ and $Fe^{3+}_{Td}$ – are shown in green, pink and yellow shades, respectively. These curves were simulated using the atomic multiplet theory, as described in **Section 2.4**. The dotted gray line depicts the typical "step-like" background (with higher intensity at the $L_2$-edge) due to transition to delocalized states.

In practice, the XMCD spectra were deduced from different set of XAS measurements alternating both the circular polarization and the direction of the applied magnetic field. Two main information were extracted from these spectra:

1. **Magnetic properties of the $Fe_{3-x}Cr_xO_4$ films.** The XMCD signal intensity is proportional to the projection of the total magnetic moment ($l+s$ at the $L_3$ and $l-s$ at the $L_2$) of the absorbing atom. The spectra provide information about the magnetic moments of different atoms or the same atom occupying different crystallographic sites (see **Section 2.5.1**). For the study of the iron chromites, these measurements probe the nature of Fe and Cr magnetic coupling in the spinel structure and the presence of ferromagnetic or ferrimagnetic long-range order.

[21] For simplicity, "magnetic induction" is sometimes called "magnetic field" throughout this thesis.

2. **Fe and Cr cationic site distribution.** As abovementioned, the $L_{2,3}$-edges of transition metals are very sensitive to the crystal field surrounding the absorbing cation. Herein, this sensitivity is exploited to obtain the Fe and Cr cation distribution in the Oh and Td sites of the spinel structure. **Figure 2.13** depicts an example of isotropic and dichroic $L_{2,3}$-signal for $Fe_3O_4$, described by the sum of each Fe species ($Fe^{2+}{}_{Oh}$, $Fe^{3+}{}_{Oh}$ and $Fe^{3+}{}_{Td}$). The absorption in the $L_{2,3}$-edges presents characteristic multiplet structures derived from Coulomb interactions, spin-orbit coupling and crystal field. **Section 2.4** describes in detail the atomic multiplet theory used in this work to simulate and explore the multiplet structures of the Fe and Cr $L_{2,3}$-edge spectra.

## 2.4 Simulation of core level spectra

In this thesis, information about the Fe and Cr local structures in the Fe-Cr-O system were obtained by the simulation of 2*p* XPS of $Cr_2O_3$ (**Chapter 3**) and $L_{2,3}$-edge XAS spectra of $Fe_{3-x}Cr_xO_4$ series (**Chapter 4**). Briefly, the shape of a core level spectrum ($I_{CLS}$) can be described by the probability of the system in its initial state ($\Phi_i$) transits to a final state ($\Phi_f$) by absorbing the incident photon with energy $h\nu$. Considering a monoelectronic representation, this probability is formalized by the Fermi golden rule [16]:

$$I_{CLS} = \frac{2\pi}{\hbar}\left|\langle\Phi_f|T|\Phi_i\rangle\right|^2 \delta_{E_f - E_i - h\nu} \tag{2.13}$$

where $\delta_{E_f-E_i-h\nu}$ is a function for energy conservation, so the energy of the final state ($E_f$) is equal to the energy of the initial state ($E_i$) plus the X-ray energy. The transition operator ($T$) describes the one photon transition. For photoemission phenomenon, the transition operator is written as an annihilation operator. For $L_{2,3}$ absorption, $T$ is the dipole matrix element (ê·r) that takes into account the selection rule of the photo-excitation and the polarization of the incident X-ray. Hence, ê·r dictates that excitation occurs between orbitals whose moments differ by at most one ($\Delta L = 0, \pm 1$) while the spin is conserved ($\Delta S = 0$). The polarization vector (ê) is written in an orthonormal reference ($\vec{e}_x, \vec{e}_y, \vec{e}_z$), where z-axis is the axis of quantification. For circularly-polarized X-ray (*i.e.,* XMCD process), the x-ray absorption cross section $\sigma^+$ is given by the vector $\hat{e}^+ = -1/\sqrt{2}\ (\vec{e}_x + i\vec{e}_y)$, while $\sigma^-$ is defined by the vector $\hat{e}^- = 1/\sqrt{2}\ (\vec{e}_x - i\vec{e}_y)$.

The initial and final state wave functions – $\Phi_i$ and $\Phi_f$ – are not exactly known, consequently in practical calculations one must make approximations. Extensive discussion about the different approaches used in the analysis of core level spectra can be found in the literature [16], [24], [38]. In this work, I chose a localized approach based on atomic multiplet theory in order to describe many-body effects: the *crystal field multiplet* (CFM). This approach has been shown over the last 30 years very fruitful to simulate core level spectra [16], [31]. Herein, an atomic model describes the interaction within the absorbing atom. Crystal field effects include the symmetry aspects of the solid and the effect of bonding is introduced as a perturbation. This approach can be justified if the intra-atomic

multiplet interactions are much larger than the one between the atoms, so charge-transfer effects are disregarded. Indeed, in the case of XAS, the multiplet coupling effect and the crystal field effect play a more important role than the charge-transfer effect. However, in the XPS process, the multiplet coupling effect usually plays a minor role compared to that of the charge-transfer effect. Thus, CFM was chosen to study the XPS spectrum of $Cr_2O_3$ only because in this specific case, the satellite peak attributed to charge transfer excitations was not located in the region of interest of the spectrum (see **Section 3.3**). The following section introduces basic concepts of the CFM theory necessary for the comprehension of the manuscript. Special attention is given to terms and parameters used in the simulations.

### 2.4.1 Fundamentals of crystal field multiplet theory

In CFM theory [16], [38], [39], the solid system is mimicked by considering the transition metal as an isolated ion surrounded by a distribution of charges. The first part of the simulation consists in calculate the energy levels in the initial and final state multiplets. A given multielectronic state is described with quantum mechanics in terms of the following Hamiltonian (expressed in atomic units):

$$H_{atom} = H_{Kin} + H_{e/N} + H_{e/e} + H_{SO} \tag{2.14}$$

where $H_{Kin}$ is the kinetic energy of electrons, $H_{e/N}$ is the nucleus-electron Coulomb attraction, $H_{e/e}$ is the electron-electron repulsion, and $H_{SO}$ is the spin-orbit coupling of each electron. The kinetic energy term ($H_{Kin} = {}^{-\hbar^2}/_{2m}\nabla^2$) covers the electron mass $m$ and the derivatives to the three directions $x$, $y$, and $z$. The nuclear term ($H_{e/N} = -Ze^2/r$) describes the Coulomb attraction of the nucleus with the atomic number $Z$ in an $r$ distance. These two terms are the same for all electron in a given atomic configuration, therefore defining its average energy. This leaves the two remaining terms ($H_{e/e} = \sum_{pairs} e^2/r_{ij}$ and $H_{SO} = \sum_{i=1}^{N} \zeta(r_i) l_i \cdot s_i$) as the important interactions, which determine the energies of the various electronic symmetry configurations within the atomic configuration.

For $2p^6 3d^n$ initial state configurations, the multiplet consists only of the $3d$-$3d$ Coulomb interactions developed in spherical harmonics (see reference [38] for mathematical details). The radial parts – $F^0_{dd}$, $F^2_{dd}$ and $F^4_{dd}$ – are calculated within the HF approximation and are corrected by hand to account the iono-covalence of the bonds. The isotropic interaction, $F^0$, only shifts the average energy position of the spectra, but does not affect the multiplets. Because of that, in the calculations herein performed, $F^0$ is disregarded and the calculated spectra were shifted to match the experimental ones. The multipole terms of the $3d$-$3d$ interactions, $F^2_{dd}$ and $F^4_{dd}$, determine the multiplet splitting and the Hund's rules[22] for the ground state. Relativistic effects due to $3d$ spin-orbit coupling are rather small and this energetic contribution is parametrized in terms of the spin-orbit interaction $\zeta_{3d}$.

[22] The Hund's rules [40] are a set of conditions to determine the term symbol (*i.e.* the angular momentum quantum numbers represented as $^{2S+1}L_J$) for the ground state. The rules dictate that the term symbol of the ground state must have the maximum total spin quantum number (S), the maximum total orbital quantum

For $2p^5 3d^n$ (XPS) and $2p^5 3d^{n+1}$ (XAS) final state configurations, the Hamiltonian is extended with two terms related to the $2p$ core hole. First, the $2p$-$3d$ Coulomb ($F^k_{pd}$) and exchange ($G^k_{pd}$) interactions. The radial parts of these multipole interactions – $F^2_{pd}$, $G^1_{pd}$ and $G^3_{pd}$ – are again parametrized in Slater-Condon integrals solved within the HF limits. The second term is the spin-orbit coupling of the $2p$ hole, which is parametrized in terms of the spin-orbit interaction $\zeta_{2p}$. This term causes the split of the $2p$ edge into the $2p_{3/2}$ ($L_3$) and $2p_{1/2}$ ($L_2$). Therefore, it was adjusted by hand in this work to match the edge energy positions (*e.g.,* the edge maxima) of the experimental spectra. The value of each parameter used in this work is discussed in detail in **Section 3.3** and **Section 4.5**.

The second part of the simulation consists in include solid-state effects by considering the crystal field. When a transition metal ion is placed in a crystal, its five degenerate $3d$ orbitals lose their degeneracy and become split in energy. One describes the split terms using group theory according to the point group geometry of the cationic site. **Figure 2.14** shows the crystal field splittings of transition metal $3d$ orbitals in the symmetries concerned by this study, *i.e.,* tetrahedral ($T_d$), octahedral ($O_h$) and trigonal ($C_{3v}$). When the transition metal ion is in a 6-fold coordination with six identical ligands situated along the Cartesian axes, electrons in $3d$ orbitals are repelled and the barycenter of the degenerate levels is raised. Since lobes of the $e_g$ orbitals point towards the ligands, electrons in these two orbitals are destabilized compared to the ones in the three $t_{2g}$ orbitals that are projected between ligands. The energy separation between the $t_{2g}$ and $e_g$ orbitals is designed by the crystal field splitting term: $\Delta_o$ or 10Dq. Values of 10Dq can be estimated experimentally from positions of absorption bands in visible-region spectra or from plots of thermodynamic data for series of similar compounds of transition elements [41]. An analogous energy separation exists in structures containing tetrahedral coordination sites. However, in this configuration, the ligands sit on alternate vertices of a cube with the cation at the center. Thus, electrons in the $t_2$ orbitals are now more repelled by the ligands than are electrons in the $e$ orbitals[23]. When the metal-ligand distances are identical, the tetrahedral crystal field splitting parameter ($\Delta_t$) relates to the octahedral parameter $\Delta_o$ by the following relation: $\Delta_t = {}^{-4}/_{9}\,\Delta_o$. The negative sign implies that the energy of the two groups of $d$ orbitals is reversed in the two coordination, as shown in **Figure 2.14**.

In the $C_{3v}$ symmetry (case of $Cr_2O_3$), the high-symmetry of the 6-fold polyhedron is broken by changing the interatomic Cr-O distances and O-Cr-O angles (see **Section 1.2.1**). Thus, more than one energy separation occurs between $3d$ orbitals of the cation. In the $C_{3v}$ model [42], [43], the components of the $t_{2g}$ set are $z^2$ for $a_1$ and a linear combination of the other $d$ components for $e$. Hence, electrons in the two $e$ orbitals are repelled to a greater extent than are those in the $a_1$ orbital that points towards the center of the triangle formed by the ligands. The strength of the crystal field is described by optical parameters, *e.g.* in König-Kremer notation (Dq, Dσ and Dτ) [44], which are related to specific $d$ cubic orbitals, as described in **Table 2.1**. The success of the CFM model in

number (L) and the maximum total angular momentum quantum number (J) if the shell is more than half-full ($J_{MAX}$ = L+S).

[23] In tetrahedral coordination, the subscript $g$ in the nomenclature of the two groups of orbitals is omitted due to lack of symmetry center.

simulating core level spectra relies exactly on the fact that it explains properties that are strongly determined by symmetry considerations.

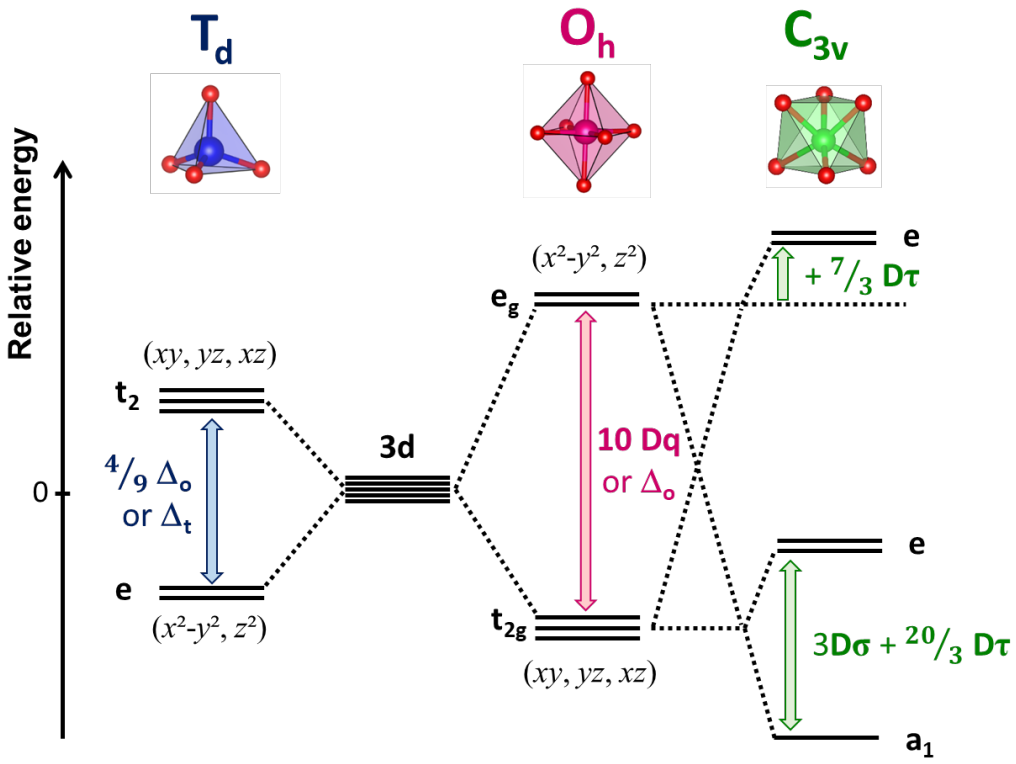


**Figure 2.14.** Energy level diagram showing the 3*d* atomic orbitals splitting after applying a crystal field for tetrahedral (4-fold), octahedral (6-fold) and trigonal (6-fold) coordination. The energy between orbitals is given in terms of the crystal field parameters (Dq, Dσ and Dτ).

**Table 2.1** – Energy of the 3*d* orbitals in terms of the crystal-field parameters (Dq, Dσ and Dτ) in the $C_{3v}$ point group. Here, the $C_3$ axis is oriented along the $z$-axis and one of the three $C_2$ axes along the $x$-axis.

| Γ | Energy expressed in terms of D | Orbitals |
|---|---|---|
| $a_1(t_{2g})$ | $-4\mathrm{Dq} - 2\mathrm{D\sigma} - 6\mathrm{D\tau}$ | $a_1 = -d_{3z^2-r^2}$ |
| $e(t_{2g})$ | $-4\mathrm{Dq} + \mathrm{D\sigma} + {}^2/_3\,\mathrm{D\tau}$ | $e_+ = -\frac{d_{x^2-y^2}}{\sqrt{3}} - \frac{id_{xy}}{\sqrt{3}} + \frac{d_{xz}}{\sqrt{6}} - \frac{id_{yz}}{\sqrt{6}}$, $e_- = -\frac{d_{x^2-y^2}}{\sqrt{3}} + \frac{id_{xy}}{\sqrt{3}} + \frac{d_{xz}}{\sqrt{6}} + \frac{id_{yz}}{\sqrt{6}}$ |
| $e(e_g)$ | $+6\mathrm{Dq} + {}^7/_3\,\mathrm{D\tau}$ | $e_+ = \frac{d_{x^2-y^2}}{\sqrt{6}} + \frac{id_{xy}}{\sqrt{6}} + \frac{d_{xz}}{\sqrt{3}} - \frac{id_{yz}}{\sqrt{3}}$, $e_- = \frac{d_{x^2-y^2}}{\sqrt{6}} - \frac{id_{xy}}{\sqrt{6}} + \frac{d_{xz}}{\sqrt{3}} + \frac{id_{yz}}{\sqrt{3}}$ |

In the CFM model, the crystal field is regarded as a perturbation to the atomic result. The CFM Hamiltonian ($H_{CFM}$) consists of the atomic Hamiltonian (Equation 2.14) to which a crystal field is added:

$$H_{CFM} = H_{atom} + H_{CF} \qquad (2.15)$$

The crystal field Hamiltonian ($H_{CF}$) is written as the electronic charge times a potential $\varphi(r)$ that describes the surroundings. $H_{CF}$ is given in second quantization[24] [39] and then expanded on renormalized spherical harmonics $C_{k,m}$:

$$H_{CF} = \sum_{k=0}^{\infty} \sum_{m=-k}^{k} A_{k,m} C_{k,m}(\theta, \varphi) \tag{2.16}$$

$$\text{with } C_{k,m}(\theta, \varphi) = \sqrt{\frac{4\pi}{2k+1}} Y_{k,m}(\theta, \varphi) \tag{2.17}$$

The matrix element $\varphi(r)$ is determined with respect to the atomic $3d$ orbitals: $\langle 3d|\varphi(r)|3d\rangle$. As it was done for $H_{atom}$, the matrix element can be separated into a spherical ($A_{k,m}$) and radial ($C_{k,m}$) part. The radial part yields the strength of the crystal field interactions and can be written as a linear combination of the crystal field parameters in a given point group [39], [44], [45]. For instance, assuming a $C_{3v}$ local symmetry, the $H_{CF}$ is written as defined by König-Kremer [44]:

$$\begin{aligned} H_{CF}^{C_{3v}} &= A_{2,0}C_{2,0} + A_{4,0}C_{4,0} + A_{4,3}\left(C_{4,3} - C_{4,-3}\right) \\ &= -7\mathrm{D}\sigma C_{2,0} - (14\mathrm{Dq} + 21\mathrm{D}\tau)C_{4,0} + 2\sqrt{70}\mathrm{Dq}\left(C_{4,3} - C_{4,-3}\right) \end{aligned} \tag{2.18}$$

In addition to $H_{CF}$, when an external magnetic field ($B_{app}$) is applied to the system (*e.g.* XMCD experiments), another term has to be added to $H_{CFM}$ to take into account the interactions between the magnetic field and the intrinsic magnetic moment of the atom. This term is the Zeeman Hamiltonian ($H_{Zee}$), which is composed by a spin part interacting with the local mean exchange field created by magnetic neighbors ($B_{exc}$) and an orbital part interacting with $B_{app}$:

$$H_{Zee} = \mu_B \gamma B_{exc} S_Z + \mu_B B_{app} L_Z \tag{2.19}$$

where $\gamma$ is the gyromagnetic ratio and $\mu_B$ the Bohr magneton ($\mu_B = {|e|\hbar}/{2m} > 0$). Here, one supposes that $B_{exc}$ has always the same direction as $B_{app}$, which by definition is oriented along the $z$-axis. Therefore, only the $z$ contributions of the spin and orbital angular momentum operators, $S_Z$ and $L_Z$, are written in Equation 2.19.

## 2.4.2 QUANTY – a quantum many body script language

In this thesis, all core level spectra were simulated using the quantum many-body program QUANTY [46]–[48] within the graphical interface CRISPY [49]. This code uses second quantization

[24] The core of the second quantization is to use creation and annihilation operators instead of eigenvalues and eigenfunctions to solve Schrödinger equation (or to handle the Fock states). In general, second quantization is the preferred technique when considering many particles problem.

and Lanczos recursion method [50] to calculate Green functions – $G(\omega)$ – thus avoiding the explicit calculation of final states:

$$G(\omega) = \left\langle \psi_i \middle| \hat{T}^{\dagger} \frac{1}{\omega - \hat{\mathrm{H}} + \imath\Gamma/2} \hat{T} \middle| \psi_i \right\rangle \tag{2.20}$$

where $\omega$ is the energy, $\psi_i$ is a many-particle wave function from the initial state, $\hat{T}$ is the transition operator in second quantization, $\hat{\mathrm{H}}$ is the Hamiltonian of the system in the final state, and $\Gamma$ is the $2p$ core-hole lifetime. The absolute intensities and the population of the initial states are calculated in a given temperature following the Boltzmann law. The Green's function solution is a sharp peak spectrum. Therefore, to account for spectral broadening, the peaks are convoluted by a Lorentzian and a Gaussian function characterized by their FWHM. The first describes the broadening due to sample imperfections and the $2p$ core-hole lifetime, while the second comprises the experimental setup and the instrumental resolution.

As abovementioned, the Hamiltonian of the system in the final state ($\hat{\mathrm{H}}$) is described in terms of the $3d$–$3d$ and $2p$–$3d$ Coulomb ($F^k_{dd}$, $F^k_{pd}$) and exchange ($G^k_{pd}$) interactions, the $2p$ ($\zeta_{2p}$) and $3d$ ($\zeta_{3d}$) spin-orbit coupling, and the local symmetry. Thus, each of these parameters was given as input in the QUANTY code according to the specific case to be calculated: $2p$ XPS of $Cr_2O_3$ (**Chapter 3**) or $L_{2,3}$-edge XAS spectra of $Fe_{3-x}Cr_xO_4$ series (**Chapter 4**).

## 2.5 Magnetic characterization

The study of compositional effects on magnetic properties of $Fe_{3-x}Cr_xO_4$ thin films (**Chapter 5.2**) is a central part of this thesis. Two techniques were used to probe the magnetism of these layers in different levels: XMCD spectroscopy and vibrating sample magnetometry (VSM). From XMCD analyses, the local magnetic ordering as well as the magnetic moments of the species were evaluated owing to the sum rules of XMCD. From VSM measurements, the magnetism of the films was characterized at macroscopic scale by analyzing hysteresis loops. The following sections provide a brief description of each technique, underlining the data treatment used in this work.

### 2.5.1 XMCD sum rules

In the early 1990s, Thole *et al.* [51] and Carra *et al.* [33] proposed two sum rules that relate the normalized integrated XMCD signals to the expected value of orbital angular momentum $\langle L_Z \rangle$ and spin momentum $\langle S_Z \rangle$ of valence electronic states:

$$\langle L_Z \rangle = \frac{\int_{L_{2,3}} \sigma_{\mathrm{XMCD}}\left(\frac{1}{\hbar\omega}\right) d\hbar\omega}{\int_{L_{2,3}} \sigma_{\mathrm{iso}}\left(\frac{1}{\hbar\omega}\right) d\hbar\omega} 2n_h \tag{2.21}$$

$$\langle S_Z \rangle = \frac{3}{2}\frac{\int_{L_3} \sigma_{\mathrm{XMCD}}\left(\frac{1}{\hbar\omega}\right) d\hbar\omega - 2\int_{L_2} \sigma_{\mathrm{XMCD}}\left(\frac{1}{\hbar\omega}\right) d\hbar\omega}{\int_{L_{2,3}} \sigma_{\mathrm{iso}}\left(\frac{1}{\hbar\omega}\right) d\hbar\omega} n_h - \frac{7}{2}\langle T_Z \rangle \qquad (2.22)$$

where $n_h$ is the number of valence $d$ holes, $\langle T_Z \rangle$ is the magnetic dipole term and the integrations are over the entire $L_2$, $L_3$ or $L_{2,3}$-edge. Here, $\sigma_{\mathrm{XMCD}} = (\sigma^+ - \sigma^-)$, $\sigma_{\mathrm{iso}} = (\sigma^+ + \sigma^- + \sigma^0)/3$ and $\sigma^0$ the linear dichroic contribution. The expectation values, $\langle L_Z \rangle$ and $\langle S_Z \rangle$, are given in Hartree atomic units and can be compared with the results of CFM calculations [52]. The orbital and spin magnetic moments can be expressed in Bohr magneton by the relation: $m_L = -\langle L_Z \rangle \mu_B$ and $m_S = -2\langle S_Z \rangle \mu_B$, respectively.

Although XMCD sum rules have been widely used to estimate orbital and spin magnetic moments of various materials [32], [53], [54], their application to solids may be complicated. Indeed, these rules have been reviewed in a number of publications [52], [55] . There are many reasons to be cautious about their results. First, Equations 2.21 and 2.22 were derived for atoms and, therefore, neglect band structure effects and transitions into $s$ orbitals. In experimental $L_{2,3}$ spectra, one finds not only localized $2p \rightarrow 3d$ transitions, but also transitions to delocalized states that form the typical step-like background (**Figure 2.13**). Additional complication is the number of valence holes ($n_h$), which is not precisely known.

Others sources for uncertainty are the rate of polarization and magnetization and the incomplete separation of $L_3$ and $L_2$-edges. The first issue can be easily overcome by working with samples that exhibit near 100% remanence. In DEIMOS beamline, the magnetic field is always parallel to the beam direction. Therefore, no correction had to be made to compensate for incomplete photon polarization or nonparallel alignment of the incident beam. The second problem however is more difficult to handle. In general, the sum rules do not hold for complex oxides with mixed electronic structure. For the $Fe_{3-x}Cr_xO_4$ series, the sum rules cannot be applied for Fe species because it is not possible to separate precisely the $Fe^{2+}$ from the $Fe^{3+}$ contribution.

In this work, the sum rules were applied only for Cr, since this species has a single oxidation state and symmetry. Few assumptions had to be made in order to verify the individual orbit and spin sum rules for Cr in the $Fe_{3-x}Cr_xO_4$ series. First, one assumed that the linear dichroic contribution is $\frac{1}{2}(\sigma^+ + \sigma^-)$. In addition, a step-function continuum background spectrum with a 2:1 $L_3/L_2$ intensity ratio was considered. For the number of valence holes ($n_h$), one supposed the value of 7. Finally, one also assumed that $\langle T_Z \rangle$ is negligible[25], since the Cr atoms in these thin films are in a cubic environment (*i.e.* Oh). **Section 5.2.2** discusses in detail the results of the sum rules in comparison with CFM calculations for the iron chromites thin films.

## 2.5.2 VSM magnetometry

On a macroscopic scale, ferromagnetic and ferrimagnetic materials exhibit characteristic hysteresis loops when varying the external magnetic field at a given temperature. In the VSM

[25] According to CFM calculation, $\langle T_Z \rangle$ is equal to 0.0001 $\hbar$, which is much lower than $\langle S_Z \rangle$ ($\langle S_Z \rangle_{Cr}$ = 1.5 $\hbar$ for $Cr^{3+}$). Therefore, it can be neglected.

apparatus [56], these hysteresis loops are acquired by measuring the voltage (V) that is induced in the detections coils when a magnetic sample vibrates periodically in the presence of a magnetic field ($\mu_0 H_{ext}$). The measured voltage is the time derivative of the induced flux ($V = -d\phi/dt$), which is related to the magnetic moment ($\mu$) of a sample by the reciprocity theorem:

$$\phi = \left(\frac{B}{I}\right)\mu \tag{2.23}$$

where $B$ is the magnetic field produced by the effective current ($I$) flowing in the detection coils. Combining the detected voltage ($V$) with the equation above, it is possible to measure $\mu$ as a function of $\mu_0 H_{ext}$.

In this work, in-plane magnetic measurements were carried out using a VSM magnetometer in a quantum design physical properties measurement system (7 Tesla PPMS-VSM) available in my host laboratory (SPEC/LNO). Magnetic hysteresis loops were recorded with magnetic field up to 2 Tesla applied along the $[11\bar{2}0]$ axis of the $\alpha$-$Al_2O_3(0001)$ substrate. For $\mu_0 H_{ext}$ = 2 T, the iron chromites are at magnetic saturation, so all the magnetic domains are aligned with the external magnetic field. As discussed in **Section 1.3.2.2**, the $Fe_{3-x}Cr_xO_4$ series pass through low-temperature phase transitions, which influence their magnetic properties. Therefore, three temperatures were considered for the measurements: 10 K, 100 K and 300 K. Two data treatment were needed before analyzing the VSM cycles. In order to obtain a signal from the magnetic deposited layers only, the diamagnetic contributions of the sample holder and substrate were removed by subtracting linear contributions (whose slope is about $-10^{-7}$ A.m$^2$) from raw data (**Figure 2.15a**). Note that the measured $\mu$ is proportional to the volume of the sample. Therefore, to assess the intrinsic magnetic properties of the $Fe_{3-x}Cr_xO_4$ series, one presented the VSM results (**Figure 2.15b**) as moment per unit volume or *magnetization* (M). Three important information are extracted from these magnetic hysteresis cycles:

1. **Saturation magnetization ($M_S$).** Saturation magnetization is reached when all the magnetic domains of the ferromagnetic material are aligned with the external magnetic field in such a way that increasing $\mu_0 H_{ext}$ will no longer increase the magnetization of the material. Thus, $M_S$ values are given by the pseudo-plateau of the hysteresis loops and they can be related to the total magnetic moment of the material.

2. **Saturation remanence ($M_R$).** Magnetic remanence is the magnetization that remains at zero field ($\mu_0 H_{ext}$ = 0 T) after the application of a magnetic field large enough to reach saturation. $M_R$ values are measured at the zero-field intercept and they can be related to the average magnetic moment of the material, which depends on the size of the magnetic domains.

3. **Coercive force ($\mu_0 H_c$).** The coercive force measures the ability of a ferromagnetic or ferrimagnetic material to remain magnetized even if the external magnetic field varies. The values of $\mu_0 H_c$ are half the width of the middle section of the hysteresis loops along the $\mu_0 H$

axis. Materials with high coercivity are said to be *magnetically hard* and are typically used to make permanent magnets. Meanwhile, materials with low coercivity are called *magnetically soft* and are used for example in transformer and inductor cores. The $\mu_0 H_c$ values are sensitive to the grain size of a phase and they describe changes in magnetic hardness and in the structure of ferromagnetic materials.

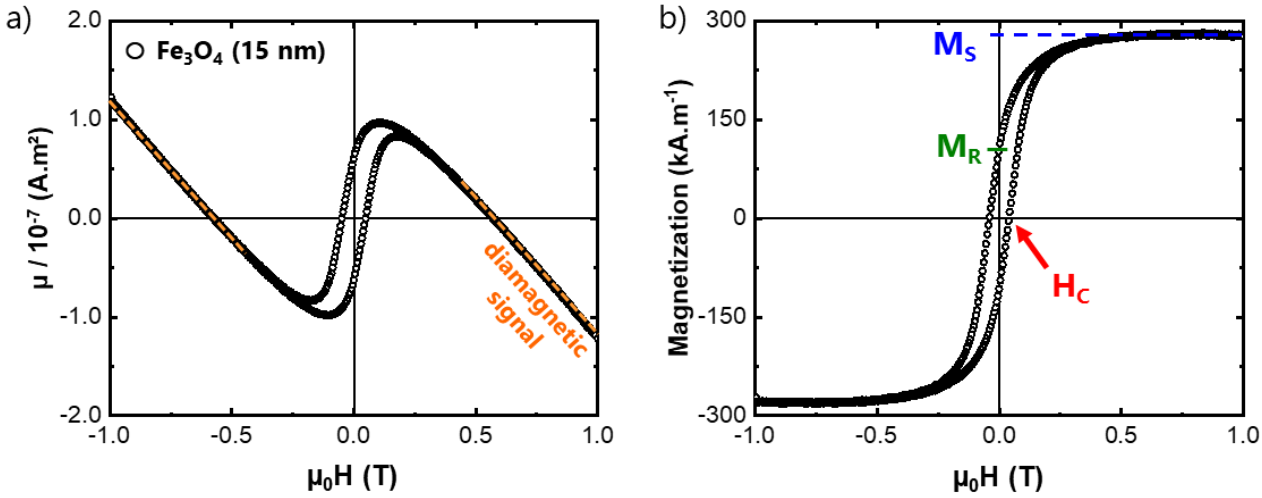


**Figure 2.15**. Hysteresis loops of $Fe_3O_4$ thin film (a) before and (b) after subtraction of diamagnetic contributions. Highlighted the loop parameters: saturation magnetization ($M_S$), saturation remanence ($M_R$) and coercive force ($H_c$).

## 2.6 Simulation of magnetic properties

The magnetic properties of the $Fe_{3-x}Cr_xO_4$ series were further explored in this work using the VAMPIRE code[26]. This code is based on atomistic spin model (ASM) to simulate magnetic nanomaterials. A complete description of the ASM model and the code architecture can be found in the literature [57]. Briefly, VAMPIRE has a number of dedicated functions for generating atomic systems within the nearest neighbor approximation. Herein, the spin dynamic simulations are performed on a rigid atomic structure. It has been specifically designed to simulate nanoparticles, multilayer films, surface anisotropy and roughness, all with fully atomistic resolution. This software has been successfully used to give insight into the processes governing the complex behavior of magnetic systems, including exchange bias in nanoparticles [58] and multilayers [59], microstructural effects (*e.g.* antiphase boundaries) [60], and temperature effects and properties [61]. In this work, two particular issues were addressed with VAMPIRE:

1. **The Curie temperature**. The changes in the value of Curie temperature due to different cationic arrangements in the $Fe_{3-x}Cr_xO_4$ series are discussed in **Section 5.2.3**.

[26] VAMPIRE software package (version 5.0) available from https://vampire.york.ac.uk.

2. **Hysteresis cycles at low temperature**. Anomalies observed in the hysteresis cycles at 10 K are discussed in **Section 5.2.3** in the light of cationic defects and microstructural effects.

The following sections contain a brief description of the ASM model and spin dynamics. Especial attention is given to the key parameters used in the simulation.

### 2.6.1 The spin Hamiltonian

The physical basis of ASM is the localization of unpaired electrons to atomic sites, which leads to an effective local atomistic magnetic moment. In ASM model, the fundamental spin-dependent interactions at the atomic level are described by the classical spin Hamiltonian ($H_S$), which is the sum of the exchange interactions, magnetic anisotropy and contributions of externally applied magnetic fields. $H_S$ typically has the form:

$$H_S = -\sum_{i<j} J_{ij} S_i \cdot S_j - k_u \sum_i (S_i \cdot e)^2 - \mu_S \sum_i B_{app} \cdot S_i \qquad (2.24)$$

where $S_i$ is a unit vector denoting the orientation of the local spin moment ($S_i = \mu_S/|\mu_S|$) and $S_j$ is the spin moment direction of neighboring atoms. Herein, the important parameters are the exchange interaction between atomic sites $i$ and $j$ ($J_{ij}$), the anisotropy constant ($k_u$) and the atomic spin moment ($\mu_S$). To perform ASM simulations, each of these parameters had to be explicitly declared in the input files, as described in detail in **Section 5.2.3**.

In most magnetic materials, the exchange interactions are the dominant contribution and give rise to the atomic ordering of the spin directions. It is important to note here the significance of $J_{ij}$ sign. If neighboring spins align in parallel (*i.e.,* ferromagnetic interactions), $J_{ij}$ is positive. However, if the spins prefer to align anti-parallel (*i.e.,* antiferromagnetic interactions), $J_{ij}$ is negative. For instance, in spinel ferrites, the exchange interactions between irons in octahedral and tetrahedral sites are typically negative because of the anti-parallel alignment of these sites [62]. Due to the strong distance dependence of the exchange interaction, the first term in Equation 2.24 is often truncated to include nearest neighbors only. Obtaining the exchange energy may be done via *ab initio* methods [63], [64] or phenomenologically, as for example, using experimental values of Curie temperatures ($T_C$) [62] within the mean field expression:

$$J_{ij} = \frac{3k_B T_C}{\epsilon n} \qquad (2.25)$$

where $k_B$ is the Boltzmann constant, $n$ is the number of nearest neighbors and $\epsilon$ is a correction factor to include spin wave fluctuations in different crystal lattices [65].

While the exchange energy determines the magnetic ordering at the atomic level, which is usually isotropic, the thermal stability of a magnetic material is dominated by the magnetic anisotropy (*i.e.,* preferred orientation for spins to align). In crystals, the interaction of atomic electron

orbitals with the local crystal environment gives rise to the magnetocrystalline anisotropy (MCA), which is the preference for spin moments to align with particular crystallographic axes. The simplest form of anisotropy is of the uniaxial type (second term in Equation 2.24), where the spins prefer to lie along a single preferred axis ($e$) often called the easy axis. The strength of this anisotropy is given by the uniaxial anisotropy constant ($k_u$), which has positive value for alignment along the $z$-axis and negative value for alignment around the $x-y$ plane. Materials with a cubic crystal structure, such as spinel oxides, have a different anisotropy known as cubic anisotropy. This type of anisotropy has typically three principal directions that are energetically easy, hard and very hard magnetization directions. The cubic anisotropy is given by the expression:

$$H_{ani}^{cub} = \frac{k_c}{2}\sum_i (S_x^4 + S_y^4 + S_z^4) \tag{2.26}$$

where $k_c$ is the cubic anisotropy energy per atom, and $S_x$, $S_y$ and $S_z$ are the respective $x$, $y$ and $z$ components of the spin moment ($S$). The values of the anisotropy constants can be determined via *ab initio* methods [66] or from macroscopic properties [67]. For example, the atomistic MCA ($k_u$) is derived from the macroscopic anisotropy constant ($K_u$) by the relation:

$$k_u = \frac{K_u a^3}{n_{at}} \tag{2.27}$$

where $a$ is the unit cell size and $n_{at}$ is the number of atoms per unit cell. The value of $K_u$ is given in J·m$^{-3}$ and can be estimated for a single domain particle using the anisotropy field ($H_a$):

$$H_a = \frac{2K_u}{M_S} \tag{2.28}$$

where $M_S$ is the saturation magnetization (in J.T$^{-1}$.m$^{-3}$) found in the magnetic hysteresis cycles (see **Section 2.5.2**) in a given temperature.

The last term in the spin Hamiltonian (Equation 2.24) describes the coupling of the spin system to an external magnetic field, denoted as $B_{app}$. The applied field is used to change direction of the spins and it is typically considered in the simulation of hysteresis loops, for example.

## 2.6.2 Integration methods: spin dynamics *vs.* Monte Carlo methods

It is important to highlight that Equation 2.24 describes only the energetics of the system, but provides no information regarding the dynamic behavior. For that, integration methods are introduced to atomistic spin models. In this study, hysteresis cycles were simulated by spin dynamics using the Landau-Lifshitz-Gilbert (LLG) equation [68], [69]:

$$\frac{\partial S_i}{\partial t} = -\frac{\gamma}{(1+\lambda^2)}[S_i \times B_{\text{eff}}^i + \lambda S_i \times (S_i \times B_{\text{eff}}^i)] \tag{2.29}$$

where $S_i$ is a unit vector describing the direction of the magnetic spin moment of site $i$, $\gamma$ is the gyromagnetic ratio, $\lambda$ is the microscopic damping[27] and $B_{\text{eff}}^{i}$ is the net magnetic field on each spin. The first term in Equation 2.29 is the precession of the magnetization due to interaction of an atomic spin with an applied field. Meanwhile, the second term represents the relaxation of the magnetization due to energy transfer from the heat bath to the system in order to align the magnetization along the field direction. Overall, the atomistic LLG equation defines the interaction of an atomic spin moment $i$ with an effective magnetic field, which is given by the negative first derivative of the spin Hamiltonian (Equation 2.24):

$$B_{\text{eff}}^{i} = -\frac{1}{\mu_S}\frac{\partial H_S}{\partial S_i} \tag{2.30}$$

Note that in its standard form the LLG equation is only applicable to simulations at zero temperature. In order to account for thermodynamic fluctuations of the spin moments, a thermal field term ($B_{\text{th}}^{i}$) is added to Equation 2.30. Herein, one considered the Langevin dynamics method developed by Brown [70]. This approach represents the thermal fluctuations on each atomic site using a Gaussian distribution ($\Gamma(t)$) as white noise:

$$B_{\text{th}}^{i} = \Gamma(t)\sqrt{\frac{2\lambda k_B \mathrm{T}}{2\mu_S \Delta t}} \tag{2.31}$$

where $k_B$ is Boltzmann constant, T is the system temperature and $\Delta t$ is the integration time step.

Spin dynamics have proven to be particularly useful for acquiring dynamic information about the magnetic properties or reversal processes for a system [61]. However, this method is not the optimal one for determining equilibrium properties. Therefore, simulation of Curie temperatures were performed using Monte Carlo Metropolis (MC) algorithm [71]. This algorithm provides a natural way to simulate temperature effects in cases where dynamics are not needed due to rapid convergence to equilibrium. For a classical spin system, MC methods proceeds as follows. First, the initial spin direction ($S_i$) of a random spin is changed arbitrarily to a new trial position ($S_i'$), named trial move. One evaluates the difference in energy ($\Delta E = E(S_i') - E(S_i)$) between the old and new positions. Then, the trial move is accepted with the probability:

$$P = \exp\left(\frac{-\Delta E}{k_B T}\right) \tag{2.32}$$

by comparison with a uniform random number between 0 and 1. Probabilities greater than 1 are accepted unconditionally as they correspond to a reduction in energy. This procedure is repeated

[27] The damping parameter is the coupling strength between the magnetization and the heat bath. In the atomistic LLG, $\lambda$ accounts for local intrinsic contributions such as spin-lattice and spin-electron interactions. The maximum effective damping is given by $\lambda$ = 1.

until N trial moves have been attempted, where N is the total number of spins in the system. Each set of N trial moves is a MC step.

In general, LLG spin dynamics and MC simulations of temperature dependent magnetization are in good agreement [57]. Spins dynamics are usually much longer to compute, as they require low time step and slower convergence to equilibrium. However, for large systems (*e.g.,* in simulation of hysteresis cycles), LLG model may be more efficient since MC algorithms are difficult to parallelize.

## 2.7 Electronic transport measurements

In addition to magnetic behavior, another important macroscopic property assessed for the $Fe_{3-x}Cr_xO_4$ thin films was the electronic transport (**Chapter 5.3**). In-plane electrical measurements were performed using standard four-probe dc method in a quantum design physical properties measurement system (PPMS) available in my host laboratory (SPEC/LNO). This instrument is specially designed to measure electronic properties of magnetic single crystals and thin films at a given temperature and in the presence (or not) of a magnetic field. Herein, resistance *versus* temperature curves were recorded over a wide temperature range (10 K < T < 300 K) thanks to the cryogenic system containing both liquid nitrogen and liquid helium reservoirs. Two different electrical configurations are possible in this setup: the two-probe and the four-probe dc method. In the two-probe configuration, a dc voltage (or a current) is applied between two electrical contacts and the induced current (or voltage) is measured. According to Ohm's law, the measured resistance ($R$) will then be the sum of the resistances of both the sample ($R_{sample}$) and the contacts ($R_{contact}$):

$$R = R_{sample} + \sum R_{contact} \tag{2.33}$$

If the resistance of the contacts is much smaller than that of the sample, the two-probe method is enough to obtain $R_{sample}$. Otherwise, one should consider a different configuration. For instance, the contribution of contacts to the measured resistance can be eliminated using the four-probe method (**Figure 2.16**). In this configuration, two contacts are used to pass the current across the sample, while two additional contacts measure the induced voltage. **Figure 2.16** depicts the equivalent circuit in the four-probe configuration, for which the sample resistance ($R_{sample}$) is given by:

$$R_{sample}(I - i) = \left(R_{C_2} + R_{C_3}\right)i + V \tag{2.34}$$

where $I$ is the current applied by the two exterior contacts, $i$ is the current passing through the voltmeter, and $V$ is the measured voltage. Since the impedance of the voltmeter is very high, $i$ is negligible and the contact resistances $R_{C_2}$ and $R_{C_3}$ are excluded. In this configuration, the integrate electronics of the PPMS enable direct current resistance measurements up to 4 MΩ.

Herein, the four-probe method was preferred over the two-probe to study the semiconductor behavior of $Fe_{3-x}Cr_xO_4$ thin films. As discussed in **Section 1.3.2.3**, different conduction mechanisms

may be proposed for a material as a function of its temperature dependent conduction behavior. Resistance curves were then recorded as function of temperature with no applied magnetic field. Note that resistance is a property dependent of the geometry of a particular sample. In order to probe the intrinsic electric behavior of the samples, resistivity ($\rho$) was calculated by dividing the measured resistance ($R$) by the path length of the current ($l$) and multiplying by the cross-sectional area of the sample ($e \times L$):

$$\rho(\Omega \cdot m) = R(\Omega) \times \frac{e \times L}{l} \tag{2.35}$$

where e is the thickness and L is the width of the thin film, as illustrated in **Figure 2.16**. The results are expressed in $\Omega$.m.

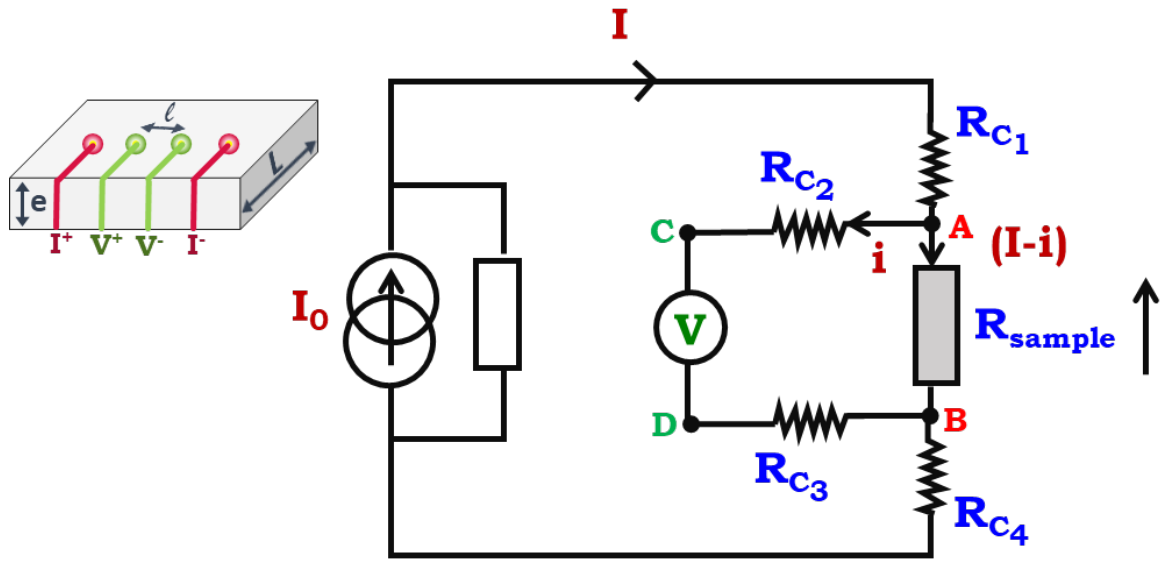


**Figure 2.16.** The four-probe dc method. This configuration consists of four probes arranged linearly in a straight line at equal distance $l$ from each other. A constant current (I-i) is passed through the two outer probes and the potential drop (V) across the middle two probes is measured. At left, the geometry of the measurement highlights the values of path length of the current ($l$) and the cross-sectional area of the sample ($e \times L$). At right, the circuit diagram where points A and B represent the current contacts ($I^+$, $I^-$) and points C and D are the voltage contacts ($V^+$, $V^-$).

## 2.8 References

[1] M. A. Herman and H. Sitter, *Molecular Beam Epitaxy*, vol. 7. Berlin, Heidelberg: Springer Berlin Heidelberg, 1989.

[2] S. A. Chambers, "Epitaxial growth and properties of thin film oxides," *Surface Science Reports*, no. 39, pp. 105–180, 2000.

[3] S. Vishwanath, P. Dang, and H. G. Xing, "Chapter 20 - Challenges and Opportunities in Molecular Beam Epitaxy Growth of 2D Crystals: An Overview," in *Molecular Beam Epitaxy (Second Edition)*, Second Edition., M. Henini, Ed. Elsevier, 2018, pp. 443–485.

[4] P. K. Larsen and P. J. Dobson, Eds., *Reflection High-Energy Electron Diffraction and Reflection Electron Imaging of Surfaces*, vol. 188. Boston, MA: Springer US, 1988.

[5] S. Hasegawa, *Reflection High-Energy Electron Diffraction*. John Wiley & Sons, Inc., 2012.

[6] H. Wilman, "The Interpretation and Application of Electron-Diffraction `Kikuchi-Line' Patterns - Part I. The Determination of the Crystal Unit Cell, its Orientation and the Crystal Symmetry," *Proceedings of the Physical Society*, vol. 60, no. 4, pp. 341–360, 1948.

[7] C. A. Schneider, W. S. Rasband, and K. W. Eliceiri, "NIH Image to ImageJ: 25 years of image analysis," *Nature Methods*, vol. 9, no. 7, pp. 671–675, Jul. 2012.

[8] J. I. Langford and A. J. C. Wilson, "Scherrer after sixty years: A survey and some new results in the determination of crystallite size," *Journal of Applied Crystallography*, vol. 11, no. 2, pp. 102–113, Apr. 1978.

[9] F. Ott, *SimulReflec*. 2007. [Online]. Available: https://www-llb.cea.fr/prism/programs/simulreflec/simulreflec.html

[10] L. G. Parratt, "Surface Studies of Solids by Total Reflection of X-Rays," *Physical Review*, vol. 95, no. 2, pp. 359–369, Jul. 1954.

[11] T. C. Huang, R. Gilles, and G. Will, "Thin-film thickness and density determination from x-ray reflectivity data using a conventional power diffractometer," *Thin Solid Films*, vol. 230, no. 2, pp. 99–101, 1993.

[12] B. Sitaud, P. L. Solari, S. Schlutig, I. Llorens, and H. Hermange, "Characterization of radioactive materials using the MARS beamline at the synchrotron SOLEIL," *Journal of Nuclear Materials*, vol. 425, no. 1–3, pp. 238–243, Jun. 2012.

[13] E. Snoeck *et al.*, "Quantitative analysis of strain field in thin films from HRTEM micrographs," *Thin Solid Films*, vol. 319, no. 1, pp. 157–162, 1998.

[14] R. F. Egerton and M. Watanabe, "Characterization of single-atom catalysts by EELS and EDX spectroscopy," *Ultramicroscopy*, vol. 193, pp. 111–117, Oct. 2018.

[15] G. Noircler, F. Lebreton, E. Drahi, P. de Coux, and B. Warot-Fonrose, "STEM-EELS investigation of c-Si/a-AlOx interface for solar cell applications," *Micron*, vol. 145, p. 103032, 2021.

[16] F. De Groot and A. Kotani, "Core level spectroscopy of solids. CRC Press, Boca Raton," Jan. 2008.

[17] D. R. Hartree, "The Wave Mechanics of an Atom with a Non-Coulomb Central Field. Part I. Theory and Methods," *Mathematical Proceedings of the Cambridge Philosophical Society*, vol. 24, no. 1, pp. 89–110, 1928.

[18] P. S. Miedema, F. Borgatti, F. Offi, G. Panaccione, and F. M. F. de Groot, "Iron 1s X-ray photoemission of $Fe_2O_3$," *Journal of Electron Spectroscopy and Related Phenomena*, vol. 203, pp. 8–13, 2015.

[19] M. C. Biesinger, B. P. Payne, A. P. Grosvenor, L. W. M. Lau, A. R. Gerson, and R. St. C. Smart, "Resolving surface chemical states in XPS analysis of first row transition metals, oxides and hydroxides: Cr, Mn, Fe, Co and Ni," *Applied Surface Science*, vol. 257, no. 7, pp. 2717–2730, Jan. 2011.

[20] J. H. Van Vleck and A. Sherman, "The Quantum Theory of Valence," *Reviews of Modern Physics*, vol. 7, no. 3, pp. 167–228, Jul. 1935.

[21] R. L. Rowell, "Photon, electron, and ion probes of polymer structure and properties: Edited by D. W. Dwight, T. J. Fabish, R. H. Thomas, American Chemical Society Symposium Series 162, Washington, D. C., 1981. 442 pp," *Journal of Colloid and Interface Science*, vol. 88, no. 2, pp. 605–606, 1982.

[22] D. A. Shirley, "High-Resolution X-Ray Photoemission Spectrum of the Valence Bands of Gold," *Physical Review B*, vol. 5, no. 12, pp. 4709–4714, Jun. 1972.

[23] S. Tanuma, C. J. Powell, and D. R. Penn, "Calculations of electorn inelastic mean free paths. II. Data for 27 elements over the 50-2000 eV range," *Surface and Interface Analysis*, vol. 17, no. 13, pp. 911–926, Dec. 1991.

[24] F. de Groot, "High-Resolution X-ray Emission and X-ray Absorption Spectroscopy," *Chemical Reviews*, vol. 101, no. 6, pp. 1779–1808, Jun. 2001.

[25] C. S. Schnohr and M. C. Ridgway, Eds., *X-Ray Absorption Spectroscopy of Semiconductors*, vol. 190. Berlin, Heidelberg: Springer Berlin Heidelberg, 2015. doi: 10.1007/978-3-662-44362-0.

[26] M.-A. Arrio, S. Rossano, Ch. Brouder, L. Galoisy, and G. Calas, "Calculation of multipole transitions at the Fe K pre-edge through p-d hybridization in the Ligand Field Multiplet model.," *EPL - Europhysics Letters*, vol. 51, pp. 454–460, 2000.

[27] I. LLorens *et al.*, "X-ray absorption spectroscopy investigations on radioactive matter using MARS beamline at SOLEIL synchrotron," *Radiochimica Acta*, vol. 102, no. 11, pp. 957–972, Nov. 2014.

[28] B. Ravel and M. Newville, "ATHENA, ARTEMIS, HEPHAESTUS: data analysis for X-ray absorption spectroscopy using IFEFFIT.," *Journal of synchrotron radiation*, vol. 12, no. Pt 4, pp. 537–541, Jul. 2005.

[29] S. I. Zabinsky, J. J. Rehr, A. Ankudinov, R. C. Albers, and M. J. Eller, "Multiple-scattering calculations of x-ray-absorption spectra," *Physical Review B*, vol. 52, no. 4, pp. 2995–3009, Jul. 1995.

[30] M. Newville, B. Ravel, D. Haskel, J. J. Rehr, E. A. Stern, and Y. Yacoby, "Analysis of multiple-scattering XAFS data using theoretical standards," *Physica B: Condensed Matter*, vol. 208–209, pp. 154–156, 1995.

[31] F. M. F. de Groot, J. C. Fuggle, B. T. Thole, and G. A. Sawatzky, "2*p* x-ray absorption of 3*d* transition-metal compounds: An atomic multiplet description including the crystal field," *Physical Review B*, vol. 42, no. 9, pp. 5459–5468, Sep. 1990.

[32] F. M. F. de Groot, "X-ray absorption and dichroism of transition metals and their compounds," *Journal of Electron Spectroscopy and Related Phenomena*, vol. 67, no. 4, pp. 529–622, Aug. 1994.

[33] P. Carra, B. T. Thole, M. Altarelli, and X. Wang, "X-ray circular dichroism and local magnetic fields," *Physical Review Letters*, vol. 70, no. 5, pp. 694–697, Feb. 1993.

[34] W. L. O'Brien and B. P. Tonner, "Orbital and spin sum rules in x-ray magnetic circular dichroism," *Physical Review B*, vol. 50, no. 17, pp. 12672–12681, Nov. 1994.

[35] T. Funk, A. Deb, S. J. George, H. Wang, and S. P. Cramer, "X-ray magnetic circular dichroism—a high energy probe of magnetic properties," *Coordination Chemistry Reviews*, vol. 249, no. 1–2, pp. 3–30, Jan. 2005.

[36] P. Ohresser *et al.*, "DEIMOS: A beamline dedicated to dichroism measurements in the 350–2500 eV energy range," *Review of Scientific Instruments*, vol. 85, no. 1, p. 013106, Jan. 2014.

[37] L. Joly, E. Otero, F. Choueikani, F. Marteau, L. Chapuis, and P. Ohresser, "Fast continuous energy scan with dynamic coupling of the monochromator and undulator at the DEIMOS beamline," *Journal of Synchrotron Radiation*, vol. 21, no. 3, pp. 502–506, May 2014.

[38] R. D. Cowan, *The theory of atomic structure and spectra*. CA: University of California Press: Berkeley, 1981.

[39] V. Vercamer *et al.*, "Calculation of optical and K pre-edge absorption spectra for ferrous iron of distorted sites in oxide crystals," *Physical Review B*, vol. 94, no. 24, pp. 245115-1-245115–15, Dec. 2016.

[40] F. Hund, *Linienspektren und Periodisches System der Elemente*. 1927.

[41] R. G. Burns, *Mineralogical Applications of Crystal Field Theory*. Cambridge University Press, 1993.

[42] S. K. Kang, H. Tang, and T. A. Albright, "Structures for $d^0$ $ML_6$ and $ML_5$ complexes," *Journal of the American Chemical Society*, vol. 115, no. 5, pp. 1971–1981, Mar. 1993.

[43] P. H. Butler, *Point Group Symmetry Applications: Methods and Tables*. Boston, MA: Springer US, 1981.

[44] E. Konig and S. Kremer, *Ligand field: energy diagrams*. New York: Plenum Press, 1977.

[45] A. Juhin *et al.*, "X-ray linear dichroism in cubic compounds: The case of $Cr^{3+}$ in $MgAl_2O_4$," *Physical Review B*, vol. 78, no. 19, pp. 1–19, Nov. 2008.

[46] M. W. Haverkort, M. Zwierzycki, and O. K. Andersen, "Multiplet ligand-field theory using Wannier orbitals," *Physical Review B*, vol. 85, no. 16, Apr. 2012.

[47] M. W. Haverkort, G. Sangiovanni, P. Hansmann, A. Toschi, Y. Lu, and S. Macke, "Bands, resonances, edge singularities and excitons in core level spectroscopy investigated within the dynamical mean-field theory," *Europhysics Letters*, vol. 108, no. 5, p. 57004, Dec. 2014.

[48] Y. Lu, M. Höppner, O. Gunnarsson, and M. W. Haverkort, "Efficient real frequency solver for dynamical mean field theory," *Physical Review B*, vol. 90, Feb. 2014.

[49] M. Retegan, *Crispy: version 0.7.3*. 2019. [Online]. Available: https://dx.doi.org/10.5281/zenodo.1008184

[50] M. Taillefumier, D. Cabaret, A.-M. Flank, and F. Mauri, "X-ray absorption near-edge structure calculations with the pseudopotentials: Application to the *K* edge in diamond and α-quartz," *Physical Review B*, vol. 66, no. 19, p. 195107, Nov. 2002.

[51] B. T. Thole, P. Carra, F. Sette, and G. van der Laan, "X-ray circular dichroism as a probe of orbital magnetization," *Physical Review Letters*, vol. 68, no. 12, pp. 1943–1946, Mar. 1992.

[52] C. Piamonteze, P. Miedema, and F. M. F. de Groot, "Accuracy of the spin sum rule in XMCD for the transition-metal L edges from manganese to copper," *Physical Review B*, vol. 80, no. 18, p. 184410, Nov. 2009.

[53] H. Wang *et al.*, "L-edge sum rule analysis on 3d transition metal sites: from $d^{10}$ to $d^0$ and towards application to extremely dilute metallo-enzymes," *Physical Chemistry Chemical Physics*, no. 12, pp. 8166–8176, 2018.

[54] D. Maganas, J. K. Kowalska, C. Van Stappen, S. DeBeer, and F. Neese, "Mechanism of $L_{2,3}$-edge x-ray magnetic circular dichroism intensity from quantum chemical calculations and

experiment—A case study on $V^{(IV)}$ /$V^{(III)}$ complexes," *The Journal of Chemical Physics*, vol. 152, no. 11, p. 114107, Mar. 2020.

[55] C. T. Chen *et al.*, "Experimental Confirmation of the X-Ray Magnetic Circular Dichroism Sum Rules for Iron and Cobalt," *Physical Review Letters*, vol. 75, no. 1, pp. 152–155, Jul. 1995.

[56] S. Foner, "Versatile and Sensitive Vibrating-Sample Magnetometer," *Review of Scientific Instruments*, vol. 30, no. 7, pp. 548–557, Jul. 1959.

[57] R. F. L. Evans, W. J. Fan, P. Chureemart, T. A. Ostler, M. O. A. Ellis, and R. W. Chantrell, "Atomistic spin model simulations of magnetic nanomaterials," vol. 26, no. 10, p. 103202, Feb. 2014.

[58] R. F. L. Evans, D. Bate, R. W. Chantrell, R. Yanes, and O. Chubykalo-Fesenko, "Influence of interfacial roughness on exchange bias in core-shell nanoparticles," *Physical Review B*, vol. 84, no. 9, p. 092404, Sep. 2011.

[59] S. Jenkins, R. W. Chantrell, and R. F. L. Evans, "Exchange bias in multigranular noncollinear $IrMn_3$ / CoFe thin films," *Physical Review B*, vol. 103, no. 1, p. 014424, Jan. 2021.

[60] R. Moreno, S. Jenkins, V. K. Lazarov, and R. F. L. Evans, "Role of anti-phase boundaries in the formation of magnetic domains in magnetite thin films," *Journal of Physics: Condensed Matter*, vol. 33, no. 17, p. 175802, Apr. 2021.

[61] R. F. L. Evans, U. Atxitia, and R. W. Chantrell, "Quantitative simulation of temperature-dependent magnetization dynamics and equilibrium properties of elemental ferromagnets," *Physical Review B*, vol. 91, no. 14, p. 144425, Apr. 2015.

[62] C. M. Srivastava, G. Srinivasan, and N. G. Nanadikar, "Exchange constants in spinel ferrites," *Physical Review B*, vol. 19, no. 1, pp. 499–508, Jan. 1979.

[63] D. Das and S. Ghosh, "Density functional theory based comparative study of electronic structures and magnetic properties of spinel $ACr_2O_4$ (A = Mn, Fe, Co, Ni) compounds," *Journal of Physics D: Applied Physics*, vol. 48, no. 42, p. 425001, Oct. 2015.

[64] L. Udvardi, L. Szunyogh, K. Palotás, and P. Weinberger, "First-principles relativistic study of spin waves in thin magnetic films," *Physical Review B*, vol. 68, no. 10, p. 104436, Sep. 2003.

[65] D. A. Garanin, "Self-consistent Gaussian approximation for classical spin systems: Thermodynamics," *Physical Review B*, vol. 53, no. 17, pp. 11593–11605, May 1996.

[66] R. Řezníček, V. Chlan, H. Štěpánková, P. Novák, and M. Maryško, "Magnetocrystalline anisotropy of magnetite," vol. 24, no. 5, p. 055501, Jan. 2012.

[67] K. Abe, Y. Miyamoto, and S. Chikazumi, "Magnetocrystalline Anisotropy of Low Temperature Phase of Magnetite," *Journal of the Physical Society of Japan*, vol. 41, no. 6, pp. 1894–1902, 1976.

[68] L. LANDAU and E. LIFSHITZ, "3 - On the theory of the dispersion of magnetic permeability in ferromagnetic bodies Reprinted from Physikalische Zeitschrift der Sowjetunion 8, Part 2, 153, 1935.," in *Perspectives in Theoretical Physics*, L. P. PITAEVSKI, Ed. Amsterdam: Pergamon, 1992, pp. 51–65.

[69] G. Dresselhaus, "Spin-Orbit Coupling Effects in Zinc Blende Structures," *Physical Review*, vol. 100, no. 2, pp. 580–586, Oct. 1955.

[70] W. Brown, "Thermal fluctuation of fine ferromagnetic particles," *IEEE Transactions on Magnetics*, vol. 15, no. 5, pp. 1196–1208, 1979.

[71] N. Metropolis, A. W. Rosenbluth, M. N. Rosenbluth, A. H. Teller, and E. Teller, "Equation of State Calculations by Fast Computing Machines," *The Journal of Chemical Physics*, vol. 21, no. 6, pp. 1087–1092, 1953.

# Chapter 3:

# Effect of strain on the crystal field of $Cr_2O_3$ thin films

The first part of this PhD thesis is a comprehensive study of the impact of lattice strain on the electronic structure of $Cr_2O_3$ thin films. Herein, features of the **Cr 2*p* photoemission spectra** are explored by means of **crystal field multiplet calculations** in order to quantify strain-induced changes in the crystal field around the $Cr^{3+}$ cation. To do so, XPS spectra from monocrystalline $\alpha$-$Cr_2O_3$(0001) thin films are acquired to calibrate parameters used in the theoretical calculations. A **quantitative relation** is established between **distortions** of the $CrO_6$ octahedron and the **crystal field** splitting of chromium $d$-orbitals. Then, the problem is transposed to polycrystalline samples of $Cr_2O_3$ grown by exposing the Ni30Cr alloy to an oxygen-rich environment at high temperature.

## 3.1 The challenges in interpreting photoemission spectra

The first part of the thesis aims to evaluate the early stages of growth of $\alpha$-$Cr_2O_3$ layers. As discussed in **Section 1.2.3**, this study is placed on two contexts: (*i*) in the use of strain engineering to control physical properties (*e.g.,* Néel temperature and magnetic anisotropy) of epitaxial $\alpha$-$Cr_2O_3$ thin films and (*ii*) in the evaluation of the growth of protective oxide layers during the oxidation of a chromia-forming alloy. In both cases, owing to the thinness of these oxide scales, the study of their physicochemical and microstructure evolutions can be very challenging. In this regard, surface sensitive analytical techniques, such as X-ray photoemission spectroscopy (XPS), have proven to be well suited for the study of such thin layers [1], [2]. Combined with structural information provided by diffraction techniques [3], one may obtain a rough understanding of the oxide growth process [4], [5].

Interestingly, for both epitaxial films [5] and polycrystalline samples [6], it has been shown that the transition from the initial state of oxide nucleation to the thickening of complete $Cr_2O_3$ layers introduces changes in the binding energy and the multiplet splitting features of the Cr 2*p* XPS spectra. These changes are probably related to the evolution of the fine structure of chromium. Yet, a comprehensive investigation of the XPS spectra acquired through the growth of $\alpha$-$Cr_2O_3$ is still lacking.

Accounting for the shape evolution of the Cr 2*p* XPS spectra of $Cr_2O_3$ is in fact a challenging task. As discussed in **Section 2.3.1**, many-body effects, such as multiplet splitting and shake-up, promote additional fine structure to the spectral core lines, drawing complex multi-peaks envelopes. Indeed, Cr 2*p* XPS spectrum of $Cr_2O_3$ (**Figure 2.9**) shows broad asymmetric peaks that have long complicated its understanding. Diverse interpretations have been given in the literature [7], particularly regarding the Cr oxidation state in this compound. For instance, some authors [8] have suggested that the asymmetric spectrum is due to mix of $Cr^{3+}$ and $Cr^{6+}$ species. Because multiplet peaks are sensitive to changes in the local crystal field geometry, oxidation state and charge transfer effects [9], theoretical calculations of the multiplet structure [10] have shown that these spectral signatures can be useful to detect differences in surface chemistry.

In this chapter, the line-shape differences of the Cr 2*p* core-level spectra are explored in order to assess strain-induced changes in the electronic structure of the $Cr^{3+}$ cation. A multi-electronic semiempirical method is applied to understand the effect of the local crystal field geometry in the redistribution of intensity of the spectral lines. As discussed in **Section 1.2.3**, the study is performed in two steps. First, XPS spectra from $\alpha$-$Cr_2O_3$(0001) thin films grown by oxygen-plasma-assisted molecular beam epitaxy (O-MBE) are analyzed under different strain scenarios. These "model" samples are used to evaluate the crystal field parameters needed to perform the theoretical calculations. Then, the problem is transposed to polycrystalline samples of $Cr_2O_3$ grown by exposing the Ni30Cr alloy to an oxygen-rich environment at high temperature.

## 3.2 Epitaxial growth of α-$Cr_2O_3$ thin films

As introduced in **Section 2.1**, the MBE growth is fundamentally a recrystallization process in which gaseous atoms condense on a template created by the substrate in order to form a single crystal film. Thus, both crystallographic structure and morphology (*e.g.,* 2D layer-by-layer or 3D islands) of the films are influenced by the crystallographic properties of the substrate, such as crystal symmetry and in-plane lattice constant. Here I aimed to prepare α-$Cr_2O_3$ thin films in three model strain scenarios: completely relaxed, under compressive or under tensile strain. To do so, I chose to grow α-$Cr_2O_3$ directly on α-$Al_2O_3$(0001) substrate or on α-$Fe_2O_3$(0001) buffer layer grown on the same sapphire substrate. Both α-$Al_2O_3$ and α-$Fe_2O_3$ also have corundum-like crystal structure that favors the epitaxial growth of the corundum phase α-$Cr_2O_3$. Moreover, these three oxides, α-$Al_2O_3$, α-$Cr_2O_3$, and α-$Fe_2O_3$, have in-plane lattice parameters equal to 0.476, 0.492 and 0.503 nm, respectively [12]. A quantitative comparison of in-plane lattice parameters of the substrate and film is given by the lattice mismatch: $f = (a_{\text{film}} - a_{\text{substrate}})/a_{\text{substrate}}$, where both lattice parameters ($a$) are in the growth plane. Of the many types of crystal imperfections, the one that the crystal grower always has to deal with is the strain in the epitaxial layers caused by the lattice mismatch between the substrate and the film [11]. Here the in-plane lattice mismatches are +3.36% for α-$Cr_2O_3$ on α-$Al_2O_3$ (compressive strain) and -2.19% for α-$Cr_2O_3$ on α-$Fe_2O_3$ (tensile strain).

The growth conditions of these α-$Cr_2O_3$ layers on α-$Al_2O_3$ substrate and α-$Fe_2O_3$/α-$Cr_2O_3$ bilayers was inspired by previous work performed in one of my host laboratories (SPEC/LNO) [13], [14] and the literature [3]. Prior to each deposition, the sapphire substrates systematically underwent two cleaning steps. The first one was performed outside the MBE, before attaching the substrate to the sample holder. In this step, the substrate is immersed in an aqueous solution of $H_2O_2$/$NH_4OH$/$H_2O$ (1:1:100) under stirring for five minutes. The second step occurred *in situ* by heating the sample holder to 723 K and then exposing it to a flux of oxygen plasma (rf power 350 W, $P_{O_2,plasma}$ of 0.26 Torr) for 10 minutes. These two cleaning steps effectively removed from the substrate surface the pollution layer (*e.g.,* carbon oxides) that hinders the first growth reactions and leads to poorly crystallized thin films. After cleaning the substrates, the mechanical shutters in front of the Fe and/or Cr Knudsen cells were opened and the deposition began.

**Table 3.1** summarizes all optimized growth conditions used in this work. As discussed in **Section 2.1**, the MBE growth is mainly governed by the kinetics of the surface reactions between the impinging beams and the outermost atomic layers of the substrate. It usually requires high temperatures and very good ultra-high vacuum (UHV) conditions. According to previous studies [13], [14], optimal growth is achieved around 723 K. Thus, the sample holder temperature was kept at ~723 K during deposition of all samples. The base pressure was $10^{-10}$ mbar and the residual pressure was $10^{-7}$ mbar inside the UHV growth chamber. The plasma was activated by a rf power of 350 W. The metal evaporation rates were 0.30 Å.min$^{-1}$ for Cr and 0.20 Å.min$^{-1}$ for Fe, which were calibrated *in situ* using a quartz balance. Optimal plasma conditions were achieved under of 0.42 Torr inside the quartz cavity. The slow metal evaporation rates and high $P_{O_2,plasma}$ ensured fully oxidized α-$Cr_2O_3$ and α-$Fe_2O_3$ layers with high crystalline quality.

**Table 3.1** – Optimal experimental O-MBE conditions for the growth thin films of α-$Cr_2O_3$(0001) and α-$Fe_2O_3$(0001) on α-$Al_2O_3$(0001) substrate.

| Layer | Substrate temperature (K) | Residual pressure (mbar) | Fe evaporation rate (Å.min$^{-1}$) | Cr evaporation rate (Å.min$^{-1}$) | $P_{O_2,plasma}$ (Torr) |
|---|---|---|---|---|---|
| **α-$Cr_2O_3$** | 723 | $10^{-7}$ | – | 0.30 | 0.42 |
| **α-$Fe_2O_3$** | 723 | $10^{-7}$ | 0.20 | – | 0.42 |

During the growth, RHEED patterns were monitored in real time in order to control the crystalline structure of the atomic layers. They were recorded with the 30 keV primary beam aligned parallel to $[10\bar{1}0]$ and $[1\bar{1}00]$ azimuths of sapphire. **Figure 3.1** shows the evolution of these images for the growth of 16 nm thick α-$Cr_2O_3$ directly on α-$Al_2O_3$(0001) substrate. At the very beginning (first 10 minutes), the RHEED patterns show diffraction spots and Kikuchi lines similar to the monocrystalline substrate (see **Figure 2.2**). Over time, the rods increase in intensity and define themselves. No extra lines appear (or disappear) since α-$Cr_2O_3$ and α-$Al_2O_3$ have the same crystal symmetry. After 30 minutes of growth (~5 nm), the RHEED images exhibit sharp streaks without spots, indicating a bidimensional growth mode. This morphology is maintained until the end of the growth (~150 minutes).

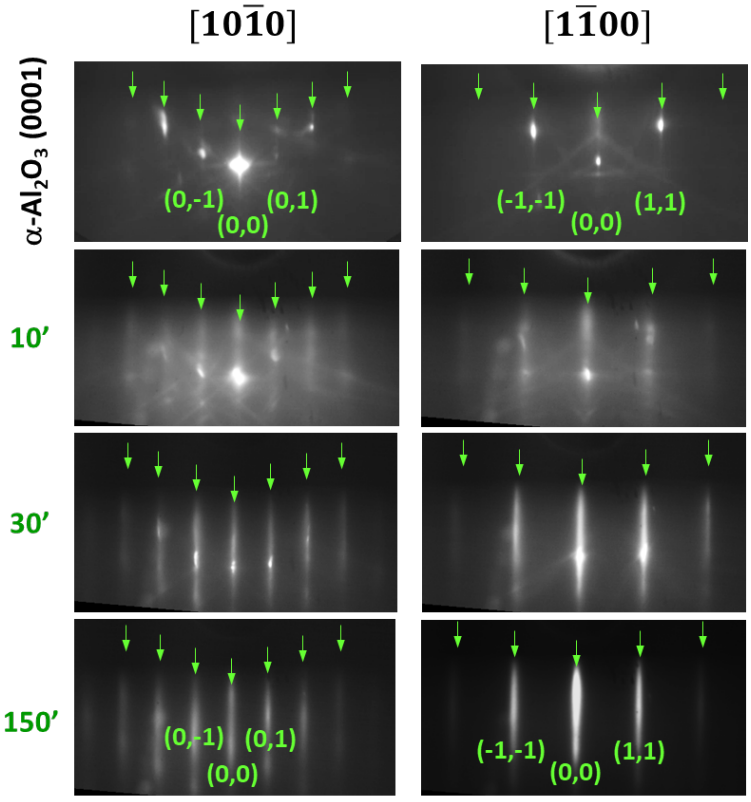


**Figure 3.1.** RHEED patterns recorded during growth of 15 nm thick α-$Cr_2O_3$(0001) directly on α-$Al_2O_3$(0001) substrate. The streaks of α-$Cr_2O_3$ are at almost the same position as the substrate and have their intensity reinforced during growth. Images recorded with the 30 keV primary beam aligned parallel to $[10\bar{1}0]$ and $[1\bar{1}00]$ azimuths of sapphire.

**Figure 3.2** depicts the evolution of the RHEED patterns during the growth of the α-$Fe_2O_3$/α-$Cr_2O_3$ bilayers. For the first 100 minutes, the α-$Fe_2O_3$ buffer is grown on the α-$Al_2O_3$(0001) substrate. Such procedure was optimized years ago [11], [14], [15]. At the very beginning (about 10 minutes), the RHEED patterns of α-$Fe_2O_3$ also show diffraction spots and Kikuchi lines similar to the substrate. The intensity of the rods is reinforced, suggesting at first a layer-by-layer growth. However, over the time, the rods become slightly diffuse. The growth of α-$Fe_2O_3$ on the α-$Al_2O_3$(0001) is more complex than the one of α-$Cr_2O_3$, because of the bigger lattice mismatch (+5.7%). According to the literature [16], the lattice constant of the first monolayers of α-$Fe_2O_3$(0001) is expanded relative to that of the bulk, contrary to what was expected for a positive mismatch. The same was found in this study during the treatment of the RHEED patterns (see **Section 3.3**). This expansion was described as a basic hexagonal structure for the first monolayers with a random distribution of ferric ions over the octahedral sites between the close-packed oxygen layers. Beyond these first monolayers, the ordered corundum structure is formed and the growth mode changes.

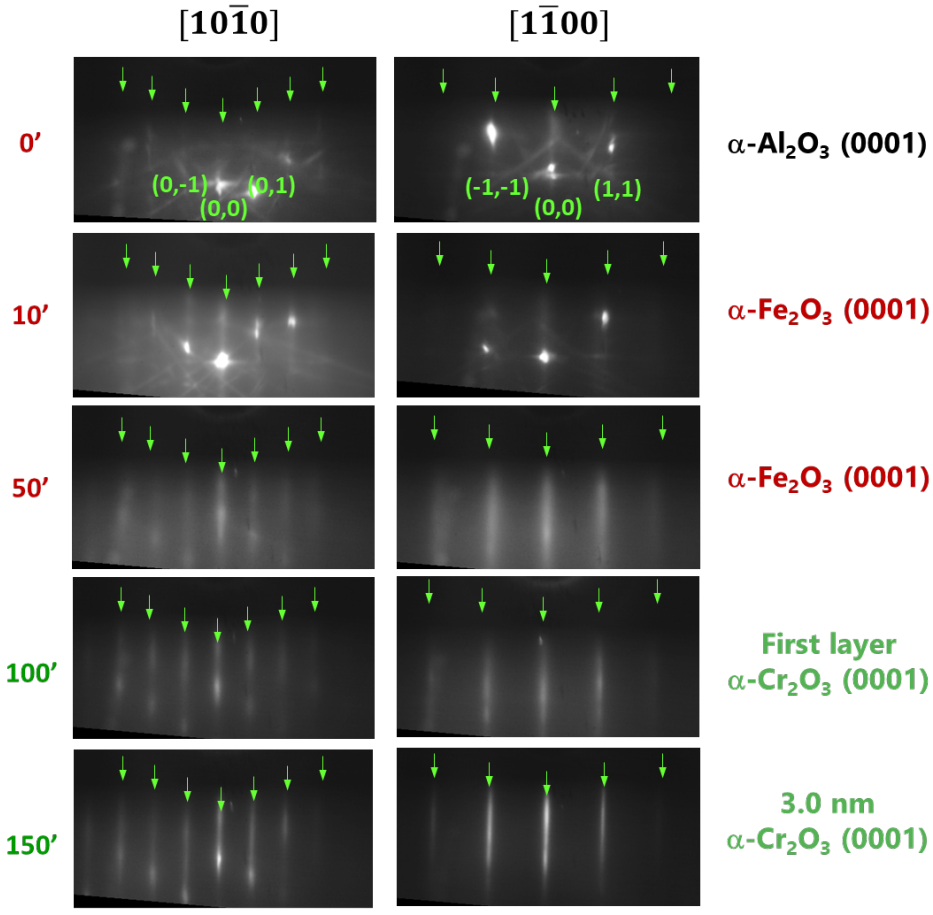


**Figure 3.2.** RHEED patterns recorded during growth of 3 nm thick α-$Cr_2O_3$(0001) after growing 6 nm of α-$Fe_2O_3$(0001) buffer. The streaks of α-$Fe_2O_3$ (or α-$Cr_2O_3$) are at almost the same position as the substrate (or the buffer) and have their intensity reinforced during growth. Images recorded with the 30 keV primary beam aligned parallel to $[10\bar{1}0]$ and $[1\bar{1}00]$ azimuths of sapphire.

Because of the relatively large mismatch between α-$Fe_2O_3$ and $Al_2O_3$, the system quickly undergoes strain relief (within ~2 monolayers) by significant mass transport, which leads to the

formation of 3D islands after the period of 2D growth. The emergence of the first islands causes the diffusion effect in the RHEED rods, as observed in **Figure 3.2** after 50 minutes of growth. Interestingly, growing $\alpha$-$Cr_2O_3$ on this slightly rough buffer surface does not affect its crystalline quality. On the contrary, the RHEED rods become more intense and sharper after growing 3 nm of $\alpha$-$Cr_2O_3$ over the $\alpha$-$Al_2O_3$/$\alpha$-$Fe_2O_3$ system.

### 3.2.1 Structural investigation

In the study of strain-induced effects, a perfect epitaxial growth is mandatory as structural defects (*e.g.* grain boundaries) promote relaxation phenomena [17] and disturb the analysis. Hence, a comprehensive structural characterization was performed to confirm that the structure and epitaxial nature of the films have not evolve during deposition or after exposure to air.

Following the growth, the thickness of each sample was estimated by the Cr evaporation rate (~0.30 Å·min$^{-1}$) and confirmed *ex situ* by X-ray reflectivity (XRR) measurements. **Figure 3.3a** depicts the fit of the XRR patterns performed using Parratt's formulism (see **Section 2.2.2**) in a representative sample. Considering the theoretical values for the atomic density ($1.9\times10^{28}$ m$^{-3}$) and the structure factors ($f$ = 71.51 fm and $f'$ = 4.77 fm), the fit yields a thickness ($t$) of 16.4 nm and roughness ($\sigma_{XRR}$) of 0.1 nm. This characteristic low roughness was also deduced from atomic force microscopy (AFM) topographic images ($\sigma_{AFM}$ = 0.1 nm), as depicted in **Figure 3.3b**.

In this study, the photoemission spectra are mainly discussed for the early stages of oxide growth (see **Section 3.3**). Thus, these samples are ultrathin films. According to the fit of the XRR patterns (**Figure 3.4**), they are less than 10 nm thick, so X-ray diffraction (XRD) could not be performed on laboratory equipment to confirm the phase and crystalline structure of these films. Nonetheless, **Figure 3.3c** shows XRD scans acquired using a standard diffractometer running in the $\theta$-$2\theta$ Bragg–Brentano geometry and rocking curve (see **Section 2.2.2**) for a thicker $\alpha$-$Cr_2O_3$(0001) layer grown directly on sapphire. The high crystalline quality proven for this sample is representative of all O-MBE samples shown in this chapter, as they were prepared under the same growth conditions. The $\theta$-$2\theta$ patterns exhibit only (000$l$) peaks, which confirms that the film grew aligned with the substrate lattice, following the c-axis orientation of the corundum structure. By fitting the (0006) Bragg peak with a Gaussian function, one found the same out-of-plane lattice parameter $c$ equals to 1.371 $\pm$ 0.002 nm as for a bulk structure [12]. Thus, this film is already relaxed. The rocking curve (**Figure 3.3c** inset) obtained on this peak ($\Delta\Omega$ = 0.1°) is typical of thin films with high crystalline quality. As discussed in **Section 2.2.2**, the peak width for a particular reflection is inversely proportional to the domain size, according to the Debye-Scherrer equation. Herein, the domain size calculated using this relation corresponds to the film thickness, indicating the single-crystalline nature of the films.

Cross-sectional TEM images (**Figure 3.5**) were also acquired for the representative 16 nm thick $\alpha$-$Cr_2O_3$ sample grown on $\alpha$-$Al_2O_3$. Low magnification TEM micrograph (**Figure 3.5a**) shows that the film is homogeneous and has a constant thickness of 16.1 nm. This measurement is in good agreement with the thickness found in the XRR measurements ($t_{XRR}$ = 16.4 nm). The high-resolution

TEM images (**Figure 3.5b**) shows a perfectly flat α-$Cr_2O_3$/α-$Al_2O_3$ interface with no noticeable parasite phases at atomic scale. The α-$Cr_2O_3$ follows nicely the template created by the substrate in a layer-by-layer growth mode [3]. This film exhibits a single-crystalline structure with minimal structural defects. The HRTEM image is consistent with the highly crystallographically oriented or "textured" thin film observed in the XRD scans.

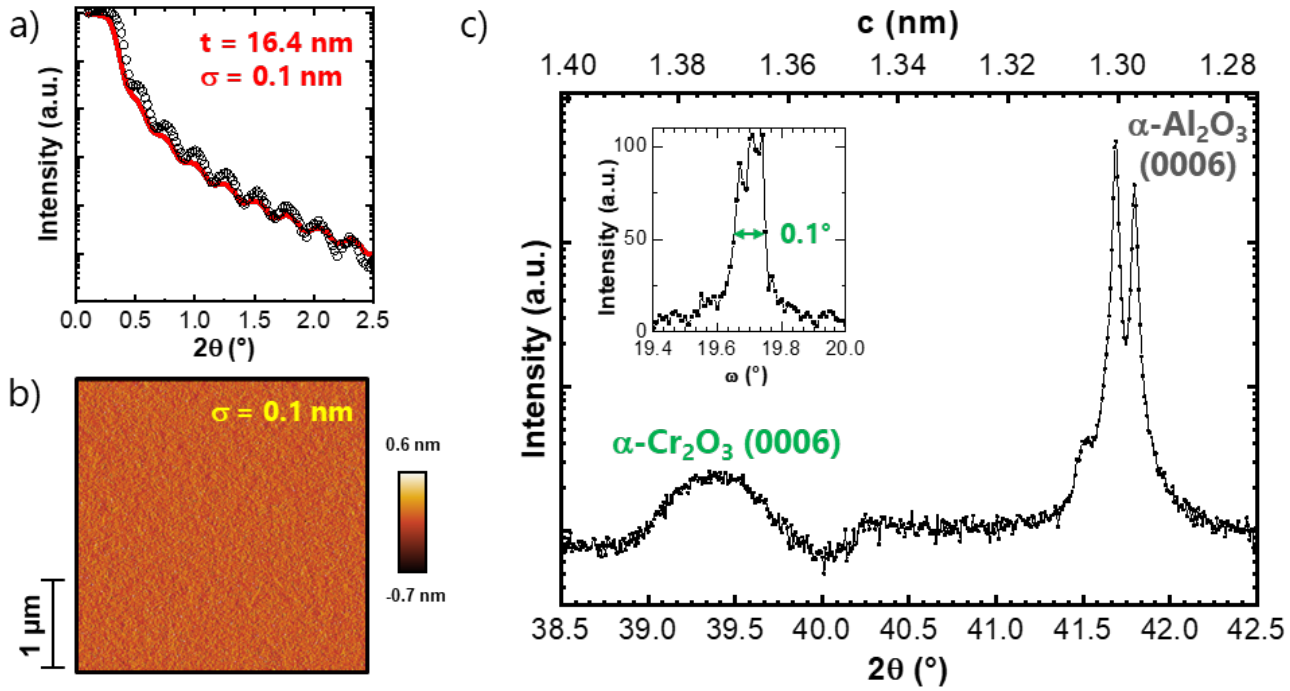


**Figure 3.3.** Structural characterization of a representative α-$Cr_2O_3$ (0001) grown on α-$Al_2O_3$ (0001) substrate. (a) The thickness of the film, *t*, is obtained by the fit (red line) of the XRR pattern (black circles) using Parratt's formulism (see **Section 2.2.2**). The roughness retrieved in the XRR fit ($\sigma_{XRR}$ = 0.1 nm) is the same as the one derived from the (b) AFM image ($\sigma_{AFM}$ = 0.1 nm). (c) The θ-2θ XRD scan shows the (0006) Bragg peak for α-$Cr_2O_3$ layer (2θ = 39.4°, c = 1.37 nm) and α-$Al_2O_3$ substrate (2θ = 41.7°, c = 1.30 nm). In inset, the rocking curve on the (0006) peak (ΔΩ = 0.1°) confirms the high crystalline quality of the film.

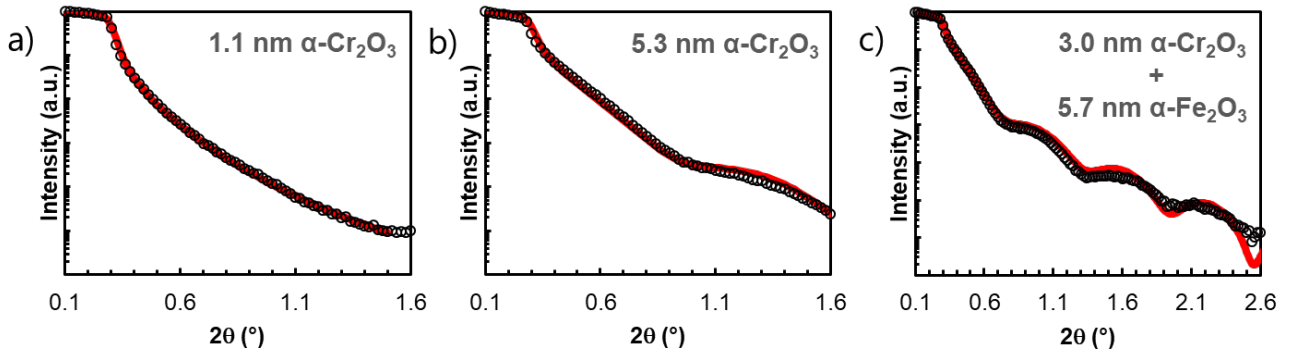


**Figure 3.4.** X-ray reflectivity pattern (black circles) of (a) 1.1 nm and (b) 5.3 nm thick α-$Cr_2O_3$(0001) thin films grown on α-$Al_2O_3$(0001) as well as (c) 3.0 nm thick α-$Cr_2O_3$(0001) thin films grown on α-$Fe_2O_3$(0001) buffer. In the top, the obtained thickness obtained by fitting (red line) the XRR data. The fit parameters used for all samples are the atomic density of $1.9 \times 10^{28}$ $m^{-3}$, the structure factors of 71.51 (*f*) and 4.77 (*f'*). The roughness of these samples is around 0.5 nm.

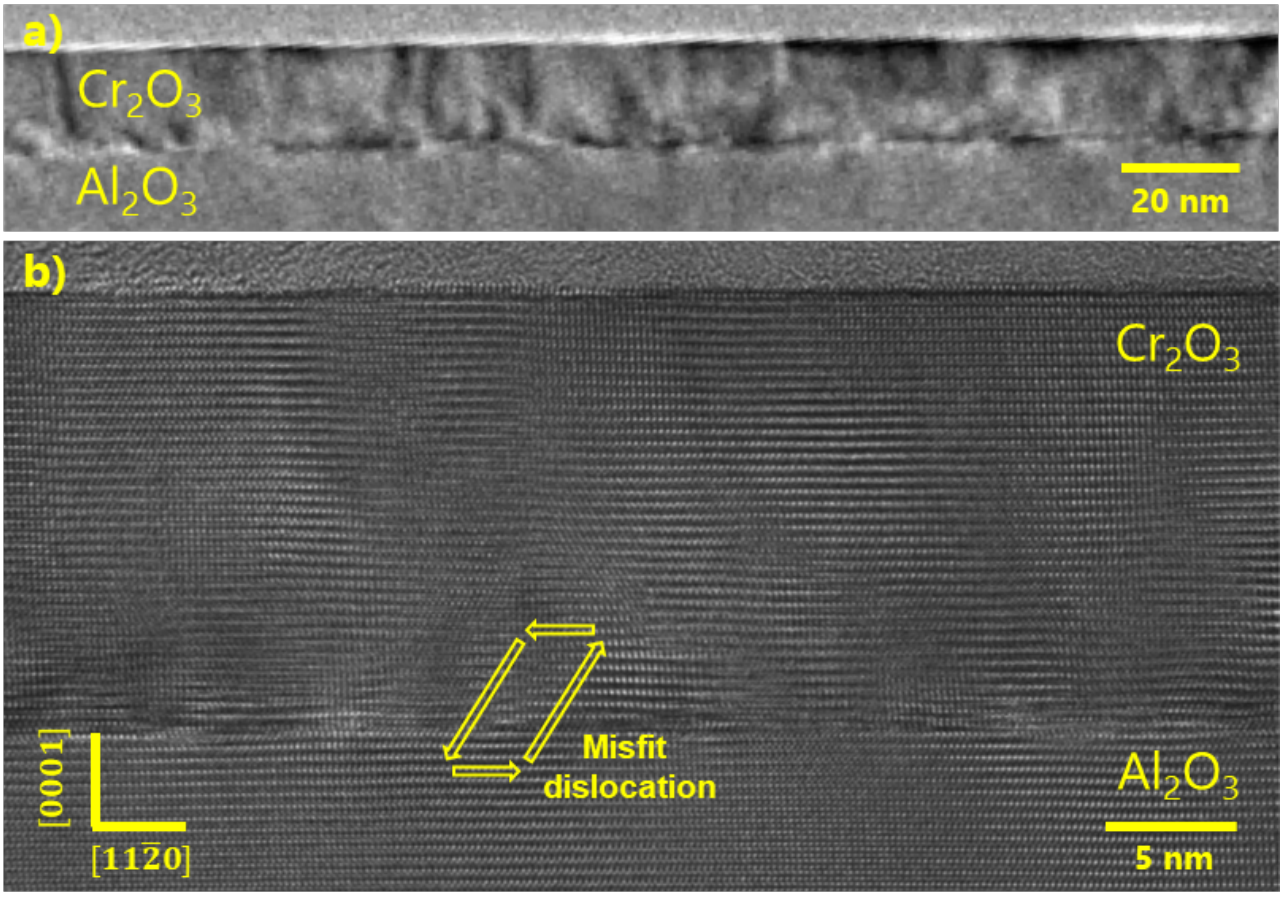


**Figure 3.5.** Cross-sectional TEM images of a representative α-$Cr_2O_3$ (0001) grown on α-$Al_2O_3$ (0001) substrate. (a) Low magnification TEM shows the homogeneity in thickness and structure of the 16.1 nm thick film. Herein, the interfaces epoxy/α-$Cr_2O_3$ (top) and α-$Cr_2O_3$/α-$Al_2O_3$ (bottom) are clearly determined. (b) High-resolution TEM depicts the epitaxial nature of the growth and the layer-substrate interface. The images were recorded with the beam aligned along the [$1\bar{1}00$] crystallographic orientation.

### 3.2.2 Chemical investigation

The purity of the films was first evaluated *ex situ* by XPS measurements. **Figure 3.6a** depicts the survey scan of the representative 16 nm thick α-$Cr_2O_3$ thin film grown on α-$Al_2O_3$, in which no elements other than Cr 2*p* (~580 eV), O 1*s* (~530 eV) and C 1*s* (~285 eV) is observed. For α-$Cr_2O_3$ thin films with less than 10 nm of thickness, the signal of Al from the substrate (*e.g.,* ~75 eV for Al 2*p*) also appears in the survey scan. Likewise, for α-$Cr_2O_3$ thin films grown on α-$Fe_2O_3$ buffer (**Figure 3.6b**), the Fe 2*p* signal (~720 eV) is also observed. Because the XPS measurements were performed *ex situ*, the Cr:O ratio could not be measured due to carbon oxide contaminations and the influence of the substrate (or the buffer) under the film.

The stoichiometry and homogeneity of the representative 16 nm thick α-$Cr_2O_3$ were then investigated using electron energy-loss spectroscopy (EELS) and energy dispersive X-ray spectroscopy (EDX). Since these techniques are highly localized, different areas of the sample were probed to assure the homogeneity of the films. Whereas STEM-EELS yields a relative composition of (38 ± 2)% of Cr and (62 ± 2)% of O, STEM-EDX measured (39 ± 2)% of Cr and (61 ± 2)% of O in the

α-$Cr_2O_3$ thin film. The results are coherent and very close to the 2:3 ratio expected between Cr and O, so the optimized growth conditions used in this work (**Table 3.1**) are able to produce stoichiometric films. Moreover, STEM-EELS (**Figure 3.7**) presented minimal fluctuations in the Cr and O signals throughout the layers and no composition gradient. Therefore, the films are homogeneous.

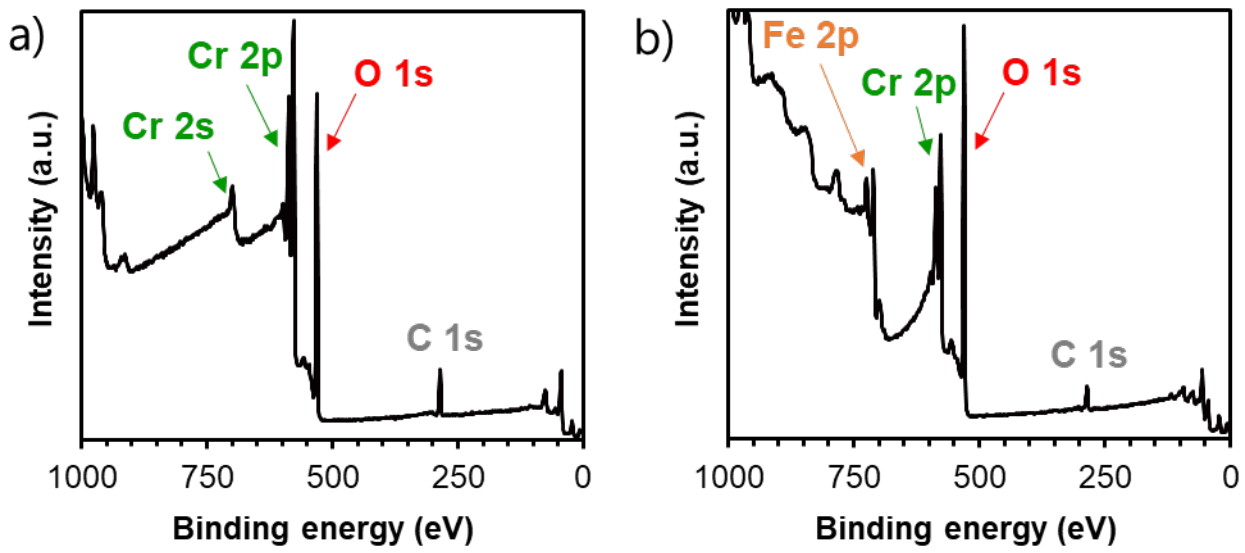


**Figure 3.6.** Survey scan XPS spectrum of (a) 16 nm thick α-$Cr_2O_3$(0001) thin films grown on α-$Al_2O_3$(0001) and (b) 3.0 nm thick α-$Cr_2O_3$(0001) thin films grown on α-$Fe_2O_3$(0001) buffer.

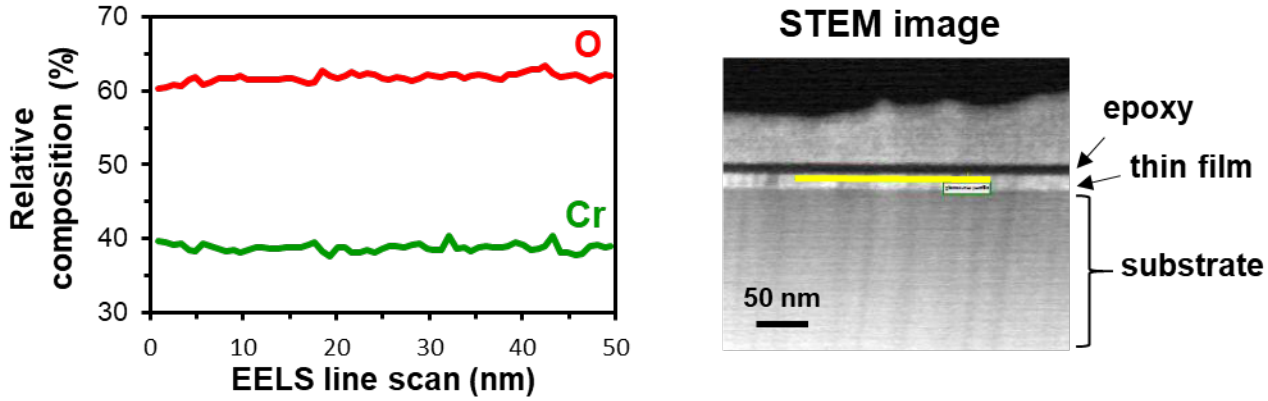


**Figure 3.7.** At left, Cr and O relative compositions measured using STEM-EELS for 16 nm thick α-$Cr_2O_3$(0001) thin films grown on α-$Al_2O_3$(0001). At right, STEM images show the position of the horizontal line scan.

## 3.3 α-$Cr_2O_3$ under different strain scenarios

Once the crystalline quality and purity of the α-$Cr_2O_3$ thin films was ensured, different strain scenarios were taken into account. The growth stresses and relaxation mechanisms are intimately related to the kinetics of film growth. Owing to the inherent stiffness of most oxides, strain energy

usually accumulates rapidly with film thickness, resulting in misfit dislocations, film buckling, morphological transformation from 2D layer-by-layer to 3D island growth, or coincidence lattice formation [11]. **Figure 3.8** depicts the evolution of the in-plane lattice parameter *vs.* coverage (dotted lines) extracted from the RHEED images (see **Figure 2.3**) acquired with the primary beam aligned parallel to $[1\bar{1}00]$ azimuth. For simplicity's sake, the spacing between the $(11)$ and $(\bar{1}\bar{1})$ streaks in pixel is normalized to a value of 100% for $\alpha$-$Al_2O_3$. Thus, values of 96.64% and 94.33% are obtained for bulk $\alpha$-$Cr_2O_3$ and $\alpha$-$Fe_2O_3$ (dashed lines in **Figure 3.8**), respectively. For $\alpha$-$Cr_2O_3$ grown on $\alpha$-$Al_2O_3$(0001), the strain energy accumulates rapidly with film thickness due to the lattice mismatch of +3.36%. As shown in HRTEM image (**Figure 3.5b**), this system undergoes strain relief by nucleating misfit dislocations and relaxes completely up to few nanometers. Therefore, three $\alpha$-$Cr_2O_3$ single layers with thicknesses of 1.1, 5.3 and 16.4 nm were selected (**Figure 3.8** left) to evaluate the Cr $2p$ XPS spectrum of $\alpha$-$Cr_2O_3$ under high ($+2.8 \pm 0.5$ %) or moderate ($+1.5 \pm 0.5$ %) compressive strain as well as fully relaxed (~0%). Meanwhile, for the study of $\alpha$-$Cr_2O_3$ under tensile strain, the film was grown on $\alpha$-$Fe_2O_3$ buffer. In this bilayer, $\alpha$-$Cr_2O_3$ should remain under lateral tension up to several Angstroms, exhibiting similar in-plane lattice parameter as the $\alpha$-$Fe_2O_3$ buffer [3]. Herein, one selected a $\alpha$-$Fe_2O_3$ film thickness of 5.7 nm associated to a fully relaxed state. On this relaxed buffer layer, an ultrathin film of 3.0 nm thickness of $\alpha$-$Cr_2O_3$ was grown successfully. As predicted, the $Cr_2O_3$ layer exhibited a partial in-plane tensile strain of $-1.6 \pm 0.5$ % (**Figure 3.8** right).

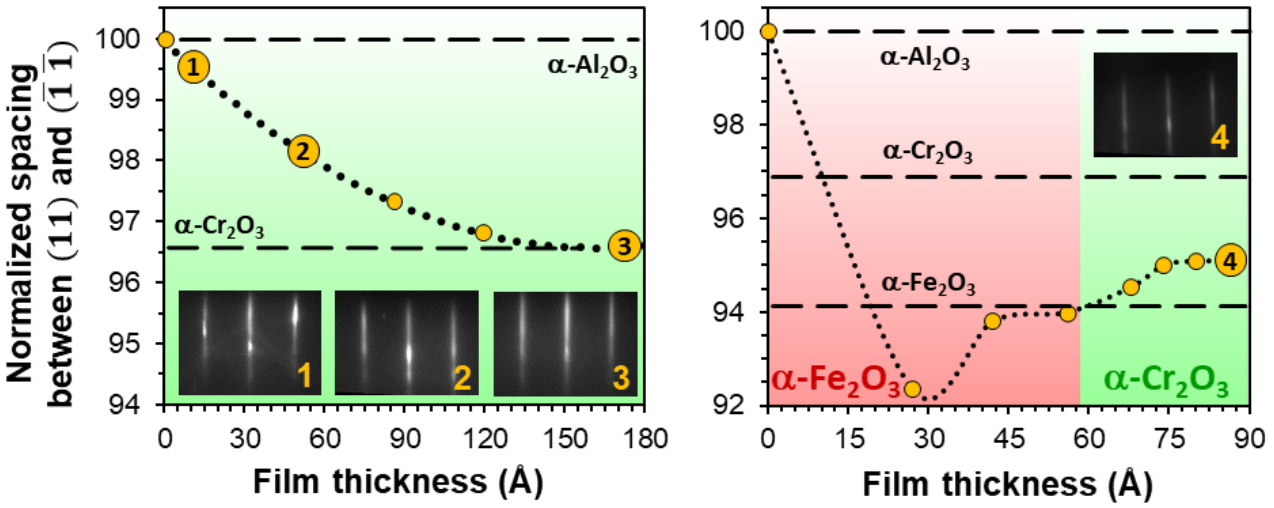


**Figure 3.8.** Evolution of the relative RHEED streak spacing during the growth of $\alpha$-$Cr_2O_3$ (0001) under compressive ($\alpha$-$Cr_2O_3$ on $\alpha$-$Al_2O_3$ substrate, left image) and tensile ($\alpha$-$Cr_2O_3$ on $\alpha$-$Fe_2O_3$ buffer, right image) in-plane strain. The inset RHEED images were acquired with the 30 keV beam aligned along the $[1\bar{1}00]$ azimuth.

E*x situ* XPS analyses were carried out for each strain scenario, as shown in **Figure 3.9**. Overall, **Figure 3.9** depicts a typical Cr $2p$ XPS spectrum for Cr(III) oxide, which is known for its particularly complex spectral shape due to the coupling between the $2p$ core-hole and the unpaired electrons in the $3d$ outer shell [9]. One recognizes two single asymmetrical peaks for Cr $2p_{3/2}$ and Cr $2p_{1/2}$ envelopes, centered respectively at 576.5 eV and 586.5 eV. The Cr $2p_{1/2}$ envelope exhibits minor changes in all strain scenarios, whereas the multiplet splitting features of the Cr $2p_{3/2}$ envelope

steadily evolve with the in-plane lattice parameter. For high compressive strain (**Figure 3.9$_1$**), the multiplet peak at 575.5 eV (A) is less intense than the one at 577.0 eV (B) and the splitting of the Cr $2p_{3/2}$ envelope is indistinct. For moderate compressive strain or for relaxed films (**Figure 3.9$_{2\text{-}3}$**), striking splitting of the Cr $2p_{3/2}$ envelope was observed, for which the multiplet peaks A and B have almost the same intensity. In the case of the bilayer, *i.e.* for high tensile strain of $Cr_2O_3$ (**Figure 3.9$_4$**), the multiplet peak A is also less intense than B; however, contrary to the high compressive strain scenario (**Figure 3.9$_1$**), one observed in **Figure 3.9$_4$** a prominent shoulder at 578.5 eV (C). In order to account for all these subtle changes in the spectral signatures of the Cr $2p_{3/2}$ XPS spectra, semiempirical crystal field multiplet (CFM) calculations were performed.

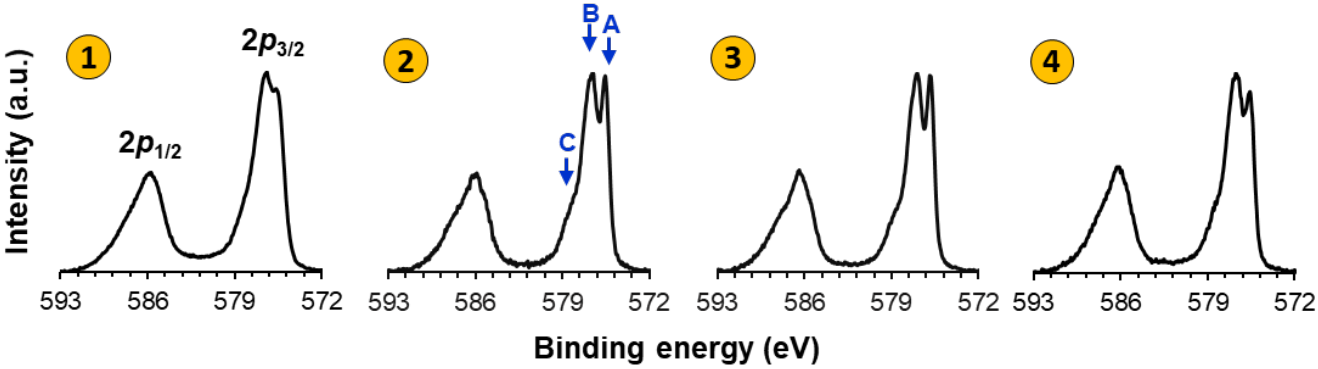


**Figure 3.9.** High-resolution Cr $2p$ XPS spectra for $\alpha$-$Cr_2O_3$ under high (1) and moderate (2) compressive strain as well as for a fully relaxed film (3) and under high tensile strain (4). A Shirley-type background subtraction was employed for all spectra.

## 3.4 CFM simulations: from multiplet splitting to the local structure

In the CFM theory, the solid system is mimicked by considering the transition metal as an isolated ion embedded in a crystal field potential. To simulate Cr $2p$ XPS spectra, the multi-electronic states are described in terms of the $3d$–$3d$ and $2p$–$3d$ Coulomb ($F^k_{dd}$, $F^k_{pd}$) and exchange ($G^k_{pd}$) interactions, the $2p$ ($\zeta_{2p}$) and $3d$ ($\zeta_{3d}$) spin-orbit coupling, and the local symmetry ($C_{3v}$). Herein, the $Cr^{3+}$ electronic configurations of relevance are $3d^3$ for initial states and $2p^5 3d^3$ for final states. In the Cr $2p$ XPS of $Cr_2O_3$, the satellite peak assigned to charge transfer excitations sits close to the $2p_{1/2}$ position (~589 eV), broadening this line [18], [19]. Since this zone of the spectrum is not interesting in this study (*i.e.,* only minor changes are observed in all strain scenarios), additional electron configurations resulting from ligand charge transfer (*e.g.,* $3d^{n+1}\underline{L}$) were neglected.

As discussed in **Section 2.4**, the *ab initio* Hartree-Fock (HF) values of the Slater-Condon integrals were scaled down in order to account the iono-covalent behavior of the Cr-O chemical bond. The reduction factors of $F^2_{dd}$ and $F^4_{dd}$ for the initial state were obtained by comparison of the

HF values with the ones determined by the experimental Racah B and C parameters[28] ($B = 9F^2_{dd} - 5F^4_{dd}$ and $C = 5\ F^4_{dd}/63$). For experimental B = 0.057 eV and C = 0.433 eV [20], the HF values of $F^2_{dd}$ and $F^4_{dd}$ are reduced by 54% and 81%, respectively. The same scaling factors were applied for $F^2_{dd}$ and $F^4_{dd}$ in the final state. $F^2_{pd}$ and $G^1_{pd}$ were scaled to 80% of the associated atomic values, while $G^3_{pd}$ was considered at 100% to fit the distance between multiplet peaks.

The effects of the local symmetry are accounted by the crystal field parameters in a given point group symmetry. As shown in **Figure 1.2**, the $Cr^{3+}$ cations in the corundum structure lay on the center of a slightly distorted octahedron, where a $C_3$ rotation axis traverses the cation and the center of the two equilateral triangles formed by the oxygen ions. Thus, this system can be reasonably approximated by the $C_{3v}$ point group [22], [23] and parametrized in terms of Dq, Dσ and Dτ parameters [24]. Optimization of these three parameters is the key to this work and is explained in detail below. For clarity, **Table 3.2** summarizes all atomic and crystal field parameters optimized in this work.

**Table 3.2** – Energy values (in eV) and reduction factors of the electronic structure parameters of $Cr^{3+}$ used for calculating the 2*p* XPS spectra of $Cr_2O_3$.

| Parameter | $F^2_{dd}$ | $F^4_{dd}$ | $F^2_{pd}$ | $G^1_{pd}$ | $G^3_{pd}$ | $\zeta_{2p}$ | $\zeta_{3d}$ | Dq | Dσ | Dτ |
|---|---|---|---|---|---|---|---|---|---|---|
| **Ground state $3d^3$** | 5.82 | 5.47 | - | - | - | - | 0.035 | 0.208 | 0.60 | * |
| **Final state $2p^5 3d^3$** | 6.26 | 5.89 | 5.29 | 3.88 | 2.72 | 5.67 | 0.047 | 0.208 | 0.60 | * |
| **Reduction factor** | 0.54 | 0.81 | 0.80 | 0.80 | 1.00 | 1.00 | 1.00 | - | - | - |

* Dτ parameter was adjusted to reproduce the experimental XPS spectra. Its value varied from -0.30 to -0.24 eV depending on film thickness.

The CFM model considers the crystal field surrounding the metal ion in terms of symmetry reduction. The introduction of an octahedral field ($O_h$) breaks the degeneracy of the spherical 3*d* orbitals into two subsets of $t_{2g}$ and $e_g$ orbitals. The symmetry reduction from $O_h$ to $C_{3V}$ is associated to a further splitting of the $t_{2g}$ orbital subset into $a_1 + e$ (**Figure 2.14**). The energy splitting (δ) between the geometric centers of $a_1$ and $e$ orbitals is therefore proportional to distortions in the $CrO_6$ octahedral center. For instance, δ is calculated as ~2 meV in a fully relaxed $Cr_2O_3$ crystal [20]. However, this value may increase as strain is applied.

[28] The Racah parameters for $Cr_2O_3$ can be obtained from experimental absorption spectra using the position of the $^4A_{2g}$ and $^2E_g$ energy levels: $E(^2E_g) - E(^4A_{2g}) = 3.05C + 7.9B - 1.8B^2/Dq$ [20]. This equation follow the classical work of Tanabe and Sugano [21], where the energy matrix was written in terms of Dq and Racah parameters A, B and C. The result of this work is the well-known *Tanabe-Sugano diagrams* that plot the energy levels of all 3*d*-ions as a function of Dq/B ratio.

In the basis of the $C_{3v}$ symmetry (see **Section 2.4.1**), δ is related to the crystal field parameters through the relationship: $\delta = 3D\sigma + 20/3D\tau$ [25], [26]. In order to reduce the number of possible free adjustable parameters, Dq was set to the experimental value of 0.208 eV [20]. Then, several spectra were calculated using all combinations of Dσ and Dτ values ranging from -1.0 to +1.0 eV. The Dσ parameter shows itself marginally sensitive compared to Dτ. Variations of Dσ between 0.5 and 0.7 eV barely affect the Cr 2*p* spectral shape. Hence, the value of Dσ was set to +0.600 eV. For fixed values of Dq and Dσ, **Figure 3.10** shows that the Dτ parameter controls the relative energies between the valence orbitals, which determine different fine structure for the XPS spectra. For Dτ positive (not shown) or lower than -0.34 eV (left of region I), the Cr $2p_{3/2}$ envelope appears mostly as a single asymmetrical peak. As Dτ value decreases from 0 to -0.34 eV, the relative intensity of the multiplet peaks A and B changes, leading to a progressive decrease in the intensity of the multiplet peak A at lower binding energy and the appearance of a shoulder C at the left of the main peak (high-energy part). For optimal Dq (0.208 eV) *and Dσ* (0.600 eV), the range of $-0.300 < D\tau < -0.240$ eV with $\delta = \pm 200$ meV was then particularly interesting for this study.

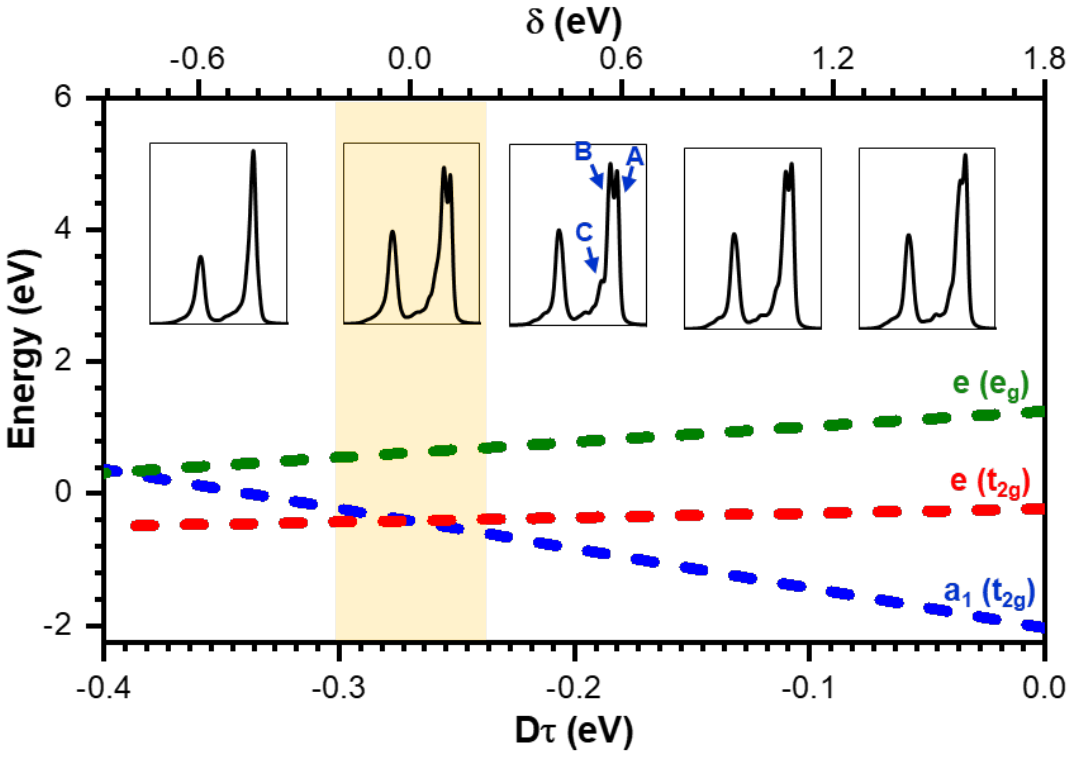


**Figure 3.10.** Evolution of the $Cr^{3+}$ calculated spectral shape (top insets) with the D*τ* parameter when D*σ* = 0.600 eV and Dq = 0.208 eV. In yellow shade, the optimal values of D*τ* ($-0.300 < D\tau < -0.240$ eV and $\delta = \pm 200$ meV) used to calculate the XPS spectra for thin films under different strain scenario. In the bottom, the relative energies of the valence orbitals $a_1(t_{2g})$ (blue dashed line), $e(t_{2g})$ (red dashed line) and $e(e_g)$ (green dashed line) are determined by the CF parameters through the relationship: $a_1(t_{2g}) = -4Dq - 2D\sigma - 6D\tau$, $e(t_{2g}) = -4Dq + D\sigma + 2/3D\tau$ and $e(e_g) = +6Dq + 7/3D\tau$.

Optimal Dτ values were obtained by adjusting the calculated Cr $2p_{3/2}$ envelope to the experimental one in each strain scenario, to which a crystal field splitting δ parameter was associated. Here the fit criterion was to best match the relative intensity and position of the multiplet peaks A

and B. **Figure 3.11** describes the results of the CFM simulations for α-$Cr_2O_3$(0001) thin films under high (**Figure 3.11a**) and moderate (**Figure 3.11b**) in-plane compression, fully relaxed (**Figure 3.11c**) and under in-plane tension (**Figure 3.11d**). For a fully relaxed film, the Cr 2*p* XPS spectrum is well fitted with Dτ = -0.270 ± 0.005 eV for which the $t_{2g}$ orbital subset is fully degenerated (δ = 0). When an in-plane compression is applied, Dτ value decreases and δ increases proportionally to the amount of strain. For instance, the spectrum of 1.1 nm α-$Cr_2O_3$ film, highly compressed through mismatch with α-$Al_2O_3$ substrate, is well fitted with Dτ = -0.295 ± 0.005 eV for which δ = 170 meV. In turn, the spectrum of partial relaxed 5.3 nm film is well fitted with Dτ = -0.280 ± 0.005 eV for which δ = 70 meV. For these samples, the 3*d* orbital diagrams (**Figure 3.11** inset) showed that the higher the in-plane compression, the more destabilized is $a_1$ in relation to $e$ orbitals. Interestingly, the tension scenario showed an opposite tendency: the in-plane tension increases the Dτ value, which decreases δ by stabilizing $a_1$ in relation to $e$ orbitals. For instance, the spectrum of 3.0 nm α-$Cr_2O_3$ film, strained through mismatch with α-$Fe_2O_3$ buffer, is well fitted with Dτ = -0.260 ± 0.005 eV for which δ = -70 meV.

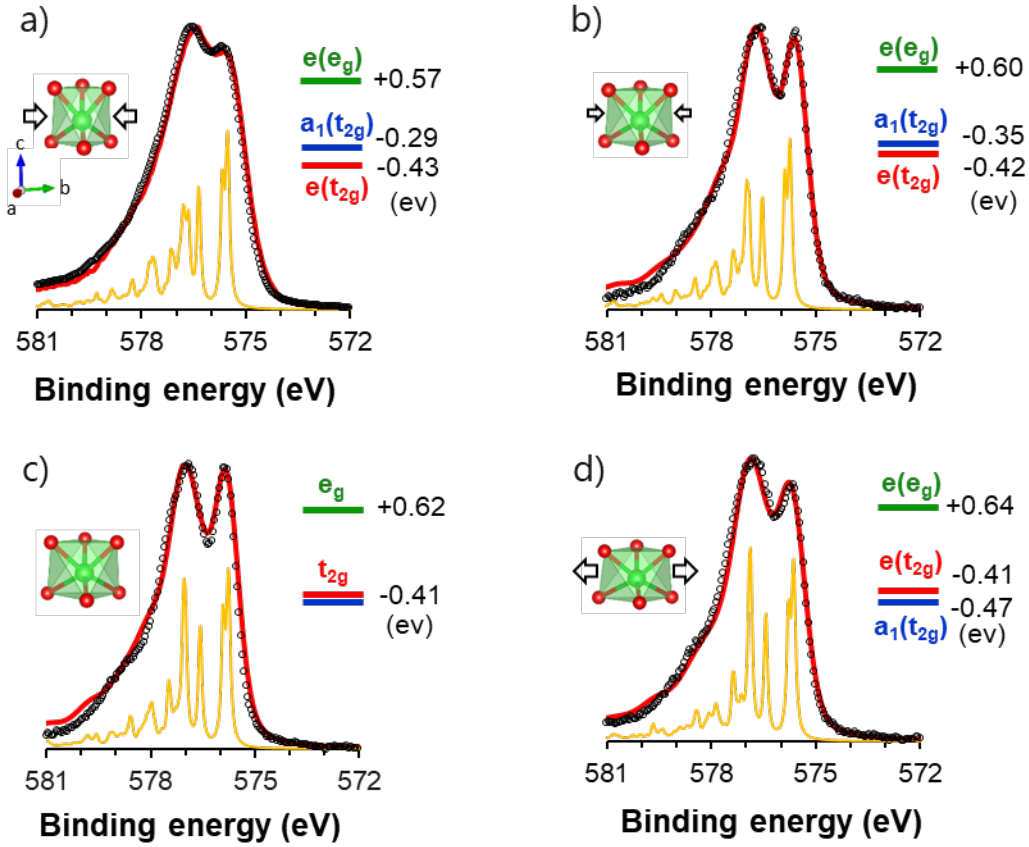


**Figure 3.11.** Calculated Cr 2*p* XPS spectra (red line) in comparison with the experimental spectra (black circles) for α-$Cr_2O_3$(0001) thin films under (a) high and (b) moderate compressive strain as well as (c) fully relaxed and (d) under in-plane tension. Below each spectrum (yellow line), the calculated stick diagrams (FWHM = 0.1 eV) are shown, which were further convoluted (red line) with a Lorentzian function (FWHM = 0.3 eV) and a Gaussian function (FWHM = 0.7 eV) to mimic the experimental broadening of the spectral lines. At the top right, the relative 3*d* orbital diagram are plotted for Dq = 0.208 eV, Dσ = 0.600 eV and (a) Dτ = -0.295 ± 0.005 eV, (b) -0.280 ± 0.005 eV, (c) -0.270 ± 0.005 eV and (d) -0.260 ± 0.005 eV. At the top left, a schematic representation of the $CrO_6$ distortions is depicted.

The decreasing energy of $a_1$ regarding $e$ orbital when switching from compression to tension scenario is indeed coherent with deformations in the $xy$ plane. In the $C_{3v}$ representation [27], the $a_1$ orbital corresponds to the $z^2$ component of the $t_{2g}$ subset oriented along the $C_3$ axis (**Table 2.1**). By compressing (or stretching) the $xy$ plane, the top three as well as the bottom three ligands come closer (or move apart). Epitaxial thin films of $\alpha$-$Cr_2O_3$(0001) compensate the in-plane lattice strain by relaxation of out-of-plane lattice parameter and internal angles, as indicated by HRTEM [3], [28]. Hence, a lateral compression of $\alpha$-$Cr_2O_3$(0001) layer limits the space of the $z^2$ component and destabilizes $a_1$ (**Figure 3.11a**), whereas a lateral tension acts in the opposite way (**Figure 3.11d**).

## 3.5 Quantitative relation between crystal field splitting δ and epitaxial strain

As depicted in **Figure 3.12**, a quantitative relation can be drawn between the energy splitting δ extracted from experimental photoemission spectra (**Figure 3.11**) and the residual strains determined using the RHEED images (**Figure 3.8**). Herein, one observes that δ decreases under increasing strain and crosses zero at a small negative value of strain (about -0.2%). These results bring great support to theoretical predictions reported recently by Mu and Belashchenko [29]. In that paper, first-principle calculations were performed to assess the effect of epitaxial strain on magnetocrystalline anisotropy of pure $Cr_2O_3$. The epitaxial strain was simulated by constraining the in-plane lattice parameters of the hexagonal unit cell and relaxing both the c parameter and all internal degrees of freedom. As shown in **Figure 3.12**, for a given amount of in-plain strain, they calculated the splitting of the $t_{2g}$ states at the Γ point, which represents the crystal-field parameter δ. Likewise, they also found that δ decreases under increasing strain and passes through zero at a small positive value of strain. In fact, both experimental findings (*i.e.,* XPS+CMF) and results of first-principle calculations are almost superimposed.

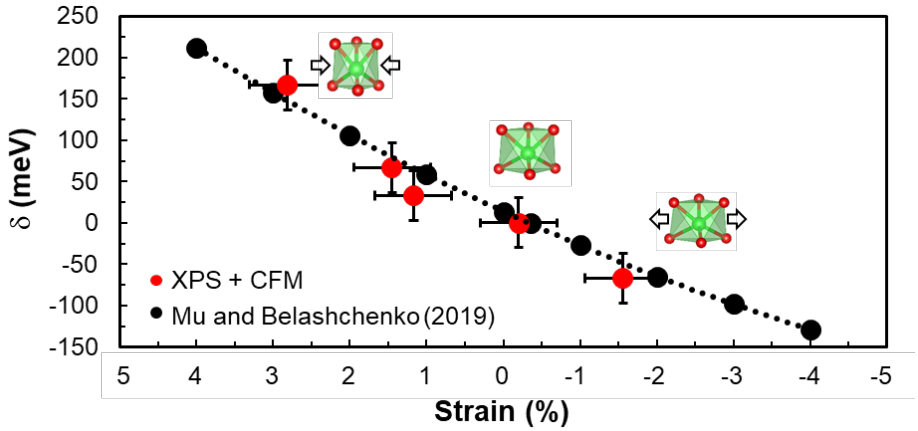


**Figure 3.12.** Evolution of the $t_{2g}$ level splitting δ with epitaxial strain. Herein, XPS+CFM methodology (red circles) is compared to theoretical predictions (black circles) reported by Mu and Belashchenko [29]. The positive or negative sign of the δ parameter indicates that $a_1$ orbital is above or below $e$ orbital, respectively. In inset, schematic representation of the $CrO_6$ distortions are depicted.

These results are very promising as they prove that the alliance of XPS and CFM calculations is a convenient tool for understanding the influence of strain on the electronic structure of complex oxides. Many interesting applications can be found for this methodology, such as in the tuning of $Cr_2O_3$ magnetocrystalline anisotropy in order to enhance the operating temperature of this magnetoeletric antiferromagnet oxide in high-performance spintronic devices [30]. In this regard, the energy splitting $\delta$ is a key parameter. According to literature [29], even small changes of 30 meV in $\delta$ are enough to make positive the magnetocrystalline anisotropy of $Cr_2O_3$. In our study, this value of $\delta$ appears in $\alpha$-$Fe_2O_3$-buffered $Cr_2O_3$ layers under 1.6% of lateral tension (**Figure 3.12**), for which an enhanced magnetocrystalline anisotropy energy is known [31], [32].

In the next section, the XPS+CFM methodology is extrapolated to the study of the growth of $Cr_2O_3$ protective layers during the oxidation of a commercial chromium-forming alloy (Ni30Cr).

## 3.6 CFM simulations for $Cr_2O_3$ protective layers: the case of Ni30Cr oxidation

The XPS instrument used in this work is equipped with a temperature control system that goes from 223 K up to 973 K and a gas dosing system for carrying out *in situ* reactions in the preparation chamber annexed to the spectrometer. Thus, polycrystalline $Cr_2O_3$ samples were prepared by exposing a mirror polished Ni30Cr sheet (5 × 10 $mm^2$, 99.5% in purity) to a controlled leak of oxygen. The oxidation was performed at 973 K under $10^{-5}$ mbar of pure $O_2$ atmosphere. The growing of the oxide layer was followed by *in situ* XPS measurements, acquired with parabolic time steps ($t$ = 0, 1, 4, 9, 16 and 25 minutes) until no further changes were noticed in the spectral shape (**Figure 3.13a**). The thickness ($d$) of the $Cr_2O_3$ layer formed was calculated by the attenuation of the intensity I of the Ni $2p_{3/2}$ substrate peak, following the equation: $I_{Ni} = I_{Ni}^{\infty} \times e^{-d/\lambda_{Ni,Cr_2O_3}}$, where the mean escape depths ($\lambda$) for Ni $2p$ photoelectrons in the oxide layer is set to 7 monolayers. The thickness of the $Cr_2O_3$ layer were estimated for 1 and 4 minutes and subsequently extrapolated using the Wagner-parabolic law. Herein, the $Cr_2O_3$ layers obtained at 1, 4, 9, 16, 25 minutes have thicknesses of about 0.7, 4.4, 8.1, 11.8 and 15.5 nm, respectively.

As expected for the oxidation of Ni30Cr at high temperature [6], only $Cr_2O_3$ layers were formed, without any oxidation of nickel. **Figure 3.13b** depicts a typical metallic nickel $2p$ XPS spectrum [1], where the main $2p_{3/2}$ and $2p_{1/2}$ asymmetric peaks are at 852.6 eV and 870.0 eV, respectively. No change in the position of the main peaks or in the satellites structure were observed during the alloy oxidation process. Therefore, nickel did not oxidize and pure $Cr_2O_3$ was formed in the experimental conditions applied. The non-formation of mixed nickel-chromium oxides is very important for the study of spectral shape evolution, since it influences considerably the Cr $2p$ spectral fine structure [1].

In **Figure 3.13a**, the oxidation of Ni30Cr is depicted as measured by XPS: from clean alloy up to 25 minutes under oxygen leak. Overall, a typical evolution of the Cr $2p$ XPS spectrum with oxidation time was observed, as already reported elsewhere [6]. Before exposure to oxygen (spectrum at the

bottom), the XPS spectrum exhibits features of metallic chromium. One recognizes two single asymmetrical peaks for Cr $2p_{3/2}$ and Cr $2p_{1/2}$ envelopes, centered respectively at 573.8 eV and 583.1 eV. Then, at the first stage of the oxidation (spectrum at 1 minute), two broad peaks at 576.5 eV (Cr $2p_{3/2}$) and 586.5 eV (Cr $2p_{1/2}$) belonging to chromium (III) oxide smoothly grow at the expense of the ones of metallic chromium. These peaks eventually take over after 4 minutes of oxygen exposure (*i.e.,* growth of 4.4 nm $Cr_2O_3$ layer). Interestingly, the shape evolution of the Cr $2p$ XPS spectra during Ni30Cr oxidation is comparable to the previous ones for epitaxial $\alpha$-$Cr_2O_3$ grown by O-MBE. The Cr $2p_{1/2}$ envelope exhibits marginal changes as the film grows, while the Cr $2p_{3/2}$ envelope shows significant evolution. From 4 minutes (4.7 nm layer) to 25 minutes (15.5 nm layer) of oxidation, striking splitting of the Cr $2p_{3/2}$ envelope is discernable, along with a shoulder in the high-energy part (~577 eV) unveiled as the oxide layers grow.

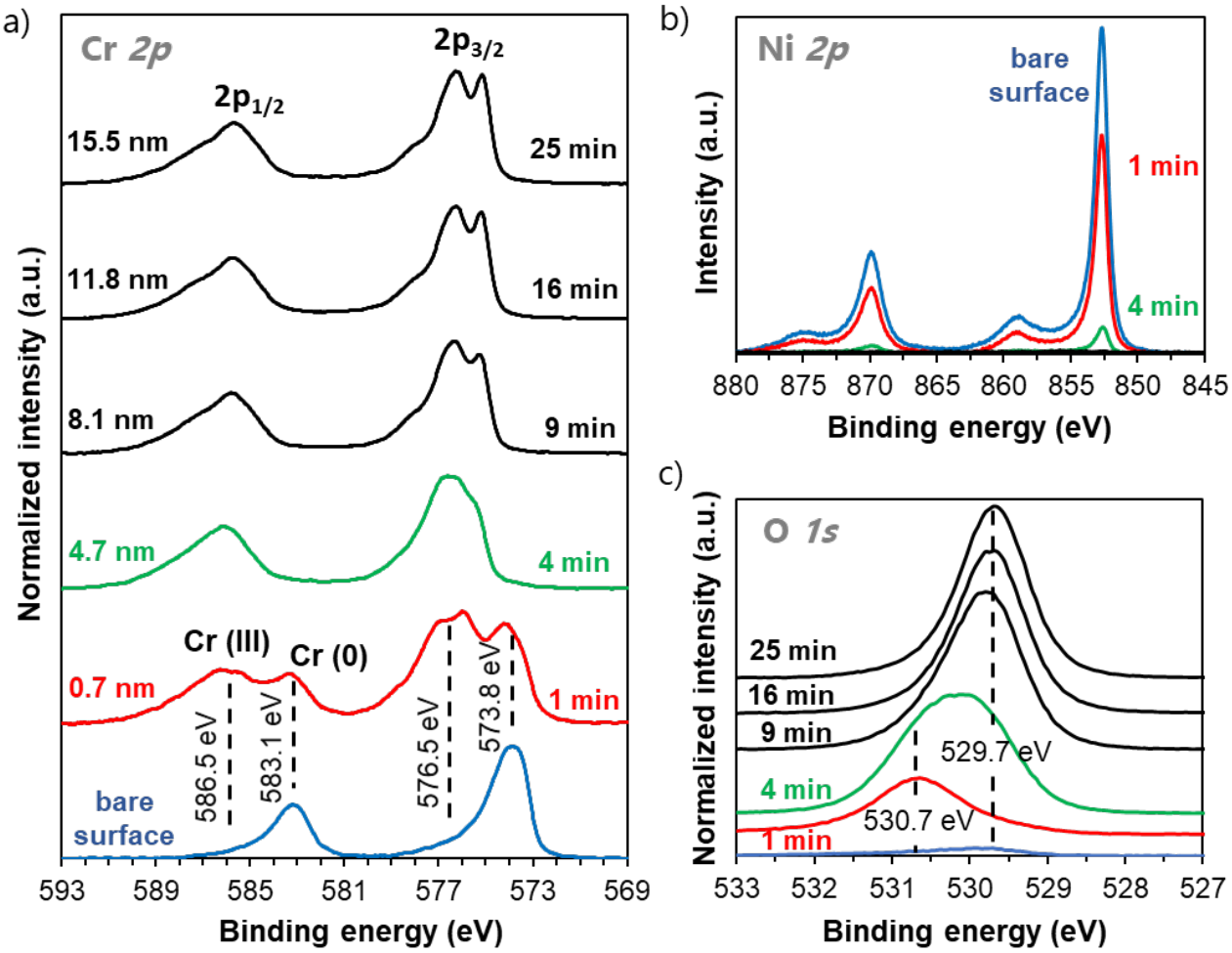


**Figure 3.13.** High-resolution (a) Cr $2p$, (b) Ni $2p$ and (c) O $1s$ XPS spectra as function of oxidation time of Ni30Cr alloy.

In order to comprehend the changes in the local structural of Cr during the formation of $Cr_2O_3$ protective layers, the XPS+CFM methodology was applied. The CF parameters for the $Cr_2O_3$ spectra acquired during the oxidation of Ni30Cr alloy were derived out of the results obtained for the O-MBE films. The Dq and Dσ values were kept to 0.208 eV and 0.600 eV respectively, while the Dτ

parameter was adjusted to give the best fit possible to the experimental spectra. Once again, the fit criterion was to best match the relative intensity and position of the multiplet peaks A (~575.5 eV) and B (~577.0 eV). Similar to the epitaxial films grown on $\alpha$-$Al_2O_3$, D$\tau$ values progressively increased with the oxide growth, taking a value of -0.329 ± 0.001 eV for 4.4 nm film (**Figure 3.14a**), -0.325 ± 0.001 eV for 8.1 nm film (**Figure 3.14b**), -0.280 ± 0.01 eV for 11.8 nm film (**Figure 3.14c**), and -0.270 ± 0.01 eV for 15.5 nm (**Figure 3.14d**).

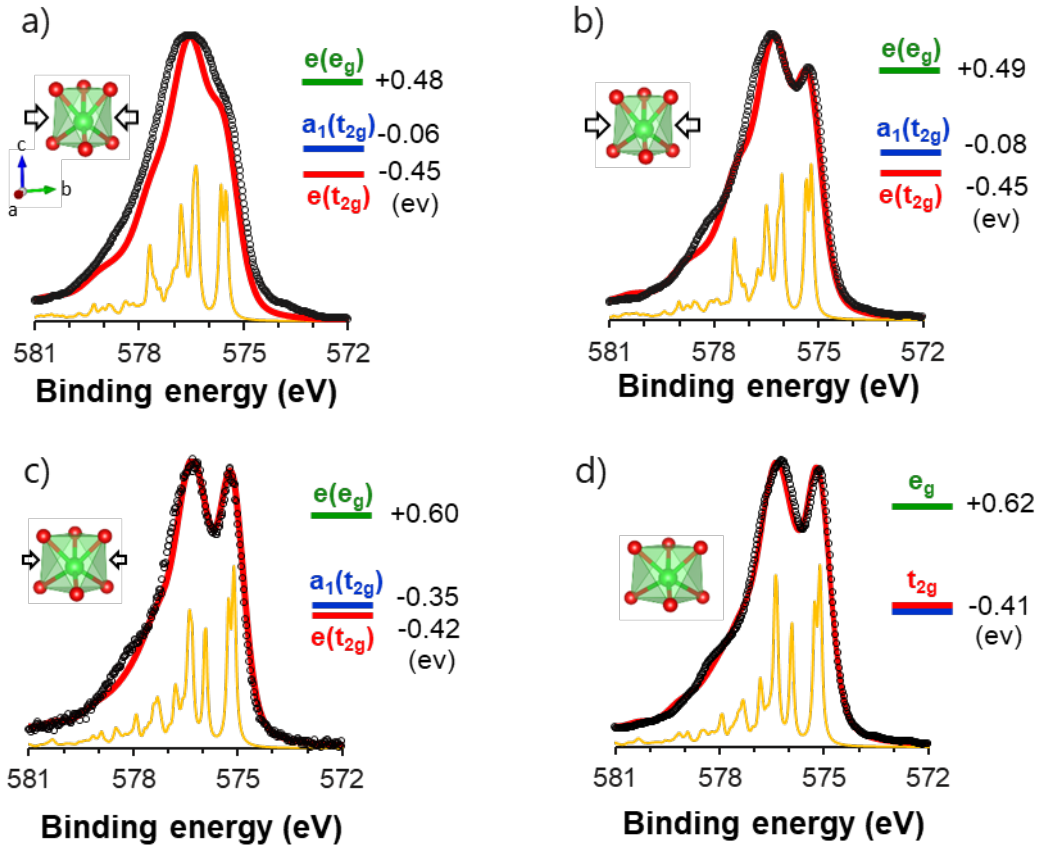


**Figure 3.14.** Calculated Cr 2*p* XPS spectra (red line) in comparison with the experimental spectra (black circles) for (a) 4.4 nm, (b) 8.1 nm, (c) 11.8 nm and (d) 15.5 nm film. Below each experimental spectrum, the theoretical spectrum (yellow line) with stick diagrams (FWHM = 0.1 eV) are shown. At the top right, the 3*d* orbital diagram ($a_1(t_{2g})$ blue, $e(t_{2g})$ red and $e(e_g)$ green line) is plotted for D$\tau$ = -0.329 ± 0.001 eV (a), D$\tau$ = -0.325 ± 0.001 eV (b), D$\tau$ = -0.28 ± 0.01 eV (c) and D$\tau$ = -0.27 ± 0.01 eV (d). A Shirley-type background subtraction was employed for all Cr 2*p* experimental spectra.

At very early oxidation stage (**Figure 3.14a**), the CFM method poorly fitted the Cr $2p_{3/2}$ envelope. This is because polycrystalline samples exhibit several local structures, which may naturally broaden the peaks in comparison to the calculated spectrum. Moreover, at the very beginning of the oxide layer growth, chemisorbed oxygen may be attached to the metallic surface and the Cr cations may be not complete oxidized. This is suggested by the O 1*s* XPS spectra shown in **Figure 3.13c**. Herein, the main contribution peak in the 529.0-530.5 eV range is attributed to the anionic sub-lattice oxygen of $Cr_2O_3$, as confirmed elsewhere [1]. Significant shifts towards lower energies of the core-level O 1*s* were observed as the oxidation proceeds: relative to the bulk (*t* = 25 minutes), the O 1*s*

shifts by 1.0 eV and 0.5 eV in the $t$ = 1- and 4-minutes films, respectively. In addition, the O 1$s$ line at $t$ = 4 minutes sample is very large, indicating two different degrees of oxidation for the oxygen species. Similar trends were found during the initial oxidation reaction on the Ni-Cr alloys surface years ago [35], [36].

Even if the model cannot fully describe the spectrum at the very beginning of the alloy-to-oxide transformation, geometry statements can be done for the evolution of Cr 2$p$ XPS spectra from 4 to 25 minutes of oxidation. One interesting feature is the increase of the Dτ parameter with oxidation time – or sample thickness – from -0.329 up to -0.270 eV. This corresponds to the decrease of the crystal field splitting (δ) of $e$ and $a_1$ orbitals to full degeneracy (**Figure 3.10**). Therefore, $CrO_6$ octahedra are significantly distorted with respect to their $C_{3v}$ site symmetry at the onset of the oxidation, and then are gently relaxed as the oxidation proceeds. Extrapolating the tendency shown in **Figure 3.12**, a compressive strain of -6.5% is associated to Dτ value equals to -0.325 eV (or δ = 367 meV), which is coherent with the large in-plane mismatch imposed by the metallic substrate[29] in the beginning of the oxide growth. As a result, α-$Cr_2O_3$ layers develop negative growth strain during Ni30Cr oxidation in a similar manner as for epitaxial layers on α-$Al_2O_3$ substrate, keeping in mind that the strain is in-plane during the oxide growth and that the α-$Cr_2O_3$ layer align its c-axis perpendicular to the surface.

Some piece of information available in literature corroborate these findings. Actually, the existence of residual stress and its relaxation processes are known for oxide scales [39]. According to DRX and Raman experiments, residual stresses for α-$Cr_2O_3$ layer growing on Ni30Cr are usually compressive, in the order of few GPa [40]–[42]. Additionally, recent DRX studies [6], [43], [44] point out that the growth of α-$Cr_2O_3$ layer operates along the c-axis during the oxidation of NiCr alloys and also in pure chromium. Interestingly, similar evolution of the Cr 2$p$ XPS spectrum with oxidation time has been also reported for both systems [6], [45], displaying a splitting of the Cr $2p_{3/2}$ envelope for thick layers.

The growth stresses and relaxation mechanisms relate closely to the detailed mechanism of oxide growth. As shown in **Section 3.3**, for α-$Cr_2O_3$ grown epitaxially on $Al_2O_3$ (0001) (or α-$Fe_2O_3$ buffer), the strain energy accumulates rapidly with film thickness due to the lattice mismatch. This system undergoes strain relief by nucleating misfit dislocations and relaxes completely up to few nanometers. However, for polycrystalline $Cr_2O_3$ grown by Ni30Cr oxidation, the residual stress is a complex summation of growth stresses and thermal stresses. The system relaxes via creep and the critical thickness depends on the growth kinetics and the microstructure of chromia scales [39], [44]. In this study, a relaxed chromium oxide layers upon Ni30Cr oxidation were found at tens of nanometers.

Whatever the microstructure (*i.e.* MBE layers [3], [5], oxidation layers [45] or polycrystalline powder [46]), well-defined splitting of Cr $2p_{3/2}$ XPS envelope is often observed in "relaxed" α-$Cr_2O_3$. More importantly, it coincides to a fully degeneracy of $e$ and $a_1$ orbitals according to CFM simulations

[29] Ni30Cr has a tetragonal crystal structure described by the space group I4/mmm with a = 0.435 nm [37], [38], which imposes in-plane lattice mismatch of about 13% to the oxide layer.

established in this work, with Dτ value of about -0.27 eV. Therefore, this particular spectral shape of the Cr $2p_{3/2}$ XPS envelope can be considered as a fingerprint of relaxed $CrO_6$ octahedra in α-$Cr_2O_3$.

## 3.7 Summary of results

In this chapter, the influence of epitaxial strain on the electronic structure of α-$Cr_2O_3$(0001) thin films was probed by combining X-ray photoemission spectroscopy and crystal field multiplet calculations. Herein, multiplet features of Cr $2p_{3/2}$ envelope were interpreted in the light of deformations in the $CrO_6$ octahedron. In general, in-plane lattice strain introduces distortions in the $CrO_6$ octahedron and splits the $3d$ orbital triplet $t_{2g}$ into $e$ and $a_1$ orbitals. For relaxed thin films, the lines-shape of the Cr $2p$ core levels are well reproduced when the $t_{2g}$ subset is fully degenerated. In-plane tensile strain stabilizes $a_1$ with respect to $e$ orbitals, whereas compressive strain destabilizes $a_1$ orbitals. A quantitative relation was drawn between the energy splitting between $e$ and $a_1$ orbitals (δ) extracted from experimental XPS spectra and the residual strain determined using a diffraction method. This methodology proved to be very useful in understanding the crystal field variations with strain, which is essential for tuning the physical properties of α-$Cr_2O_3$ thin films.

It is important to highlight that the combination of XPS data with CFM calculations is a very powerful, but poorly explored approach that provides in one measurement not only chemical, but also structural information for $Cr_2O_3$ thin films. For instance, similar evolution of the XPS spectra has also been reported for α-$Cr_2O_3$ epitaxial films growing on Pt(111) [5], [47]. Yet, divergent interpretations were given for the XPS spectra, mainly provided by electron diffraction patterns (LEED or RHEED) of the initial stages of growth. Zhang *et al.* [47] suggested that a metastable cubic spinel $Cr_3O_4$(111) layers composes the first stages of deposition with simultaneous presence of $Cr^{2+}$ and $Cr^{3+}$. Meanwhile, in a more recent work, Chambers and Droubay [5] interpreted the broad Cr $2p$ spectrum as being due to the formation of a metastable γ-$Cr_2O_3$ layer with $Cr^{3+}$ ions distributed among tetrahedral and octahedral sites. In this work, different explanation can be provided in light of the XPS+CFM results obtained for α-$Cr_2O_3$ grown on α-$Al_2O_3$ and α-$Fe_2O_3$ buffer. The evolution of the XPS spectra for α-$Cr_2O_3$ epitaxial films on Pt(111) may be also related to in-plane strain generated by the compressive misfit of 2%, which gently decreases with growth.

Using XPS+CMF simulation, one was also able to revisit the microstructure of α-$Cr_2O_3$ polycrystalline layers grown during the oxidation of a commercial chromium-forming alloy. Herein, one evidenced that (*i*) an in-plane strain does exist in α-$Cr_2O_3$ layer up to thickness of 8.1 nm; (*ii*) α-$Cr_2O_3$ crystallite shows a preferential orientation along the c-axis in the hexagonal setting; and (*iii*) there is a compressive strain relaxation with thickening.

Although promising, the XPS+CFM methodology shows more limitations in describing the spectrum of polycrystalline samples. Since several local structures are found for $Cr_2O_3$ crystallites, the spectra are wider and consequently the parameter fit is less reliable. For instance, a reasonably good fit (residual sum of squares (RSS) equals to 0.5) for the 8.1 nm thick layer (or 9 minutes upon oxidation) could be found for this sample either under compression (Dτ = -0.325 ± 0.001 eV) or under tension (Dτ = -0.250 ± 0.005 eV). The criteria used to differentiate the quality between the

different fits were the position and the intensity ratio between the two most intense multiplet peaks at low-binding energy (peak A and B, **Figure 3.10**). Contrary to the fit with $D\tau$ = -0.325 eV, the fit in tension described well the shoulder at high-energy part (peak C at ~577 eV) in expense of a worse description of the position and the intensity ratio between peak A and B.

Even though parameter fitting for extreme cases (highly tensioned or highly compressed polycrystalline films) is ambiguous, one can broadly state that the shape and features of the Cr $2p_{3/2}$ XPS measured in $\alpha$-$Cr_2O_3$ can be used as structural tool when combined with CFM calculations. Such approach is very convenient since it calls only for XPS measurements and calculations with low computational cost.

## 3.8 References

[1] L. Marchetti, F. Miserque, S. Perrin, and M. Pijolat, "XPS study of Ni-base alloys oxide films formed in primary conditions of pressurized water reactor," *Surface and Interface Analysis*, vol. 47, no. 5, pp. 632–642, May 2015.

[2] V. Maurice, G. Despert, S. Zanna, P. Josso, M.-P. Bacos, and P. Marcus, "XPS study of the initial stages of oxidation of α2-Ti3Al and γ-TiAl intermetallic alloys," *Acta Materialia*, vol. 55, no. 10, pp. 3315–3325, Jun. 2007.

[3] S. A. Chambers, Y. Liang, and Y. Gao, "Noncommutative Band Offset at $\alpha$-$Cr_2O_3$/$\alpha$-$Fe_2O_3$(0001) Heterojunctions," *Physical Review B*, vol. 61, pp. 13223–13229, 2000.

[4] C. Palacio, H. J. Mathieu, and D. Landolt, "AES, XPS and EELS study of the initial oxidation of polycrystalline chromium," *Surface Science*, vol. 182, pp. 41–55, 1987.

[5] S. A. Chambers and T. Droubay, "Role of oxide ionicity in electronic screening at oxide/metal interfaces," *Physical Review B*, vol. 64, no. 7, Jul. 2001.

[6] L. Bataillou *et al.*, "Growth Kinetics and Characterization of Chromia Scales Formed on Ni–30Cr Alloy in Impure Argon at 700 °C," *Oxidation of Metals*, Feb. 2020.

[7] M. C. Biesinger, B. P. Payne, A. P. Grosvenor, L. W. M. Lau, A. R. Gerson, and R. St. C. Smart, "Resolving surface chemical states in XPS analysis of first row transition metals, oxides and hydroxides: Cr, Mn, Fe, Co and Ni," *Applied Surface Science*, vol. 257, no. 7, pp. 2717–2730, Jan. 2011.

[8] A. Bumajdad, S. Al-Ghareeb, M. Madkour, and F. A. Sagheer, "Non-noble, efficient catalyst of unsupported $\alpha$-$Cr_2O_3$ nanoparticles for low temperature CO Oxidation," *Scientific Reports*, vol. 7, no. 1, p. 14788, Nov. 2017.

[9] M. C. Biesinger, C. Brown, J. R. Mycroft, R. D. Davidson, and N. S. McIntyre, "X-ray photoelectron spectroscopy studies of chromium compounds," *Surface and Interface Analysis*, vol. 36, no. 12, pp. 1550–1563, Dec. 2004.

[10] R. P. Gupta and S. K. Sen, "Calculation of multiplet structure of core p -vacancy levels. II," *Physical Review B*, vol. 12, no. 1, pp. 15–19, Jul. 1975.

[11] S. A. Chambers, "Epitaxial growth and properties of thin film oxides," *Surface Science Reports*, no. 39, pp. 105–180, 2000.

[12] R. E. Newnham and Y. M. Haan, "Refinement of the α-$Al_2O_3$, $Ti_2O_3$, $V_2O_3$ and $Cr_2O_3$ structures," *Zeitschrift für Kristallographie*, no. 117, pp. 235–237, 1962.

[13] S. Gota, E. Guiot, M. Henriot, and M. Gautier-Soyer, "Atomic-oxygen-assisted MBE growth of α-$Fe_2O_3$ on α-$Al_2O_3$(0001): Metastable FeO(111)-like phase at subnanometer thicknesses," *Physical Review B*, vol. 60, p. 14387, 1999.

[14] A. Barbier *et al.*, "Dislocation network driven structural relaxation in hematite thin films," *Materials Science and Engineering: B*, vol. 144, no. 1–3, pp. 19–22, Nov. 2007.

[15] A. Barbier *et al.*, "Electronic and crystalline structure, morphology, and magnetism of nanometric $Fe_2O_3$ layers deposited on Pt(111) by atomic-oxygen-assisted molecular beam epitaxy," *Physical Review B*, vol. 72, no. 24, Dec. 2005.

[16] T. Fujii, D. Alders, F. C. Voogt, T. Hibma, B. T. Thole, and G. A. Sawatzky, "In situ RHEED and XPS studies of epitaxial thin α-$Fe_2O_3$(0001) films on sapphire," *Surface Science*, vol. 366, no. 3, pp. 579–586, 1996.

[17] F. Spaepen, "Interfaces and stresses in thin films," *Acta Materialia*, vol. 48, pp. 31–42, 2000.

[18] E. Ünveren, E. Kemnitz, S. Hutton, A. Lippitz, and W. E. S. Unger, "Analysis of highly resolved x-ray photoelectron Cr 2*p* spectra obtained with a $Cr_2O_3$ powder sample prepared with adhesive tape," *Surface and Interface Analysis*, vol. 36, no. 1, pp. 92–95, Jan. 2004.

[19] M. Aronniemi, J. Sainio, and J. Lahtinen, "Chemical state quantification of iron and chromium oxides using XPS: the effect of the background subtraction method," *Surface Science*, vol. 578, no. 1–3, pp. 108–123, Mar. 2005.

[20] M. G. Brik, N. M. Avram, and C. N. Avram, "Crystal field analysis of energy level structure of the $Cr_2O_3$ antiferromagnet," *Solid State Communications*, vol. 132, no. 12, pp. 831–835, Dec. 2004.

[21] Y. Tanabe and S. Sugano, "On the absorption spectra of complex ions. I," *Journal of the Physical Society of Japan*, vol. 9, no. 5, pp. 753–766.

[22] Y. Tanabe, M. Muto, and E. Hanamura, "Theory of nonlinear optical susceptibilities of antiferromagnetic $Cr_2O_3$," *Solis State Communications*, vol. 102, no. 9, pp. 643–646, 1997.

[23] M. O. J. Y. Hunault *et al.*, "Direct Observation of $Cr^{3+}$ 3*d* States in Ruby: Toward Experimental Mechanistic Evidence of Metal Chemistry," *The Journal of Physical Chemistry A*, vol. 122, no. 18, pp. 4399–4413, May 2018.

[24] E. Konig and S. Kremer, *Ligand field: energy diagrams*. New York: Plenum Press, 1977.

[25] V. Vercamer *et al.*, "Calculation of optical and K pre-edge absorption spectra for ferrous iron of distorted sites in oxide crystals," *Physical Review B*, vol. 94, no. 24, pp. 245115-1-245115–15, Dec. 2016.

[26] A. Juhin *et al.*, "X-ray linear dichroism in cubic compounds: The case of $Cr^{3+}$ in $MgAl_2O_4$," *Physical Review B*, vol. 78, no. 19, pp. 1–19, Nov. 2008.

[27] S. K. Kang, H. Tang, and T. A. Albright, "Structures for $d^0$ $ML_6$ and $ML_5$ complexes," *Journal of the American Chemical Society*, vol. 115, no. 5, pp. 1971–1981, Mar. 1993.

[28] T. C. Kaspar *et al.*, "Impact of lattice mismatch and stoichiometry on the structure and bandgap of $(Fe,Cr)_2O_3$ epitaxial thin films," *Journal of Physics: Condensed Matter*, vol. 26, no. 13, p. 135005, Apr. 2014.

[29] S. Mu and K. D. Belashchenko, "Influence of strain and chemical substitution on the magnetic anisotropy of antiferromagnetic $Cr_2O_3$: An *ab-initio* study," *Physical Review Materials*, vol. 3, no. 3, Mar. 2019.

[30] T. Nozaki and M. Sahashi, "Magnetoelectric manipulation and enhanced operating temperature in antiferromagnetic $Cr_2O_3$ thin film," *Japanese Journal of Applied Physics*, vol. 57, no. 9, p. 0902A2, Sep. 2018.

[31] N. Shimomura, S. P. Pati, T. Nozaki, T. Shibata, and M. Sahashi, "Enhancing the blocking temperature of perpendicular-exchange biased $Cr_2O_3$ thin films using buffer layers," *AIP Advances*, vol. 7, no. 2, p. 025212, Feb. 2017.

[32] T. Nozaki *et al.*, "Large perpendicular exchange bias and high blocking temperature in Al-doped $Cr_2O_3$/Co thin film systems," *Applied Physics Express*, vol. 10, no. 7, p. 073003, Jul. 2017.

[33] W. H. Blades and P. Reinke, "From Alloy to Oxide: Capturing the Early Stages of Oxidation on Ni–Cr(100) Alloys," *ACS Applied Materials & Interfaces*, vol. 10, no. 49, pp. 43219–43229, Dec. 2018.

[34] L. Luo *et al.*, "In situ atomic scale visualization of surface kinetics driven dynamics of oxide growth on a Ni–Cr surface," *Chemical Communications*, vol. 52, no. 16, pp. 3300–3303, 2016.

[35] S.-P. Jeng, P. H. Holloway, and C. D. Batich, "Surface passivation of Ni/Cr alloy at room temperature," *Surface Science*, vol. 227, no. 3, pp. 278–290, Mar. 1990.

[36] J.-C. Dupin, D. Gonbeau, P. Vinatier, and A. Levasseur, "Systematic XPS studies of metal oxides, hydroxides and peroxides," *Physical Chemistry Chemical Physics*, vol. 2, no. 6, pp. 1319–1324, 2000.

[37] D. Connetable, M. Mathon, and J. Lacaze, "First principle energies of binary and ternary phases of the Fe-Nb-Ni-Cr system," *Computer coupling of phase diagrams and thermochemistry*, vol. 35, pp. 588–593, 2011.

[38] A. V. Progrushchenko and Yu. M. Lebedev, "X-ray stuy of heat expansion of nickel-chromium alloys," *Ukrains'kii Fizichnii Zhurnal (Russian Edition*, vol. 14, pp. 282–286, 1969.

[39] S. J. Bull, "Modeling of Residual Stress in Oxide Scales," *Oxidation of Metals*, vol. 49, p. 17, 1998.

[40] M. Kemdehoundja, J. F. Dinhut, J. L. Grosseau-Poussard, and M. Jeannin, "High temperature oxidation of Ni70Cr30 alloy: Determination of oxidation kinetics and stress evolution in chromia layers by Raman spectroscopy," *Materials Science and Engineering: A*, vol. 435–436, pp. 666–671, Nov. 2006.

[41] M. Guerain *et al.*, "Residual stress determination in oxide layers at different length scales combining Raman spectroscopy and X-ray diffraction: Application to chromia-forming metallic alloys," *Journal of Applied Physics*, vol. 122, no. 19, p. 195105, Nov. 2017.

[42] M. Guerain *et al.*, "Stress release in $\alpha$-$Cr_2O_3$ oxide thin films formed on Ni30Cr and Fe47Cr alloys," *Journal of Alloys and Compounds*, vol. 718, pp. 223–230, 2017.

[43] L. Latu-Romain *et al.*, "Duplex n- and p-Type Chromia Grown on Pure Chromium: A Photoelectrochemical and Microscopic Study," *Oxidation of Metals*, vol. 86, no. 5–6, pp. 497–509, Dec. 2016.

[44] B. Panicaud *et al.*, "Stress determination in a thermally grown oxide on Ni38Cr alloy by use of micro/nanogauge gratings," *Materials Science and Engineering: A*, vol. 812, p. 141079, 2021.

[45] J.-T. Li *et al.*, "XPS, time-of-flight-SIMS and polarization modulation IRRAS study of Cr2O3 thin film materials as anode for lithium ion battery," *Electrochimica Acta*, vol. 54, no. 14, pp. 3700–3707, May 2009.

[46] B. P. Payne, M. C. Biesinger, and N. S. McIntyre, "X-ray photoelectron spectroscopy studies of reactions on chromium metal and chromium oxide surfaces," *Journal of Electron Spectroscopy and Related Phenomena*, vol. 184, no. 1–2, pp. 29–37, Feb. 2011.

[47] L. Zhang, M. Kuhn, and U. Diebold, "Growth, structure and thermal properties of chromium oxide films on Pt(111)," *Surface Science*, vol. 375, no. 1, pp. 1–12, Mar. 1997.

# Chapter 4:

# Chemical and structural characterization of $Fe_{3-x}Cr_xO_4$ thin films

The second part of this PhD thesis is a comprehensive study of the effects of substitutional Cr on the **structural** and **chemical** properties of high quality **$Fe_{3-x}Cr_xO_4$ epitaxial thin films**. First, particular features of the growth on sapphire substrates are shown, including the **optimal growth conditions** to obtain films of high crystalline quality. To prove the film **quality**, a complete structural and microstructural characterization is carried out. Then, complete chemical and fine structure investigations are performed by means of various spectroscopic methods. Herein, information on **nominal composition**, **cation redox** and **cationic disorder** are highlighted. **Distortions** on the cation local environments caused by the Cr insertion in the spinel structure are also evidenced. Emphasis is placed on the **crystal field multiplet parameters** used in the **simulation of core level spectra** to obtain the cationic site distribution.

# 4.1 Epitaxial growth of $Fe_{3-x}Cr_xO_4$ thin films

Stoichiometric series of epitaxial $Fe_{3-x}Cr_xO_4(111)$ thin films were grown on monocrystalline $\alpha$-$Al_2O_3(0001)$ substrates by oxygen-plasma-assisted molecular beam epitaxy (O-MBE). The growth of this series was inspired by the growth of $Fe_3O_4(111)$ previously-optimized [1]–[3] in my host laboratory (SPEC/LNO). Prior to the deposition, the substrates were cleaned in a $H_2O_2/NH_4OH/H_2O$ solution and then *in situ* through exposure to the oxygen plasma, for the same reasons as explained in **Section 3.2** (*i.e.* growth of $Cr_2O_3$). **Table 4.1** summarizes optimized growth conditions of the main compositions treated in this work. During deposition, the residual pressure was about $10^{-7}$ mbar inside the ultrahigh-vacuum growth chamber, while the sample holder temperature was fixed to about 723 K. The metal evaporation rates were calibrated *in situ* using a quartz balance. As empirically demonstrated [1]–[3] global evaporation rate (oxygen + metal) of around one or two angstrom per minute is ideal for 2D growth mode in this setup. Therefore, I looked for the minimum evaporation rate of Fe that would induce the growth of the spinel phase, so that I could later add Cr and still get films of high crystalline quality. For $Fe_3O_4$, Fe evaporation rate was set to ~0.35 Å.min$^{-1}$. Optimal plasma conditions were achieved under a molecular oxygen pressure ($P_{O_2,plasma}$) of 0.22 Torr inside the quartz cavity, activated by a radio-frequency power of 350 W.

In order to control the crystalline structure of the oxide formed during deposition, RHEED patterns were acquired in real time with the beam aligned parallel to $[10\bar{1}0]$ and $[1\bar{1}00]$ azimuths and, therefore, probing respectively the so-called $D_1$ and $D_2$ directions. **Figure 4.1** depicts the evolution of RHEED images during the first 60 minutes of $Fe_3O_4$ growth[30]. At the very beginning, the RHEED patterns show diffraction spots and Kikuchi lines exactly like the substrate (see **Section 2.2.1**).

**Table 4.1** – Optimal experimental O-MBE conditions for the growth of $Fe_{3-x}Cr_xO_4(111)$ thin films on $\alpha$-$Al_2O_3(0001)$ substrate.

| Layer | Substrate temperature (K) | Residual pressure (mbar) | Fe evaporation rate (Å.min$^{-1}$) | Cr evaporation rate (Å.min$^{-1}$) | $P_{O_2,plasma}$ (Torr) |
|---|---|---|---|---|---|
| **$Fe_3O_4$** | 723 ± 10 | $10^{-7}$ | 0.35 ± 0.02 | 0 | 0.220 ± 0.001 |
| **$Fe_{2.8}Cr_{0.2}O_4$** | 723 ± 10 | $10^{-7}$ | 0.35 ± 0.02 | 0.05 ± 0.02 | 0.220 ± 0.001 |
| **$Fe_{2.5}Cr_{0.5}O_4$** | 723 ± 10 | $10^{-7}$ | 0.35 ± 0.02 | 0.12 ± 0.02 | 0.220 ± 0.001 |
| **$Fe_{2.3}Cr_{0.7}O_4$** | 723 ± 10 | $10^{-7}$ | 0.35 ± 0.02 | 0.21 ± 0.02 | 0.240 ± 0.001 |
| **$Fe_{1.8}Cr_{1.2}O_4$** | 723 ± 10 | $10^{-7}$ | 0.35 ± 0.02 | 0.32 ± 0.02 | 0.240 ± 0.001 |
| **$Fe_{1.6}Cr_{1.4}O_4$** | 723 ± 10 | $10^{-7}$ | 0.35 ± 0.02 | 0.38 ± 0.02 | 0.240 ± 0.001 |
| **$Fe_{1.3}Cr_{1.7}O_4$** | 723 ± 10 | $10^{-7}$ | 0.35 ± 0.02 | 0.44 ± 0.02 | 0.240 ± 0.001 |

[30] It takes about 180 minutes to grow 15 nm thick films under these experimental conditions.

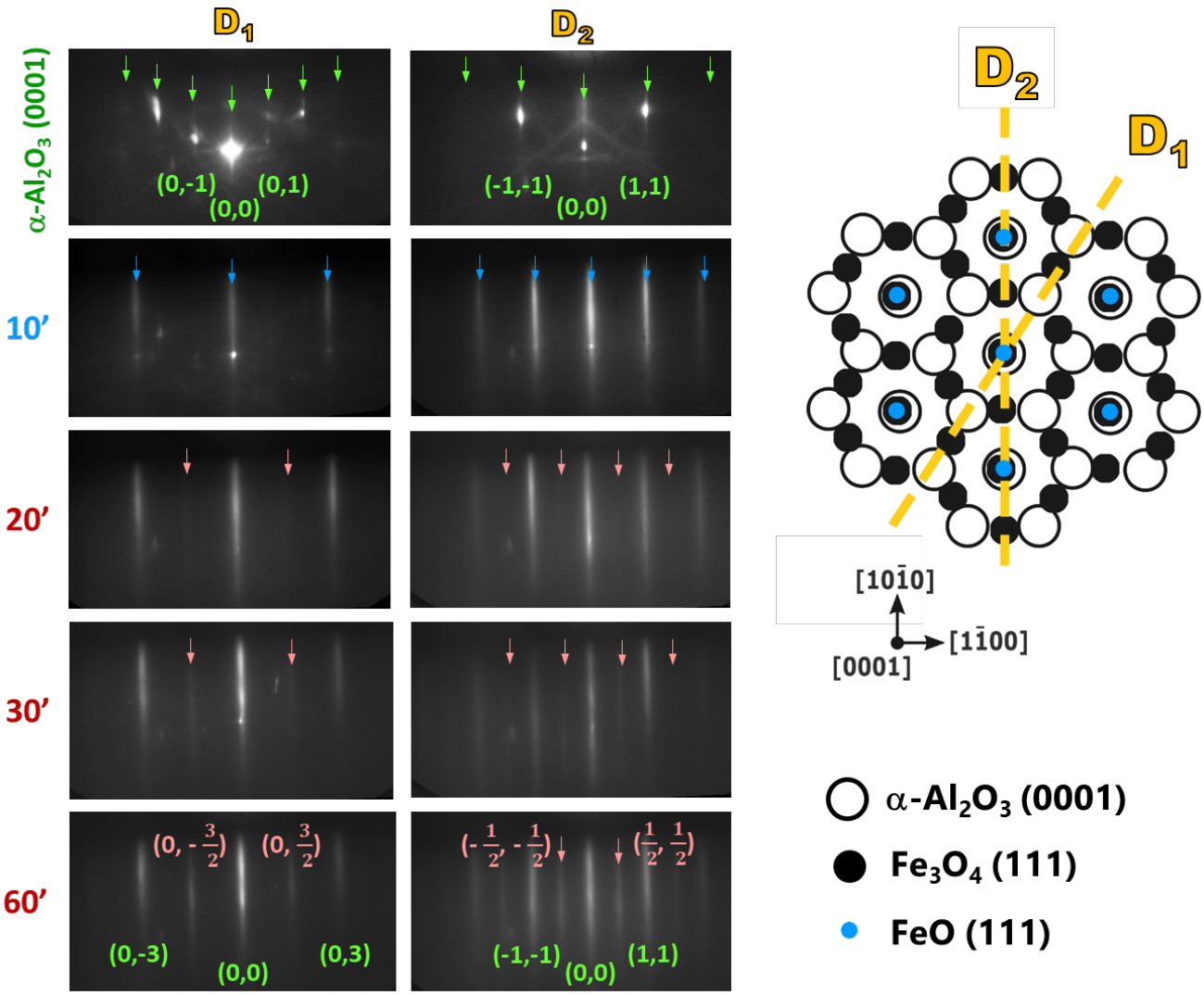


**Figure 4.1.** At left, RHEED patterns recorded during growth of 15 nm thick $Fe_3O_4$(111) on α-$Al_2O_3$(0001) substrate. The patterns were recorded along the $[10\bar{1}0]$ and $[1\bar{1}00]$ directions (assigned in the hexagonal real space of the substrate), probing respectively $D_1$ and $D_2$ directions. At right, schema of the reciprocal lattices of different iron oxides and sapphire. White circles correspond to the corundum (0001) termination of α-$Al_2O_3$ (or α-$Fe_2O_3$). Black circles (*i.e.* (0, 3/2) and (1/2, 1/2) rods and equivalents) correspond to the inverse spinel (111) termination of $Fe_3O_4$ (or γ-$Fe_2O_3$). Small blue circles (*i.e.* (0,3) and (1,1) rods and equivalents) correspond to the fcc (111) termination of FeO, which coincides with the oxygen sublattice common to all the consider oxides. In this representation, lattice parameter differences are not considered.

After 10 minutes, the (0,1) and (0,2)-type rods completely disappear and just (0,3)-type rods remain in direction $D_1$, while all (1,1)-type rods are reinforced in $D_2$. These rods correspond to (0,1) and (1,1) plans of a face-centered cubic (fcc) lattice and, therefore, suggest the formation of the thermodynamically unstable phase FeO on the initial stages of (111) growth. The parametric disagreement of this phase is higher (~14%) than the one expected (~10%) for FeO grown on α-$Al_2O_3$(0001). Thus, this initial dilated phase is probably a 8×8 coincidence lattice [3, p. 43], which persist for the first 20 minutes (~4 monolayers) into the $Fe_3O_4$ growth. Then, additional (0, 3/2) and (1/2, 1/2)-type rods (pink arrows in **Figure 4.**) representative of the spinel (111) termination appears in direction $D_1$ and $D_2$, respectively. During growth, these intermediate rods persist and intensify, so

the film maintains a spinel structure with a 2D growth mode. For a 15 nm thick $Fe_3O_4$, the RHEED patterns have sharp diffraction streaks and no spots, as depicted in **Figure 4.2** (top).

For the growth of the $Fe_{3-x}Cr_xO_4$ series, the evaporation rate of Fe was kept to 0.35 Å.min$^{-1}$, while the one of Cr steadily varied from 0.05 to 0.45 Å.min$^{-1}$ in order to adjust the composition. Although the Fe:Cr evaporation ratio increased linearly with the Fe:Cr atomic ratio, this parameter can only be used as a first guess of the composition. The uniformity in composition and in thickness of films grown by MBE depends not only on the uniformities of the beam fluxes, but also on the geometrical relationship between the configurations of the sources and the substrate. Moreover, one must consider the sticking coefficients, *i.e.* the ratio between the number of atoms adhering to the substrate surface and the number of atoms arriving there, which are specie-dependent [4]. Since different species have different adsorption energies on the substrate surface and different abilities to migrate and aggregate adatoms, the composition estimated by the metal evaporation rates must be confirmed posteriorly by spectroscopic techniques (**Section 4.4**). Regarding the plasma conditions, no many changes were made; $P_{O_2,plasma}$ was slightly increased from 0.22 Torr to 0.24 Torr for higher Cr concentrations ($x \geq 0.7$). In fact, it was not feasible to increase $P_{O_2,plasma}$ value to higher than 0.25 Torr as it over oxidized the system to the corundum phase ($Fe_{2-x}Cr_xO_3$). Since the experiment was limited in atomic oxygen flux, the growth of epitaxial films with $x$ higher than 1.7 was not possible in this setup.

The RHEED patterns of the iron chromites evolved with deposition time in a manner similar to that of $Fe_3O_4$ (**Figure 4.**). In the early stages of epitaxy, an initial layer of the halite phase persisted for the first monolayers. Then, additional (0, 3/2) and (1/2, 1/2)-type rods (pink arrows) are observed in the RHEED patterns, which is typical of the spinel structure. **Figure 4.2** shows the RHEED patterns for 15-20 nm thick $Fe_{3-x}Cr_xO_4$ thin films grown on $\alpha$-$Al_2O_3$ substrates. Note that the quality of RHEED images decreases considerably with increasing chromium content. For $x < 1.4$, the RHEED patterns exhibit sharp streaks and no spots, indicating a bidimensional growth mode and layers of high crystalline quality without secondary phases. However, for $x \geq 1.4$, the RHEED images are blurred and the streaks are almost indistinguishable. In fact, the degradation of the quality of RHEED images was visible early in the growth; mere ten minutes of deposition were enough to blur completely the images (middle **Figure 4.3**).

There are some possible reasons for the reduction in crystalline quality with increasing chromium concentration. First, the higher Cr content ($x$) is achieved by increasing the Cr evaporation rate, which in turn increases the overall growth rate, and consequently, the surface roughness. As shown in **Figure 2.2**, rapid growth favors the growth of 3D islands, which is translated by spots in RHEED images. Second, it seems that the growth of the spinel phase on the corundum substrate first requires the formation of a metastable halite phase. As discussed in **Section 1.1**, the halite phase is only thermodynamically stable over a very narrow range of $x$. Because Cr does not naturally assume a 2+ oxidation state, the lack of electroneutrality in $Fe_{1-x}Cr_xO$ is compensated by introducing vacancies to the cation sublattice. Therefore, even if MBE growth occurs outside of thermodynamic equilibrium, a highly Cr-concentrated halite phase is not very likely.

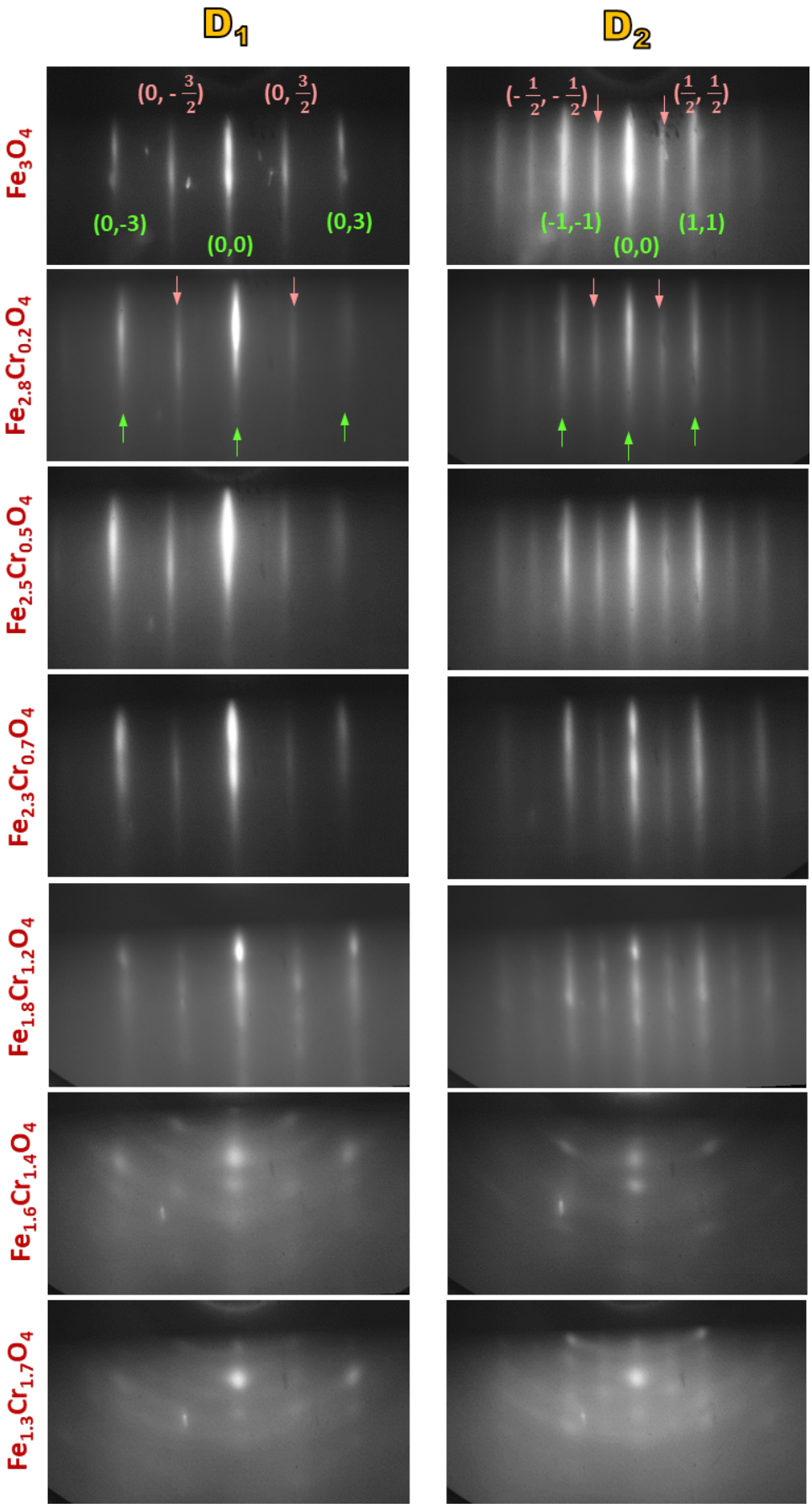


**Figure 4.2.** RHEED patterns of 15-20 nm thick $Fe_{3-x}Cr_xO_4(111)$ thin films recorded along the $[10\bar{1}0]$ ($D_1$) and $[1\bar{1}00]$ ($D_2$) directions.

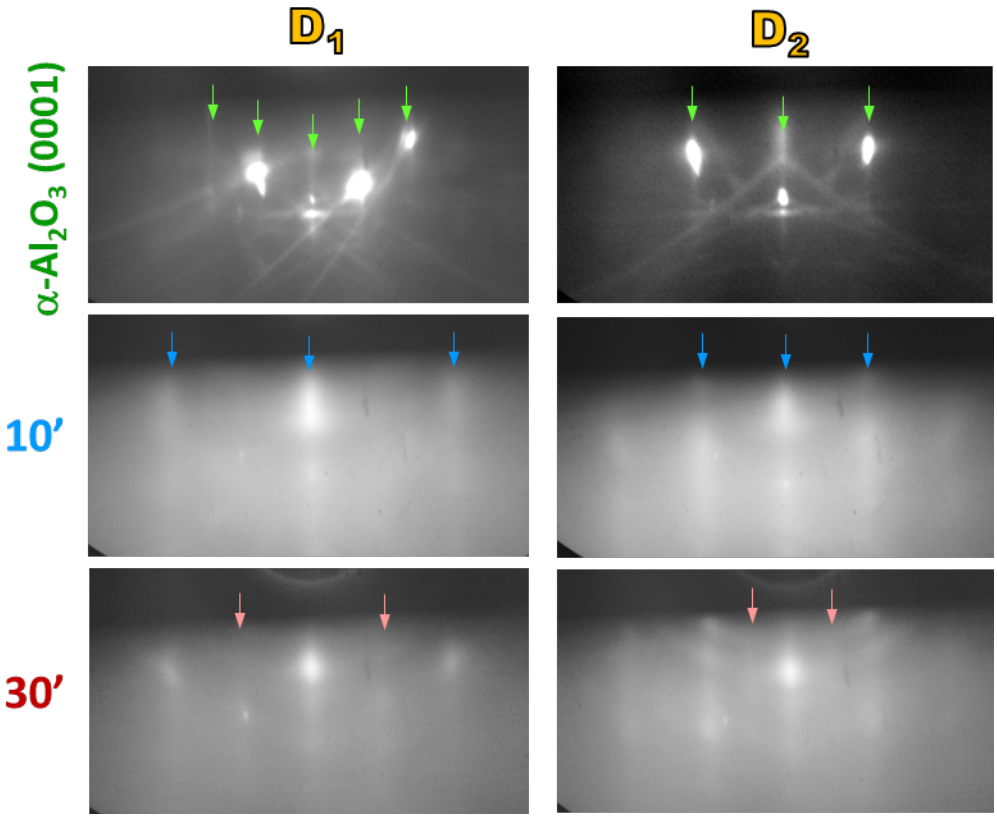


**Figure 4.3.** RHEED patterns recorded during growth of 15 nm thick $Fe_{1.7}Cr_{1.3}O_4(111)$ on $\alpha$-$Al_2O_3(0001)$ substrate. The patterns were recorded along the $[10\bar{1}0]$ and $[1\bar{1}00]$ directions (assigned in the hexagonal real space of the substrate), probing respectively $D_1$ and $D_2$ directions.

Despite the difficulties in synthesizing films with high Cr content, very good epitaxy is still found for a wide range of compositions. At first glance, this is surprising, since sapphire is not the substrate that seems best suited for spinel phase growth in terms of lattice mismatch. In fact, the oxygen sublattice of iron chromites are about 8% larger than that of $\alpha$-$Al_2O_3(0001)$.

Many assays were made in an attempt to improve the crystalline quality of $Fe_{3-x}Cr_xO_4$ layers with $x \geq 1.4$. As discussed in **Section 2.1**, the growth in the O-MBE setup is controlled in theory by three parameters: the substrate temperature, the metal evaporation rate and the oxygen flux. Since previous studies [1]–[3] demonstrated that ~723 K is the optimal temperature for the growth of the spinel phase on sapphire substrates, I opted to alter the metal and oxygen fluxes. However, this approach was not effective. Decreasing evaporation rate of Fe rather than increasing Cr also drove the system to the corundum phase even at low atomic oxygen flux. Moreover, the spinel phase could not be observed for any oxygen pressure deviating from the optimal value between 0.20 and 0.25 Torr. The only successful strategy found in this study was to grow 2.6 nm $Fe_3O_4(111)$ buffer in order to facilitate heteroepitaxy between the film and the substrate. In general, heteroepitaxy film quality is best when the substrate and film are of the same lattice type. **Figure 4.4** compares the RHEED patterns obtained with and without the $Fe_3O_4(111)$ buffer. A clear improvement is observed in the quality of the films that have grown on the buffer, *i.e.,* the RHEED streaks are sharper and more distinguishable. They are not, however, as well resolved as the streaks for low Cr content samples,

which means that the overall increase of growth rate is indeed a key parameter to control the surface roughness.

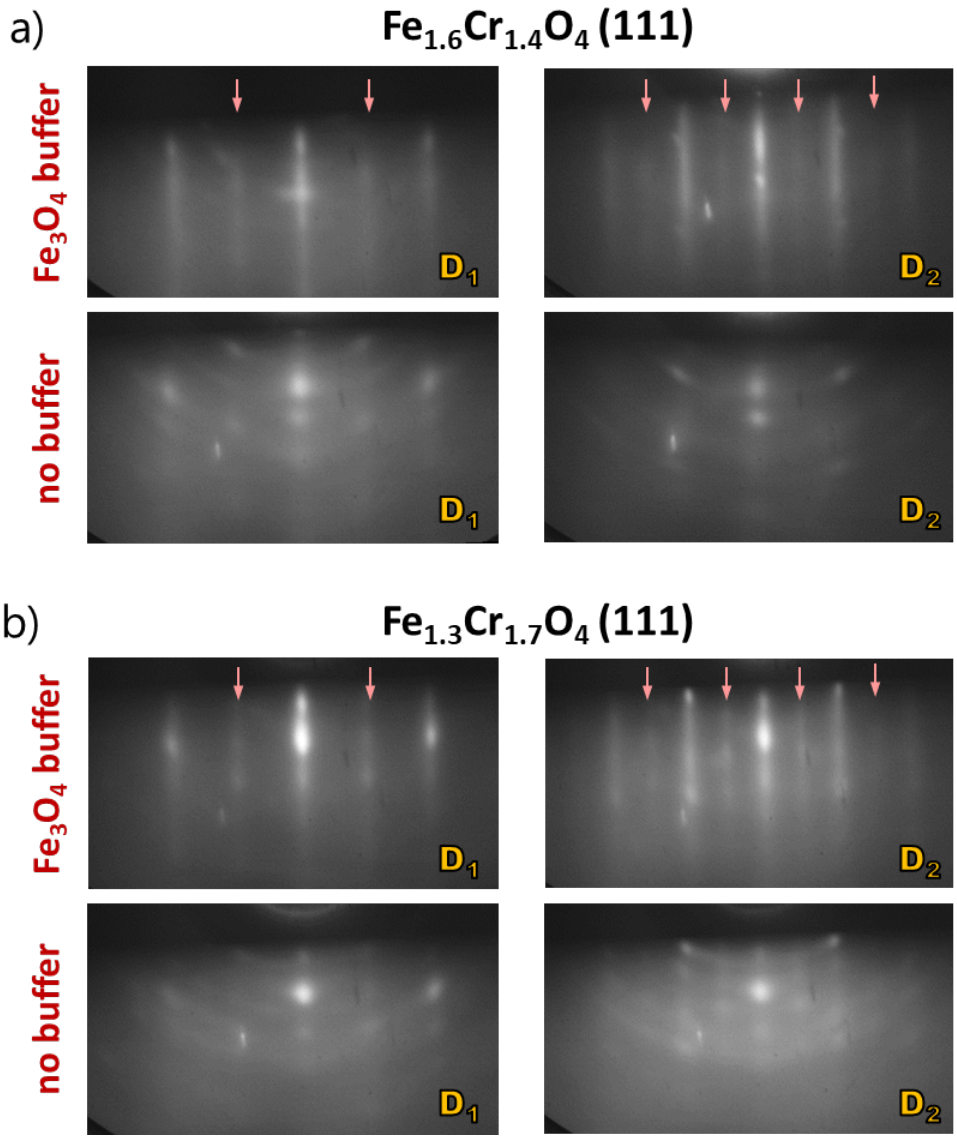


**Figure 4.4.** RHEED patterns of (a) $Fe_{1.6}Cr_{1.4}O_4$(111) and (b) $Fe_{1.3}Cr_{1.7}O_4$(111) with (top) and without (bottom) the 2.6 nm $Fe_3O_4$(111) buffer. The patterns were recorded along the $[10\bar{1}0]$ ($D_1$) and $[1\bar{1}00]$ ($D_2$) directions.

## 4.2 Structural investigation

While RHEED analysis is crucial for controlling and tracking film phase and crystalline quality during deposition, this technique is highly localized. After growth, various characterization techniques are required to confirm that the structure and single-phase nature of the films have not evolved during deposition or after exposure to air. The ensemble of *ex situ* structural measurements also provides additional information about film homogeneity, unwanted phases, and structural defects. The firsts techniques used in this study to characterize the films throughout their thicknesses were X-ray reflectivity (XRR) and diffraction (XRD).

The film thickness, roughness and density can be determined by fitting the XRR oscillations, as explained in **Section 2.2.2**. These values are shown in **Figure 4.5** (insets) for each composition. It is very important to obtain films of the same thickness when studying the effect of composition on their physical properties, since the latter are highly dependent on the former (see **Chapter 5**). Hence, the measured thicknesses were used to calibrate the growth rates and estimate the deposition times in order to obtain thicknesses ($t$) of approximately 15 nm for all films. Moreover, according to **Figure 4.5**, the fitted atomic density ($\rho$) and the X-ray scattering lengths ($f$ and $f'$) are in good agreement with theoretical values. Without structural phase transitions (*e.g.,* cubic-to-tetragonal), the atomic density and the scattering lengths for the series should be close to the magnetite values: $\rho = 1.36 \times 10^{28}$ m$^{-3}$, $f = 108.0$ fm and $f' = 9.7$ fm, respectively. For comparison's sake, these parameters for $FeCr_2O_4$ are $\rho = 1.28 \times 10^{28}$ m$^{-3}$, $f = 104.7$ fm and $f' = 8.2$ fm. Since Fe and Cr have similar standard atomic weight (55.845 and 51.996, respectively) and the spinel series have similar lattice parameters at room temperature ($a$ value varies between 0.8375 nm and 0.8410 nm, **Figure 1.5**), the series density should not evolve much with composition. Indeed, the densities in **Figure 4.5** have values around $1.3 \times 10^{28}$ m$^{-3}$ for all compositions. The same can be said for the scattering lengths, which have values around $f \cong 106$ fm and $f' = 10$ fm. Another important fitting parameter is the roughness ($\sigma$). For $x < 1.0$, the films present relatively low roughness ($\sigma \cong 0.7$ nm), which increases considerably as $x$ increases ($\sigma \cong$ 1.2-2.0 nm for $x \geq 1.2$). Note that the $Fe_3O_4$ buffer decreased $\sigma$ to values around 0.7-0.9 nm for $x \geq 1.4$, improving effectively the crystalline quality of the films, as indicated by the RHEED patterns (**Figure 4.4**).

**Figure 4.6** depicts 5 x 5 μm² AFM topographic images acquired in tapping mode comparing low and high Cr content samples. These images confirm that the film roughness increases for the latter. Prior to image acquisition, the samples were cleaned in acetone and isopropanol solution. For $x = 0.2$, the AFM image shows a homogeneous surface topography with low roughness ($\sigma_{AFM} = 0.5$ nm). However, for $x = 1.2$, several nanoscale oxide nodules are observed in the surface. In addition, a considerable overall increase in roughness ($\sigma_{AFM} = 1.0$ nm) is noticed. Note that the $\sigma$ values obtained from these images are coherent with those measured by XRR: $\sigma_{XRR} = 0.7$ nm ($x = 0.2$) and 1.2 nm ($x = 1.2$).

After probing the thicknesses and roughness of the films, $\theta$-$2\theta$ XRD measurements were performed to confirm their epitaxial nature and to obtain the out-of-plane lattice parameters ($c$). As mentioned in **Section 2.2.2**, $\alpha$-$Al_2O_3$(0001) substrates drive the growth of spinel phases toward the [111] direction, so only ($hhh$) crystallographic planes should appear in symmetrical XRD measurements. **Figure 4.7a** depicts the $\theta$-$2\theta$ XRD patterns for 15 nm thick $Fe_{2.3}Cr_{1.7}O_4$ film, where a strong diffraction peak appears at 41.7° corresponding to the (0006) plane of the substrate. The diffraction peaks of the film appear at 18.5°, 37.4° and 55.6°, which correspond to the spinel (111), (222) and (333) planes. Indeed, no planes other than the {111} plane family are observed, indicating the textured single-phase quality of these films. The same diffraction patterns were observed for all compositions with only minor variations in peak position and width. For $x < 1.4$ and for samples with buffer, the Bragg peaks are striking and the rocking curves obtained on the (222) peak (**Figure 4.7b**) are characteristic of high crystallinity ($\Delta\Omega = 0.2°$). For $x \geq 1.4$ (without buffer), however, the Bragg peaks are broader and $\Delta\Omega$ values increased to 0.3°-0.4° (not shown).

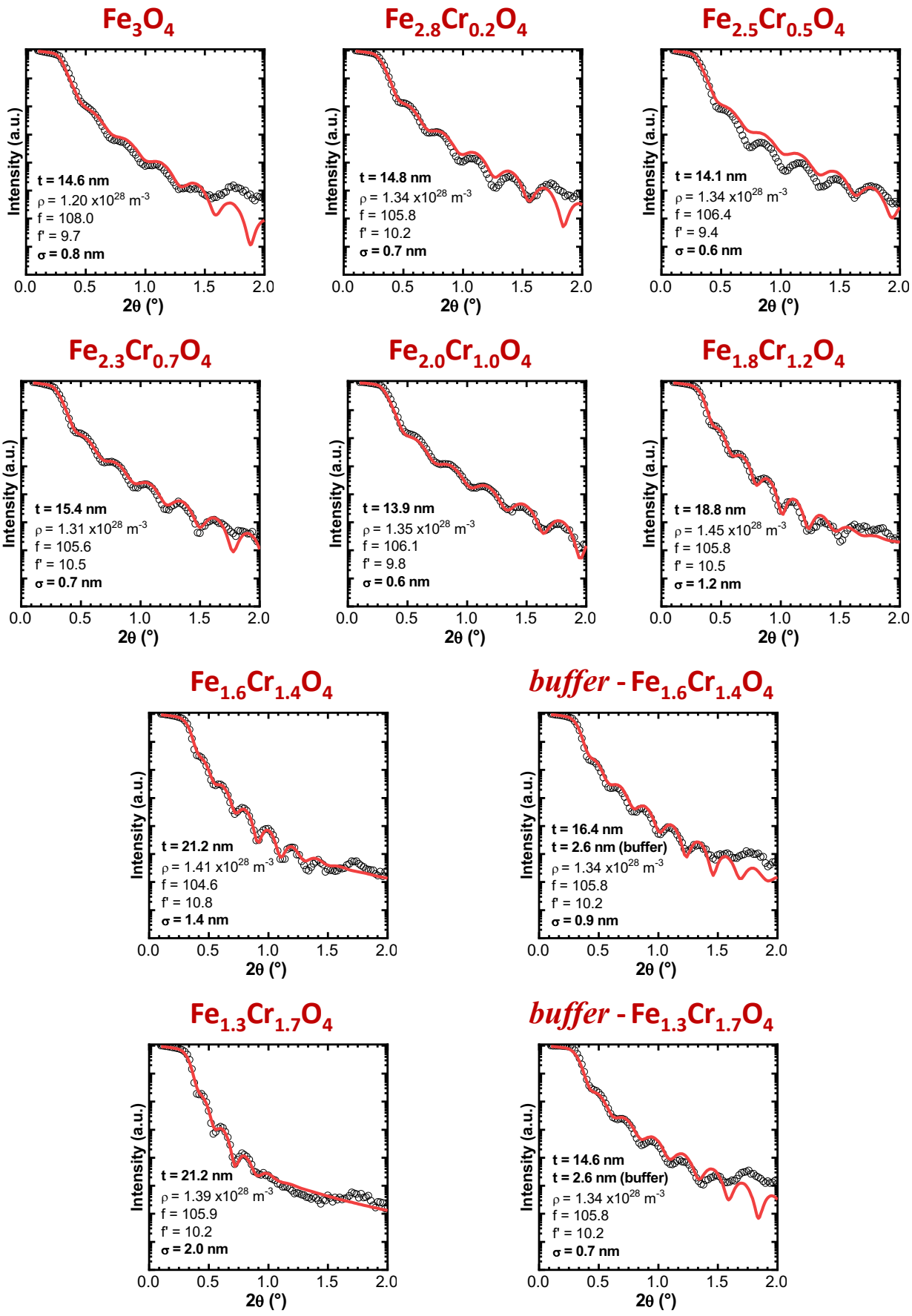


**Figure 4.5.** XRR pattern (black circles) of $Fe_{3-x}Cr_xO_4$(111) thin films. In inset, the parameters used to fit (red line) each sample: thickness ($t$), atomic density (ρ), scattering lengths ($f$ and $f'$), and roughness (σ).

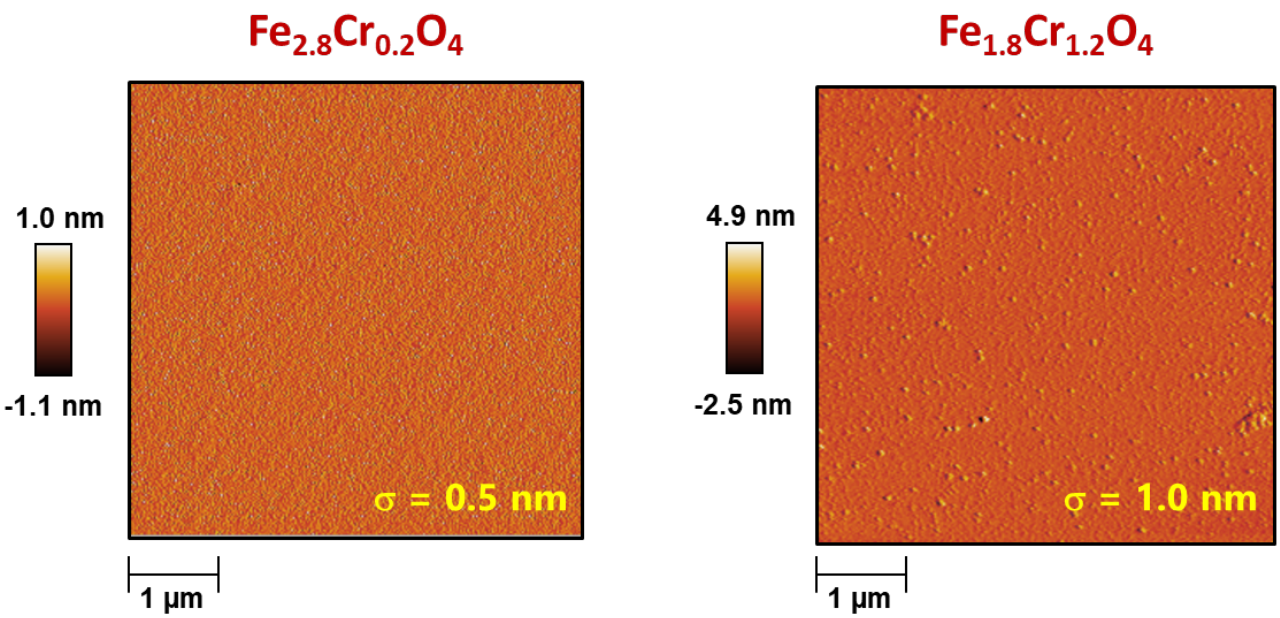


**Figure 4.6.** AFM topographic images of $Fe_{2.8}Cr_{0.2}O_4$ (left) and $Fe_{1.8}Cr_{1.2}O_4$ (right) films illustrating the increase of surface roughness (σ) as the Cr content increases.

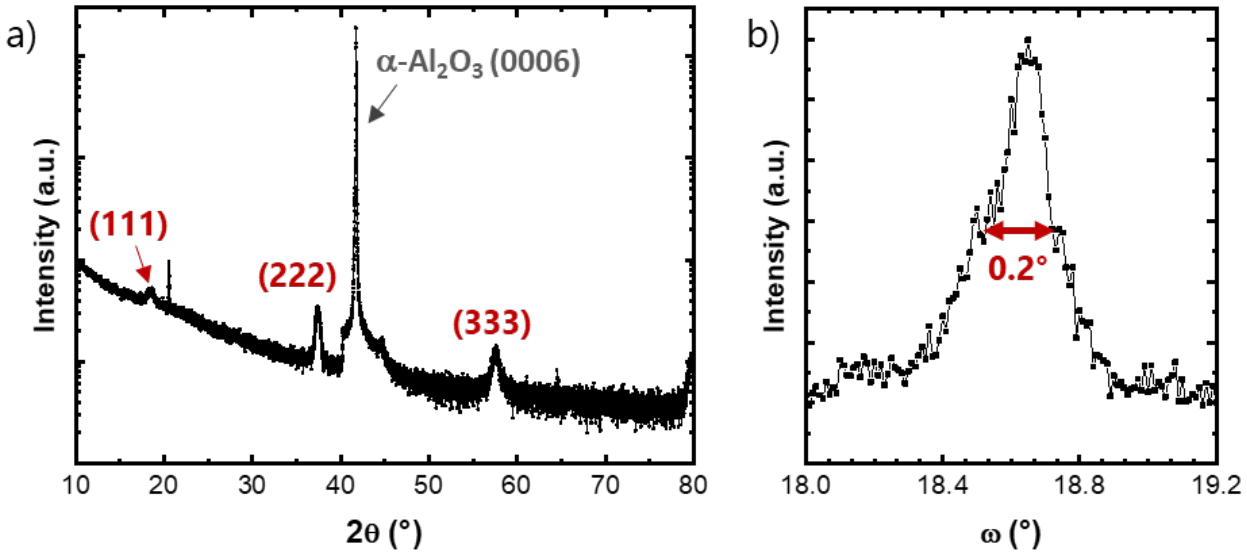


**Figure 4.7.** (a) θ–2θ XRD scan ($\lambda_{Cu}$ = 0.154 nm) for 15 nm thick $Fe_{2.3}Cr_{0.7}O_4$. The peaks at 18.5°, 37.4° and 55.6° correspond to the spinel (111), (222) and (333) planes. The intense peak at 41.7° corresponds to the (0006) Bragg peak of the sapphire substrate. (b) Rocking curve scan on the (222) peak, confirming the high crystalline quality of the film ($\Delta\Omega$ = 0.2°).

As discussed in **Section 2.2.2**, the peak width for a particular reflection is inversely proportional to the domain size. According to the Debye-Scherrer equation (Equation 2.2), the domain size corresponds to the film thickness ($D \cong 15$ nm) for all films except for $x \geq 1.4$ (without buffer). For these samples, the domain size ($D$ = 13 nm) is almost half the film thickness ($t$ = 21 nm), indicating their polycrystalline nature in depth.

For selected samples, high-resolution XRD measurements were performed on SOLEIL synchrotron. **Figure 4.8** shows a close-up view of the (222) peak of those films where the appearance of Laue oscillations reflects the structural homogeneity of the film and low density of defects. Note that the higher Cr content, the broader the Bragg peak and more indistinct are the Laue oscillations due to the decrease in film crystalline quality. These oscillations can be fitted with a Laue function (Equation 2.5) in order to determine the film thickness. For all compositions, HRXRD results are consistent with the fits of the XRR oscillations (**Figure 4.5**). Whereas the thicknesses deduced from the HRXRD measurements are $14.5 \pm 0.1$ ($x$ = 0.2), $15.1 \pm 0.1$ ($x$ = 0.7), $18.6 \pm 0.4$ ($x$ = 1.2) and $19.5 \pm 0.7$ nm ($x$ = 1.4), those deduced from XRR lab measurements are $14.8 \pm 0.2$, $15.4 \pm 0.2$, $18.8 \pm 0.2$ and $21.2 \pm 0.2$ nm, respectively. An accurate measurement of the film thickness is very important, because these values are later used in the normalization of magnetic and transport properties (**Chapter 5**).

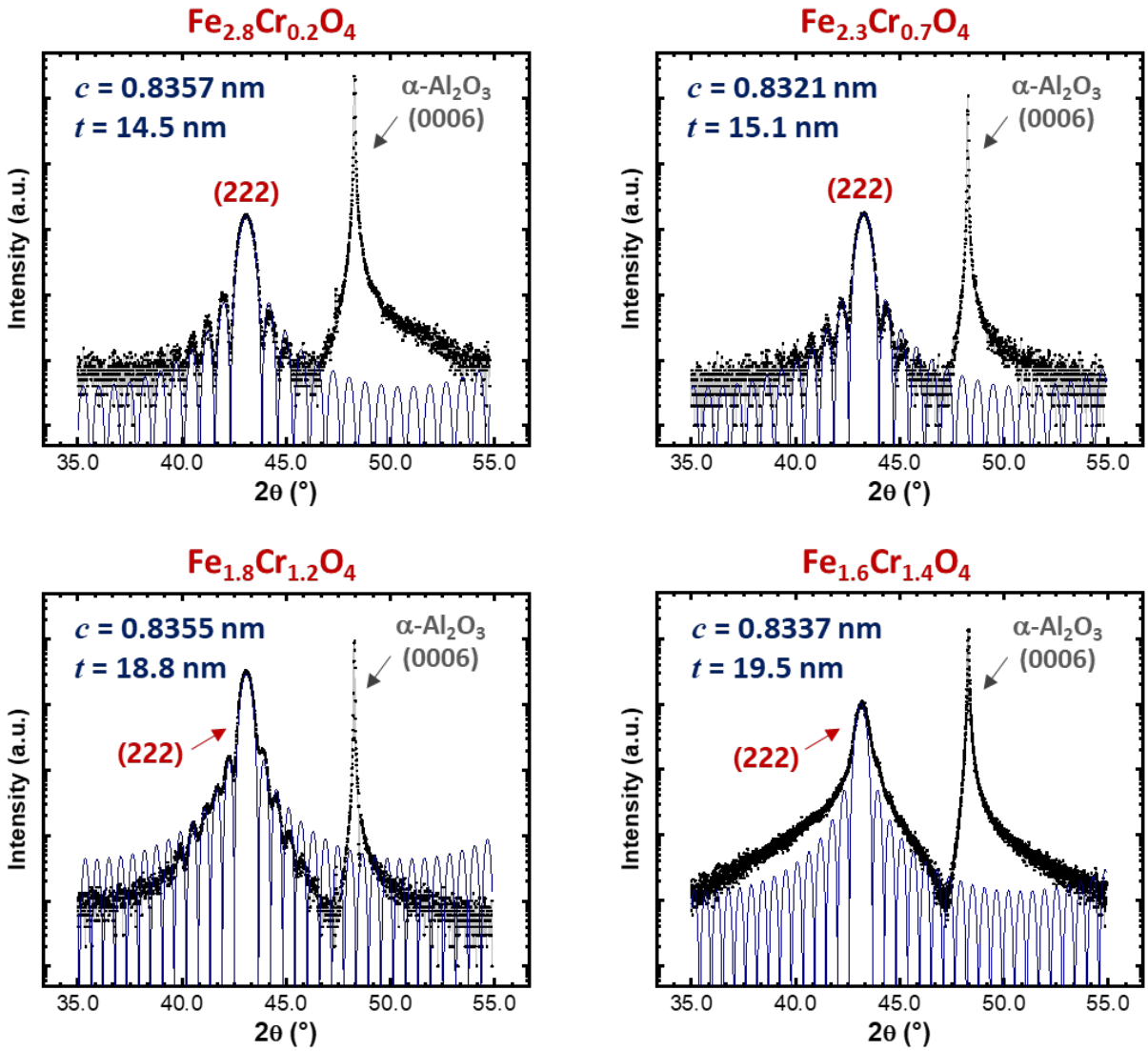


**Figure 4.8.** θ–2θ HRXRD scans (λ = 0.177 nm; 7 keV) for $Fe_{3-x}Cr_xO_4$ thin films. The intense peak at 48.3° corresponds to the (0006) Bragg peak of the sapphire substrate and the Gaussian shaped peak at 43.1° corresponds to the (222) Bragg peak of the film. The out-of-plane lattice parameter ($c$) and thickness ($t$) were determined by fitting the Laue oscillations (see Equation 2.5, **Section 2.2.2**).

The lattice parameters calculated by applying the Bragg's law (Equation 2.1) are also coherent across the different structural measures. **Figure 4.9** compares the values obtained by Gaussian fit of HRXRD peaks for films without buffer (blue circles) and XRD peaks for films with (purple circles) and without (black filled circles) buffer. Whereas the lattice parameter deduced from the HRXRD measurements are 0.8357 ± 0.0003 ($x$ = 0.2), 0.8321 ± 0.0003 ($x$ = 0.7), 0.8355 ± 0.0003 ($x$ = 1.2) and 0.8337 ± 0.0003 nm ($x$ = 1.4), those deduced from XRD lab measurements are 0.8350 ± 0.0008, 0.8321 ± 0.0008, 0.835 ± 0.002 and 0.833 ± 0.002 nm, respectively. Herein, the standard deviation of the lattice parameter increases for higher Cr content as the Bragg peaks are broader. Regarding the samples with and without the $Fe_3O_4$ buffer, the lattice parameters of 16 nm *buffer*-$Fe_{1.4}Cr_{1.6}O_4$ and 21 nm $Fe_{1.4}Cr_{1.6}O_4$ are very similar: 0.8334 ± 0.0006 nm and 0.833 ± 0.002 nm, respectively. However, the one of 15 nm *buffer*-$Fe_{1.7}Cr_{1.3}O_4$ are considerably lower (0.8298 ± 0.0008 nm) than that of 21 nm $Fe_{1.7}Cr_{1.3}O_4$ (0.833 ± 0.002 nm). This may happen because the crystal quality of the films without buffer is so poor and the Bragg peaks are so large that the XRD measurement is not accurate enough to determine the lattice parameter. However, it could also mean that the structure and/or lattice relaxation process are not the same for these films.

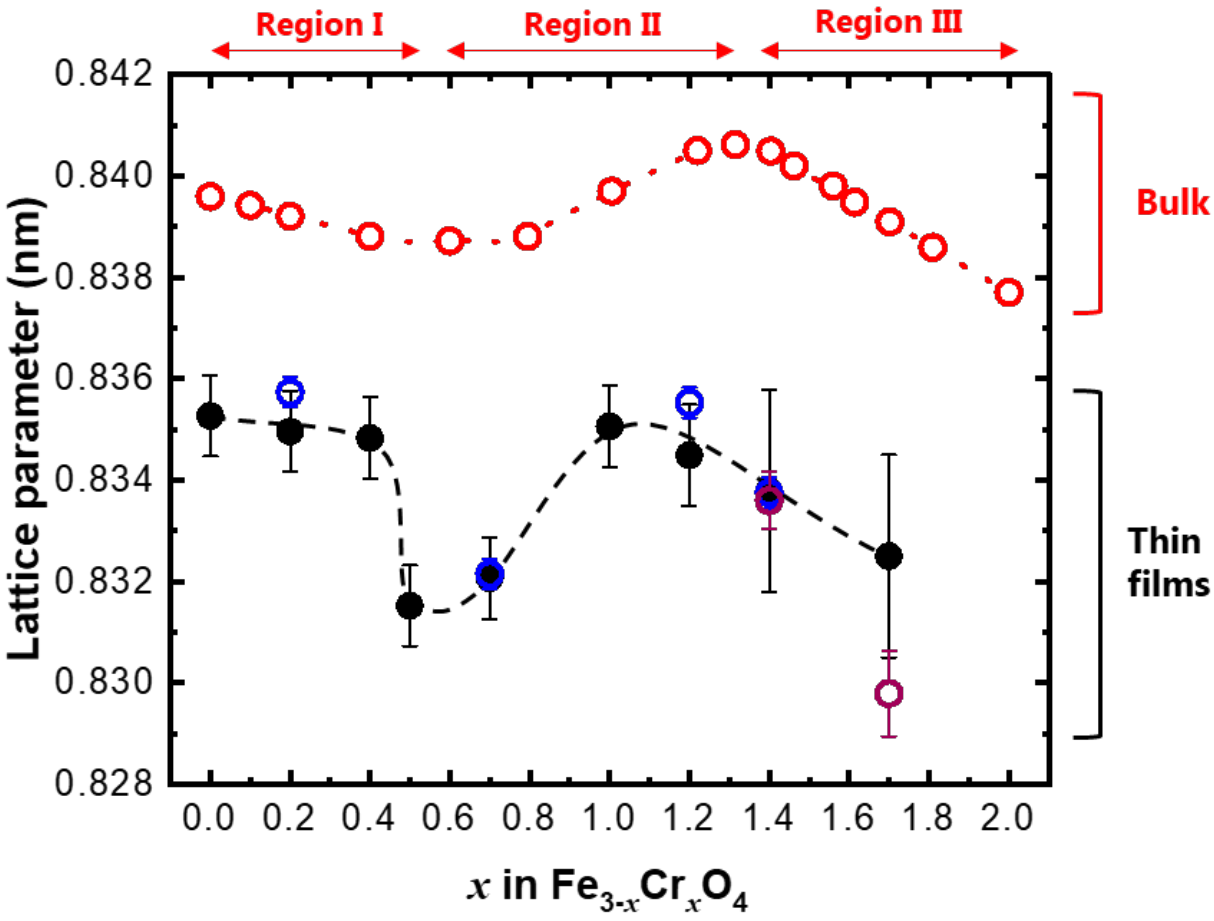


**Figure 4.9.** Room temperature lattice parameter evolution for $Fe_{3-x}Cr_xO_4$ series. The reference data for bulk samples (red circles) was taken from Francombe [5]. XRD results for thin films with and without the $Fe_3O_4$ buffer are represented in purple circles and black filled circles, respectively. For comparison's sake, HRXRD results for films without buffer are depicted as blue circles. The dashed lines are a guide to the eye.

For comparison, reference values [5] for room temperature lattice parameters of bulk samples are also depicted in **Figure 4.9** (red circles). Like bulk samples, the thin film system also can be divided (crystallographically) into three distinct regions: (I) $0 < x < 0.5$, (II) $0.6 < x < 1.1$ and (III) $1.2 < x < 2.0$. In summary, the lattice parameter decreases for $x$ up to 0.5, increases for values between 0.6 and 1.1 and then decreases again for $x$ greater than 1.2. As discussed in **Section 1.3.1**, this behavior is typically associated to changes in the cation distribution among tetrahedral (Td) and octahedral (Oh) sublattices. Small reductions of $c$ parameter for $x < 0.5$ results from the replacement of $Fe^{3+}$ by slightly smaller $Cr^{3+}$ in Oh-sites, whereas the enhancement of $c$ parameters for $0.6 < x < 1.1$ can be understood by the displacement of larger $Fe^{2+}$ into Td-sites. Compositions with high Cr content are assumed to have the normal type of spinel structure, so the lattice parameter decreases again because $Fe^{3+}$ cations are replaced by smaller $Cr^{3+}$ in Oh-sites. Note that for bulk samples the limit between regions II and III is about $x \cong 1.3$, while for thin films it is about $x \cong 1.1$. This is the first clue encountered in this work that these epitaxial films may not have the same cationic distribution as the bulk.

## 4.3 Film microstructure and interfaces

For selected samples, layer-substrate interface and structural defects were evaluated by cross-sectional TEM. **Figure 4.10** depicts TEM images of a representative $Fe_{2.8}Cr_{0.2}O_4$ film studied along the $[\bar{1}2\bar{1}0]$ direction, for which the epoxy/$Fe_{2.8}Cr_{0.2}O_4$ and the $Fe_{2.8}Cr_{0.2}O_4/Al_2O_3$ interfaces are clearly determined. These images were acquired over a significant portion of the film in order to obtain a representative image of the entire sample. Low magnification TEM (**Figure 4.10a**) shows that the film is homogeneous and has a constant thickness of 14.6 nm. This result is coherent with the thickness obtained from the fit of XRR patterns ($t_{XRR}$ = 14.8 nm) and Laue oscillations ($t_{HRXRD}$ = 14.5 nm). High-resolution TEM (**Figure 4.10b and c**) show the (111) spinel planes oriented parallel to the substrate surface, again highlighting the high crystalline quality of these epitaxial films. One observes perfectly flat and abrupt $Fe_{2.8}Cr_{0.2}O_4/Al_2O_3$ interface with no noticeable parasite phases at atomic scale. In particular, **Figure 4.10b** depicts the HRTEM micrograph in a larger observation window, where a series of spaced contrasts appears on the substrate/film interface (yellow arrows). Such contrast may be attributed to misfit dislocations, which takes part on the relaxation mechanism of these films. These features were also observed for other ferrites grown on sapphire substrate by O-MBE (*e.g.* $NiFe_2O_4$ [6] and $MnFe_2O_4$ [7]).

**Figure 4.10c** depicts the HRTEM micrograph with higher magnification. Herein, interplanar distances of 0.480 nm for planes parallel to the interface and 0.284 nm for planes perpendicular to the interface were deduced for $Fe_{2.8}Cr_{0.2}O_4$ film, which are slightly smaller from the (111) and (220) interplanar spacing obtained for bulk samples (*i.e.,* 0.485 nm and 0.297 nm, respectively). These values remained constant across the entire profile of the $Fe_{2.8}Cr_{0.2}O_4$ film, indicating a small remaining out-of-plane and in-plane strain of 1% and 4%, respectively. HRXRD measurements corroborate with these results. In **Figure 4.9**, the $c$ parameters found for all compositions are slightly smaller than the expected. For instance, $c$ = 0.8357 ± 0.0003 nm for $Fe_{2.8}Cr_{0.2}O_4$ film, while the cubic bulk lattice has

$c$ = 0.8394 ± 0.0001 nm. This residual strain is probably due to the large compressive in plane mismatch (about 8%) between the spinel oxides and the corundum substrate.

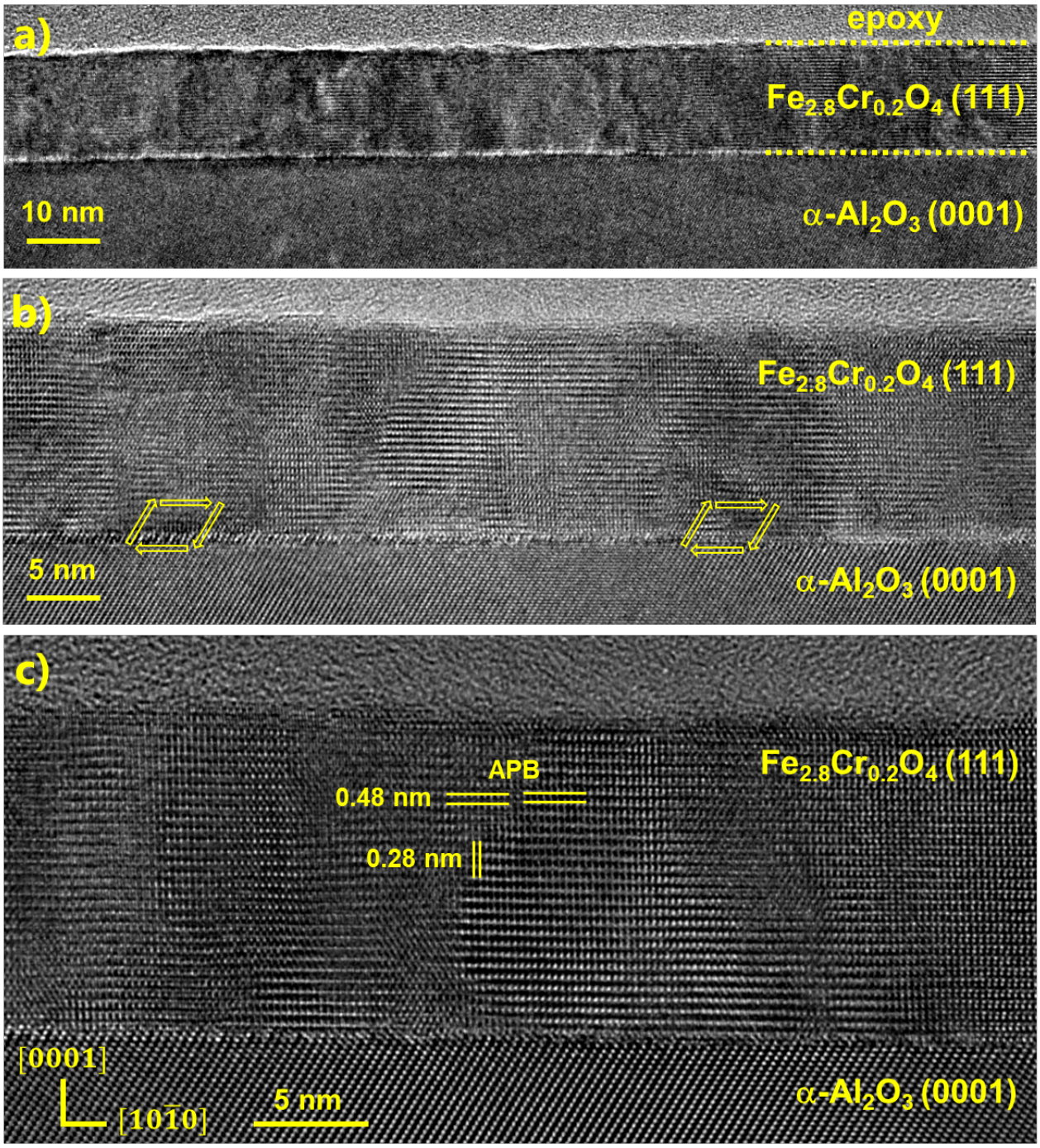


**Figure 4.10**. Cross-sectional TEM images of $Fe_{2.8}Cr_{0.2}O_4$ thin film recorded along the [$\bar{1}2\bar{1}0$] direction at increasing magnification. Low magnification TEM (a) shows the homogeneity in thickness and structure of the 15 nm thick film. HRTEM images (b) and (c) depict the epitaxial nature of the film. Yellow arrows show possible dislocations in (b). The deduced interplanar distances for this film and the presence of APBs are highlighted in (c).

When the lattice mismatch imposed by the substrate is positive, the film usually grows under in-plane compressive strain and larger out-of-plane lattice parameters are observed. The growth of

spinel iron oxides on $Al_2O_3$, however, is more complex. Analyses of the real-time RHEED patterns (**Figure 4.**) reveal that the early stages of growth are not constrained as expected, but expanded with respect to the bulk material lattice. The parametric disagreement reaches a maximum of 14% for the FeO-like phase and then the film gradually relaxes towards the lattice parameter of the bulk material. Interestingly, **Figure 4.10c** shows no trace of a FeO-like phase at the interface, unlike what was perceived in the RHEED patterns during deposition (**Figure 4.**). This initial halite phase is probably the result of a dynamic phenomenon that occurs during deposition, which does not persist after the complete growth and cooling of the film. Moreover, after the growth of 15 nm films, the in-plane lattice parameter is almost fully relaxed and only 1% of in-plane strain persists according to RHEED patterns (**Figure 4.2**). It is possible that these stresses also induce out-of-plane compressions, as observed by the $c$ values. In order to assess the extent of strain relaxation in the various films, complementary analysis (*e.g.* reciprocal space mapping [8] or geometric phase analysis [9]) are required. In fact, despite giving good insights into the microstructure of the films, the HRTEM analyses performed in this work are not accurate enough to analyze lattice spacing.

Besides showing the film structure, **Figure 4.10c** also reveals the presence of one of the most common defects known for ferrite thin films [2], [6], [7], [10], [11]: the anti-phase boundaries (APBs). This stacking defect is associated with nucleation of islands on early stages of the film growth, which leads to symmetry breaking. For example, the APB highlighted in **Figure 4.10c** results from a half-lattice translation of the cationic sublattice within an unchanged oxygen sublattice. The structure and the large in plane mismatch imposed by the sapphire substrates favor the development of APBs in spinel thin films. Thus, this defect is certainly present in all samples synthesized in this work. Identifying APBs is crucial as they influence greatly the electrical transport and the magnetic properties of thin films, which has been widely studied in epitaxial $Fe_3O_4$ [2], [10], [11] and are discussed for the iron chromites in **Chapter 5**.

The TEM images shown in **Figure 4.10** for $Fe_{2.8}Cr_{0.2}O_4$ are representative of all samples where $x < 1.4$. For comparison's sake, **Figure 4.11** shows cross-sectional TEM images of $Fe_{2.3}Cr_{0.7}O_4$ film studied along the $[\bar{1}2\bar{1}0]$ and $[1\bar{1}00]$ directions. Again, low magnification TEM (**Figure 4.11a**) shows that the film is homogeneous and has thickness of about 15.4 nm (note that $t_{XRR}$ = 15.1 nm and $t_{HRXRD}$ = 14.5 nm). HRTEM micrographs (**Figure 4.11b and c**) depict a perfectly flat and abrupt $Fe_{2.3}Cr_{0.7}O_4/Al_2O_3$ interface and confirm the epitaxial nature of this film. **Figure 4.11c** highlights the presence of APBs, which endorses that this stacking defect is present in all samples.

When comparing the HRTEM images of $Fe_{2.8}Cr_{0.2}O_4$ and $Fe_{2.3}Cr_{0.7}O_4$ films, one observes that increasing the Cr content seems to induce disorder in the crystalline structure of the film. This is even more evident in the image acquired along the $[1\bar{1}00]$ direction, where many stacking defects (*e.g.,* APBs and dislocations) are observed. To investigate further this issue, HRTEM images were acquired for $Fe_{1.8}Cr_{1.2}O_4$ and *buffer*-$Fe_{1.3}Cr_{1.7}O_4$, as illustrated in **Figure 4.12**. Herein, the increase in the amount of the crystalline nanodomains is unmistakable for both of these layers compared to the first two compositions. Indeed, it is much more difficult to recognize the (111) spinel planes oriented parallel to the substrate surface due to the complexity of the microstructure. These results corroborate well with the decrease in quality of the RHEED images.

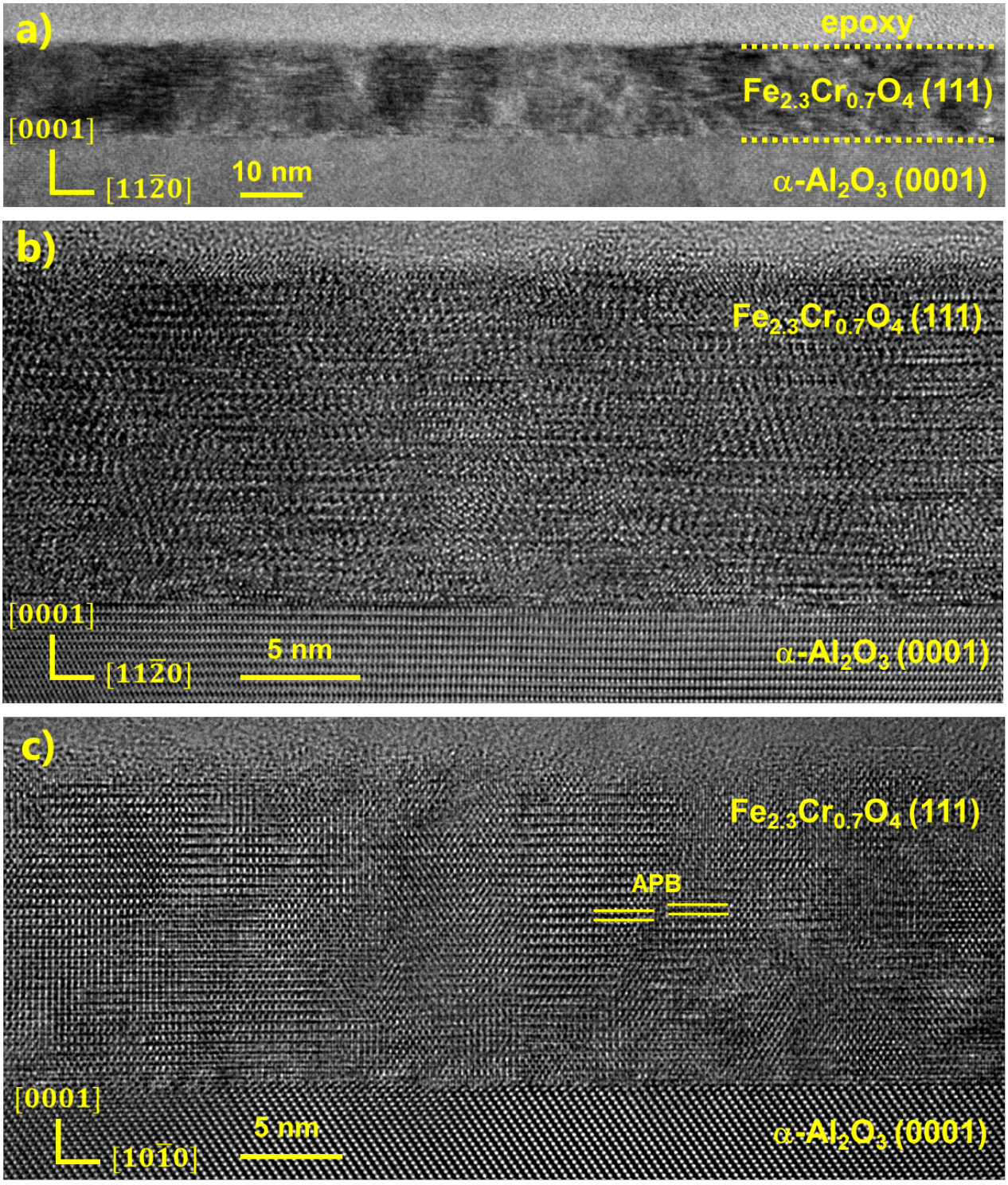


**Figure 4.11.** Cross-sectional TEM images of $Fe_{2.3}Cr_{0.7}O_4$ thin film. Low magnification TEM (a) recorded along the $[1\bar{1}00]$ direction shows the homogeneity in thickness and structure of the 15 nm thick film. HRTEM images, recorded along the $[1\bar{1}00]$ direction (b) and $[\bar{1}2\bar{1}0]$ direction (c), depict the epitaxial nature of the film.

Interestingly, it is impossible to distinguish between the buffer $Fe_3O_4$ and $Fe_{1.3}Cr_{1.7}O_4$ layers in this imaging mode. No difference in lattice parameters were detected during image processing, so the position of the $Fe_3O_4$ buffer is only given as an indication in **Figure 4.12b**. This can be explained by the great similarity in both chemistry and structure of these two iron oxides. In fact, Fe and Cr are

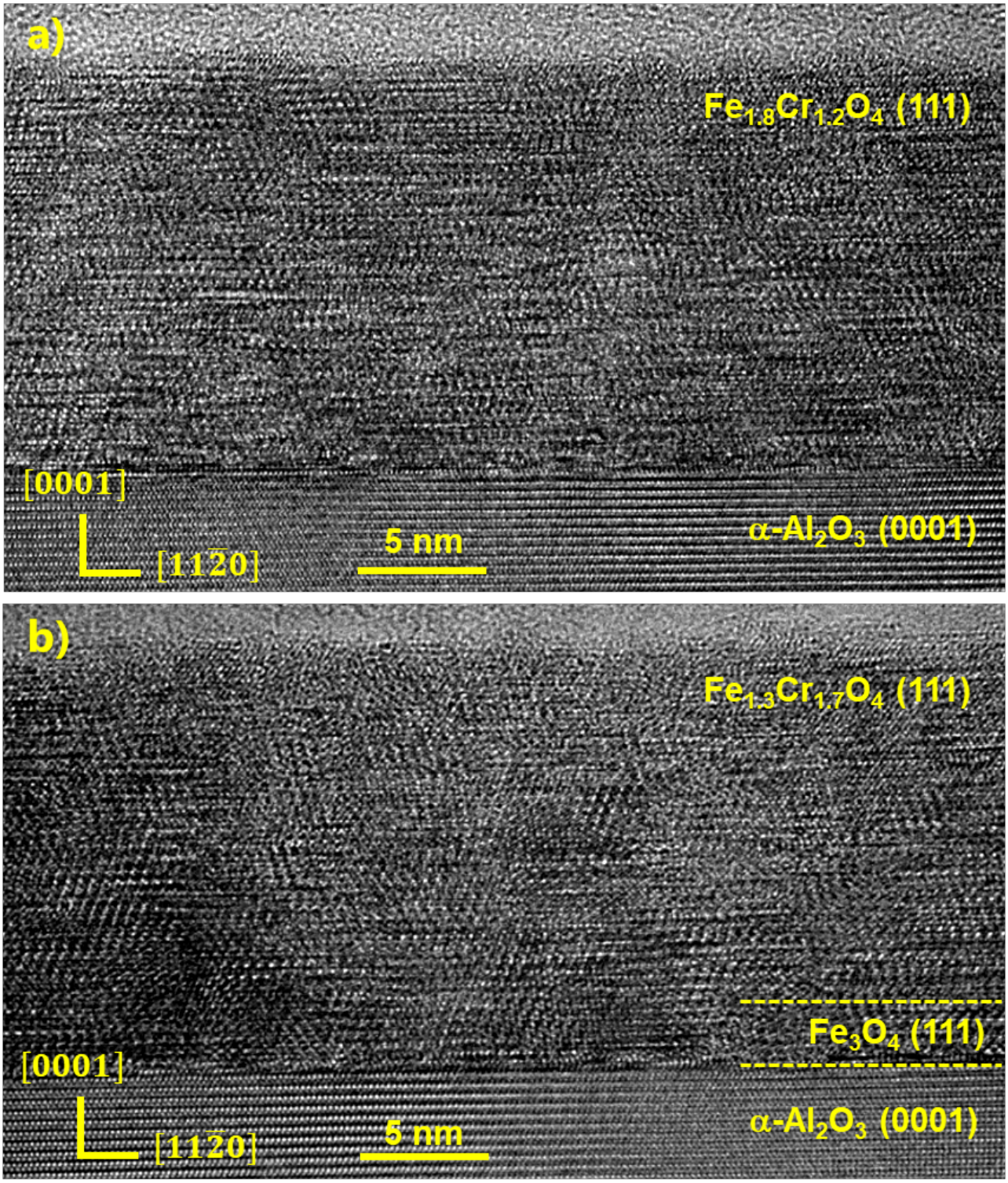


**Figure 4.12.** Cross-sectional HRTEM images of (a) $Fe_{1.8}Cr_{1.2}O_4$ (18 nm) and (b) $Fe_3O_4$ (3 nm) / $Fe_{1.3}Cr_{1.7}O_4$ (15 nm) thin films recorded along the $[1\bar{1}00]$ direction.

close in atomic number, so there is no contrast between these two species. Moreover, they have similar lattice parameter (*i.e.,* 0.8396 nm and 0.8390 nm for bulk $Fe_3O_4$ and $Fe_{1.3}Cr_{1.7}O_4$, respectively) and cubic structure, thus a perfect epitaxial relationship is expected between these two compounds. These two factors could lead to the absence of any distinguishing marks on its interface. Another

possible explanation for the lack of contrast at the interface is that the cations diffuse during growth and a pure ultrathin $Fe_3O_4$ layer no longer exists after cooling. In fact, this is what was intended for this system, that the buffer layer would completely diffuse and an essentially homogeneous iron chromite would be created. Therefore, in order to probe the nature of the film grown on buffer and other features of the iron chromites, chemical analyses were performed. The results of which are shown in detail in next sections.

**Highlights on the structure of $Fe_{3-x}Cr_xO_4$ thin films:**

- Epitaxial $Fe_{3-x}Cr_xO_4$(111) thin films (~15 nm thick) supported on $\alpha$-$Al_2O_3$(0001) were successfully prepared for the composition range of $0 \leq x \leq 1.7$.
- The crystalline quality of the films decreases as the Cr content increases:
  - For $x < 1.2$, the films have higher crystalline quality and lower surface roughness. They are homogeneous with low density of defects.
  - For $x \geq 1.2$, the films have lower crystalline quality and higher surface roughness. There is an obvious increase in the amount of nanodomains (*i.e.,* more planar defects).
- A clear improvement in crystalline quality is observed for high Cr-content films ($x \geq 1.4$) grown on a 2.6 nm-thick $Fe_3O_4$(111) buffer.
- The out-of-plane lattice parameters of all films are almost fully relaxed and only about 1% of strain persists. These parameters evolve with composition in a similar way as for bulk samples.
- Stacking defects, such as APBs, are observed in all samples.

## 4.4 Chemical investigation

After growth of the $Fe_{3-x}Cr_xO_4$ (111) series, the purity and stoichiometry of the films were first evaluated *ex situ* by XPS measurements. No elements other than Fe, Cr, O and C appeared in the survey scan spectra (not shown). **Figure 4.13** shows Cr 2*p* (575-590 eV) and Fe 2*p* (705-740 eV) XPS spectra for $0 \leq x \leq 1.4$ without buffer and $x = 1.7$ with buffer. This is because no significant differences were found for spectra of samples with and without buffer, except for $x = 1.7$. In this case, the sample without buffer showed a small peak at 706.6 eV, *i.e.* a small contribution of metallic iron. Before trying the $Fe_3O_4$ buffer layer, attempts were made to prevent $Fe^0$ formation by either increasing $P_{O_2,plasma}$ slightly during deposition or cooling the sample after synthesis under oxygen flux (since the vacuum is a reducing environment). However, both strategies failed. The former induced the formation of a corundum phase and the latter reduced the amount of $Fe^0$ observed in the Fe 2*p* XPS spectrum, but did not eliminate it. Since the presence of $Fe^0$ would have biased the results of the physicochemical property analyses, these samples were excluded from further analysis. This oxidation issues once

again confirm the small $P_{O_2,plasma}$ working window (see **Section 4.1**) found in this work for the growth of iron chromites on sapphire substrates.

Two main information were extracted from the XPS spectra: (*i*) the stoichiometry of the films and (*ii*) the oxidation state of Fe and Cr cations. The following sections not only comment on each of these features of XPS spectra, but also cross-reference and compare their results with other spectroscopies (*i.e.,* XAS, EELS and EDX).

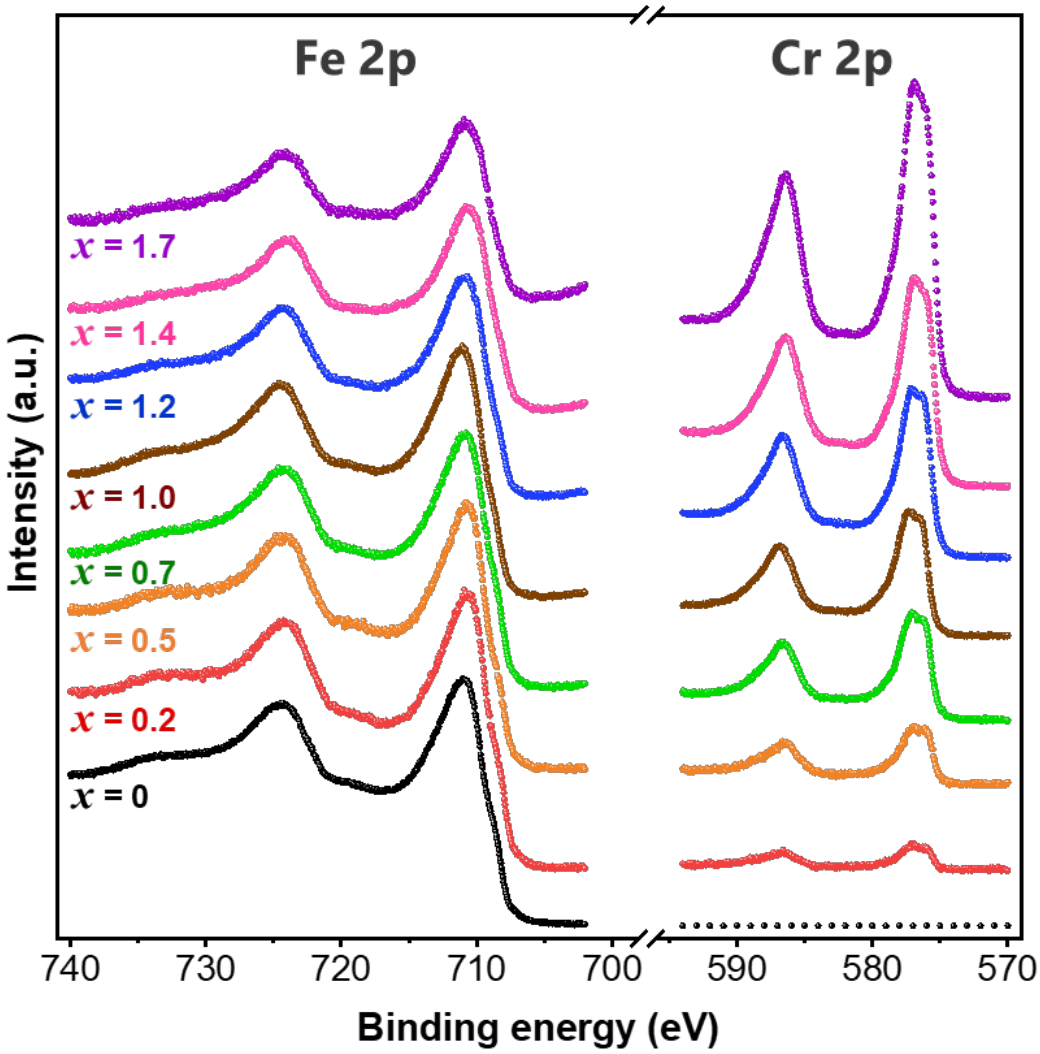


**Figure 4.13.** Fe 2*p* and Cr 2*p* photoemission spectra of $Fe_{3-x}Cr_xO_4$ thin films. The spectra were normalized with respect to the Fe $2p_{3/2}$ envelope (~711 eV) to better visualize the increase in area of the Cr peaks with increasing $x$. Color code: $x$ = 0 (black), $x$ = 0.2 (red), $x$ = 0.5 (orange), $x$ = 0.7 (green), $x$ = 1.0 (brown), $x$ = 1.2 (blue), $x$ = 1.4 (pink) and $x$ = 1.7 (violet).

### 4.4.1 The stoichiometry of $Fe_{3-x}Cr_xO_4$ films

The $x$ value of each sample was determined by the relative intensity between the Cr 2*p* and Fe 2*p* core-levels, as described by Equation 2.9 (**Section 2.3.1**). So far, all nominal composition presented in this thesis were those given by such analysis of the XPS spectra. Although very useful, these results had to be confirmed by complementary chemical analysis due to three main reasons:

1. Because XPS measurements were performed *ex situ*, the oxygen amount could not be taken into account due to contamination of the surface from air exposure. Hence, $x$ values were calculated as if the films were perfectly stoichiometric, which may not be the case.

2. XPS probes the average composition of the surface (top 5-10 nm), so nothing can be said about inhomogeneity at depth. This information is of utmost importance, especially for films grown on buffer, since inhomogeneity in composition may influence their magnetic and electronic properties.

3. While XPS provides reliable quantitative analysis, it requires a detailed analysis of the spectrum. Herein, the quantification was made after Shirley background subtraction using the entire $2p$ region (bottom left **Figure 4.14**). However, the analysis could be limited to the $2p_{3/2}$ envelope, which would decrease the Fe:Cr ratio in 35%. Furthermore, element quantification may be influenced by the choice of background function [12].

The stoichiometry and homogeneity of selected films were investigated using electron energy-loss spectroscopy (EELS) and energy dispersive X-ray spectroscopy (EDX). Since these techniques are highly localized, different areas of each sample were probed to assure the homogeneity of the films. **Table 4.2** summarizes the results of element quantification from STEM-EELS and STEM-EDX in percentage. It should be noted that these techniques have their own limitations [13]. In addition to being less sensitive to light elements (*i.e.,* $Z < 25$), the O K and Cr L peaks partially overlap in the EDX spectrum (bottom right **Figure 4.14**), which hindrance the relative quantification of these species. Regarding the EELS spectrum, the elements ratio is calculated after background subtraction (bottom middle **Figure 4.14**). Thus, like XPS, the accuracy in quantification depends on how the background is determined. In both cases, the parameters used in quantification of the $Fe_{3-x}Cr_xO_4$ series were first adjusted using the $\alpha$-$Cr_2O_3$ film (**Figure 3.7**) in order to have a 2:3 ratio between Cr and O. Indeed, STEM-EELS yields a relative composition of (38 ± 2)% of Cr and (62 ± 2)% of O, while STEM-EDX measured (39 ± 2)% of Cr and (61 ± 2)% of O in $\alpha$-$Cr_2O_3$ film.

**Table 4.2** – Fe, Cr and O element quantification (in percentage) from EELS and EDX analysis for $x = 0.2$, 0.7, 1.2 and 1.7 (sample grown on buffer).

| Layer | EELS | | | EDX | | |
|---|---|---|---|---|---|---|
| | %Fe | %Cr | %O | %Fe | %Cr | %O |
| $Fe_{2.8}Cr_{0.2}O_4$ | 40 ± 1 | 2 ± 1 | 58 ± 2 | 38 ± 2 | 3 ± 1 | 59 ± 2 |
| $Fe_{2.3}Cr_{0.7}O_4$ | 29 ± 3 | 7 ± 1 | 63 ± 3 | 34 ± 2 | 10 ± 2 | 56 ± 2 |
| $Fe_{1.8}Cr_{1.2}O_4$ | 27 ± 2 | 13 ± 3 | 59 ± 3 | 24 ± 2 | 16 ± 2 | 60 ± 2 |
| $Fe_{1.3}Cr_{1.7}O_4$ | 24 ± 2 | 16 ± 2 | 60 ± 1 | 25 ± 2 | 18 ± 2 | 57 ± 2 |

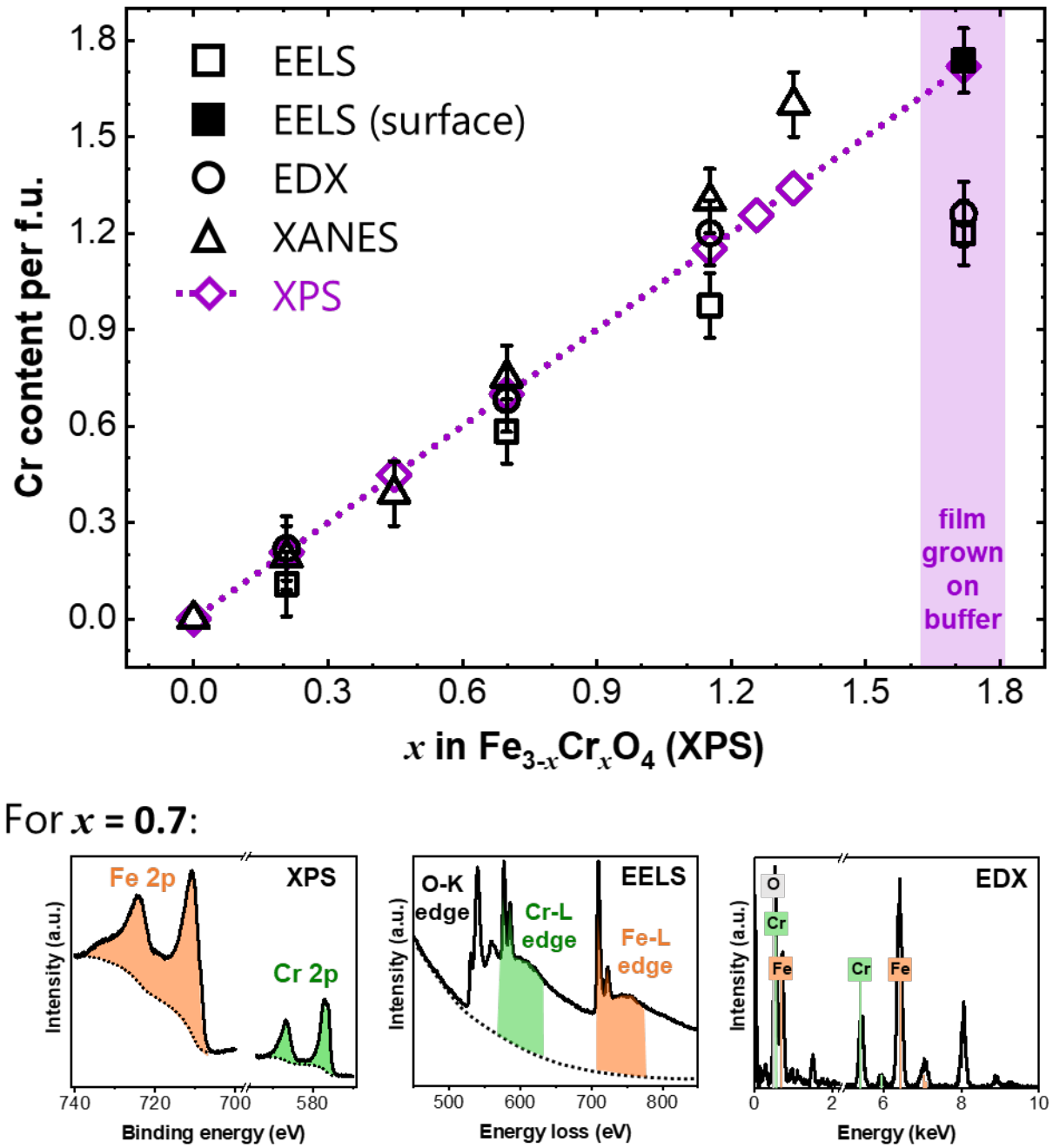


**Figure 4.14.** Nominal composition ($x$ values) obtained from STEM-EELS (squares), STEM-EDX (circles) and XANES (triangles) analyses in comparison with $x$ values extracted from the relative intensity of Fe $2p$ and Cr $2p$ XPS spectra (dotted line). The purple shade highlights the compositions grown on $Fe_3O_4$ buffer, where the black square shows the EELS composition of the film surface (first 5 nm). The insets show the spectra form and background treatment of XPS in comparison with EELS and EDX for $x$ = 0.7.

**Figure 4.14** shows the nominal composition of the films determined by STEM-EELS, STEM-EDX and XANES in comparison with the ones given by XPS measurements. For comparison's sake, the $x$ values of the films were calculated using the ratio between %Fe and %Cr shown in **Table 4.2**:

$$\frac{\%\mathrm{Fe}}{\%\mathrm{Cr}} = \frac{3-x}{x} \tag{4.1}$$

In general, a good agreement in the quantification of Fe and Cr elements was found between the STEM-EELS, STEM-EDX and core level spectroscopies. The STEM-EELS measurements yield slight lower $x$ values because they show higher O amounts (~60%) than expected for stoichiometric films (~57%). This could mean that the films are in fact slightly over oxidized. However, at this stage, one cannot give a firm statement about it because oxygen is an element known to be difficult to quantify accurately and the error bars are rather large (~3%). For samples grown directly on the substrate, STEM-EELS and STEM-EDX presented similar trends with minimal fluctuations in the Fe and Cr signals throughout the layers and no composition gradient. **Figure 4.15a** depicts the EELS scans for the 15 nm thick $Fe_{2.3}Cr_{0.7}O_4$, acquired through the horizontal and vertical yellow lines (inset **Figure 4.15a**). Herein, the relative amounts of Fe, Cr and O scanned in the film region forms a plateau. The same, however, cannot be said for films grown on buffer.

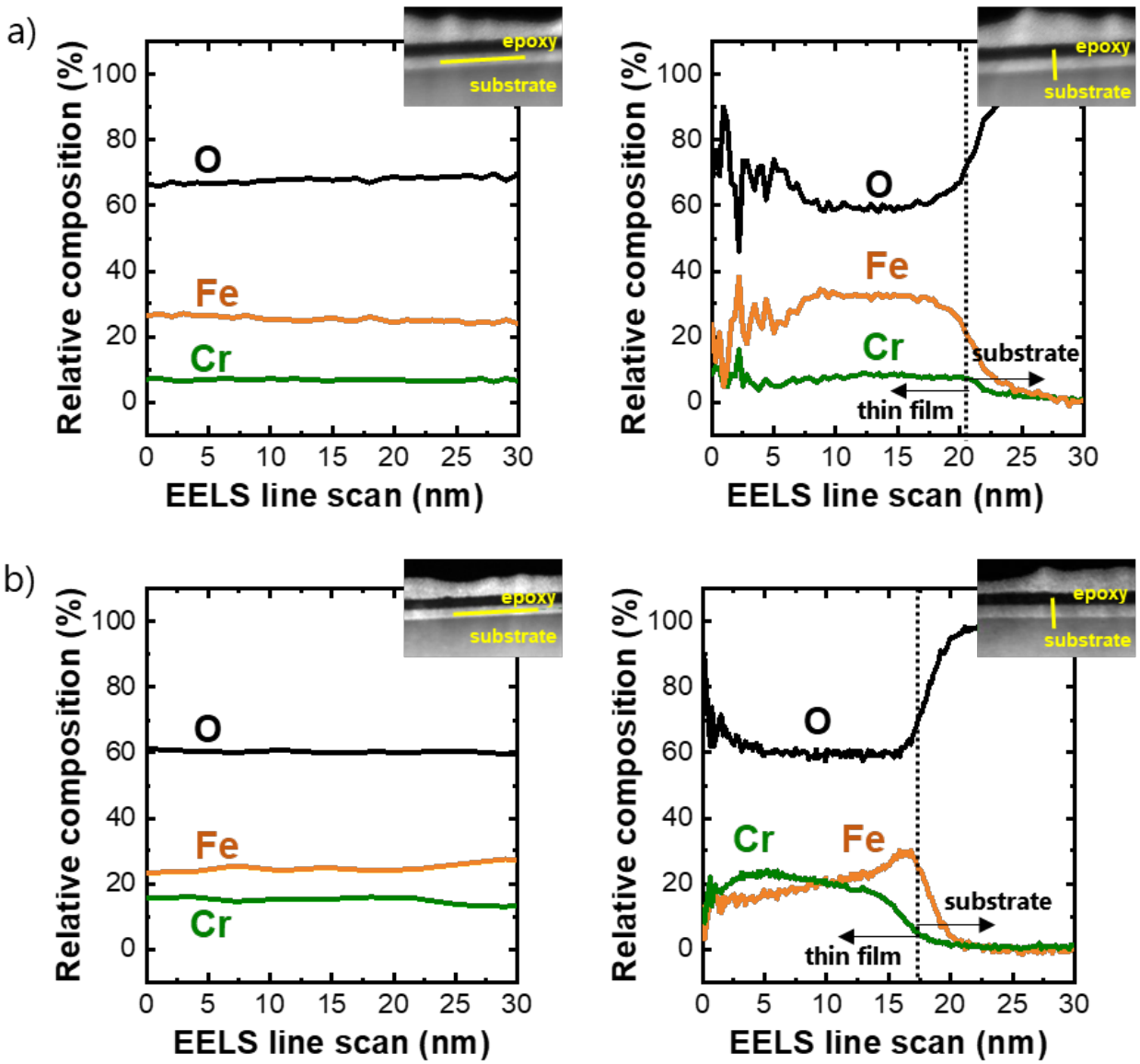


**Figure 4.15.** Fe, Cr and O relative compositions measured using STEM-EELS for (a) $x$ = 0.7 and (b) $x$ = 1.7. In inset, STEM images show the position of the horizontal (left) and vertical (right) line scan. For the latter, the measurements were performed from the epoxy to the substrate.

**Figure 4.15b** depicts the EELS scans for the 17 nm thick *buffer*-$Fe_{1.3}Cr_{1.7}O_4$, also acquired through horizontal and vertical line scans (inset **Figure 4.15b**). For the first, only few fluctuations are observed in the Fe, Cr and O relative composition and the film has globally 24 ± 2 % of Fe, 16 ± 2 % of Cr and 60 ± 2 % of O, therefore, $x \cong 1.2$. For the latter, a gradient in the relative composition of Fe and Cr is observed. Indeed, the cations diffuse between the buffer layer and the iron chromite layer. The amount of Cr slowly increases from the buffer (at ~17 nm) to the surface (at ~2 nm), while Fe behaves in the opposite way. Out of curiosity, the composition obtained for the extreme surface (first 5 nm) is similar to that given by XPS analysis ($x \cong 1.7$), which confirms the consistency between these methods.

Since a perfect control of the film composition was achieved (within an error bar of $\pm$ 0.1 for $x$), the $x$ values obtained via XPS are used from now on in this thesis for simplicity's sake.

## 4.4.2 Fe and Cr oxidation states and local environments

After confirming the Fe:Cr ratio of the $Fe_{3-x}Cr_xO_4$(111) series, interest was turned to the oxidation states and local environment of these cations. As explained in **Section 1.3.1**, bulk iron chromites have $Cr^{3+}$ cations sitting in octahedral sites (Oh), while $Fe^{2+}$ and $Fe^{3+}$ cations are distributed between the tetrahedral sites (Td) and the remaining Oh-sites. Their cation arrangement is described as: $[Fe^{3+}_yFe^{2+}_{1-y}]_{Td}[Fe^{2+}_yFe^{3+}_{2-x-y}Cr^{3+}_x]_{Oh}O_4$, where the inversion parameter ($y$) depends on the Cr content as well as the nature of the sample. As aforementioned, XPS was the first analytical technique used in this work to investigate the cation oxidation states in the films. Interestingly, **Figure 4.13** depicts very similar Cr 2*p* and Fe 2*p* XPS spectra among the components of the $Fe_{3-x}Cr_xO_4$ series. This observation is rather expected for Cr, as it is supposed to have not only the same oxidation state, but also the same local environment for all compounds. However, the differences observed between the Fe 2*p* spectra are surprisingly subtle, considering that $Fe^{2+}$ and $Fe^{3+}$ cation number ratio changes with composition (*e.g.* 1:2 in $Fe_3O_4$ and 1:1 in $Fe_2CrO_4$).

First, general comments are drawn on the oxidation state and core-level spectral features of Cr. Then, focus is placed on the Fe valence as the indicator of oxygen stoichiometry.

### 4.4.2.1 The features of Cr core level spectra

As abovementioned, Cr 2*p* XPS spectra are very similar for all components of the $Fe_{3-x}Cr_xO_4$ series. One recognizes two single asymmetrical peaks for Cr $2p_{3/2}$ and $2p_{1/2}$ envelopes centered at 576.5 eV and 586.5 eV, respectively. Such chemical shift is the same as $Cr_2O_3$ films (**Figure 2.9**), which confirms that the Cr valence in $Fe_{3-x}Cr_xO_4$ films is exclusively 3+. Note that the spectral shape, however, is considerably different from the corundum reference. The Cr $2p_{3/2}$ envelope is more symmetrical and does not present the characteristic multiplet splitting feature, as discussed in **Chapter 3**.

Differences in spectral shape are also observed in the Cr K-edge XANES results. In this technique, the edge position and the intensity of the pre-edge feature (*i.e.,* small peak on the low

energy side) are related to the formal valence state and the coordination environment of the cation. As depicted in **Figure 4.16a**, the Cr K-XANES spectra of the $Fe_{3-x}Cr_xO_4$ series are very similar between each other but slightly different from the $Cr_2O_3$ spectrum. This is because even though in both structures Cr occupies octahedral interstices, they do not have the same local structure. The $Cr^{3+}$ ions sit in a trigonal distorted octahedral site in the corundum structure, whereas in the spinel structure these ions have mostly a regular octahedral environment. Nonetheless, it is important to note that the "edge jump" for both $Fe_{3-x}Cr_xO_4$ spinels and $Cr_2O_3$ are located at similar energy position (**Figure 4.16b**), which confirms that Cr ions assume exclusively a 3+ oxidation state in these films. The small difference (~0.4 eV) observed in the "edge jump" between $Fe_{2.3}Cr_{0.7}O_4$ and $Fe_{1.6}Cr_{1.4}O_4$ is probably due to the difference in the film stoichiometry, as shown later by the Fe K-edge XANES results.

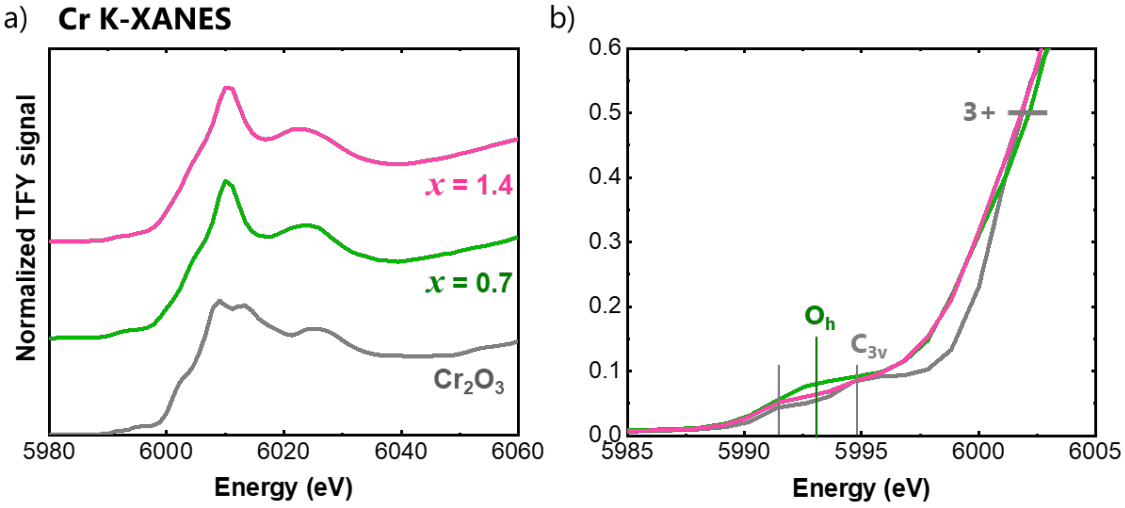


**Figure 4.16.** (a) Cr K-edge XANES spectra of $Fe_{2.3}Cr_{0.7}O_4$ (green line) and $Fe_{1.6}Cr_{1.4}O_4$ (pink line) thin films in comparison with reference $Cr_2O_3$ (gray line). (b) A zoom inspection between 5985 and 6005 eV shows the pre-edge features and the edge jump position (normalized absorbance = 0.5). Herein, 3+ valences are found for Cr in all samples.

CFM calculations were performed to comprehend the influence of the local environment on the XPS and XANES spectral shape (**Figure 4.17**). Herein, the parameters used were the same as shown in **Chapter 3** for $Cr_2O_3$ and the ones used to simulate XMCD spectra for $Fe_{2.3}Cr_{0.7}O_4$ (next section). Both Cr $2p_{3/2}$ envelope and XANES pre-edge of $Cr_2O_3$ are fitted in a $C_{3v}$ environment, while $Fe_{2.3}Cr_{0.7}O_4$ spectra are fitted in an $O_h$ environment. For the XPS (**Figure 4.17a**), calculations performed in the $C_{3v}$ symmetry show a splitting of the Cr $2p_{3/2}$ envelope, which is related to the crystal field splitting introduced by distortions in the local symmetry. On the other hand, the spectrum simulated in the $O_h$ symmetry is much more symmetrical and no significant splitting of the envelope is observed. The same trends are observed in the calculations of the XANES pre-edge (**Figure 4.17b**). Note that the $Fe_{1.6}Cr_{1.4}O_4$ films (**Figure 4.16b**) the pre-edge peak shows similar splitting as the one observed in $Cr_2O_3$. This corroborates well with the bulk structures shown in **Chapter 1**, in which the $CrO_6$ octahedra are more distorted for iron chromites with higher Cr content. It is also important to highlight that the fits are not perfect. Better description of the spectral shape could be achieved if charge transfer and *p-d* hybridizations were considered. Since the goal at this point was not to

perfectly describe these transitions, but to understand the source of the spectral differences, these simulations were not explored any further.

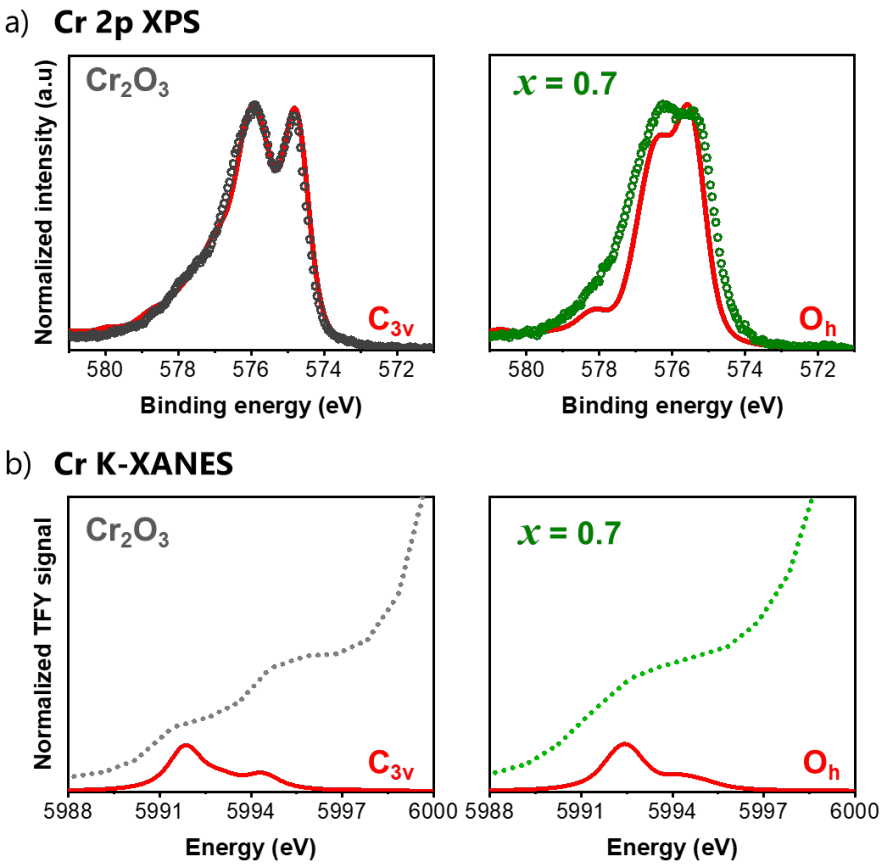


**Figure 4.17.** Calculated (a) Cr 2*p* XPS spectra and (b) Cr K-XANES pre-edge (red lines) in comparison with the experimental spectra (dots) for $Cr_2O_3$ (gray) and $Fe_{2.3}Cr_{0.7}O_4$ (green) thin films.

### 4.4.2.2 The features of Fe core level spectra

Now, general comments are drawn on the Fe valence and core-level spectral features. In $Fe_3O_4$, the Fe 2*p* XPS spectrum is usually interpreted [14] as a complex mix of $Fe^{2+}$ and $Fe^{3+}$ multiplet peaks partially overlapped. For clarity, **Figure 4.18** depicts the multiplets of both $Fe^{2+}$ and $Fe^{3+}$ components proposed by Grosvenor *et al.* [14] for bulk magnetite. Although the presence of overlapping multiplets makes it difficult to distinguish properly the two species, the large peak at 711.0 eV in the Fe $2p_{3/2}$ envelope is usually assigned to $Fe^{3+}$ whereas the shoulder at 709.0 eV is primarily a $Fe^{2+}$ contribution. Notably, the peak deconvolution proposed by Grosvenor *et al.* [14] yields for bulk magnetite a $Fe^{3+}$:$Fe^{2+}$ ratio close to the 2:1 expected.

All spectra in **Figure 4.13** show the same features specific of mixed valence iron oxides, *i.e.,* large Fe 2*p* envelopes with a shoulder on the low-binding energy side and no charge transfer satellites[31]. Curiously, the intensity of the $Fe^{2+}$ multiplets (~709.0 eV) reduces as the Cr content

[31] As shown in **Figure 2.9**, additional satellite peaks due to charge transfer appear 8 eV above the main peaks for pure $Fe^{3+}$ compounds and 4 eV above the main peaks for pure $Fe^{2+}$ compounds.

increases (**Figure 4.18**). This trend is the opposite of what is expected. In fact, $Fe_{redox}$ decreases as $x$ increases according to Fe K-XANES results (**Figure 4.19a**). One possible explanation is that the extreme surface, as investigated by XPS, is over oxidized. Thus, the disagreement between XPS and XAS is because these techniques do not probe the same depth. Another explanation is a difference in the Fe cation distribution, since the relative intensity of the multiplets related to $Fe^{2+}$ and $Fe^{3+}$ species depends on the cation distribution within the near surface and surface termination. Chambers *et al.* [15] stated the same when studying epitaxial $Fe_2CrO_4$ films grown on MgO (001). They concluded that the depletion in $Fe^{2+}$ in the near-surface region of this film was a consequence of the mixed-valence nature of Fe in both Td and Oh-sites, which requires an electronic redistribution to preserve charge neutrality at the film surface. These results, however, are ambiguous.

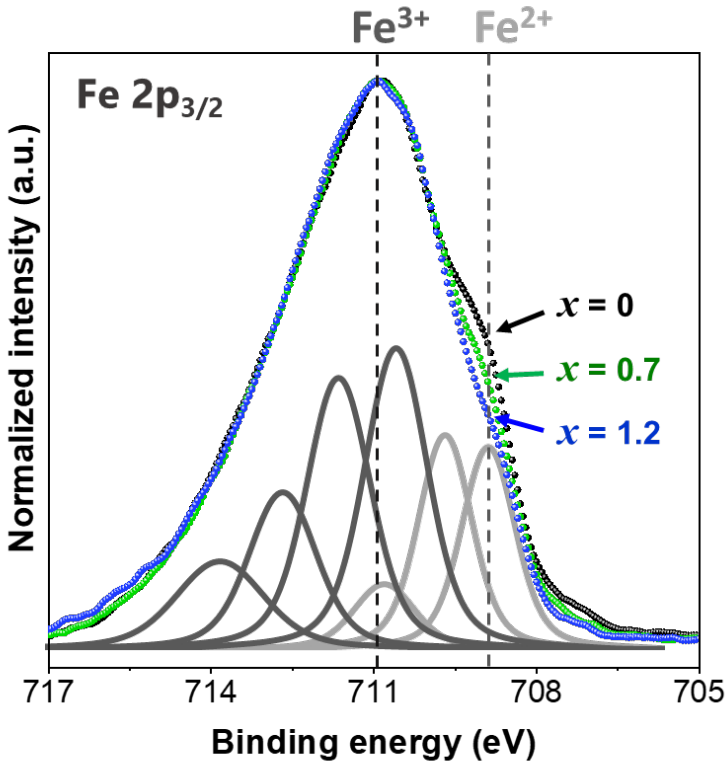


**Figure 4.18**. Normalized Fe $2p_{3/2}$ photoemission spectra of $Fe_{3-x}Cr_xO_4$ thin films after Shirley background subtraction. The spectra are composed by a complex mix of $Fe^{2+}$ (light gray lines) and $Fe^{3+}$ (dark gray lines) multiplet peaks partially overlapped. Herein, the multiplet peak parameters (position and FWHM) are the ones proposed by Grosvenor *et al.* [14]. Color code: $x$ = 0 (black), $x$ = 0.7 (green) and $x$ = 1.2 (blue).

In a recent work, Chambers *et al.* [16] also compared the Fe $2p$ XPS spectra of epitaxial $Fe_3O_4$, $Fe_2CrO_4$ and $FeCr_2O_4$ films grown on $MgAl_2O_4$(001). Overall, they observed similar spectral features for these three compounds. More importantly, no $Fe^{2+}$ satellites appeared in the $FeCr_2O_4$ spectrum. In the literature [17], no clear $Fe^{2+}$ satellites were also observed for natural chromites. The only measurable difference in the XPS spectra of the $Fe_{3-x}Cr_xO_4$ series is that the centroid of the Fe $2p_{1/2}$ envelope slightly moves towards lower energies as the $Fe^{2+}$ content increases. Therefore, in the case of iron chromites, the classical quantification (*i.e.,* multiplet peak fitting) of the $Fe^{2+}$ and $Fe^{3+}$ species with XPS is not conclusive and complementary analyses had to be performed.

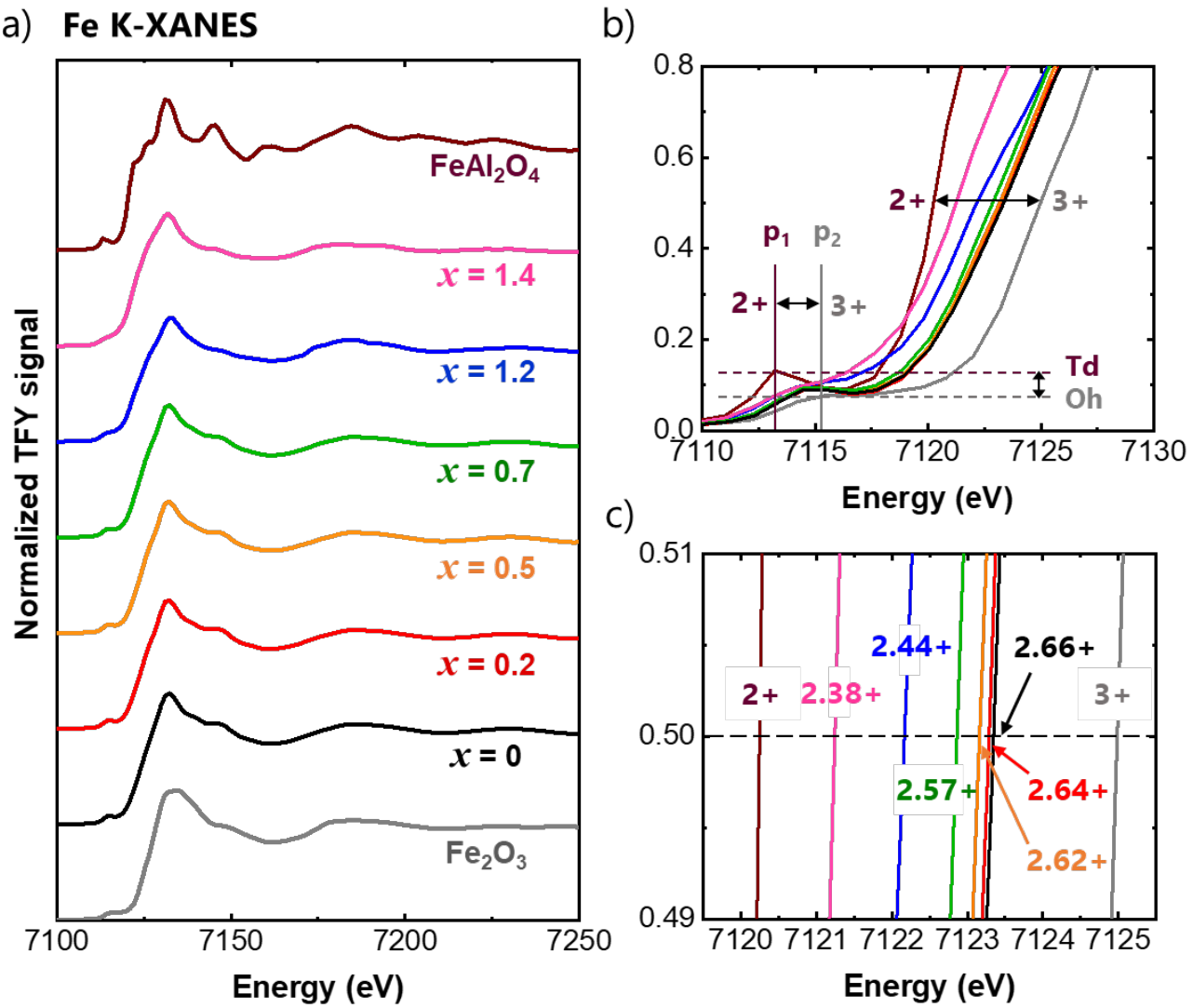


**Figure 4.19.** (a) Fe K-edge XANES spectra of $Fe_{3-x}Cr_xO_4$ thin films in comparison with reference compounds $FeAl_2O_4$ and $Fe_2O_3$. (b) A zoom inspection between 7110 and 7130 eV shows that both the pre-edge centroids position ($p_1$ and $p_2$) and the edge jump position are displaced towards lower energies as $x$ increases. (c) The edge jump position (normalized absorbance = 0.5) is therefore used to estimate the average oxidation state of Fe, taking $FeAl_2O_4$ and $Fe_2O_3$ as $Fe^{2+}$ and $Fe^{3+}$ references, respectively. Color code: $x$ = 0 (black), $x$ = 0.2 (red), $x$ = 0.5 (orange), $x$ = 0.7 (green), $x$ = 1.2 (blue), $x$ = 1.4 (pink), $Fe_2O_3$ (gray) and $FeAl_2O_4$ (dark red).

The average Fe oxidation states for the films were analyzed using the Fe K-edge shifts in comparison with various Fe standards. As depicted in **Figure 4.19b**, the positions of the "edge jump" (at ~7122 eV) of the Fe K-edge spectra are shifted to lower energies as the Cr content increases. This is because the edge positions are related to the formal valence state of the cation and therefore can be used to quantify it. In this study, the $Fe_{redox}$ of the films were estimated from edge energy position at normalized absorbance of 0.5 (**Figure 4.19c**), using $FeAl_2O_4$ and $Fe_2O_3$ as respective $Fe^{2+}$ and $Fe^{3+}$ references. Herein, the average iron redox found for the films are in good agreement with the expected for the iron chromites (within an average error of 1%). The only exception is $Fe_{1.6}Cr_{1.4}O_4$ that shows $Fe_{redox}$ value 5% lower (+2.26) than expected (+2.38). This means that the sample is under oxidized, which justifies the considerable difference found between the $x$ value determined by XPS

($x$ = 1.4) and XAS ($x$ = 1.6) in **Figure 4.14**. In fact, the $x$ values in **Figure 4.14** were calculated from the average oxidation states of iron ($Fe_{redox}$), which in turn were deduced from the position of the "edge jump". Considering the sample stoichiometric, these quantities are related as follows:

$$Fe_{redox} = \frac{2 \times n_{Fe^{2+}} + 3 \times n_{Fe^{3+}}}{n_{Fe^{2+}} + n_{Fe^{3+}}} = \frac{8 - x}{3 - x} \quad (4.2)$$

where $n_i$ is the $i$ specie concentration per formula unit.

The under oxidation of high Cr content samples is not surprising since the UHV O-MBE chamber provides a reducing environment and the synthesis was performed within an oxygen limited window. Because of these conditions, even trace amounts of metallic iron were found for samples with high Cr content, as discussed at the beginning of this section. Point defects formation, such as oxygen and cation vacancies and/or interstitials[32], is always a possibility in transition metal oxides. In this work, these defects may occur as a response to the imbalance between the low oxygen flux and excess metal flux.

It is important to note, however, that the treatment of XANES spectra also has its limitations, which produces typical error of 1% in the oxidation states and thus a $\pm$ 0.1 error bar in the $x$ values. Notably, the edge positions are very sensitive to the background subtraction (see **Section 2.3.2.1**). To add consistency to the analysis, the function used to trace the pre- and post-edge background were delimited in the same energy range and $E_0$ position. Except for $x$ = 0.2, $x$ = 0.5 and $FeAl_2O_4$ reference, which presented very curvy background, and had to be treated differently. Moreover, the precision of the $Fe_{redox}$ value depends on the quality of the references. The purity and oxidation state of these samples were also investigated using XPS. The "edge jump" of $FeAl_2O_4$ reference was at the same position as another reference: $Fe_2SiO_4$, whose XPS spectrum shows typical chemical shift and charge transfer satellites of $Fe^{2+}$ species (**Section 2.3.1**). Likewise, the XPS spectrum of the $Fe_2O_3$ reference has typical chemical shift and charge transfer satellites of $Fe^{3+}$ species, as depicted in **Figure 2.6**.

Other interesting results of Fe K-XANES measurements come from the pre-edge features (**Figure 4.19b**). This region corresponds to transitions from $1s$ to $3d$-like levels, whose features depend on the intensity of $Fe^{2+}$ and $Fe^{3+}$ contribution to Td and Oh-sites of the $Fe_{3-x}Cr_xO_4$ spinel structure. In general, the increase of Fe redox ratio shifts the pre-edge centroid position to higher energies. In addition, the intensity of the pre-edge peak is significantly higher for Fe in Td-sites than in Oh-sites [19]. As shown in **Figure 4.19b**, compositions with $0 \leq x \leq 0.5$ have similar pre-edge shape, which means that they have similar cation distribution. Briefly, the pre-edge position is shifted to lower energies in comparison with $Fe_2O_3$ reference ($p_1$), so both $Fe^{2+}$ and $Fe^{3+}$ species are presented in these films. The $Fe^{2+}$ contributions ($p_2$) are not pronounced, so these cations occupy mainly Oh-

[32] According to thermodynamic studies [18], cation vacancies and interstitials are the majority defects for $Fe_3O_4$ and iron based spinels at constant temperatures. Whereas cation vacancies are formed at high oxygen partial pressure, cation interstitials are formed at low oxygen partial pressure. Therefore, these defects are probably the majority as well in the case of iron chromites.

sites. Note that the signal intensity at $p_2$ increases as $x$ increases, which indicates that part of the $Fe^{2+}$ ions are displaced to Td-sites. However, none of the samples has $Fe^{2+}$ ions exclusively at Td-sites, since this signal is not yet very intense. In order to quantify the cation distribution, the pre-edge region can be deconvoluted either by aid of simulations (*e.g.,* CFM) or by linear combination of reference spectra. Since the signal is small and wide, background subtraction is not evident and both treatments become very challenging. The cation distribution was then obtained by analyzing another part of the absorption spectra: the Fe and Cr $L_{2,3}$-edge (**Section 4.5**).

### 4.4.3 Fe and Cr coordination shell and bond distances

To investigate further structural disorders around cations, K-shell extended X-ray absorption fine structure (EXAFS) measurements were performed for selected samples ($x$ = 0.2, 0.7 and 1.2). The corresponding spectra are shown in **Figure 4.20**, along with model fits (**Figure 4.21**) described in detail in **Section 2.3.2.1**. Herein, the EXAFS signal is the sum of all species contributions. In the classical model fit, it is described as the sum of parametrized sinusoids. Hence, an average sinusoidal signal parameterized by an average distance and a dumping due to disorder (*i.e.,* Debye-Waller parameter) is obtained. In the spinel structure, cations sit at Oh or Td-sites, so the resulting EXAFS signal is the sum of these two contributions.

In **Figure 4.20**, the three nearest coordination shells around the cations (M = Cr or Fe) are analyzed and three main distances are given by the fits: M–O, $M_{Oh}$–$M_{Oh}$ and $M_{Oh}$–$M_{Td}$. Two fitting strategies can be proposed: either exhaustively describe the diffusion pathways or consider average pathways. In order to reduce the number of fitting parameters and perform a more robust and replicable fit the second strategy was chosen. Consequently, the first M–O distance is an average of the two sites. Moreover, the second $Fe_{Oh}$ and $Cr_{Oh}$ neighbors are merged into a single contribution since the diffusion factors of Fe and Cr are almost indistinguishable. Three further simplifications of the model fit were made: (*i*) Fe and Cr were considered homogeneously distributed in the structure; (*ii*) one assumed that Cr never sits at Td-sites; and (*iii*) the $S_0^2$ parameters (*i.e.* many-body reduction factor) were determined by the respective corundum structure: $Cr_2O_3$ and $Fe_2O_3$. Herein, the aim is to understand the variations observed in the series in the light of the change in composition. To do so, all spectra were fitted using the same simplified model, even if imperfect, rather than trying to make the best possible fit for each individual piece of data.

As shown in **Figure 4.21**, good fits are found assuming that Cr sits exclusively at Oh-sites, while Fe occupies both Td and Oh-sites (*i.e.* there is a systematic presence of $Fe_{Oh}$–$M_{Oh}$ and $Fe_{Oh}$–$Fe_{Td}$ bond lengths in all films). In general, average bond distances obtained with these fits were slightly smaller compared to bulk values (**Table 4.3**). Herein, the error bars are in the last decimal digit. For instance, Cr–O, Cr–$M_{Oh}$ and Cr–$Fe_{Td}$ bonds for $Fe_{1.8}Cr_{1.2}O_4$ films have respective average lengths of 0.1978, 0.2985 and 0.3527 nm, while the same bonds for bulk $FeCr_2O_4$ have lengths of 0.1994, 0.3019 and 0.3540 nm. The same trend is found for the Fe spectra. Analysis of the nearest-neighbor Fe–O, Fe–$M_{Oh}$ and Fe–$Fe_{Td}$ distances reveals that the fitted distances lie below those for both inverse spinel

magnetite and normal spinel chromite. This finding corroborates well with the shrinkage of the out-of-plane parameter observed in the DRX results (**Figure 4.9**).

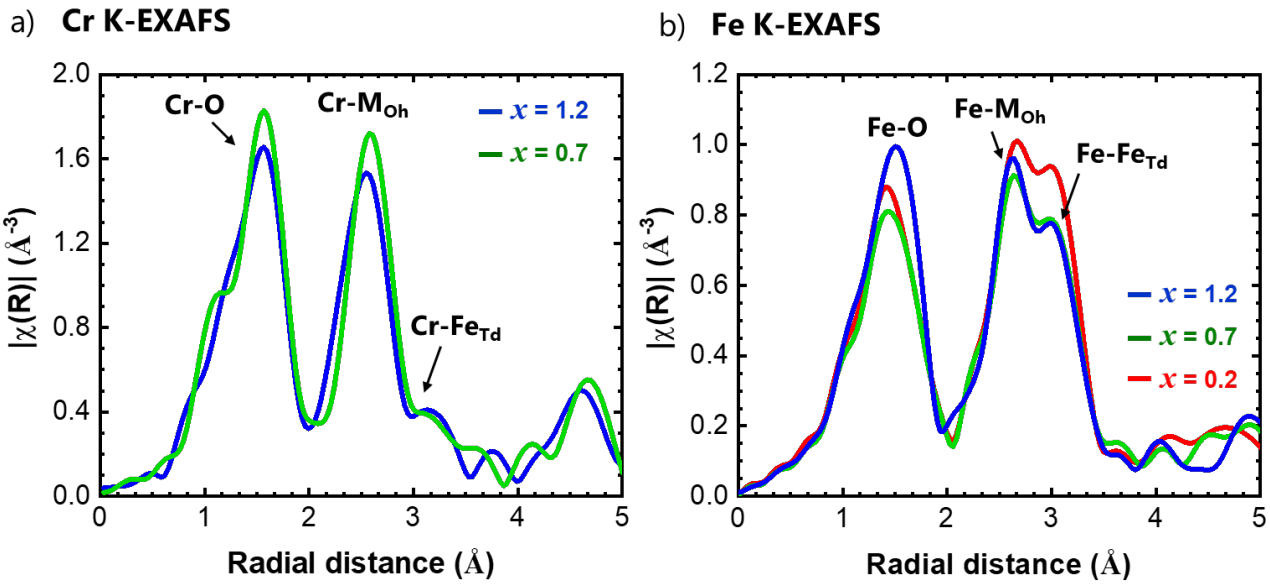


**Figure 4.20.** (a) Cr and (b) Fe K-EXAFS for representative $Fe_{3-x}Cr_xO_4$ thin films. Bond distances of the three nearest coordination shells are depicted: M–O, $M_{Oh}$–$M_{Oh}$ and $M_{Oh}$–$M_{Td}$, where M = Fe or Cr. Color code: $x$ = 0.2 (red), $x$ = 0.7 (green) and $x$ = 1.2 (blue).

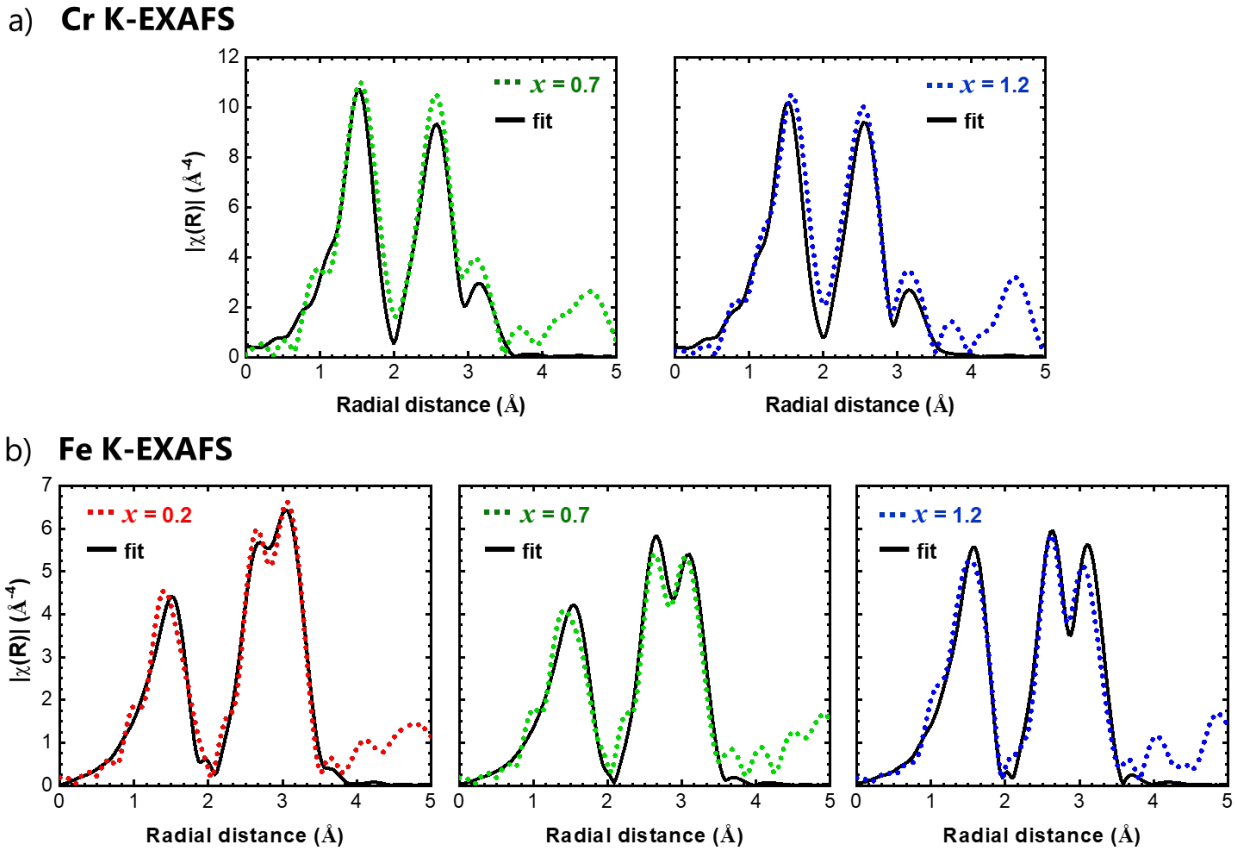


**Figure 4.21.** Measured (dots) and simulated (black lines) (a) Cr and (b) Fe K-EXAFS for representative $Fe_{3-x}Cr_xO_4$ thin films. Color code: $x$ = 0.2 (red), $x$ = 0.7 (green) and $x$ = 1.2 (blue).

**Table 4.3** – Distances obtained from fits of Cr and Fe K-EXAFS data for $Fe_{3-x}Cr_xO_4$ epitaxial thin films ($x$ = 0.2, 0.7 and 1.2), in comparison with bulk values for $Fe_3O_4$ (inverse spinel) and $FeCr_2O_4$ (normal spinel). Herein, the error bars are in the last decimal digit.

| Distances [nm] | Thin films | | | Bulk [20] | |
|---|---|---|---|---|---|
| | $Fe_{2.8}Cr_{0.2}O_4$ | $Fe_{2.3}Cr_{0.7}O_4$ | $Fe_{1.8}Cr_{1.2}O_4$ | $Fe_3O_4$ | $FeCr_2O_4$ |
| **Cr–O** | - | 0.197(4) | 0.197(9) | - | 0.199(4) |
| **Cr–$M_{Oh}$** | - | 0.299(6) | 0.298(5) | - | 0.301(9) |
| **Cr–$Fe_{Td}$** | - | 0.349(2) | 0.352(7) | - | 0.354(0) |
| **Fe–O** | 0.194(1) | 0.195(2) | 0.197(2) | 0.203(5)* | 0.199(7) |
| **Fe–$M_{Oh}$** | 0.296(4) | 0.295(3) | 0.295(3) | 0.301(7) | 0.354(0) |
| **Fe–$Fe_{Td}$** | 0.345(4) | 0.346(1) | 0.348(0) | 0.353(7) | 0.369(7) |

* This value is the weighted average between the $Fe_{Td}$–O (0.1912 nm) and $Fe_{Oh}$–O (0.2097 nm) distances.

It should be noted that EXAFS provides the average distance of all contributions in all directions, while XRD provides a measure of the lattice parameter in a specific direction (*i.e.,* 111). To be sure that the films are indeed compressed in all directions, complementary analysis (*e.g.* reciprocal space mapping [8]) are required. In addition to the overall reduction of the distances, one also observes in **Table 4.3** that the $M_{Oh}$–$M_{Oh}$ bond length decreases while the $M_{Oh}$–$Fe_{Td}$ increases as the Cr content increases. This is an important result as it suggests that larger $Fe^{2+}$ ions are displaced from Oh to Td-sites. Therefore, just like the bulk series, the thin films of $Fe_{3-x}Cr_xO_4$ evolves from the inverse to the normal spinel configuration. The remaining question is by how much. That is, what is the inversion parameter ($y$) of these films? The answer of this question is found in next section with the analyses of the Fe $L_{2,3}$-edge XAS and XMCD spectra.

## 4.5 Fine structure investigation

### 4.5.1 XAS and XMCD results at T = 300 K

In order to comprehend thoroughly the compositional effects on the physical and chemical properties of the $Fe_{3-x}Cr_xO_4$ series, the cationic site distributions in these thin films were investigated via X-ray magnetic circular dichroism (XMCD) measurements. The XMCD spectra result from the difference between spectra recorded with circularly right and left polarizations at a given absorption edge for a sample exposed to a magnetic external field parallel to the beam. An assessable XMCD signal is associated with a non-zero magnetic moment along the light propagation axis. More precisely, the XMCD signal here is related to the presence of a ferromagnetic or ferrimagnetic long-range order. Both Cr and Fe $L_{2,3}$-edge XAS and XMCD measurements were recorded at DEIMOS Beamline of synchrotron SOLEIL [21]. For simplicity, the spectra of Cr are first discussed.

### 4.5.1.1 Cr $L_{2,3}$-edge XAS and XMCD spectra

**Figure 4.22** shows the Cr $L_{2,3}$-edges XAS (upper panel) and XMCD (lower panel) spectra of four representative $Fe_{3-x}Cr_xO_4$ thin films recorded at room temperature. Similar to the Cr K-edge XANES measurements (**Figure 4.16**), the Cr $L_{2,3}$-edges XAS and XMCD spectra collected for the iron chromites presented similar features for all compositions. The spectra are divided in the spin-orbit split $L_3$ (~577 eV) and $L_2$ (~585 eV) parts. One observes that the difference between the maxima of the $L_2$ and $L_3$ edges ($\Delta L_{2\text{-}3}$) progressively increased from 7.6 eV ($x$ = 0.2) to 7.9 eV ($x$ = 1.4). Meanwhile, the difference between the two maxima of $L_3$ edges ($\Delta L_3$) progressively decreased from 1.4 eV ($x$ = 0.2) to 1.2 eV ($x$ = 1.4). For the sake of comparison, $\Delta L_{2\text{-}3}$ and $\Delta L_3$ for $\alpha$-$Cr_2O_3$ is 8.2 eV and 1.05 eV [22], respectively. The XAS spectra at $L_{2,3}$-edges probe the $3d$ orbitals. The subtle differences observed in the spectra can be due to changes in the crystal field and the covalence of Cr-O bond, which can be justified on the grounds of variations in the Cr local environment.

CFM calculations were performed in order to explore the XAS and XMCD results. These simulations described the transition for a single $Cr^{3+}$ ion from the $2p^63d^3$ ground state to the $2p^63d^4$ excited state. This transition results in atomic multiplets, parametrized by the Coulomb and exchange interactions ($F^k_{dd}$, $F^k_{pd}$, $G^k_{pd}$), the spin–orbit coupling ($\zeta_{2p}$ and $\zeta_{3d}$) and the crystal field ($\Delta$). Herein, these parameters were adjusted to minimize the differences between the calculated and the experimental spectra. The spin-orbit coupling was considered at 100% of its free ion value to match the energy difference between the $L_3$ and $L_2$ peak centers. Regarding the symmetry, both XAS and XMCD curves of Cr were described properly using only $Cr^{3+}$ ion in an Oh environment. This result confirms that $Cr^{3+}$ cations replace $Fe^{3+}$ cations exclusively at Oh-sites of the spinel structure for all samples.

The crystal field parameter ($\Delta$) and the reduced Racah parameter (B) were determined from the fitting procedure. In the Oh symmetry, the value of $\Delta$ is the energy splitting of the $3d$ level into $e_g$ and $t_{2g}$ subsets at final states. In order to account the iono-covalent behavior of the Cr-O chemical bond, the calculated Racah parameter for the free ion ($B^0$ = 0.154 eV) is reduced by a $\kappa$ factor ($\kappa = B/B^0$). As depicted in **Figure 4.23a**, for a given value of $\kappa$, increasing the value of $\Delta$ from 1.5 to 2.5 eV did not substantially change the position of the peaks, however, it had great influence in the relative intensities between the $L_{2,3}$-edges maxima and in the intensity of the low energy shoulder (~574.4 eV). Meanwhile, the $\kappa$ factor modified the general shape of the spectra and the $\Delta L_{2\text{-}3}$. When the $\kappa$ factor increases, the peak at ~574.4 eV (dark arrow in **Figure 4.23b**) disappears steadily and the $L_3$-edge maximum (~576.6 eV) is displaced towards higher energies and decreases in intensity. Hence, $\kappa$ values were determined from the experimental value of $\Delta L_{2\text{-}3}$, which progressively increased from 0.55 ($x$ = 0.2) to 0.65 ($x$ = 1.4). Then, $\Delta$ values were adjusted in order to reproduce the experimental Cr $L_{2,3}$-edges (**Figure 4.22**, red line). In particular, I checked the relative intensity of the low energy shoulder (~574.4 eV) of the isotropic spectra and the position of the respective peak in the dichroic signal. The deduced $\Delta$ progressively decreased from 2.2 eV ($x$ = 0.2) to 1.8 eV ($x$ = 1.4).

Note that the differences between the Cr $L_{2,3}$-edge spectra are more pronounced for intermediate compositions. This is due to a change in the spinel configuration for $x > 0.5$. As shown by the EXAFS results, inclusion of $Fe^{2+}$ in adjacent Td-sites causes distortions in the $CrO_6$ octahedron.

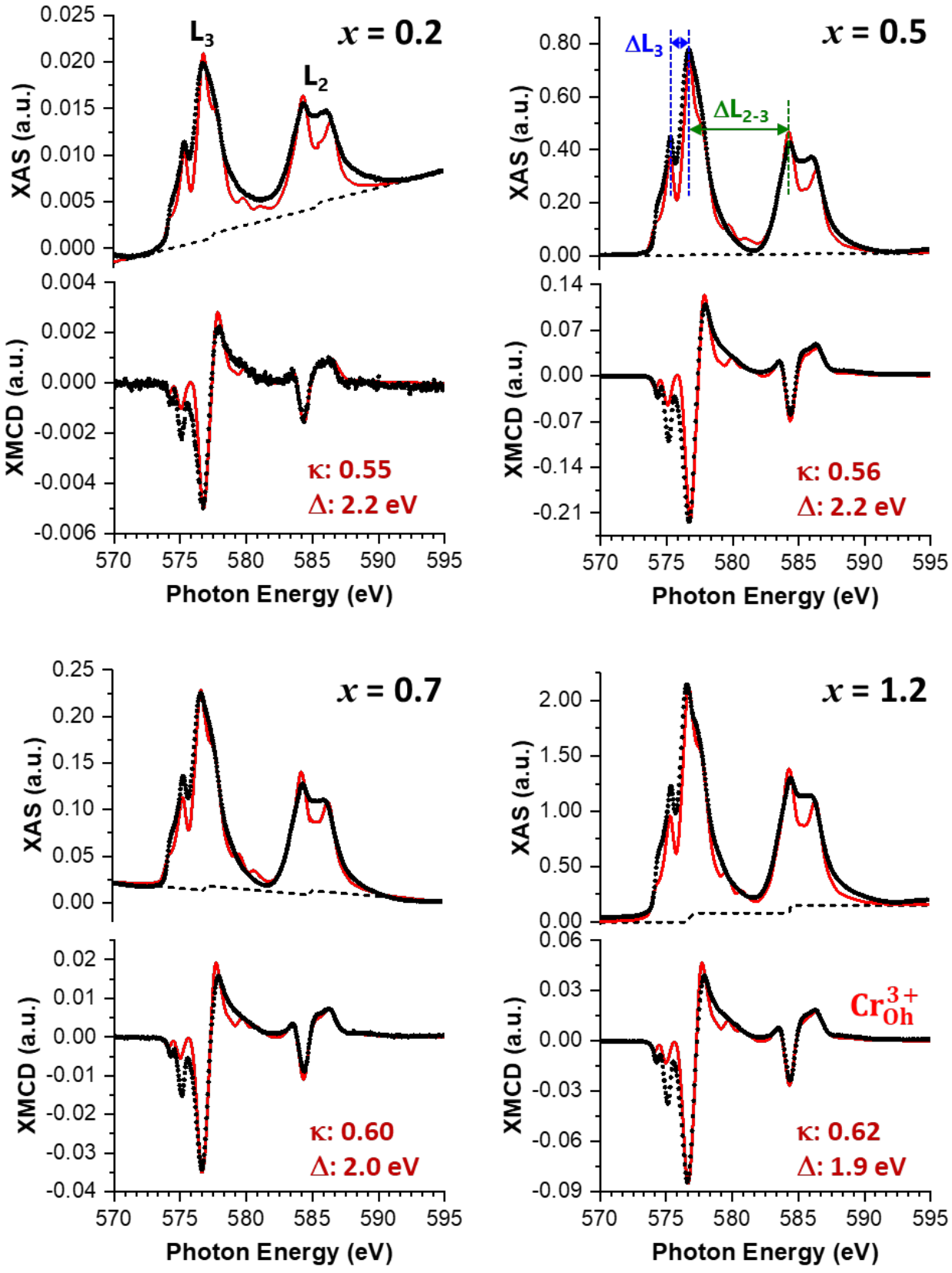


**Figure 4.22.** Experimental Cr $L_{2,3}$-edge XAS (top) and XMCD (bottom) spectra measured at B = 2.0 T and at room temperature (black dots). To facilitate comparison with calculations, which themselves have no background, the raw spectra were normalized to the pre-edge and the background constant to 1 was subtracted. After this operation, step-like backgrounds (dashed lines) were traced. In inset, the CFM parameters ($\kappa$ and $\Delta$) used in the simulation of each spectrum (red lines).

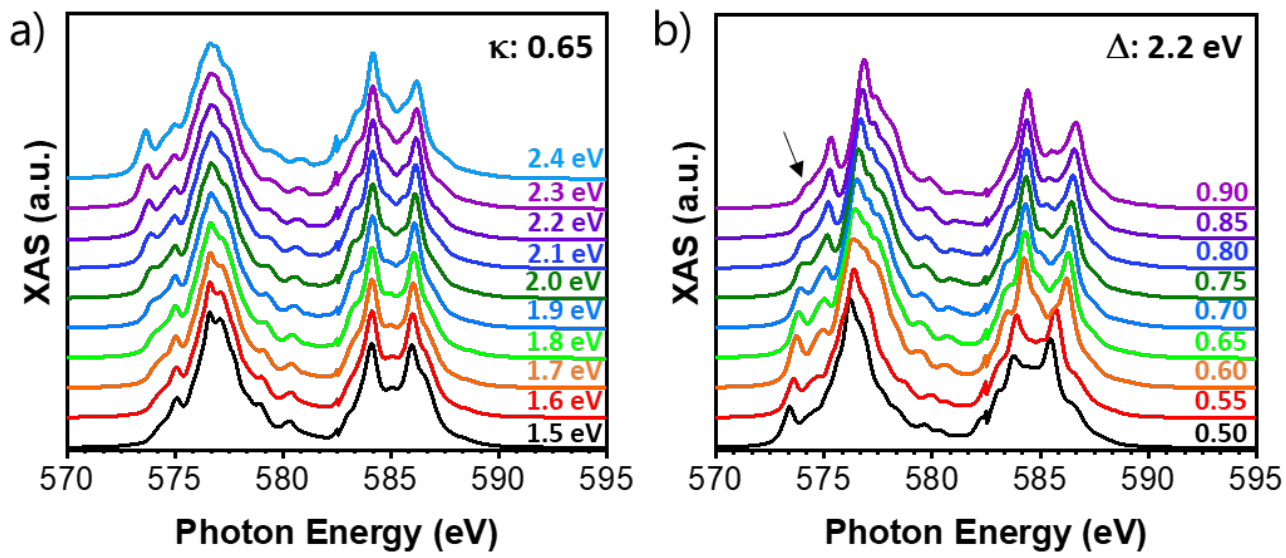


**Figure 4.23.** Calculated Cr $L_{2,3}$-edge XAS spectra with (a) $\kappa$ = 0.65 while $\Delta$ varies from 1.5 eV to 2.4 eV in 0.1 eV steps and (b) $\Delta$ = 2.2 eV while $\kappa$ varies from 0.50 to 0.90 in 0.05 steps.

Once it was proved that Cr cations sit exclusively in Oh-sites, my attention turned to the Fe cations.

### 4.5.1.2 Fe $L_{2,3}$-edge XAS and XMCD spectra

**Figure 4.24** depicts the Fe $L_{2,3}$-edge XAS and XMCD spectra of four representative iron chromite thin films ($x$ = 0.2, 0.5, 0.7 and 1.2). The spectra are divided in the spin-orbit split $L_3$ (~707 eV) and $L_2$ (~720 eV) parts and display the multiplet structure typical of the ionic nature of iron. The Fe-$L_3$ edge can be decomposed in four distinct contributions:

A. the peak at 705.5 eV comes mainly from $Fe^{2+}$ in Td-sites (blue area);

B. the one at 706.2 eV comes from $Fe^{2+}$ (green area) and $Fe^{3+}$ (pink area) ions in Oh-sites;

C. the peak at 707.3 eV comes exclusively from $Fe^{3+}$ ions in Td-sites (yellow area);

D. the one at 708.0 eV is linked to $Fe^{3+}$ ions in Oh-sites.

The $Fe_{Td}$ and $Fe_{Oh}$ (or $Cr_{Oh}$) contributions in the XMCD spectra have opposite sign, confirming the ferrimagnetic order with an antiparallel alignment between magnetic moments in Td and Oh sites. In this study, the XMCD measurements were carried out in saturated magnetic field (*i.e.,* 2 T), so the magnetization can be determined quantitatively. The size of the Fe $L_{2,3}$-edge XMCD signal reduces as the Cr content increases: from 30% of the XAS signal for $Fe_3O_4$ to only 2% of the XAS signal for $Fe_{1.6}Cr_{1.4}O_4$. Therefore, the total magnetic moment diminishes with the insertion of Cr in the magnetite structure, as confirmed later by VSM measurements (see **Section 5.2**).

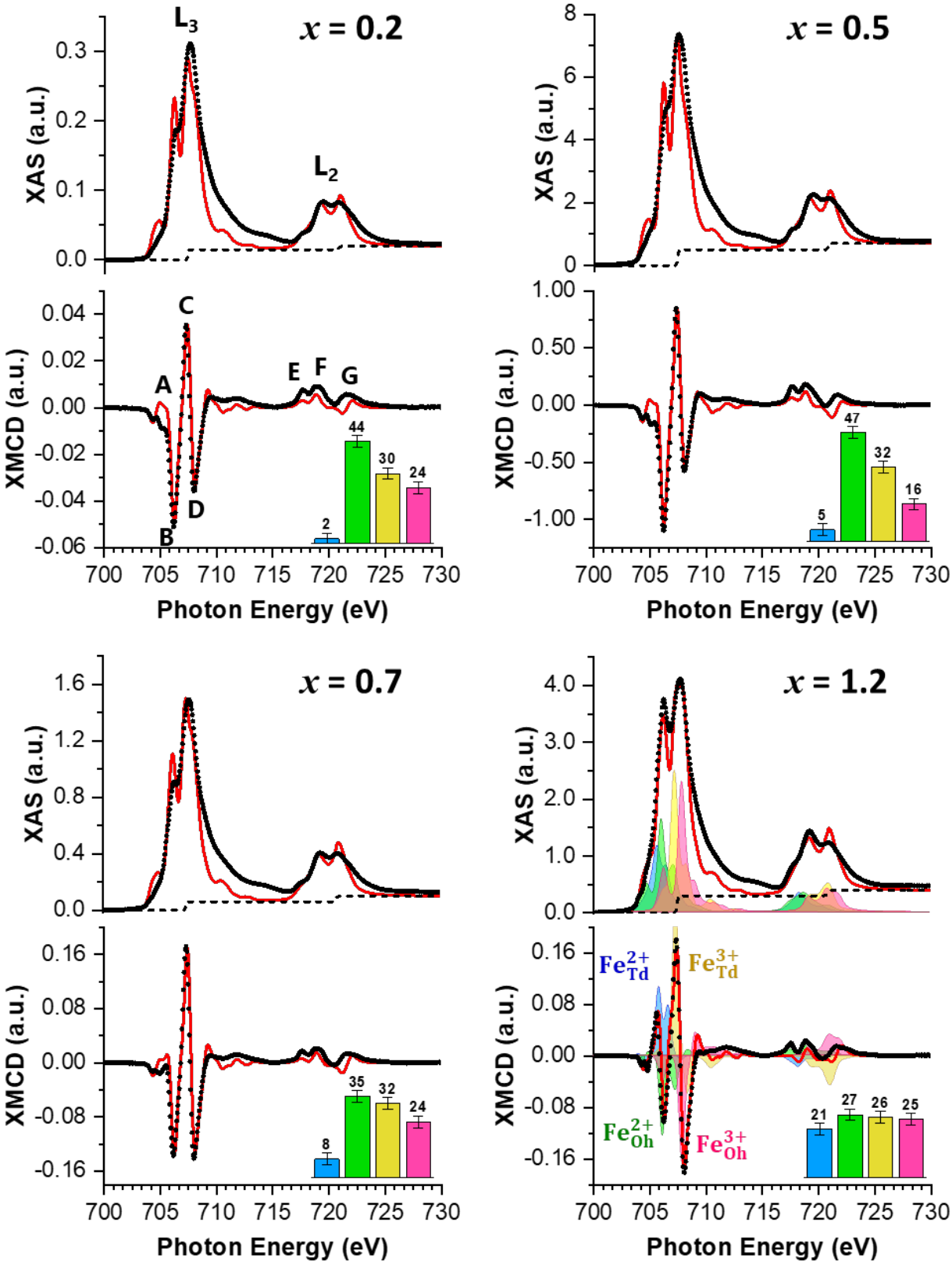


**Figure 4.24.** Experimental Fe $L_{2,3}$-edge XAS (top) and XMCD (bottom) spectra measured at B = 2.0 T and at room temperature. The calculated contribution for each iron species is shown in the right bottom spectra: $Fe^{2+}{}_{Td}$ (blue), $Fe^{2+}{}_{Oh}$ (green), $Fe^{3+}{}_{Td}$ (yellow) and $Fe^{3+}{}_{Oh}$ (pink). The red line depicts the sum of the cation contributions calculated by CFM. To facilitate comparison with calculations, the raw spectra were normalized to the pre-edge and the background constant to 1 was subtracted. After this operation, step-like backgrounds (dashed lines) were traced. In inset, the distribution of Fe species (in %).

CFM calculations were performed to interpret this complex spectral shape. They described the transitions for a single $Fe^{2+}$ (or $Fe^{3+}$) cations from the $2p^63d^6$ (or $2p^63d^5$) ground states to the $2p^53d^7$ (or $2p^53d^6$) excited states, respectively. Similar to the simulations for Cr, electron–electron interactions were reduced by a κ factor, which takes into account effects such as covalency and charge transfer. Meanwhile the energy splitting of the $3d$ level were determined by the crystal field parameter: Δ. In order to mimic the XAS and XMCD spectra of Fe, it was necessary to combine calculated curves of four independent species: $Fe^{2+}$ and $Fe^{3+}$ in both $O_h$ and $T_d$ symmetry. In the fitting procedure, $\Delta_o$, $\Delta_t$ and κ are adjustable parameters. Contrary to the Cr $L_{2,3}$-edge spectra, the position of the spectra features did not significantly change with Cr composition. For instance, the differences between the $Fe^{3+}{}_{Td}$ and $Fe^{3+}{}_{Oh}$ contributions and the $Fe^{2+}{}_{Oh}$ and $Fe^{3+}{}_{Oh}$ contributions were respective 0.7 and 1.8 eV for all dichroic spectra. Hence, $\Delta_o$, $\Delta_t$ and κ values were adjusted in order to reproduce the appropriate peak positions for both isotropic and dichroic spectra.

In general, increasing κ values shift the features towards higher energies, while increasing Δ values change the intensity ratio between features of $L_2$ and $L_3$ edges. As depicted in **Figure 4.25a-b**, κ factor and $\Delta_o$ for $Fe^{3+}$ were adjusted simultaneously to obtain CD and DG distances around 0.7 eV and 13 eV, respectively. Optimal values of κ factor was found to be around 0.60. This same factor was used to adjust $\Delta_o$ for $Fe^{2+}$ (**Figure 4.25c**) in order to obtain BE and BF distances around 12 eV and 13 eV. Optimal values of $\Delta_o$ was found to be 1.4 eV ($Fe^{2+}$) and 1.5 eV ($Fe^{3+}$), while $\Delta_t$ was approximated to -4/9 of the value for the octahedral field ($\Delta_t$ = -0.6 eV for $Fe^{2+}$ and -0.7 for $Fe^{3+}$).

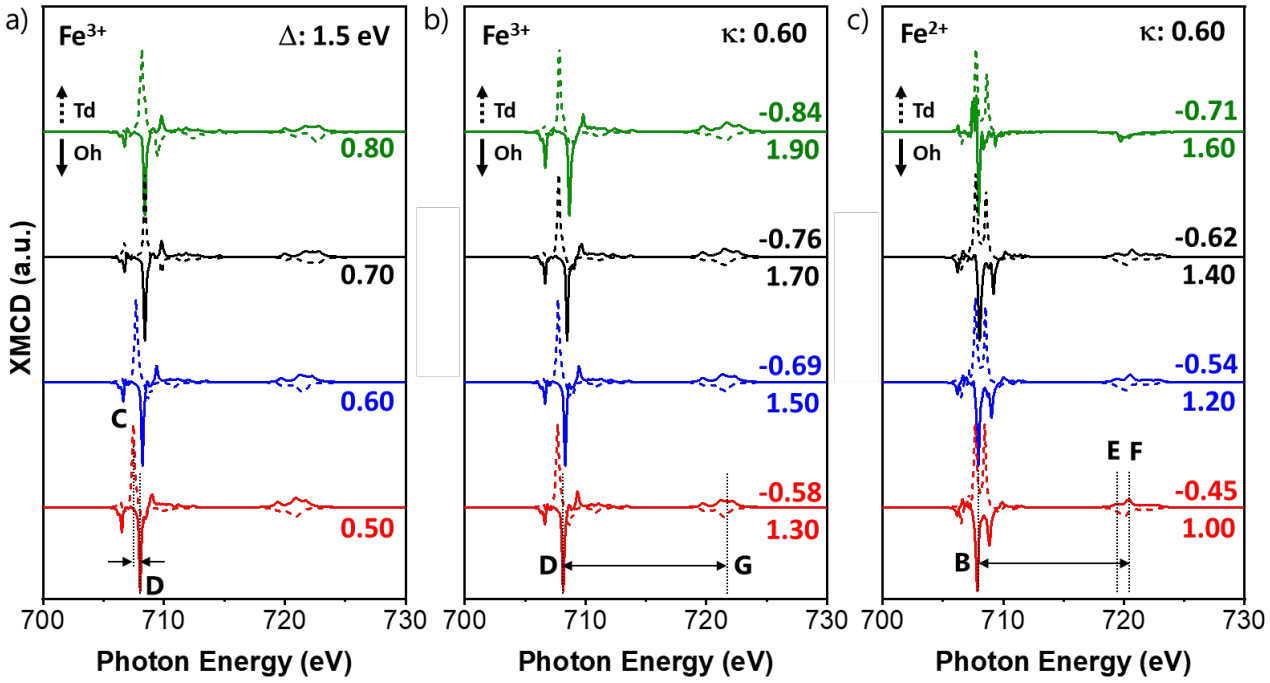


**Figure 4.25.** Calculated $L_{2,3}$-edge XAS spectra for (a) $Fe^{3+}$ with $\Delta_{Oh}$ = 1.5 eV while κ varies from 0.50 to 0.80 in 0.1 steps, (b) $Fe^{3+}$ with κ = 0.60 while $\Delta_{Oh}$ varies from 1.30 eV to 1.90 eV in 0.2 eV steps, and (c) $Fe^{2+}$ with κ = 0.60 while $\Delta_{Oh}$ varies from 1.00 eV to 1.60 eV in 0.2 eV steps. In all cases, $\Delta_t$ is approximated to -4/9 of the value for the octahedral field. The $Fe_{Oh}$ spectra (solid lines) have opposite signs than $Fe_{Td}$ spectra (dashed lines) since these species are coupled antiferromagnetically in the spinel structure.

These values are smaller than those extracted from optical spectroscopy (~2.2 eV [23], [24]) due to $2p$ hole in the excited state. However, they are consistent with the ones found in the literature for $Fe^{2/3+}$ multiplet calculations on iron oxides [7], [25], [26]. It should be noted that the shift of 0.5 eV between the maxima of the $Fe^{2+}$ and $Fe^{3+}$ calculated $L_3$-edges does not correspond to the real shift between the contributions of the two ions (~1.8 eV). The best agreement between $Fe^{2+}$ and $Fe^{3+}$ peak positions is obtained when the contribution of $Fe^{2+}$ ions is shifted by 1.4 eV from its calculated position.

The cationic site distribution of the iron chromites was then determined so that the weighted sum of each calculated contribution reproduces the intensity and shape of both dichroic and isotropic experimental spectra (**Figure 4.24**, red line). **Table 4.4** summarizes the atomic and crystal field parameters for independent Cr and Fe sites optimized in this work. To calculate XMCD spectra, external magnetic field ($H_{ex}$) was added to account for Zeeman effects. The sign of $H_{ex}$ determines the sign of the dichroic signal. The resulting sharp peaks were convoluted with a Lorentzian function (FWHM = 0.2 eV for $L_3$ edge and 0.6 eV for $L_2$ edge) and a Gaussian function (FWHM = 0.5 eV) to describe the core-hole lifetime and instrumental broadening processes.

**Table 4.4** – Energy values (eV) of atomic parameters, crystal field ($\Delta$) and external magnetic field ($H_{ex}$) considered for the simulation of XAS and XMCD curves of each specie present in the $Fe_{3-x}Cr_xO_4$ series.

| Parameter | $Cr^{3+}_{Oh}$ | | $Fe^{2+}_{Td}$ | | $Fe^{2+}_{Oh}$ | | $Fe^{3+}_{Td}$ | | $Fe^{3+}_{Oh}$ | |
|---|---|---|---|---|---|---|---|---|---|---|
| | Ground state | Final state | Ground state | Final state | Ground state | Final state | Ground state | Final state | Ground state | Final state |
| $F^2_{dd}$ | * | * | 6.60 | 7.07 | 6.60 | 7.07 | 7.23 | 7.69 | 7.23 | 7.09 |
| $F^4_{dd}$ | * | * | 4.09 | 4.40 | 4.09 | 4.40 | 4.52 | 4.81 | 4.52 | 4.81 |
| $F^2_{pd}$ | - | 5.22 | - | 4.08 | - | 4.08 | - | 4.47 | - | 4.47 |
| $G^1_{pd}$ | - | 4.79 | - | 3.00 | - | 3.00 | - | 3.34 | - | 3.34 |
| $G^3_{pd}$ | - | 2.18 | - | 1.71 | - | 1.71 | - | 1.90 | - | 1.90 |
| $\zeta_{2p}$ | - | 5.67 | - | 8.20 | - | 8.20 | - | 8.20 | - | 8.20 |
| $\zeta_{3d}$ | 0.035 | 0.047 | 0.052 | 0.067 | 0.052 | 0.067 | 0.059 | 0.074 | 0.059 | 0.074 |
| $\Delta$ | ** | ** | -0.62 | -0.62 | 1.40 | 1.40 | -0.67 | -0.67 | 1.50 | 1.50 |
| $H_{ex}$ ($10^{-4}$) | +1.2 | +1.2 | -1.2 | -1.2 | +1.2 | +1.2 | -1.2 | -1.2 | +1.2 | +1.2 |

* The calculated Racah parameter for the free ion ($B^0_X = 9F^2_{dd} - 5F^4_{dd} = 0.154$ eV) is reduced by a $\kappa$ factor: $\kappa = B_X/B^0_X$. For Cr species, the reduction factor increased from 0.55 ($x$ = 0.2) to 0.65 ($x$ = 1.4).

** The crystal field parameter was also adjusted to reproduce the experimental Cr $L_{2,3}$-edges. Its value progressively decreased from 2.2 eV ($x$ = 0.2) to 1.8 eV ($x$ = 1.4).

**Figure 4.26** summarizes the Fe and Cr cation distribution on Td and Oh-sites derived from the best fit with the measured Fe $L_{2,3}$ XMCD spectra at room temperature (**Figure 4.24**, red line). One

observes that the $Fe^{3+}_{Td}$ and $Fe^{2+}_{Oh}$ molar fractions hold their respective value of ~0.3 and ~0.4 for $x \leq 0.5$, which steadily decrease for $x > 0.5$. Meanwhile, very little (or none) $Fe^{2+}_{Td}$ contribution is observed for $x \leq 0.5$ and its molar fraction only increases for $x > 0.5$. $Fe^{3+}_{Oh}$ molar fraction steadily decreases from 0.30 to 0.14 as the $Cr^{3+}_{Oh}$ molar fraction increases from 0 to 0.17 ($x$ = 0.5), but then changes little for greater Cr content. At this point, one can affirm that, for $x \leq 0.5$, $Cr^{3+}$ mostly replaced $Fe^{3+}$ ions at Oh-sites without changing the spinel configuration. However, for $x > 0.5$, each added $Cr^{3+}$ displaced one $Fe^{2+}$ from Oh sites, thereby changing the spinel configuration. This result is consistent with the outcomes of both structural and chemical analysis.

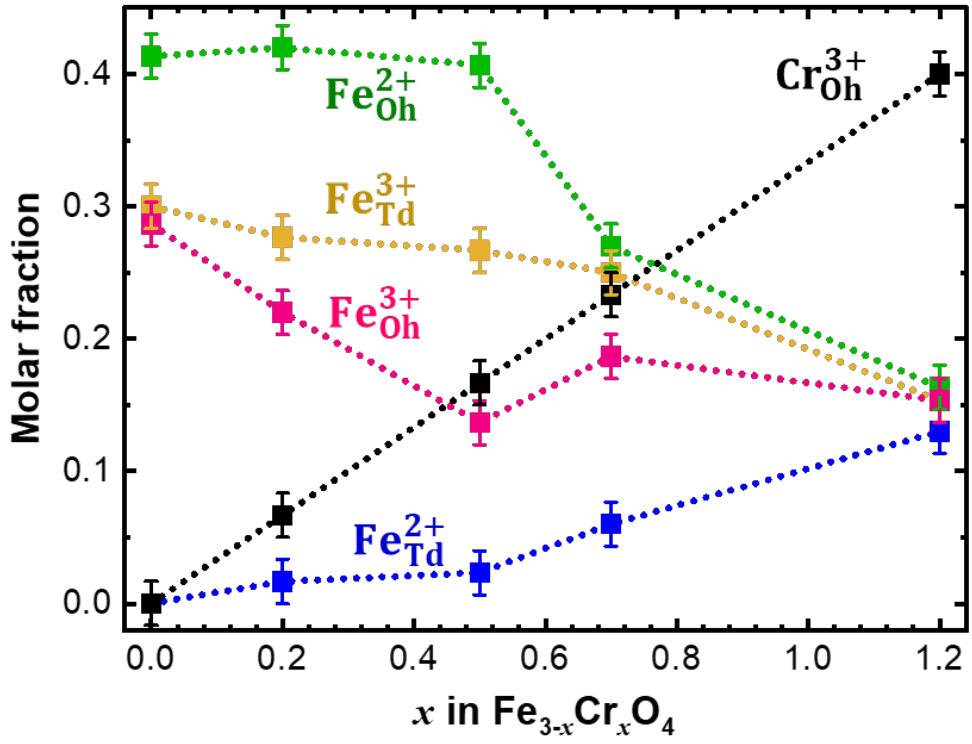


**Figure 4.26.** Molar fraction in $Fe_{3-x}Cr_xO_4$ thin films from CFM calculations. The calculated contribution for each specie is shown as: $Cr^{3+}_{Oh}$ (black), $Fe^{2+}_{Td}$ (blue), $Fe^{2+}_{Oh}$ (green), $Fe^{3+}_{Td}$ (yellow) and $Fe^{3+}_{Oh}$ (pink).

It is noteworthy that the XAS (or XMCD) quantitative analysis has an absolute uncertainty of about 10%. The inclusion of $Fe^{2+}_{Td}$ contributions up to 5% does not change significantly the quality of the fit for $x \leq 0.5$, which constitutes the error bars shown in **Figure 4.26**. Thus, small amounts of $Fe^{2+}$ can be included at Td-sites for these compositions, so that the spinel structure is not in a perfect inverse arrangement, but with an inversion ratio between 90% to 100%, as observed elsewhere [27]. By adding small contributions of $Fe^{2+}_{Td}$ at low Cr content, a linear relation (**Figure 4.27**) is found between the $Fe^{2+}_{Td}$ concentration and the increase of $Fe_{Oh}$-$Fe_{Td}$ distances observed in the EXAFS analyses (**Table 4.3**). This indicates that there are small amounts of $Fe^{2+}$ at the Td-sites for $x \leq 0.5$, even if XMCD is not sensitive enough to probe it.

Moreover, a $Fe^{3+}_{Td}$:$Fe^{2+}_{Oh}$ ratio of 3:4 is found instead of 1:1 as in an ideal spinel structure, which may be due to imperfections of the model fit. In fact, the model used here is very simple, since it does not account for charge transfer effects nor distortions in the cation local symmetry. The choice

of a simpler model was made due to its robustness and the smaller number of parameters considered in the fit. However, some adjustments could be added to the model. For instance, for higher Cr content ($x \geq 0.7$), one could consider a lower $D_{4h}$ symmetry for $Fe^{2+}_{Oh}$ to perceive Jahn-Teller effects. This symmetry can be related to an octahedron compressed or stretched along a $C_4$ axis. This distortion further splits the $t_{2g}$ set in $e_g$ and $b_{2g}$ orbitals separated by $\delta_1$ energy, which is related to the $D_{4h}$ CF parameters (Ds and Dt) through the relationship: $\delta_1$ = 3Ds - 5Dt. Likewise, the $e_g$ set is also split in $a_{1g}$ and $b_{1g}$ orbitals separated by $\delta_2$ energy, which has the following form: $\delta_2$ = 4Ds - 5Dt. Considering small distortions in the $FeO_6$ octahedron (*i.e.* Dq = 0.14 eV, Ds = 0.01 eV and Dt = 0 eV), a cationic distribution of $[Fe^{2+}_{0.29}Fe^{3+}_{0.55}]_{Td}[Fe^{2+}_{0.53}Fe^{3+}_{0.43}Cr^{3+}_{1.2}]_{Oh}O_4$ was found for $x$ = 1.2 instead of $[Fe^{2+}_{0.39}Fe^{3+}_{0.46}]_{Td}[Fe^{2+}_{0.49}Fe^{3+}_{0.46}Cr^{3+}_{1.2}]_{Oh}O_4$. As shown in **Figure 4.28**, this operation mainly increased the $Fe^{3+}_{Td}$ contributions. However, not much improvement was observed in the quality of the fit at the expense of adding two extra parameters: Ds and Dt.

The same can be said about adding charge transfer effects. Starting from the fundamental configuration $2p^63d^6$ for $Fe^{2+}$ ions, the transfer of one electron to the oxygen ligands leads to the $2p^63d^5L^1$ configuration (L = oxygen orbital). As discussed by Brice-Profeta [28, pp. 166–168], calculations that mix these two initial state configurations describe better the negative dichroic structure between 708 and 710 eV and the positive dichroic structure at 722.8 eV of the $Fe_3O_4$ XMCD signal. However, the increase in the number of parameters to be adjusted in order to consider the configuration interactions does not enable an unambiguous determination of a set of parameters for the simulation of experimental XAS and XMCD spectra.

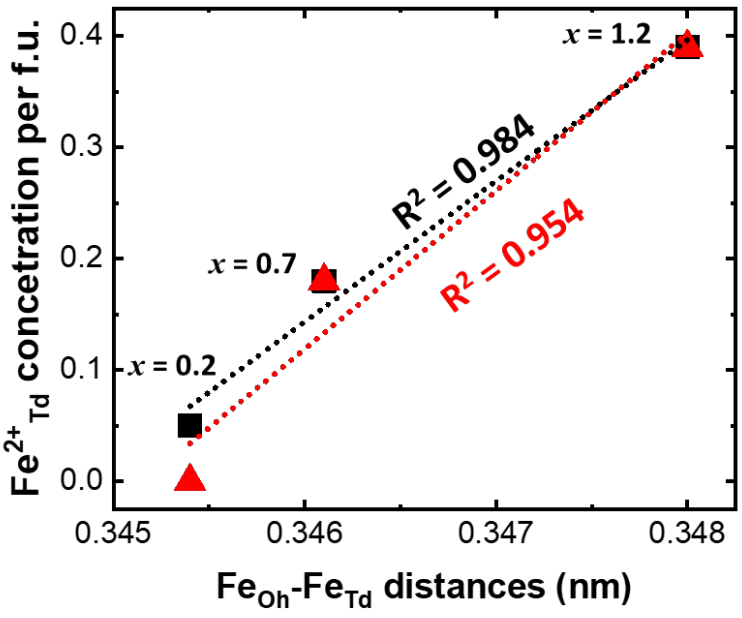


**Figure 4.27.** Linear regression between the concentrations of $Fe^{2+}_{Td}$ species probed by XMCD and the $Fe_{Oh}$–$Fe_{Td}$ distances from EXAFS analyses. Herein, the coefficient of determination ($R^2$) increases when small amounts of $Fe^{2+}$ are included in Td-sites of $Fe_{2.8}Cr_{0.2}O_4$.

Another explanation for the $Fe^{3+}_{Td}$:$Fe^{2+}_{Oh}$ ratio of 3:4 is a preferential formation of $Fe_{Oh}$-terminated (111) surfaces. The total electron yield used to record the XMCD spectra is known to be

rather surface sensitive in the soft X-ray regime [29]. The presence of $Fe_{Oh}$-terminated surface corroborates with DFT calculations [30], [31], for which $Fe_{Oh}$–O termination is found to be one of the most stable of the bulk-like terminations of $Fe_3O_4$ (111) over a broad range of oxygen chemical potentials. However, according to these studies, the energy difference between $Fe_{Oh}$–O and $Fe_{Td}$–O terminated surface is rather small (~0.03 eV) and we may probably have a mix of those two. Moreover, at first glance, a greater $Fe^{2+}$ contribution on the extreme surface is not in line with our XPS measurements, which pointed a slight over oxidation of the surface. According to XMCD results, the $Fe^{3+}{}_{Td}$:$Fe^{2+}{}_{Oh}$ ratio is ~0.7 for $x \leq 0.5$ but increases to ~0.9 for $x > 0.5$, which could explain the surprisingly similar Fe $2p$ spectra observed for the iron chromites series and the apparently over oxidation of the surface for higher Cr content.

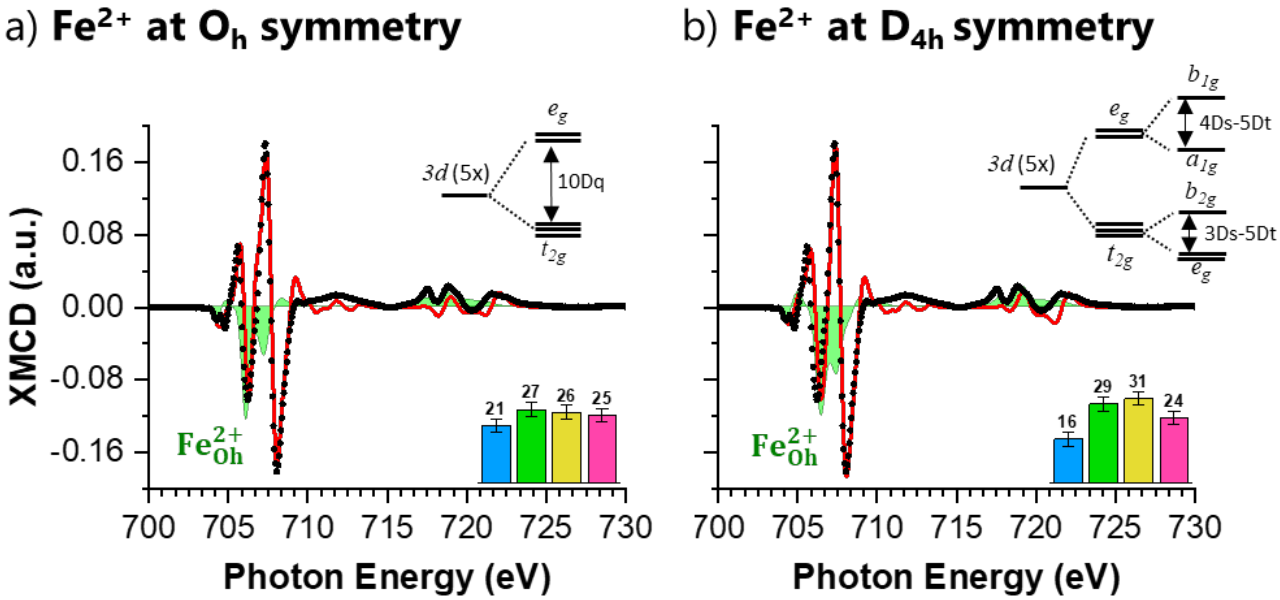


**Figure 4.28.** CFM calculations for XMCD spectra (black dots) measured at B = 2.0 T and at room temperature for $Fe_{1.8}Cr_{1.2}O_4$ thin films. The red line depicts the sum of the cation contributions calculated by CFM with (a) $Fe^{2+}$ at $O_h$ symmetry and (b) $Fe^{2+}$ at $D_{4h}$ symmetry. In inset, the energy level diagram (top) showing the 3d atomic orbitals splitting after considering the $O_h$ and $D_{4h}$ symmetry. The energy between orbitals is given in terms of the CF parameters (10Dq, Ds and Dt). At the right bottom the distribution of Fe species (in %): $Fe^{2+}{}_{Td}$ (blue), $Fe^{2+}{}_{Oh}$ (green), $Fe^{3+}{}_{Td}$ (yellow) and $Fe^{3+}{}_{Oh}$ (pink).

## 4.5.2 XAS and XMCD results at T = 4 K

As explained in **Section 1.3.2.2**, the $Fe_{3-x}Cr_xO_4$ series undergoes magnetic and structural phase transitions upon cooling from room temperature (**Figure 1.10**). Notably, the parent compound $Fe_3O_4$ shows a structural transition at 120 K (*i.e.,* Verwey temperature, $T_V$), where electrons on Oh-sites form a polaronic charge-ordered state inducing a monoclinic distortion. In order to investigate these magnetic and structural transitions, XAS and XMCD were also recorded at low temperature.

**Figure 4.29** compares the normalized XMCD spectra measured at 4 K and 300 K. A systematic shift of 0.5 eV to higher energies is observed in all spectra at 4 K. Due to the more insulator character

of the samples at low temperature (see **Section 5.3**), a very steep slope had to be removed, which introduces spurious energy shifts. This systematic error, however, did not distort the signals. The same energy differences between the $Fe^{3+}_{Td}$ and $Fe^{3+}_{Oh}$ contributions (~0.7 eV) and the $Fe^{2+}_{Oh}$ and $Fe^{3+}_{Oh}$ contributions (~1.8 eV) are found for all dichroic spectra. Therefore, all features observed in these spectra have physical meaning.

In general, the spectra at 4 K and 300 K depicted similar features. The Fe-$L_3$ edge is decomposed in the same four contributions related to the $Fe^{2+}_{Td}$, $Fe^{2+}_{Oh}$, $Fe^{3+}_{Td}$ and $Fe^{3+}_{Oh}$ species. This means that, at low temperature, these spinel compounds are still ferrimagnetic with spins at Td-sites antiparallel aligned to spins at Oh-sites. In addition, spectra at 4 K shows a systematic reduction of the B and D features related to the $Fe^{2+}_{Oh}$ and $Fe^{3+}_{Oh}$ species. Contrary to Mössbauer measurements, the $L_{2,3}$-edge XAS measurements are not able to detect charge delocalization in Fe ions[33]. Thus, the spectral difference observed in high and low temperature regime is not due to charge hopping and the establishment of a charge-ordered state at low temperature, but rather due to distortion of Fe Oh symmetry. Indeed, this spinel series may undergo cubic-to-tetragonal lattice transition at temperatures lower than 120 K [33].

Because $Fe^{2+}$ ions are Jahn-Teller active ($3d^6$, S = 2), their isotropic and dichroic contributions depend significantly on the symmetry of the crystal field. As shown in the literature, the XMCD signal calculated for $Fe^{2+}$ ions is strongly modified in the presence of tetragonal [34] or trigonal [28, pp. 159–161] distortions. **Figure 4.30** compares spectra simulated using a perfect Oh symmetry for $Fe^{2+}$ ions with those where small distortions were added to the $FeO_6$ octahedron (*i.e.,* Dq = 0.14 eV, Ds = 0.01 eV and Dt = 0 eV) for $x$ = 1.2. Herein, a better description of the dichroic signal, especially of the low energy shoulder in the C feature (~707 eV), is obtained in the $D_{4h}$ symmetry. Moreover, the cationic distribution obtained for this symmetry ($[Fe^{2+}_{0.45}Fe^{3+}_{0.54}]_{Td}[Fe^{2+}_{0.50}Fe^{3+}_{0.31}Cr^{3+}_{1.2}]_{Oh}O_4$) at 4 K is closer to the one obtained at 300 K ($[Fe^{2+}_{0.39}Fe^{3+}_{0.46}]_{Td}[Fe^{2+}_{0.49}Fe^{3+}_{0.46}Cr^{3+}_{1.2}]_{Oh}O_4$) than for perfect Oh symmetry ($[Fe^{2+}_{0.50}Fe^{3+}_{0.50}]_{Td}[Fe^{2+}_{0.41}Fe^{3+}_{0.37}Cr^{3+}_{1.2}]_{Oh}O_4$). Therefore, a distortion of the $Fe^{2+}_{Oh}$ sites should be considered for calculations at lower temperatures. However, these slight improvements in the spectra description arise from the addition of two extra parameters, which increases the complexity of the fits.

[33] Mössbauer and XAS techniques have different detection times. While characteristic detection time of Mössbauer spectroscopy is the inverse of the Larmor frequency of the nuclei (~$10^9$ $s^{-1}$), the characteristic time of the X-ray absorption process is about $10^{-15}$ s. Hence, for $Fe_3O_4$, Mössbauer spectroscopy detects a 2.5+ charge on the iron atoms above $T_V$ and 2+ and 3+ charges below $T_V$, [32] since the electron hopping frequency is inferior to the Larmor frequency of the $Fe^{57}$ nucleus at $T < T_V$. However, the electron hopping frequency for $Fe_3O_4$ remains inferior to $10^{15}$ $s^{-1}$ even above Verwey transition.

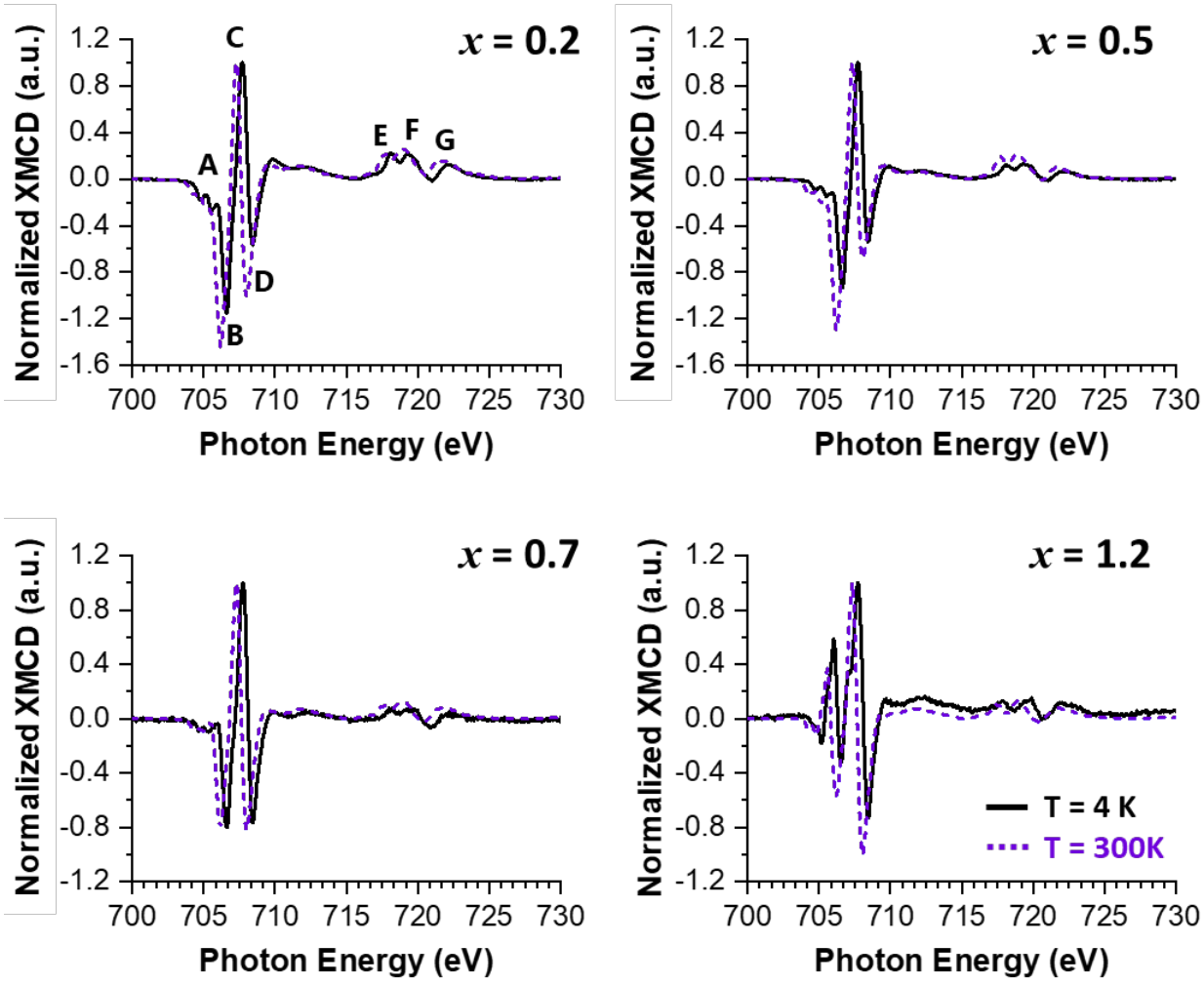


**Figure 4.29.** Normalized Fe $L_{2,3}$-edge XMCD spectra measured at B = 2.0 T and at T = 4 K (black line) in comparison with spectra recorded at T = 300 K (dashed purple line).

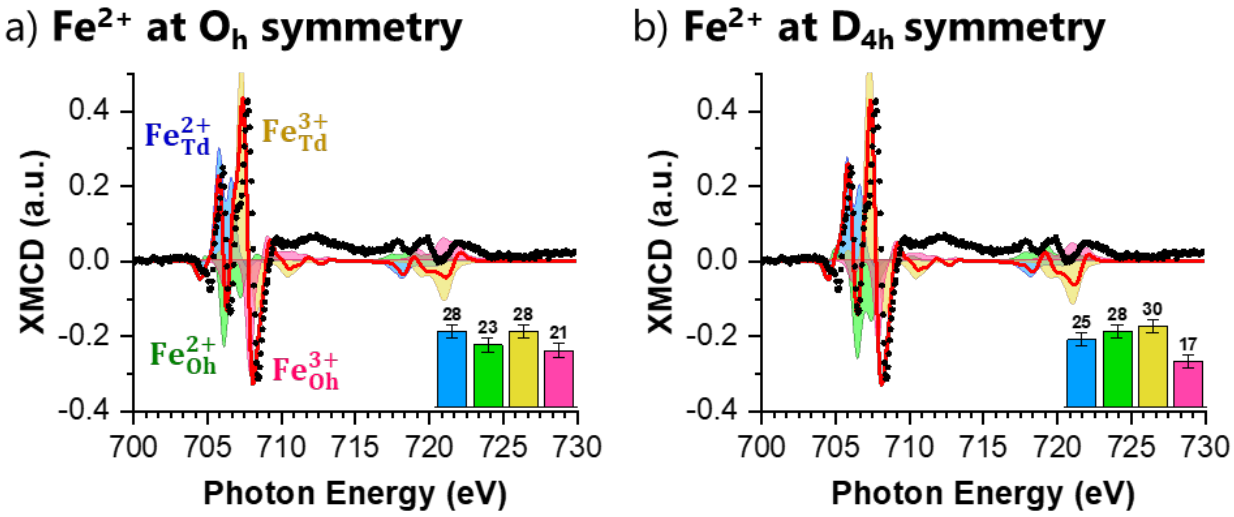


**Figure 4.30.** Experimental Fe $L_{2,3}$-edge XMCD (black dots) spectra measured at B = 2.0 T and at T = 4 K for $Fe_{1.8}Cr_{1.2}O_4$ thin films. The red line depicts the sum of the cation contributions calculated by CFM with (a) $Fe^{2+}$ at $O_h$ symmetry and (b) $Fe^{2+}$ at $D_{4h}$ symmetry. At the right bottom the distribution of Fe species (in %): $Fe^{2+}{}_{Td}$ (blue), $Fe^{2+}{}_{Oh}$ (green), $Fe^{3+}{}_{Td}$ (yellow) and $Fe^{3+}{}_{Oh}$ (pink).

**Highlights on the chemical properties of $Fe_{3-x}Cr_xO_4$ thin films:**

- A good agreement in the quantification of Fe and Cr elements are found between the STEM-EELS, STEM-EDX and core level spectroscopies.
  - For $x < 1.2$, the films are stoichiometric and homogeneous.
  - For $x \geq 1.2$, the films are slightly under oxidized.
  - Samples grown on $Fe_3O_4(111)$ buffer are not homogeneous in depth and had to be excluded from further analysis.
- The $Fe_{3-x}Cr_xO_4(111)$ thin films are formed by trivalent Cr cations at Oh-site and trivalent and divalent Fe cations shared at Oh and Td-sites of the spinel structure.
  - For $x \leq 0.5$, $Fe^{2+}$ ions sit exclusively at Oh-sites while $Fe^{3+}$ ions are shared between Td and Oh-sites (*i.e.,* inverse spinel configuration).
  - For $0.5 < x \leq 1.2$, $Fe^{2+}$ and $Fe^{3+}$ ions are found in both Td and Oh-sites (*i.e.,* intermediate spinel configuration).
- The inclusion of $Fe^{2+}$ in adjacent Td-sites caused distortions in the $CrO_6$ local environment.

## 4.6 Summary of results

Stoichiometric series of epitaxial 15 nm thick $Fe_{3-x}Cr_xO_4(111)$ thin films were successively grown on monocrystalline $\alpha$-$Al_2O_3$ (0001) substrates by O-MBE. Structural analyses confirmed that the films have bidimensional growth mode without secondary phases. For instance, $\theta$-$2\theta$ X-ray diffraction patterns exhibit only ($hhh$) peaks corresponding to the (111) orientation of the spinel structure, indicating the textured single-phase quality of these films. According to these measurements, the out-of-plane lattice parameters of the films are slightly smaller in comparison with the bulk, showing a residual strain of about 0.5%. This result corroborates with the outcomes of HRTEM micrographs and EXAFS analyses, which also indicate lattice shrinkage.

The chemical analyses showed that the iron chromite samples grown directly on the substrate were stoichiometric (or slightly under oxidized for $x \geq 1.2$) and homogeneous throughout the film. A perfect control of the film composition was achieved (within an error bar of $\pm 0.1$ for $x$) and the $x$ values obtained via XPS are used in all manuscript. Regarding the fine structure, Cr ions assume exclusively a $3+$ oxidation state and sit at Oh-sites for all films, while $Fe^{2+}$ and $Fe^{3+}$ ions populate both Td and Oh-sites. For $x \leq 0.5$, the iron chromites showed mostly an inverse spinel structure with very little $Fe^{2+}$ sitting at Oh-sites. For $x > 0.5$, $Fe^{2+}$ ions are steadily displaced to Td-sites and the spinel shows an intermediate configuration. The inclusion of bigger $Fe^{2+}$ ions at smaller Td-sites induced distortions in the local symmetry of adjacent Oh-sites, which were reflected in the shape of the K-XANES pre-edge features and in the EXAFS results.

For $x \leq 1.2$, the structural analyses showed high crystalline quality, low surface roughness (~0.7 nm) and low density of defects. For $x \geq 1.4$, important decrease of crystalline quality and increase of surface roughness (~1.4 nm) was observed. For these films, a thin layer (~2 nm) of $Fe_3O_4$ buffer was grown to facilitate the heteroepitaxy between the spinel phase and the corundum substrate. Even if a clear improvement was observed in the crystalline quality of buffered films, this approach was not effective. STEM-EELS measurements showed a vertical gradient in the relative composition of Fe and Cr for these films. Since inhomogeneity in composition would certainly disturb the magnetic and transport measurements, theses samples were excluded from further analyses.

Although very good crystalline quality was found for a wide range of composition, different growth strategies than those tried in this work (*e.g.,* changing evaporation rates and using $Fe_3O_4$ buffer) are needed to increase the quality of films with $x \geq 1.4$. For example, increasing the substrate temperature could aid the formation of the FeO-like phase early in the growth, even though this phase is not very likely for samples with high Cr content. Another strategy would be to change the buffer to a layer that would not diffuse. For example, ferrite thin films are known [35, pp. 92–94] to grow very well on Pt(111) buffers.

Other substrates could also be considered, even if finding a suitable substrate for the growth of $FeCr_2O_4$ is far from an easy task. Lee and Chern [36] proposed a series of 120 nm thick $Fe_{3-x}Cr_xO_4(111)$ thin films grown on MgO(001) by O-MBE. Therein, they also claimed that the spinel structure at $x \sim 1.5$ becomes unstable and the growth of a corundum phase is favored in their growth conditions (*i.e.,* substrate temperature ~573 K). As shown in **Figure 4.31a**, their diffraction peaks also became weaker and broader for $x \geq 1.2$ and even no diffraction could be resolved for $x > 1.5$. Note that the lattice parameter deduced by Lee and Chern [36] are also smaller than the bulk (**Figure 4.31b**). They explained that this residual strain is due to the small negative lattice mismatch imposed by the MgO substrate (around -0.34%), which keeps the film strained down to hundreds of nanometers. However, this statement is rather odd, since thin films usually undergo stress relief through nucleation of misfit dislocations and relax completely after tens of nanometers.

In the study of 40 nm thick $Fe_2CrO_4$ grow on $MgAl_2O_4(001)$ substrates (MAO), Scafetta *et al.* [16] stated that the smaller-than-expected lattice parameters found for films grown at low temperatures (~523 K) is not caused by a strain effect, but by over oxidation. Interestingly, their over oxidized films exhibit an asymmetric doublet in the (004) Bragg peak just like the films grown on MgO at ~573 K (**Figure 4.31a**). According to direct space maps analysis, this broadened region was associated with a higher $c$ parameter linked to a relaxed portion of the film, while the "smaller-$c$" feature represented the slight out-of-plane parameter shrinkage. In this thesis, the observed lattice shrinkage for the films grown on sapphire cannot be due to over oxidation. According to K-XANES results (**Figure 4.19**), the $Fe_{3-x}Cr_xO_4$ films grown on sapphire are actually slightly under oxidized. Therefore, the smaller-than-expected lattice parameters found is probably due to strain effects.

It is important to highlight that when Scafetta *et al.* [16] grew the $Fe_2CrO_4$ films at higher temperatures (~873 K), the asymmetric doublet disappeared and only a single (004) Bragg peak closer to the bulk position was observed. Hence, other temperature regimes should also be tested for the growth on $Al_2O_3$ substrates in future work. These results also indicate MAO as a suitable alternative to $Al_2O_3$ and MgO for the growth of high Cr content films. Compared to MgO, MAO

enable higher substrate temperatures during deposition because they have significantly less Mg content and then less out-diffusion of this specie. Therefore, broader range of crystallization kinetics can be accessed without introducing Mg impurities. Furthermore, the fact that MAO and $Fe_{3-x}Cr_xO_4$ are both spinels should not only facilitate heteroepitaxy but also reduce (or even, in theory, eliminate) APBs in the films[34]. Indeed, Scafetta *et al.* [16] presented some chemical results for $FeCr_2O_4$ grown on MAO. However, no structural results were shown for these layers, so nothing is known about their true crystalline quality.

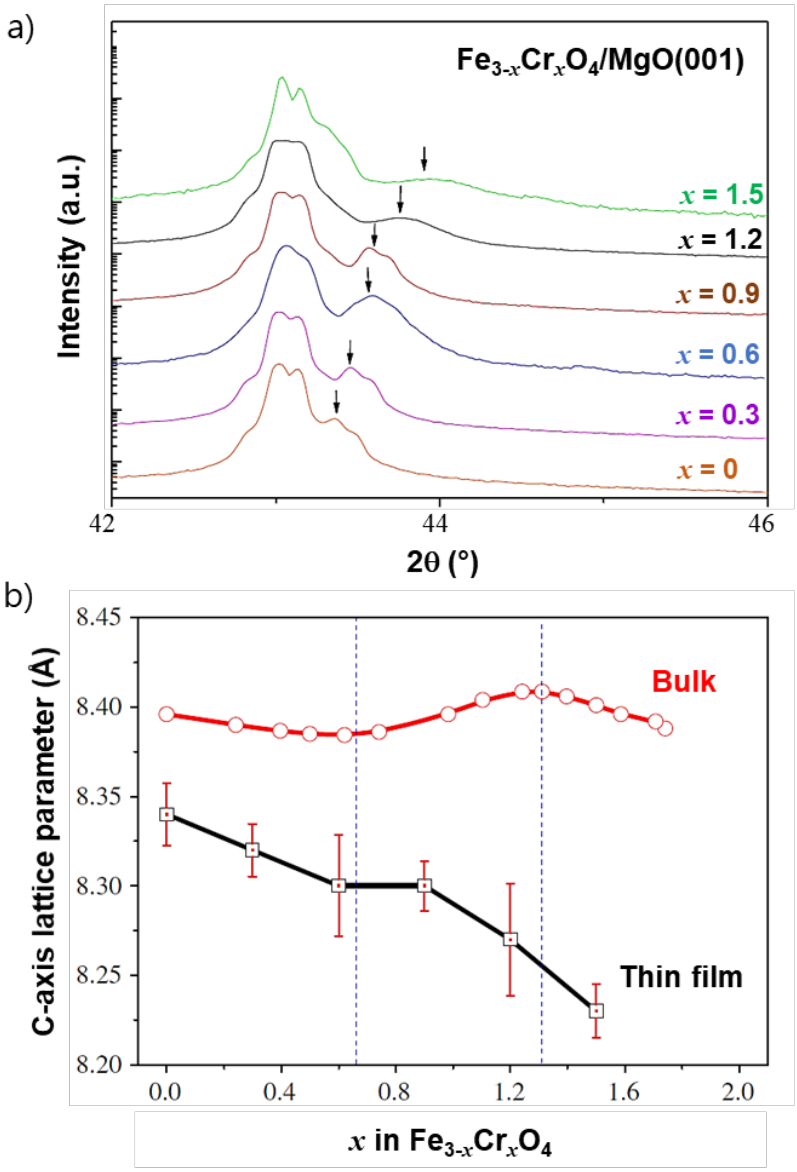


**Figure 4.31.** (a) θ-2θ XRD scans ($\lambda_{Cu}$ = 0.154 nm) for 120 nm thick $Fe_{3-x}Cr_xO_4$ films. The intense peak at ~43° corresponds to the (002) Bragg peak of MgO substrate and the adjacent broad peak (marked with an arrow) corresponds to the (004) Bragg peak of the film. (b) Evolution of the out-of-plane lattice parameter obtained from the θ-2θ XRD scans in comparison with bulk values from Robbins *et al.* [27]. Figure adapted from Lee and Chern [36].

[34] APBs, however, were still present in the 40 nm thick $Fe_2CrO_4$ films synthetized by Scafetta *et al.* [16].

## 4.7 References

[1] S. Gota, J.-B. Moussy, M. Henriot, M.-J. Guittet, and M. Gautier-Soyer, "Atomic-oxygen-assisted MBE growth of $Fe_3O_4$ (111) on α-$Al_2O_3$ (0001)," *Surface Science*, vol. 482–485, pp. 809–816, 2001.

[2] J.-B. Moussy *et al.*, "Thickness dependence of anomalous magnetic behavior in epitaxial $Fe_3O_4$(111) thin films: Effect of density of antiphase boundaries," *Physical Review B*, vol. 70, no. 17, p. 174448, Nov. 2004.

[3] A. Bataille, "Etude des propriétés physiques des films de $Fe_3O_4$ épitaxiés et de la polarisation en spin à l'interface $Fe_3O_4$/γ-$Al_2O_3$," Theses, Université Paris Sud - Paris XI, 2005. [Online]. Available: https://tel.archives-ouvertes.fr/tel-00085941

[4] M. A. Herman and H. Sitter, *Molecular Beam Epitaxy*, vol. 7. Berlin, Heidelberg: Springer Berlin Heidelberg, 1989.

[5] M. H. Francombe, "Lattice changes in spinel-type iron chromites," *Journal of Physics and Chemistry of Solids*, vol. 3, pp. 37–43, 1957.

[6] S. Matzen *et al.*, "Structure, magnetic ordering, and spin filtering efficiency of $NiFe_2O_4$(111) ultrathin films," *Applied Physics Letters*, vol. 104, no. 18, p. 182404, May 2014.

[7] S. Matzen, P. Sainctavit, C. Gatel, B. Warot-Fonrose, and Y. Zheng, "Epitaxial growth and ferrimagnetic behavior of $MnFe_2O_4$(111) ultrathin layers for room-temperature spin filtering," *PHYSICAL REVIEW B*, p. 10, 2011.

[8] P. F. Fewster, "Reciprocal space mapping," *Critical Reviews in Solid State and Materials Sciences*, vol. 22, no. 2, pp. 69–110, 1997.

[9] M. J. Hÿtch, "Measurement of displacement and strain by high-resolution transmission electron microscopy," in *Stress and Strain in Epitaxy*, M. Hanbücken and J.-P. Deville, Eds. Amsterdam: Elsevier, 2001, pp. 201–219.

[10] A. V. Ramos *et al.*, "Magnetotransport properties of $Fe_3O_4$ epitaxial thin films: Thickness effects driven by antiphase boundaries," *Journal of Applied Physics*, vol. 100, no. 10, p. 103902, Nov. 2006.

[11] K. P. McKenna *et al.*, "Atomic-scale structure and properties of highly stable antiphase boundary defects in $Fe_3O_4$," *Nature Communications*, vol. 5, no. 1, p. 5740, Dec. 2014.

[12] M. Aronniemi, J. Sainio, and J. Lahtinen, "Chemical state quantification of iron and chromium oxides using XPS: the effect of the background subtraction method," *Surface Science*, vol. 578, no. 1–3, pp. 108–123, Mar. 2005.

[13] H. Müllejans and J. Bruley, "Electron energy-loss spectroscopy (EELS) ; comparison with X-ray analysis," *Le Journal de Physique IV*, vol. 03, no. C7, pp. C7-2083-C7-2092, Nov. 1993.

[14] A. P. Grosvenor, B. A. Kobe, M. C. Biesinger, and N. S. McIntyre, "Investigation of multiplet splitting of Fe 2p XPS spectra and bonding in iron compounds," *Surface and Interface Analysis*, vol. 36, no. 12, pp. 1564–1574, Dec. 2004.

[15] S. A. Chambers *et al.*, "Electronic and Optical Properties of a Semiconducting Spinel ($Fe_2CrO_4$)," *Advanced Functional Materials*, vol. 27, no. 9, p. 1605040, Mar. 2017.

[16] M. D. Scafetta *et al.*, "Epitaxial growth and atomic arrangement in $Fe_2CrO_4$ on crystal symmetry matched (001) $MgAl_2O_4$," *Journal of Vacuum Science & Technology A*, vol. 37, no. 3, p. 031511, May 2019.

[17] M. C. Biesinger, B. P. Payne, A. P. Grosvenor, L. W. M. Lau, A. R. Gerson, and R. St. C. Smart, "Resolving surface chemical states in XPS analysis of first row transition metals, oxides and hydroxides: Cr, Mn, Fe, Co and Ni," *Applied Surface Science*, vol. 257, no. 7, pp. 2717–2730, Jan. 2011.

[18] R. Dieckmann, "Point defects and transport in non-stoichiometric oxides: Solved and unsolved problems," *Journal of Physics and Chemistry of Solids*, vol. 59, no. 4, pp. 507–525, 1998.

[19] G. Calas and J. Petiau, "Coordination of iron in oxide glasses through high-resolution K-edge spectra: Information from the pre-edge," *Solid State Communications*, vol. 48, no. 7, pp. 625–629, Nov. 1983.

[20] R. J. Hill, J. R. Craig, and G. V. Gibbs, "Systematics of the spinel structure type," *Physics and Chemistry of Minerals*, vol. 4, no. 4, pp. 317–339, 1979.

[21] P. Ohresser *et al.*, "DEIMOS: A beamline dedicated to dichroism measurements in the 350–2500 eV energy range," *Review of Scientific Instruments*, vol. 85, no. 1, p. 013106, Jan. 2014.

[22] É. Gaudry, P. Sainctavit, F. Juillot, F. Bondioli, P. Ohresser, and I. Letard, "From the green color of eskolaite to the red color of ruby: an X-ray absorption spectroscopy study," *Physics and Chemistry of Minerals*, vol. 32, no. 10, pp. 710–720, Jan. 2006.

[23] H. K. Mao and P. M. Bell, "Crystal-fiels effects in spinel: oxidation states of iron and chromium," *Geochimica et Cosmochimica Acta*, vol. 39, pp. 865–874, 1975.

[24] M. E. Sadat *et al.*, "Photoluminescence and photothermal effect of Fe3O4 nanoparticles for medical imaging and therapy," *Applied Physics Letters*, p. 6, 2014.

[25] S. Brice-Profeta, "Magnetic order in g-Fe2O3 nanoparticles: a XMCD study," *Journal of Magnetism and Magnetic Materials*, p. 12, 2005.

[26] H. Elnaggar *et al.*, "Probing the local distortion of Fe sites in $Fe_3O_4$ thin films using enhanced symmetry selection in XMLD," *Physical Review Materials*, vol. 4, no. 2, Feb. 2020.

[27] M. Robbins, G. K. Wertheim, R. C. Sherwood, and D. N. E. Buchanan, "Magnetic properties and site distributions in the system $FeCr_2O_4$-$Fe_3O_4$($Fe^{2+}Cr_{2-x}Fe_x^{3+}O_4$)," *Journal of Physics and Chemistry of Solids*, vol. 32, no. 3, pp. 717–729, Jan. 1971.

[28] S. Brice-Profeta, "Etude de l'ordre chimique et magnétique d'oxydes spinelles de taille nanométrique par dichroïsme magnétique circulaire des rayons X," 2004.

[29] T. Pohlmann, "Cation- and lattice-site-selective magnetic depth profiles of ultrathin $Fe_3O_4$ films," *Physical Review B*, p. 6, 2020.

[30] T. Yang, "Surface structures of Fe3O4 (111), (110), and (001): A density functional theory study," *Journal of Fuel Chemistry and Technology*, p. 8, 2010.

[31] J. Noh, O. I. Osman, S. G. Aziz, P. Winget, and J.-L. Bred, "Magnetite Fe3O4 (111) Surfaces: Impact of Defects on Structure, Stability, and Electronic Properties," *Chem. Mater.*, p. 12, 2015.

[32] F. Walz, "The Verwey transition - a topical review," *Journal of Physics: Condensed Matter*, vol. 14, no. 12, pp. R285–R340, Mar. 2002.

[33] J. Ma *et al.*, "Magnetic and structural phase transitions in the spinel compound $Fe_{1+x}Cr_{2-x}O_4$," *Physical Review B*, vol. 89, no. 13, Apr. 2014.

[34] A. Moewes *et al.*, "X-ray emission spectroscopy study of the Verwey transition in $Fe_3O_4$," *Journal of Physics: Condensed Matter*, vol. 15, no. 12, pp. 2017–2022, Mar. 2003.

[35] A. V. Ramos, "Epitaxial Cobalt-Ferrite Thin Films for Room Temperature Spin Filtering," Theses, Université Pierre et Marie Curie - Paris VI, 2008. [Online]. Available: https://tel.archives-ouvertes.fr/tel-00394398

[36] D. S. Lee and G. Chern, "Electrical transport properties of $Fe_{3-x}Cr_xO_4$ ferrite films on MgO (001) grown by molecular beam epitaxy," *Physica B: Condensed Matter*, vol. 407, no. 3, pp. 297–301, Feb. 2012.

# Chapter 5:

# Physical properties of $Fe_{3-x}Cr_xO_4$ thin films from the fine structure perspective

This chapter discusses the **macroscopic properties** of the $Fe_{3-x}Cr_xO_4$ epitaxial thin films from the **microscopic perspective**. First, the fine structure of the films obtained by magnetic circular dichroism measurements are compared with that of bulk systems. Then, the influence of the cation distribution on the magnetic properties and electronic transport of $Fe_{3-x}Cr_xO_4$ thin films is discussed. As expected, the total magnetic moment and the conductivity of the series decrease as the Cr content increases. Since $Fe^{2+}$ cations populate specially Oh-sites, **total magnetic moments** and **Curie temperatures** are considerably **higher** for thin films with higher Cr content. In addition, these films are **less resistive** than the bulk, because the favored Oh-to-Oh electron-hopping path is still possible.

## 5.1 Thin film vs. bulk inversion parameter

As discussed in **Chapter 1** and **Chapter 4**, an interesting aspect of the $Fe_{3-x}Cr_xO_4$ series is that those spinel oxides can adopt different spinel configurations depending on the Cr content. According to Mössbauer measurements performed on bulk samples [1], [2], this system can be divided in three regions (**Figure 5.1a**, dashed black lines):

1. **Region I**: $[Fe^{3+}]_{Td}[Fe^{2+}Fe^{3+}{}_{1-x}Cr_x]_{Oh}O_4$ for $0 \leq x \leq 0.5$
2. **Region II**: $[Fe^{3+}{}_yFe^{2+}{}_{1-y}]_{Td}[Fe^{2+}{}_yFe^{3+}{}_{2-x-y}Cr_x]_{Oh}O_4$ for $0.62 \leq x \leq 1.25$
3. **Region III**: $[Fe^{2+}]_{Td}[Fe^{3+}{}_{2-x}Cr_x]_{Oh}O_4$ for $1.5 \leq x \leq 2.0$.

The inversion ratio ($y$) steadily evolves with composition, ranging from $y = 0$ for normal ordering (*i.e.,* $FeCr_2O_4$) to $y = 1$ for an inverse arrangement (*i.e.,* $Fe_3O_4$), as shown in **Figure 5.1b**. In this work, the 15 nm thick $Fe_{3-x}Cr_xO_4$(111) thin films grown on $Al_2O_3$(0001) also showed different configurations depending on the Cr content. According to $L_{2,3}$-edge XMCD results (**Figure 5.1a**, solid lines), the films have mainly inverse spinel configuration for $0 \leq x \leq 0.5$ (*i.e.,* predominantly $Fe^{3+}$ at Td-sites), while compositions with $0.5 < x \leq 1.2$ have intermediate spinel configuration with $0.9 < y < 0.5$. Here the value of $y$ is deduced from the Td contributions ($y = M_{Fe^{3+}_{Td}}/M_{Fe^{2+}_{Td}} + M_{Fe^{3+}_{Td}}$), since the $Fe^{2+}{}_{Oh}$ contributions are generally overestimated in the fits. These findings are in overall good agreement with Mössbauer measurements performed on bulk samples. However, the transition from one spinel configuration to another is less abrupt in the films than in the bulk. As depicted in **Figure 5.1b**, the films remained an intermediate spinel for $x$ up to 1.2, while bulk samples are almost a complete normal spinel for such composition.

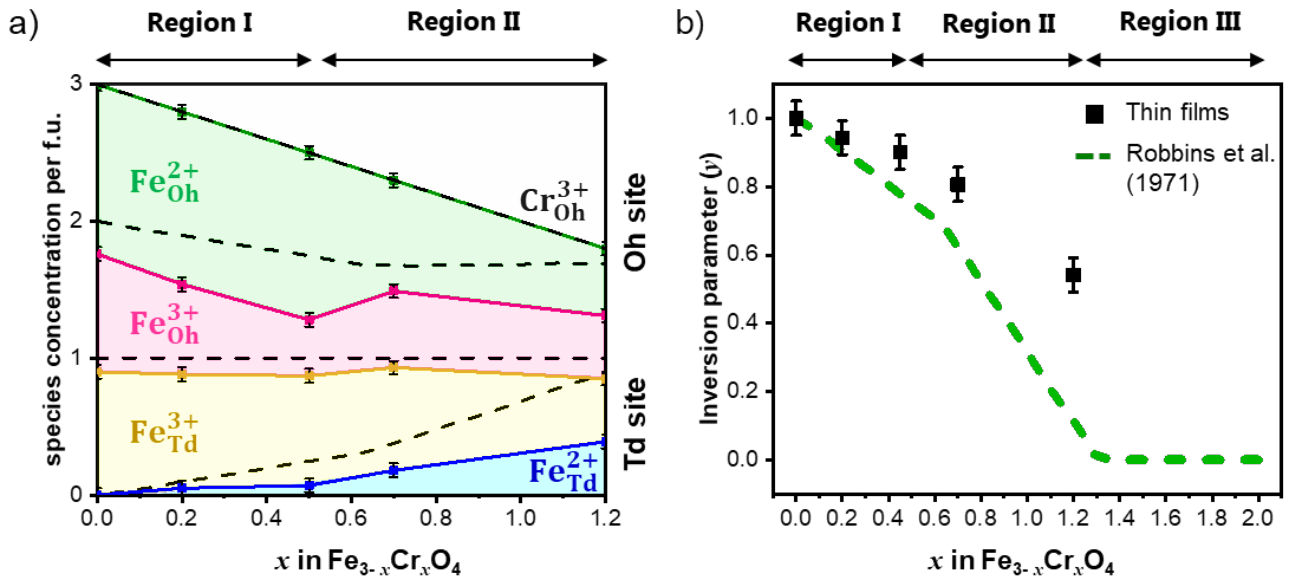


**Figure 5.1.** (a) Site distribution diagram of the species concentrations from XMCD measurements (solid lines), in comparison with values for bulk structure [1] (dashed black lines). (b) The evolution of the inversion ratio ($y$) with composition ($x$) for thin films (black squares) and bulk (dashed green line).

The same tendencies were observed for the $Fe_{3-x}Cr_xO_4$ films synthetized on MgO(001) by Lee and Chern [3]. According to subsequent $L_{2,3}$-edge XAS measurements [4], their films also have a preference for the inverse spinel configuration. Similar results were given by Chambers *et al.* [5] when growing $Fe_2CrO_4$ films on MgO(001). According to them, these films have around 10% of the Td-sites occupied by $Fe^{2+}$ ions, which is much lower than the 50% usually obtained for bulk samples. As discussed in **Section 4.6**, this is probably because oxygen-rich spinel samples crystallized at lower temperature tends to create cation vacancies, so the region of inverse configuration extended to a much higher Cr composition.

In the following sections, the influence of the cation distribution on the magnetic properties and electronic transport of the $Fe_{3-x}Cr_xO_4$ series is discussed in detail.

## 5.2 Magnetic behavior of $Fe_{3-x}Cr_xO_4$ thin films

### 5.2.1 In-plane magnetic measurements

A primary effect of replacing $Fe^{3+}$ with $Cr^{3+}$ in the $Fe_{3-x}Cr_xO_4$ series is to change the average magnetic moment on the Oh-sites and the magnetic interactions between Td-Oh and Oh-Oh sites. At first, collinear Néel configurations (see **Section 1.3.2.1**), where the spins on Td-sites of the iron chromites are coupled antiferromagnetically to spins on Oh-sites, are assumed in the same way as in the magnetite structure [6]. Thus, the total magnetic moment can be deduced using the spin moments from the formal charges of each specie ($Cr^{3+}$: $3d^3 \rightarrow 3\ \mu_B$, $Fe^{3+}$: $3d^5 \rightarrow 5\ \mu_B$, and $Fe^{2+}$: $3d^6 \rightarrow 4\ \mu_B$) and neglecting the orbital contributions. Indeed, the orbital momentum is negligible (at least for Cr) as is shown in the next section by the treatment of the XMCD signals using sum rules. Considering a stoichiometric composition with a collinear Néel configuration, the local magnetic moment should exhibit values ranging from $2(3-x)$ to $2(2-x)\ \mu_B$ per f.u., depending on the distribution of $Fe^{2+}$ and $Fe^{3+}$ cations among the spinel sublattices. The upper bound corresponds to a normal spinel ($[Fe^{2+}]_{Td}[Fe^{3+}{}_{2-x}Cr_x]_{Oh}O_4$), while the lower bound corresponds to a complete inverse spinel configuration ($[Fe^{3+}]_{Td}[Fe^{2+}Fe^{3+}{}_{1-x}Cr_x]_{Oh}O_4$). Because we are replacing $Fe^{3+}{}_{Oh}$ ($\mu = 5\ \mu_B$) by $Cr^{3+}{}_{Oh}$ ($\mu = 3\ \mu_B$), the magnetic moment should decrease linearly with composition ($x$) if the spinel oxide has the same inversion ratio ($y$).

In order to comprehend the effect of increasing Cr content in the magnetic properties of $Fe_{3-x}Cr_xO_4$ series, in-plane magnetic hysteresis loops (M-H curves) of samples with different compositions were recorded using vibrating sample magnetometry (VSM). The measurements were performed at temperatures (T) equal to 10 K, 100 K and 300 K and magnetic field up to 2 T applied along the $[11\bar{2}0]$ axis of the $\alpha$-$Al_2O_3$ substrate. **Figure 5.2a-c** depicts the [-0.6, 0.6] Tesla part of the M-H curves. For all measured temperatures, the $Fe_{3-x}Cr_xO_4$(111) thin films exhibited a ferromagnetic behavior and an easy in-plane magnetization for $x$ up to 1.4. Contrary to bulk samples [7], the hysteresis loops of the thin films were not square. The atomic dipoles align progressively with the increase (or decrease) of the magnetic field, showing much slower approach to saturation. In fact, thin film oxides typically

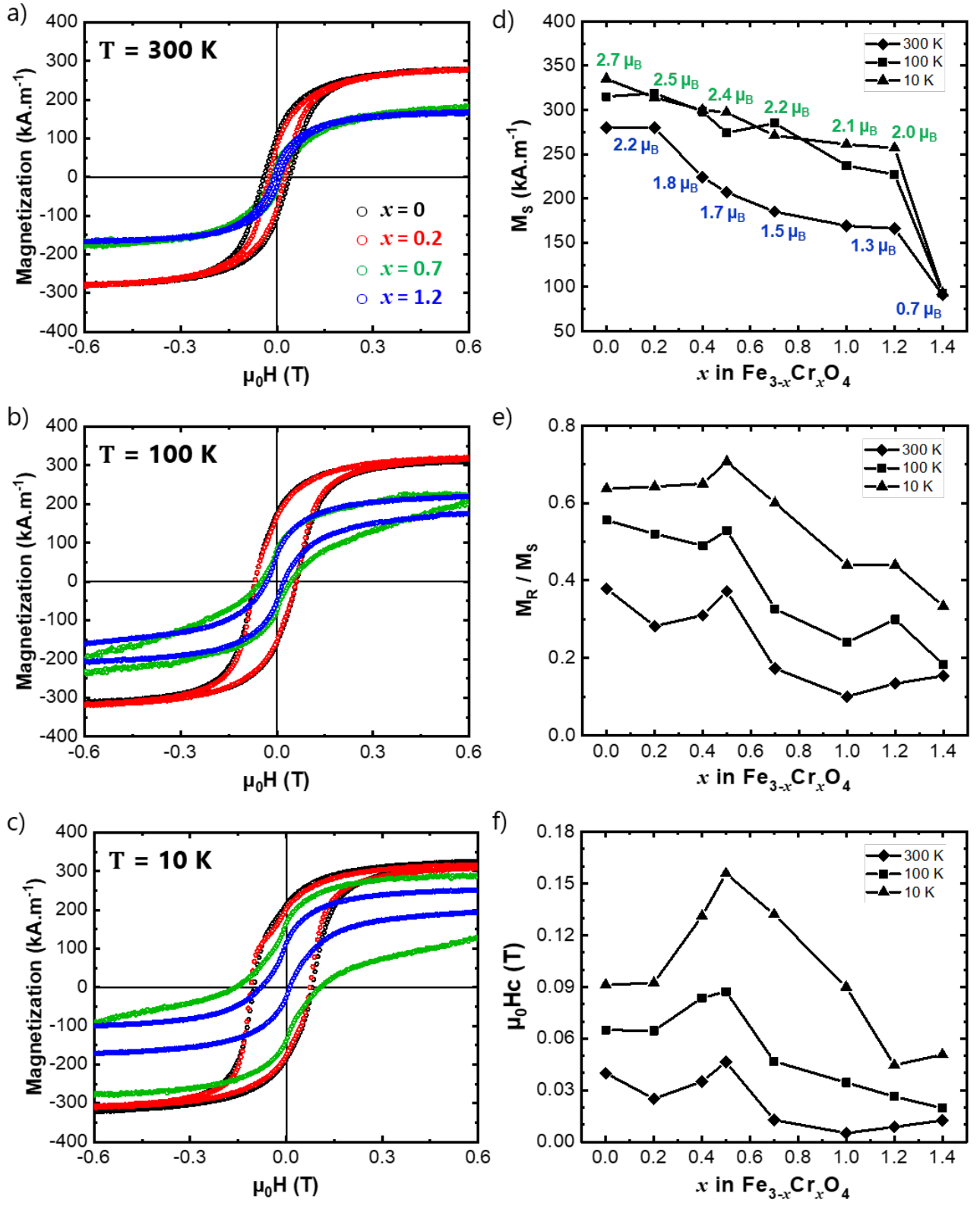


**Figure 5.2.** Magnetic behavior in $Fe_{3-x}Cr_xO_4$ thin films. At left, the in-plane magnetic hysteresis loops at (a) T = 300 K, (b) T = 100 K and (c) T = 10 K. At right, (d) saturation magnetization $M_S$, (e) remanent magnetization $M_R$ and (f) coercive field $\mu_0 H_C$ for T = 300 K (diamonds), T = 100 K (squares) and T = 10 K (triangles). The local magnetic moment at T = 300 K (blue) and T = 10 K (green) is expressed in $\mu_B$ per f.u. in (d). The statistical uncertainties (not shown) are smaller than the point size (~2%). Color code: for $x$ = 0 (black circles), $x$ = 0.2 (red circles), $x$ = 0.7 (green circles) and $x$ = 1.2 (blue circles).

have thickness-dependent magnetic properties [6]. In general, the magnetic coercive field ($\mu_0H_C$) and remanent magnetization ($M_R$) decrease with decreasing thickness. This shape-variation of the M-H curves occurs because each spin has more neighboring sites when thickness increases, which results in higher spin-spin interaction and larger critical temperature [8]. Herein, all films are 15 to 20 nm thick, and they all exhibit a much slower approach to saturation than bulk specimens do.

Another reason for the strong deviation of the magnetic properties of epitaxial thin films compared to bulk samples is the presence of anti-phase boundaries (APBs). As discussed in the literature [9], different magnetic couplings (ferromagnetic, antiferromagnetic) can exist across the APB. However, one of the stronger interactions at the APB interface is rather antiferromagnetic. Thus, not only saturation is more difficult to achieve, but also the average magnetic moment ($M_S$) of the thin film may be reduced. For instance, the magnetic moment measured for $Fe_3O_4$ (2.2 $\mu_B$ per f.u.) is considerably lower than the bulk value of 4.2 $\mu_B$ per f.u. [7]. This phenomenon has been widely studied for magnetite thin films [6], [10] and also affects the magnetic properties of all our iron chromite series. Indeed, the $M_S$ values are consistently lower than lower bound on the magnetic moment corresponding to an inverse spinel configuration, *i.e.,* 4 $\mu_B$ per f.u. for $x$ = 0 and 1.2 $\mu_B$ per f.u. for $x$ = 1.4.

For all probed temperatures, the saturation magnetization (**Figure 5.2d**) and remanent magnetization (**Figure 5.2e**) of the $Fe_{3-x}Cr_xO_4$ films decreases as $x$ increases. At room temperature, $M_S$ values ranged from 280 kA.m$^{-1}$ to 90 kA.m$^{-1}$ for $0 \leq x \leq 1.4$, while $M_R$ reached from 38% to 15% of the magnetization at 1.5 T for this same range of $x$ values. Likewise, the coercive field (**Figure 5.2f**) also decreased with $x$, ranging from 0.040 T ($x$ = 0) to 0.012 T ($x$ = 1.4). The same trends were observed for lower temperatures, for which the magnetic properties are shifted to higher values. It should be noted that both $M_R$ and $\mu_0H_C$ showed local maxima values for $x$ around 0.5. For example, $M_R$ = 37% and $\mu_0H_C$ = 0.046 T for $Fe_{2.5}Cr_{0.5}O_4$ at room temperature. For single magnetic phase, the values of $M_R$ and $\mu_0H_C$ can be used to describe changes in the magnetic hardness and in the structure of materials. Briefly, magnetic materials are described as being "hard", if they show large values of $M_R$ and $\mu_0H_C$, or "soft" if these parameters are small. Therefore, it appears that increasing Cr content decreases the magnetic hardness of the $Fe_{3-x}Cr_xO_4$ thin films, except for $x$ values around 0.5. Even if it is tempting to assume that the anisotropy of these films is sensitive to the Cr content, $M_R$ and $\mu_0H_C$ values must be interpreted with caution. As abovementioned, the shape of the M-H curves indeed depends on the film microstructures (*e.g.,* density of APBs and size of magnetic domains).

Supplementary information can also be obtained from the temperature dependence of magnetic hysteresis loops. For a single ferromagnetic phase, the slope and the hysteresis-loop parameters change quantitatively with temperature in a relatively smooth fashion. Discontinuities in the temperature dependence of these parameters can be produced by phase transitions, such as the Verwey transition in $Fe_3O_4$ or the collinear-to-conical transition in $FeCr_2O_4$ (see **Section 1.3.2**). They can also be associated to the magnetic interactions of two magnetic phases having different Curie points or to the coupling of discrete spin systems [11]. As shown in **Figure 5.2d**, similar values of saturation magnetization were found for samples at T = 10 K and 100 K. Nonetheless, at room temperature, $M_S$ values were not only lower, but also the differences between the temperatures increase as the Cr content increases. As for bulk samples (**Figure 1.8**), one expected similar $M_S$ values

for $x \leq 0.2$ at low and high temperatures. The observed difference of ~50 kA.m$^{-1}$ is originated from magnetic contributions of the $\alpha$-$Al_2O_3$ substrate, as the entire sample is probed in the VSM measurements. At first glance, this is unexpected, since sapphire is supposed to be a non-magnetic substrate. However, impurities and structural defects create a weak ferromagnetic signal in their M-H curves [12], which increases upon cooling. For $x > 0.2$, in addition to the contribution of the substrate, the film composition also plays a role. As discussed in **Section 1.3.2.1**, at finite temperature, the thermal energy competes with the force of the magnetic exchange. Since increase in Cr-content is supposed to weaken the strong Td-Oh magnetic interactions, a temperature dependence of the saturation behavior is expected due to magnetic anisotropy [1].

Another interesting aspect of the M-H curves is that the loops are shifted in the negative field direction after cooling to 10 K from a positive field. For $Fe_3O_4$, this shift is 0.019 T and the coercivity is 0.091 T at such temperature (**Figure 5.3a**). Similar behavior was observed in the literature [7] for epitaxial films of magnetite prepared using different techniques (*e.g.* sputtering), but not for bulk samples. For the $Fe_{3-x}Cr_xO_4$ thin films, not only the loop shift increased with Cr content, but one also observed ripples in the curves for $0.2 \leq x \leq 0.5$ at 10 K (**Figure 5.3b**) and constriction of the loops for $x \geq 0.7$ (**Figure 5.3c-d**) at all temperatures. For example, a negative shift of 0.056 T and a coercivity of 0.16 T were found for $Fe_{2.5}Cr_{0.5}O_4$ thin films at T = 10 K. The small ripples observed in the curves at 10 K disappear upon heating (*i.e.,* such anomaly is not observed at T = 100 K). For $x \geq 0.7$, there are not ripples in the curves, but rather a constriction of the loop. A negative shift is also observed for these compositions. Whereas $Fe_{2.3}Cr_{0.7}O_4$ thin films show a shift of 0.050 T and a coercivity of 0.13 T at T = 10 K, a shift of 0.066 T and a coercivity of 0.045 T were found for $Fe_{1.8}Cr_{1.2}O_4$ thin films. Note that the shifts decrease as the temperature increases (*e.g.,* 0.006 T for $Fe_3O_4$ and 0.009 T for $Fe_{1.8}Cr_{1.2}O_4$ thin films at 100 K) and disappears at around 200 K (not shown).

Interestingly, similar anomalies were also observed in the M-H curves of $Fe_{3-x}Cr_xO_4$ bulk samples. According to Wasilewski *et al.* [11], at room temperature, samples with $x < 0.7$ are characterized by hysteresis loop typical of single-phase ferrimagnetic spinels, while constricted loops appears in the compositional range of $0.7 < x < 1.3$. Moreover, they also observed shifted loops and ripples in the M-H curves measured at 77 K for field-cooled samples with $x > 0.7$. Wasilewski *et al.* [11] associated these features with a system containing two magnetic phases. According to them, during the synthesis of the solid solution series, FeO-type submicroscopic phase or microstate are created due to incipient reduction. The spin system of this antiferromagnetic phase, which has ordering temperature of 198 K, couples with that of the host ferrimagnetic spinel. Thus, the magnetic exchange anisotropy involving this coupling leads to the different hysteresis loop shapes depending on the Cr content. For thin films, HRXRD (**Figure 4.8**) and HRTEM (**Figure 4.10**) measurements depicted only single phase $Fe_{3-x}Cr_xO_4$, so a FeO-like phase does not appear to be the origin of the loop shift. Other possible explanations for this behavior at cryogenic temperatures are the presence of cationic defects, structural defects (*e.g.,* APBs), and surface and interface effects. Further investigations are required to clarify the matter.

In the following sections, the magnetism of the $Fe_{3-x}Cr_xO_4$ thin films is investigated from the microstructure perspective. First, the cation site distribution obtained from XMCD measurements are used to understand the evolution of local magnetic moment with composition. Then, atomistic

calculations are performed to comprehend the magnetic properties of these films at low temperatures.

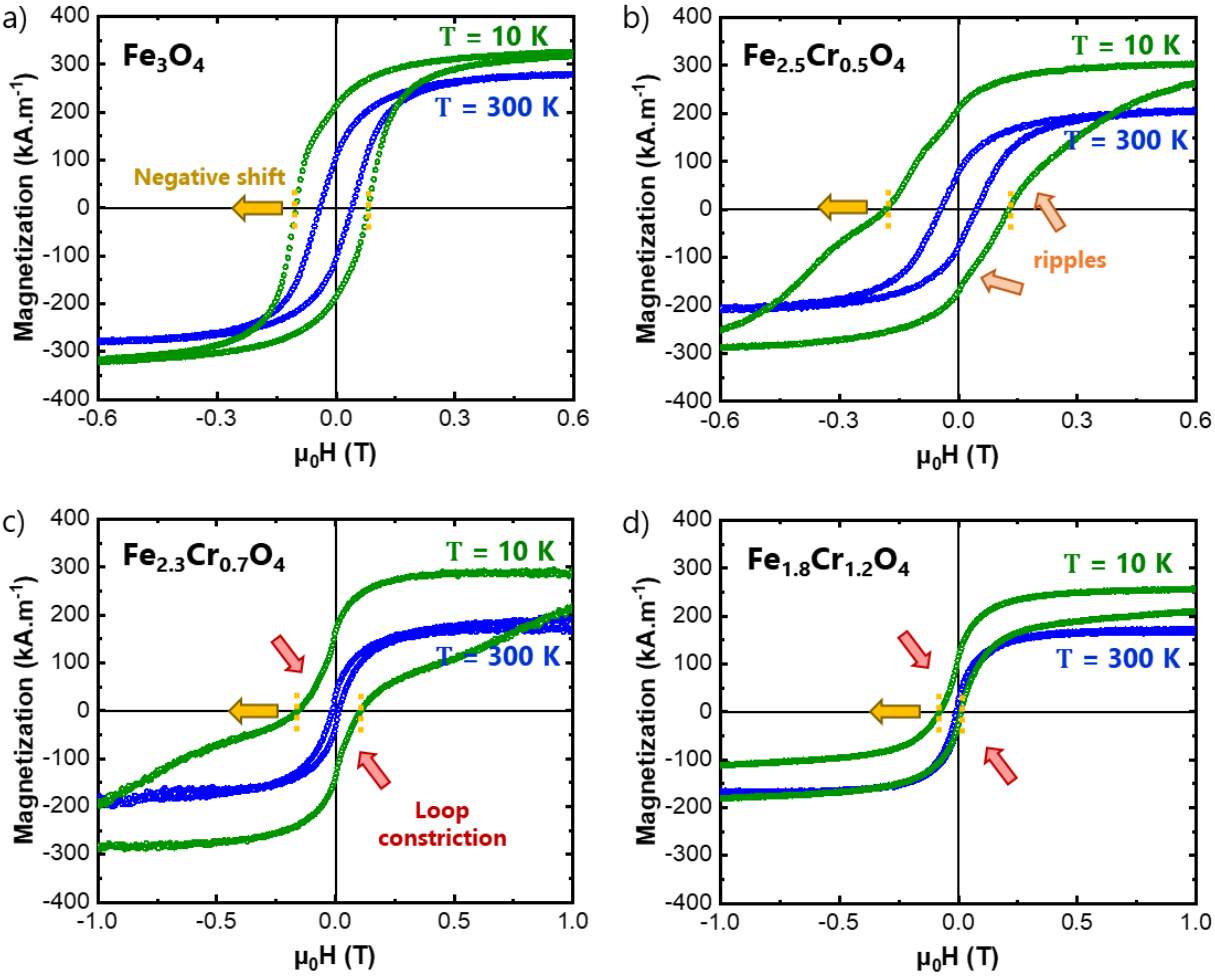


**Figure 5.3.** M-H curves for (a) $Fe_3O_4$, (b) $Fe_{2.5}Cr_{0.5}O_4$, (c) $Fe_{2.3}Cr_{0.7}O_4$, and (d) $Fe_{1.8}Cr_{1.2}O_4$ at T = 10 K (green circles) and T = 100 K (blue circles). Loop anomalies at low temperature, such as negative shift, ripples and loop constriction, are highlighted by yellow, orange and red arrows, respectively.

## 5.2.2 Magnetic properties vs. cationic site distribution

**Figure 5.4** compares the total magnetic moment ($\mu_{total}$) obtained from VSM measurements (**Figure 5.2d**) for thin films with the bulk values shown in the literature [1], [11] at high (T = 300 K) and low (T ≤ 10 K) temperatures. At room temperature (**Figure 5.4a**), the film values decreased more smoothly with composition $x$ than the bulk. Whereas bulk $\mu_{total}$ dropped sharply from 3.8 to 0.3 $\mu_B$ per f.u. within the composition range of $0 \leq x \leq 1.2$, the film values decreased gently from 2.2 to 1.3 $\mu_B$ per f.u. within the same range and then dropped to 0.7 $\mu_B$ per f.u. for $x$ = 1.4. Note that the films with high Cr content ($x \geq 1.2$) show higher magnetic moments ($\mu_{total} > 0$) than the bulk. This is probably due to changes in the inversion ratio ($y$) observed in **Figure 5.1b**. To delve deeper into this issue, **Figure 5.4** (open black squares) shows the expected average magnetic moment calculated from the $y$ values deduced from the Fe XMCD fits. According to the XMCD measurements, the Oh-site

moments align parallel to one another and antiparallel to the Td-site moments, as observed in other Cr containing spinels [13], [14]. Assuming that formal charges can be used to estimate the spin moments of each specie, the corresponding magnetic moment is $2(3-x-y)$ $\mu_B$ per f.u., as aforementioned. As depicted in **Figure 5.4**, the local magnetic moment deduced from the cationic site distribution decreases gradually with Cr content. Although they evolve with composition in a similar way than the VSM measurements, they are shifted to higher values. This can be explained by the presence of APBs (**Figure 4.10**), as discussed in the last section.

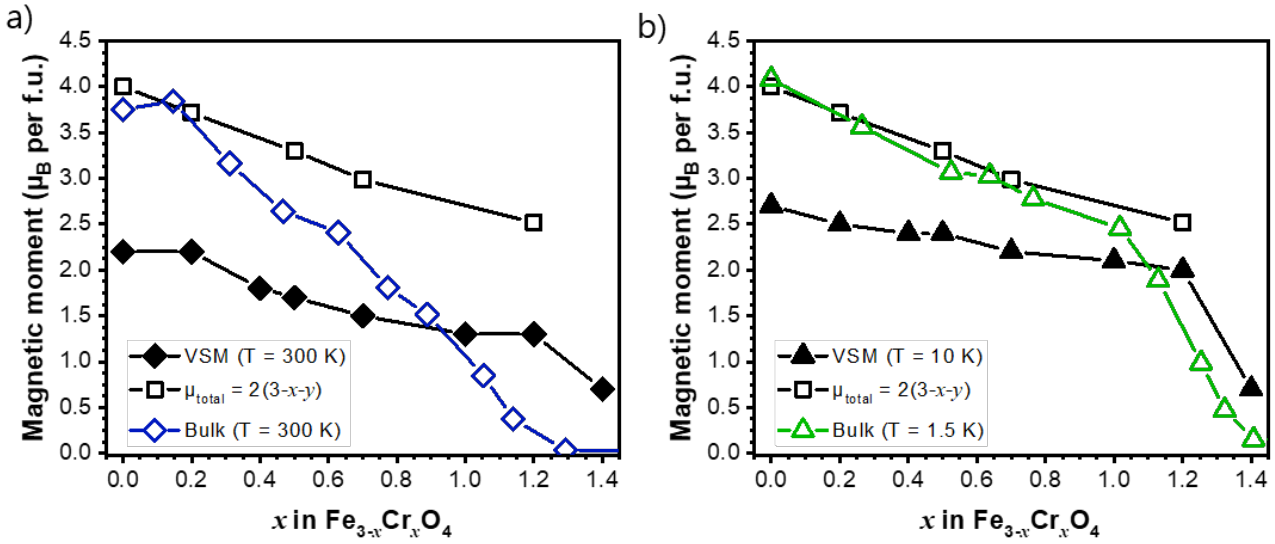


**Figure 5.4.** Evolution of local magnetic moment with composition for bulk samples (blue diamonds [11] and green triangles [1]) in comparison with thin films at (a) T = 300 K and (b) T = 10 K. The VSM results are shown as black diamonds, while values deduced form the cationic site distribution are in black open squares. Herein, the evolution of local magnetic moment with inversion ratio calculated from the Td contributions ($y = M_{Fe^{3+}_{Td}}/M_{Fe^{2+}_{Td}} + M_{Fe^{3+}_{Td}}$).

Finding a similar evolution of the magnetic moments measured by VSM compared to those deduced by the Néel model implies that the Fe and Cr moments are mostly collinear in the thin films. As discussed in **Section 1.3.2.1**, the Néel model is only valid for $x$ up to 0.5 in bulk samples [1], [11], [15]. However, for thin films, this model is apparently valid for further compositions. A possible explanation lies in the fact that the thin films maintained an intermediate spinel configuration with higher inversion ratio for larger Cr content. In fact, increasing the amount of $Fe^{2+}$ displaced at Td-sites (*i.e.,* to decrease $y$) weakens the Td-Oh antiferromagnetic interactions in the spinel structure. Likewise, increasing the amount of $Cr^{3+}$ in Oh-sites increases the strength of the next-nearest neighbor Oh-Oh antiferromagnetic interactions. Depending on the competing force of these interactions, they may tilt the cation spin moments in the spinel sublattices. Therefore, the local magnetic moment should decrease proportionally to the amount of $Fe^{2+}$ ions displaced to Td-sites and $Cr^{3+}$ ions occupying Oh-sites. For bulk samples, the Néel model is valid for $x$ up to 0.5, whose inversion ratio is 0.75. Since the thin films keep a higher inversion ratio of 0.80 for $x$ up to 0.7, the Néel model should indeed be valid up to this film composition. On the other hand, $y$ = 0.5 for $x$ = 1.2, so for this composition the spin moments of $Cr^{3+}$ ions should be slightly canted.

The more canted the spin moments, the greater must be the negative slope of the total magnetic moment versus Cr content curve. For low temperatures (**Figure 5.4b**), where the thermal energy should not greatly influence the spin rotation, the slope of the $\mu_{total}$ vs. $x$ curves obtained from VSM results and the one based on the cation distribution are not exactly the same. One observes that the results from the Néel model (open black squares) have higher negative slope for the same composition range than VSM results. This is very surprising since the slope is proportional to the attenuation of the spin moments and it is not possible to have less canted spins than a completely collinear model. There are two possible explanations for such outcome. First, the magnetic behavior of a thin film relates closely to the average domain size of the APBs. As observed in epitaxial $Fe_3O_4$(111) thin films [6], the higher the APBs domain size, the higher the total magnetic moment. For example, films with 50 nm thick APBs domain size have $\mu_{total}$ = 3.2 $\mu_B$ per f.u., while films with 25 or 10 nm thick domain size have $\mu_{total}$ = 2.7 $\mu_B$ per f.u. Hence, the films would only display the same evolution of local magnetic moment with composition than the ideal Néel model if they had the same microstructure. Which is not the case. As discussed in **Section 4.3**, increasing Cr content in the $Fe_{3-x}Cr_xO_4$ thin films disturbs the crystalline microstructure and increases the planar defects. Especially for $Fe_{1.8}Cr_{1.2}O_4$ films (**Figure 4.12**), where the increase of crystalline nanodomains is clear. Furthermore, the difference in the local magnetic moment evolution can also be motivated by cation defects. As shown in **Section 4.4.2**, the samples with higher Cr content ($x \geq 1.2$) are under oxidized, which definitely influences the total magnetic moment of the sample.

Further clarification on the compositional effects on magnetic properties of $Fe_{3-x}Cr_xO_4$ thin films (*e.g.,* deviation from Néel model) could be obtained by measuring the local magnetic moments of the species using the XMCD sum rules (see **Section 2.5.1**). Unfortunately, the sum rules cannot be applied for Fe species because it is not possible to separate the $Fe^{2+}$ from the $Fe^{3+}$ contributions at different sites. However, in principle, it could be used for Cr since it has a single oxidation state and symmetry. This analysis requires accurate integration of the dichroic signal over the individual $L_2$ and $L_3$ edges as well as across the entire $L_{2,3}$ isotropic signal. To do so, the spin-orbit coupling on the $2p$ shell ($\zeta_{2p}$) should be sufficiently large that there is no mixing of the final state configurations corresponding to the $L_2$ and $L_3$ edges. According to self-consistent Hartree-Fock calculations (see **Table 4.4**), $\zeta_{2p}$ is equal to 5.67 eV for the $2p^5 3d^4$ excited state of $Cr^{3+}$ ion. This value is very close to the Coulomb interactions ($F^k_{dd}$, $F^k_{pd} \cong$ 5-6 eV), which hampers the separation between the $L_2$ and $L_3$ edges. Indeed, the high-energy tail of the Cr $L_3$ dichroic signal overlaps the onset $L_2$ signal, as depicted in **Figure 4.22** (raw spectra).

**Figure 5.5** shows the integration of the Cr $L_{2,3}$-edge normalized XAS and the XMCD spectra for $Fe_{2.5}Cr_{0.5}O_4$ thin film. The local spin moment ($m_S$) is given by the relation:

$$m_S = -3n_h\left(\frac{\mathrm{p}-2\mathrm{u}}{\mathrm{r}}\right) \qquad (\mu_B \text{ per atom}) \tag{5.1}$$

where $n_h$ is the number of holes in the valence band and p, u and r are the integrations over the $L_2$ and $L_3$ dichroic signal and the $L_{2,3}$-edge XAS, as defined in **Section 2.5.1** and in **Figure 5.5**. Since the

$L_{2,3}$-edges cannot be completely separated, $m_S$ cannot be accurately determined due to its explicit dependence on p. In contrast, the orbital moment ($m_L$) is given by:

$$m_L = -2n_h\left(\frac{q}{r}\right) \qquad (\mu_B \text{ per atom}) \tag{5.2}$$

where q is the integration over the entire dichroic signal as defined in **Figure 5.5**. The $m_L$ value can be determined with at least semi-quantitative accuracy. Usually, the experimental error bars of the XMCD results are estimated to be 4% for $m_S$ and $m_L$ [16]. For $Fe_{2.5}Cr_{0.5}O_4$, this analysis yielded $m_S$ and $m_L$ values of 1.29 ± 0.05 and 0.026 ± 0.001 $\mu_B$ per Cr atom, respectively. These values are less than half of the ones calculated by CFM for $Cr^{3+}{}_{Oh}$ ($\Delta$ = 2.2 eV): $m_S$ = 3.00 and $m_L$ = 0.064 $\mu_B$ per Cr atom. The differences can be due not only to the poorly separation of the $L_{2,3}$-edges, but also to the estimation of $n_h$. Here the number of valence holes for $Cr^{3+}$ ions (*i.e.,* $3d^3$) is approximated to 7. However, it is known that $n_h$ depends on the covalency of the bonds and its value is in fact not precisely known.

Not many conclusions about the local magnetic moments or the deviations from Néel model can be drawn from this approach due to its inaccuracy in the case of Cr cations.

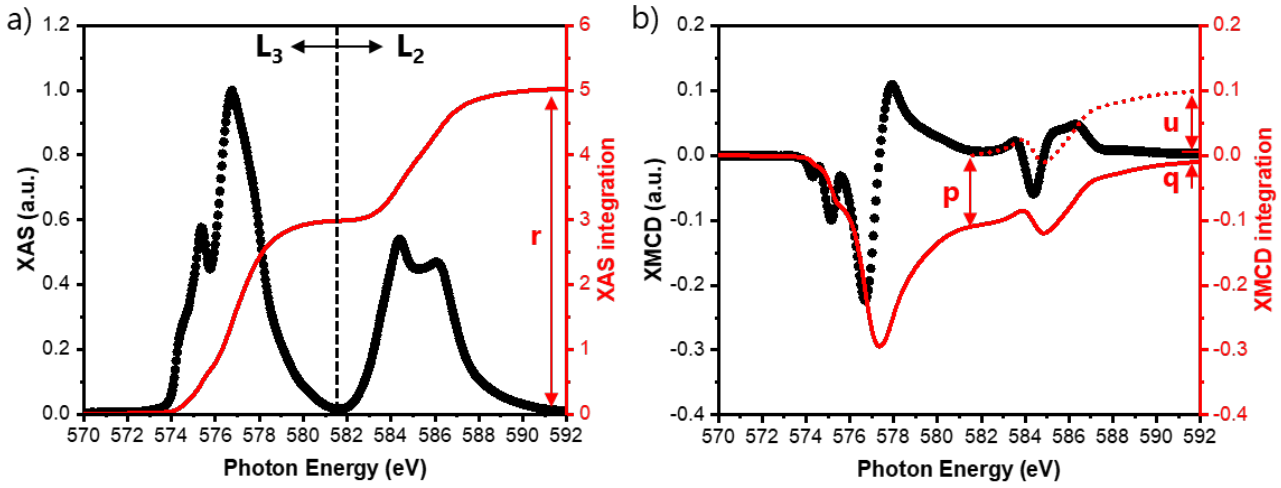


**Figure 5.5.** At left axis, Cr $L_{2,3}$-edge (a) XAS and (b) XMCD spectra of $Fe_{2.5}Cr_{0.5}O_4$ measured in total electron yield mode at B = 2.0 T and at room temperature. At right axis, the integration of these spectra from which the spin and orbital moments of Cr can in principle be extracted. The XAS spectrum is shown after the subtraction of the continuum step-like background, for which a 2:1 $L_3/L_2$ intensity ratio is considered.

After analyzing the VSM and XMCD results, few questions remain about the evolution of the magnetic properties of $Fe_{3-x}Cr_xO_4$ thin films with Cr content. First, why do the films with $x \geq 1.2$ have greater magnetic moment than the measured for bulk samples at both high and low temperature? Why is there an increase in hardness ($H_C$ and $M_R$) for films with $x \cong 0.5$? Why do we observe shifted loops and ripples in the M-H curves measured at 10 K? The next section discusses the theoretical simulations carried out in order to delve deeper into these issues.

## 5.2.3 Atomistic simulation of magnetic properties

### 5.2.3.1 Magnetic properties of $Fe_{3-x}Cr_xO_4$ bulk series

To model the magnetic properties of the $Fe_{3-x}Cr_xO_4$ series, simulations were performed using an atomistic spin model (ASM) with the VAMPIRE software package. In this model, the spin-dependent interactions are described by the Heisenberg spin Hamiltonian, in which each magnetic moment is localized on its corresponding atom (see **Section 2.6**). Three important parameters had to be given: the atomic spin moment on each Fe and Cr site ($\mu_S$), the anisotropy constant ($k_u$) and the exchange interaction between atomic sites $i$ and $j$ ($J_{ij}$). The spin moments were deduced from the formal charges of each specie ($\mu_{Fe^{2+}}$ = 4 $\mu_B$, $\mu_{Fe^{3+}}$ = 5 $\mu_B$ and $\mu_{Cr^{3+}}$ = 3 $\mu_B$). The anisotropy constant values were the ones estimated by Mössbauer spectroscopy for the bulk parent compounds: $k_u$ = 1.35 × $10^4$ J.m$^{-3}$ for $Fe_3O_4$ [17] and $k_u$ = 6.30 × $10^2$ J.m$^{-3}$ for $FeCr_2O_4$ [18]. For intermediate compositions, in-between values were considered (*i.e.,* linear regression between the values of the extreme compositions). As shown in **Figure 5.6**, the bulk values are in good agreement with the macroscopic anisotropy constant ($K_u$) estimated using the M-H curves of the thin films at low temperature: $K_u = (M_S \times H_C)/2$. The only exception is $x$ around 0.5, for which the constant is two times larger than the one estimated for bulk materials. In fact, the magnetic anisotropy in a system of finite size is determined by the balance of magnetocrystalline and shape anisotropy. It depends greatly in the microstructure and surface and interface interactions. Hence, for simplicity, only the estimated bulk values were used in the simulations.

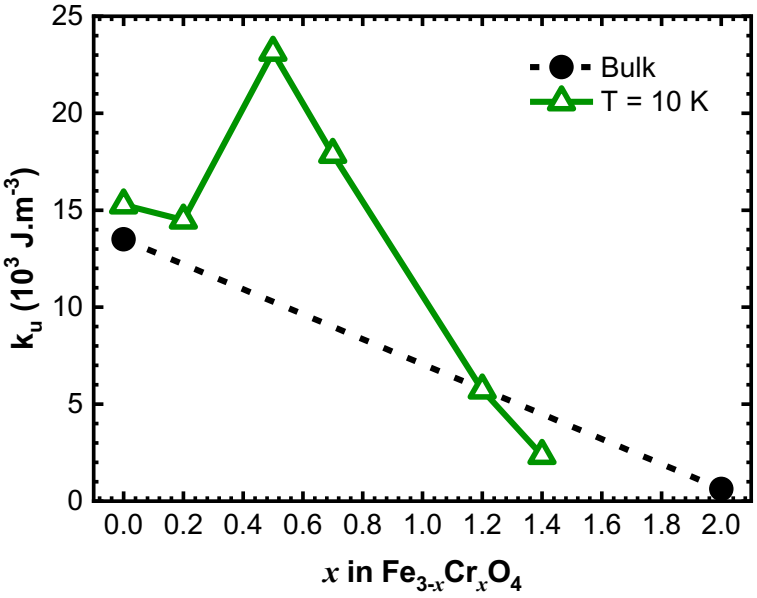


**Figure 5.6.** Anisotropy energy constant of the bulk parent compounds (black circles) – $Fe_3O_4$ [17] and $FeCr_2O_4$ [18] – in comparison with $Fe_{3-x}Cr_xO_4$ thin films (green triangles) at T = 10K.

The last parameter to be set in the simulation inputs is the exchange interaction between atomic sites $i$ and $j$ ($J_{ij}$). As discussed in **Section 1.3.2.1**, the exchange interactions in spinel oxides

are due mainly to super exchange. Hence, their values strongly depend on the angle formed by the two interacting cations (Fe and Cr) and the corresponding mediating O atom. Because the oxygen atoms are nonmagnetic, they do not need to be explicitly simulated within the atomistic spin model. The first nearest neighbor interactions were fitted in order to exactly reproduce the experimental Curie temperature (**Figure 5.7**). As for bulk $Fe_3O_4$, strong antiferromagnetic exchange interactions were considered between the iron Td and Oh sublattices. In addition, one considered a weaker antiferromagnetic exchange between tetrahedral Fe atoms and a ferromagnetic one between octahedral Fe atoms. These constants reproduced well the antiparallel orientation described by Néel [19] and they are in a good agreement with those obtained from ab-initio calculations [20]. In the same way, one took antiferromagnetic exchanges between $Fe^{2+}_{Td}$–$Fe^{2+}_{Td}$, $Fe^{2+}_{Td}$–$Cr^{3+}_{Oh}$, and $Cr^{3+}_{Oh}$–$Cr^{3+}_{Oh}$, as predicted for bulk $FeCr_2O_4$ by ab-initio calculations [21]. These constants reproduced well the conical magnetic state observed for this compound at low temperature [15].

Because there is no ab-initio investigations on the exchange interactions for the intermediate spinel configuration, the parameters between $Fe^{3+}_{Td}$–$Cr^{3+}_{Oh}$, $Fe^{2+}_{Oh}$–$Cr^{3+}_{Oh}$ and $Fe^{3+}_{Oh}$–$Cr^{3+}_{Oh}$ sites were roughly adjusted to reproduce the Curie temperature (**Figure 5.7**). **Table 5.1** summarizes the $J_{ij}$ values obtained in this work, which are consistent with the ones found in the literature for ASM simulations of iron oxides. For example, Moreno *et al.* [22] defined the nearest neighbors exchange interaction values for bulk magnetite as $-6.31 \times 10^{-22}$ J, $9.76 \times 10^{-22}$ J and $-50.7 \times 10^{-22}$ J for the exchanges between $Fe_{Td}$–$Fe_{Td}$, $Fe_{Oh}$–$Fe_{Oh}$ and $Fe_{Td}$–$Fe_{Oh}$, respectively.

**Table 5.1** – Exchange parameters (expressed in Joule) used to reproduce the Curie temperature of $Fe_{3-x}Cr_xO_4$ bulk series.

| $J_{ij}$ ($10^{-22}$ J) | | Atomic site *i* | | | | |
|---|---|---|---|---|---|---|
| | | $Fe^{2+}_{Td}$ | $Fe^{2+}_{Oh}$ | $Fe^{3+}_{Td}$ | $Fe^{3+}_{Oh}$ | $Cr^{3+}_{Oh}$ |
| Atomic site *j* | $Fe^{2+}_{Td}$ | -4.29[a] | -13.6 | -3.25 | -46.8 | -13.6[b] |
| | $Fe^{2+}_{Oh}$ | -13.6 | +8.08[c] | -46.8[d] | -10.1[e] | +11.8 |
| | $Fe^{3+}_{Td}$ | -3.25 | -46.8 | -2.20[f] | -58.5[g] | -36.0 |
| | $Fe^{3+}_{Oh}$ | -46.8 | -10.1 | -58.5 | -12.6 | -11.8 |
| | $Cr^{3+}_{Oh}$ | -13.6 | +11.8 | -36.0 | -11.8 | -10.4[h] |

For comparison, the exchange interactions obtained from ab initio calculations [20], [21] are: (a) $-1.07 \times 10^{-22}$ J; (b) $-4.53 \times 10^{-22}$ J; (c) $11.36 \times 10^{-22}$ J; (d) $-52.6 \times 10^{-22}$ J; (e) $-1.38 \times 10^{-22}$ J; (f) $-1.23 \times 10^{-22}$ J; (g) $-52.6 \times 10^{-22}$ J; (h) $-4.61 \times 10^{-22}$ J.

**Figure 5.7** depicts the Curie temperatures ($T_C$) calculated using the ASM model in comparison with the ones determined experimentally for bulk samples. The simulated system consists of a rigid cube ($8.4 \times 8.4 \times 8.4$ nm$^3$ in size), for which periodic boundary conditions (PBC) were applied to reduce finite-size effects by eliminating the surface. Herein, the lattice parameter and the inversion ratio used as input for the simulation were the ones presented by Robbins *et al.* [1]. The cations were randomly distributed among the Td and Oh sublattices. The temperature-dependent magnetization curves were calculated via the Monte Carlo algorithm (see **Section 2.6.2**), using 10,000 equilibration

steps and 10,000 averaging steps. Although the form of the magnetization curve is known to be seriously in error in this method (see next section), a good estimate of the $T_C$ is usually obtained within 1% of the experimental values [23]. This result confirms the ability of the ASM model to relate microscopic exchange interactions to the macroscopic Curie temperature.

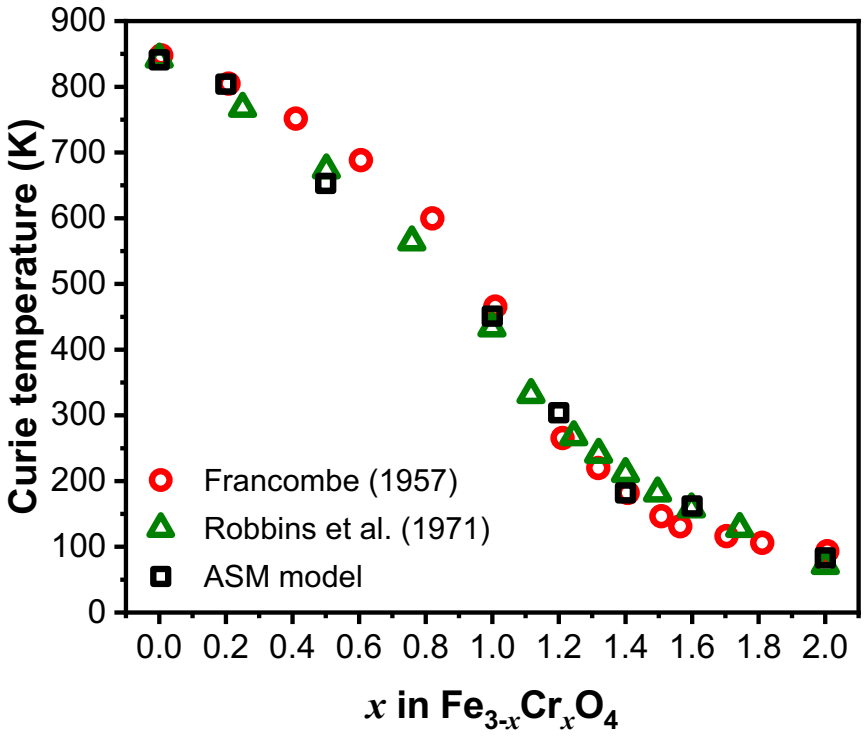


**Figure 5.7.** Calculated Curie temperature (black squares) for $Fe_{3-x}Cr_xO_4$ bulk series in comparison with experimental data taken from the literature: Francombe [24] (red circles) and Robbins *et al.* [1] (green triangles). Herein, the error bars are the size of the point (~1%).

By adjusting the exchange parameters (**Table 5.1**), not only the $T_C$ was well reproduced for the $Fe_{3-x}Cr_xO_4$ bulk series (**Figure 5.7**), but also the ground state spin structures are coherent with the expected for this system. **Figure 5.8** depicts the spin structures found after cooling to 0 K using a linear cooling function over 1,000,000 Monte Carlo steps. For this calculation, a smaller cubic system ($2.1 \times 2.1 \times 2.1$ nm$^3$ in size) in PBC was considered. According to Ma *et al.* [15], the $Fe_{3-x}Cr_xO_4$ bulk series has a collinear spin structure for $x < 1.4$ and a conical spin structure for $x \geq 1.4$ at low temperature. As explained in **Section 1.3.2.2**, this change in magnetic structure occurs due to the competition between the antiferromagnetic Oh-Oh interactions with the strong Td-Oh interactions. For all compositions, **Figure 5.8** shows that the spins on Td-sites of the iron chromites are coupled antiferromagnetically to spins on Oh-sites. This result corroborates well with the XMCD findings for the films. Interestingly, the magnetic moments lied in different planes depending on the Cr content. Whereas for $x < 0.5$ (*i.e.* inverse spinel configuration) the magnetic moments aligned closely to the (100) planes, the ones of intermediate compositions ($0.5 \leq x < 1.4$) lied in plane along the (111) planes. Canted magnetic moments were only observed for high Cr content ($x > 1.4$). As shown in **Figure 5.8**, $FeCr_2O_4$ forms a conical structure around the [001] direction.

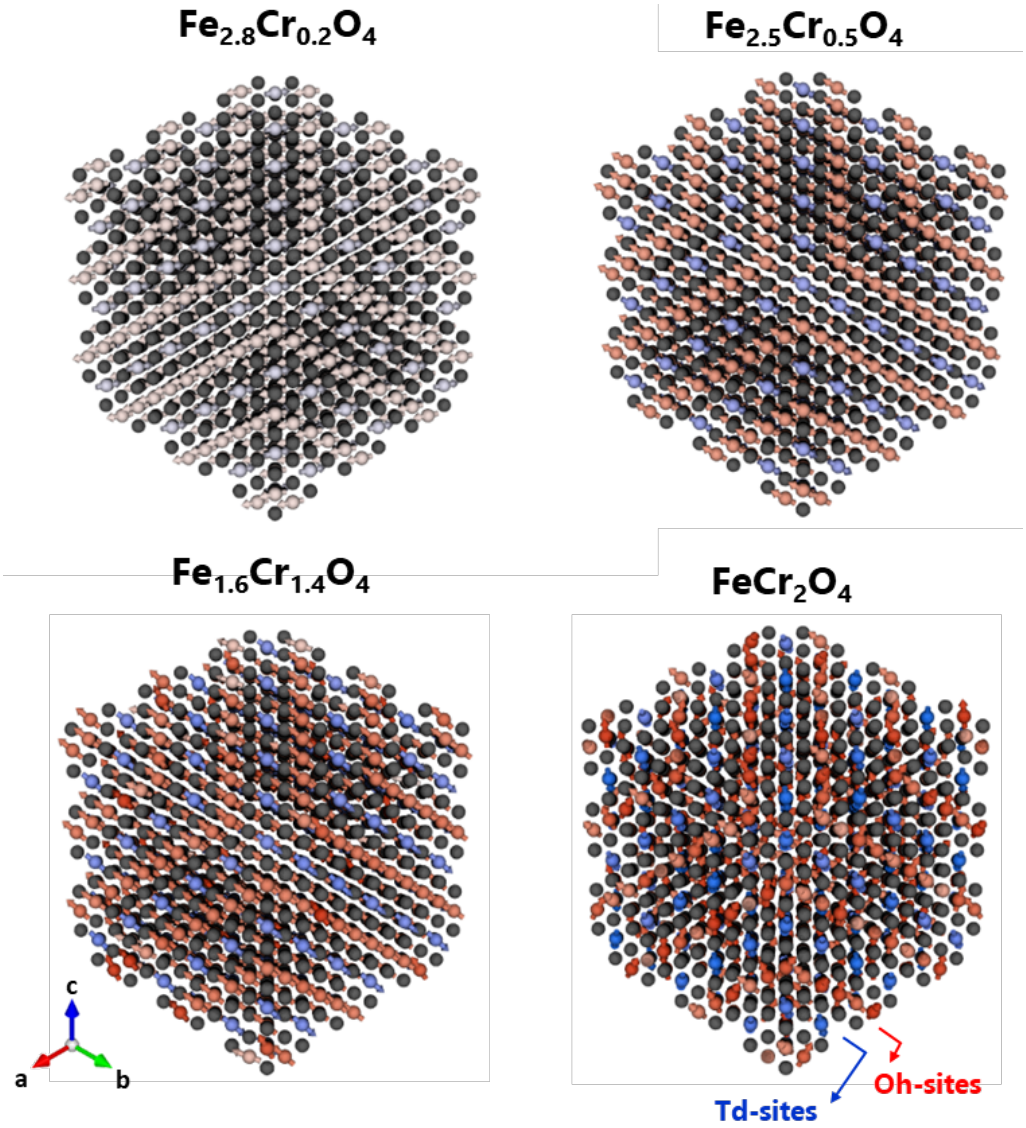


**Figure 5.8.** View on <111> direction of the simulated ground state spin structure of $Fe_{3-x}Cr_xO_4$ bulk series at T = 0 K. The non-magnetic oxygen atoms were depicted as black spheres. The spins on Td-sites (spin down, blue spheres) are coupled antiferromagnetically to spins on Oh-sites (spin up, red spheres).

Once it was ensured that the parameters set in the simulation inputs described the magnetic properties of the bulk properly, the film properties were investigated.

### 5.2.3.2 Magnetic properties of $Fe_{3-x}Cr_xO_4$ thin films

One of the most interesting points in the analysis of the magnetic properties of the iron chromite films is the higher magnetic moments that were found for $x \geq 1.2$ (**Figure 5.4**). In fact, those samples still showed magnetization at room temperature, *i.e.,* near (or above) the Curie temperature of bulk samples. This result seems to be closely related with the higher inversion ratio of the films. While bulk $Fe_{1.8}Cr_{1.2}O_4$ has almost a completely normal spinel structure ($y \cong 0.1$), the film still has 25% of the Oh-sites occupied with $Fe^{2+}$ ($y \cong 0.5$). The higher $y$, the greater the Td-Oh interaction strength.

Consequently, the spin moments become more collinear and the $T_C$ of these materials are increased due to the electron hopping effect between Td-Oh sites (see **Section 1.3.2.2**).

To probe the influence of the cationic site distribution on the $T_C$, **Figure 5.9** shows temperature-dependent magnetization curves of $Fe_{1.8}Cr_{1.2}O_4$ calculated for $y$ = 0.1 and $y$ = 0.5. These curves were calculated in PBC for an 8.4 × 8.4 × 8.4 $nm^3$ cube size via the Monte Carlo algorithm (10,000 equilibration steps and 10,000 averaging steps). According to ASM simulations, the increase of inversion ratio from 0.1 to 0.5 leads to a considerable increase in $T_C$ from 305 K to 480 K. This value could not be confirmed experimentally because the temperature in the PPMS-VSM system used in this work does not heat up much above the room temperature. However, the calculated gap of almost 200 K for $T_C$ is consistent with what is found in the literature for bulk samples. As shown in **Figure 5.7**, $T_C$ values of the $Fe_{3-x}Cr_xO_4$ series increase sharply with the increase of the inversion ratio, *i.e.* in the $0.5 \leq x \leq 1.2$ compositional range. For example, the difference between the $T_C$ of bulk $Fe_{1.8}Cr_{1.2}O_4$ ($y$ = 0.1) and bulk $Fe_{2.2}Cr_{0.8}O_4$ ($y$ = 0.5) is almost 250 K. Therefore, the observed increase in magnetization for the films is definitely related to the increase in their inversion ratio.

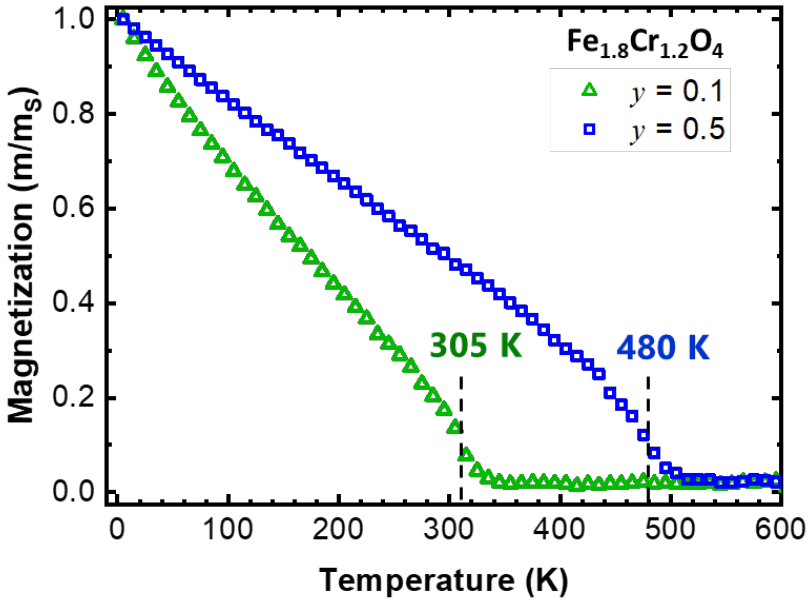


**Figure 5.9.** Simulated temperature-dependent magnetization for $Fe_{1.8}Cr_{1.2}O_4$ with $y$ = 0.1 (green triangles) and $y$ = 0.5 (blue squares).

Another outstanding point in the analysis of the $Fe_{3-x}Cr_xO_4$ thin films is the difference found for the M-H curves. As shown in **Figure 5.2a-c**, the series can be divided into two regions based on the shapes of the hysteresis loops at 300 K. Region I ($0 \leq x \leq 0.5$) was characterized by normal M-H curves typical of single-phase thin films ("square-type" loop), while Region II ($0.7 \leq x \leq 1.4$) showed constricted hysteresis loops. Upon cooling, two phenomena add up. First, all loops were shifted in the negative field direction after cooling to 10 K from a positive field. Herein, the greater the Cr content, the greater the negative shift. Secondly, small ripples were observed in the curves for $0.2 \leq x \leq 0.5$ and saturation was much harder to achieve for $0.7 \leq x \leq 1.2$. Interestingly, similar behavior was observed for $Fe_{3-x}Cr_xO_4$ bulk samples with $x > 0.7$ [11].

In order to investigate the influence of the composition and the cation distribution in the shape of the hysteresis loop, spin dynamics simulations were performed solving the stochastic Landau-Lifshitz-Gilbert equation (see **Section 2.6.2**). A hysteresis loop simulation was run with the magnetic field aligned perpendicular to the [111] direction (*i.e.,* in the plane of the film). The field was applied between ± 1.0 T in steps of 0.005 T in 1-nanosecond hysteresis loops. To ensure a converged coercivity, the simulations were run in the limit of critical damping ($\lambda = 1$) to accelerate the convergence. These computational details are consistent with the ones found in the literature [25] for spin dynamics simulations to obtain hysteresis loops and evaluate magnetic phenomena such as the exchange bias. **Figure 5.10** depicts the produced hysteresis loops for bulk systems in comparison with thin films for few selected compositions. Both systems have the same size: $10 \times 6 \times 6$ nm$^3$. To simulate a thin film, PBC were only taken into account for $\vec{a}$ and $\vec{b}$ directions, so no PBC was added to the $\vec{c}$ direction, which is parallel to the [111] axis of the spinel structure. For the bulk, the cations were randomly distributed among the Td and Oh sublattices, following the structure determined by Robbins *et al.* [1]. Likewise, the cation distribution for the thin films was the one determined by the XMCD measurements (**Figure 5.**).

**Figure 5.10** shows preliminary results for these calculations, in which both bulk and thin films produced simulated square loops. For $Fe_3O_4$, the simulations were performed considering that both systems have perfect inverse spinel configuration. Because of surface effects, one observes a small increase in the coercivity from 0.04 T to 0.06 T and a small shift of the loop. As the Cr content increases, the influence of chemical composition and cation distribution are added to the surface effects. $Fe_{2.5}Cr_{0.5}O_4$ and $Fe_{1.8}Cr_{1.2}O_4$ compositions showed very similar simulated loops ($\mu_0 H_C = 0.05$ T) for their bulk systems. However, in the film form, one observes that the coercivity as well as the shift increase as $x$ increases. It should be noted that the sign of the shift depended on the exposed surface. Considering systems of the same size, positive shift was observed in $Fe_{Td}$–O terminated surface (**Figure 5.10** red circles), while negative shift was observed in $Fe_{Oh}$–O terminated surface (**Figure 5.10** blue circles). Hence, this feature may be related to a surface and interface effect. Indeed, it has been shown in the literature [7] that the shift in the field-cooled M-H curve decreases with increasing thickness. However, it does not disappear even for thicker films (~6 μm of thickness).

Even if it is tempting to assume that the negative shifts observed in the experimental M-H curves (**Figure 5.3**) is mainly due to exposed $Fe_{Oh}$–O surfaces, the results of the ASM simulations must be interpreted with caution. Exposing a given surface is the same as creating dangling bonds to a specific cationic site. That is to say, an imbalance arises between the exchange interactions. Therefore, shifts can also be obtained by creating defects in the structure. For instance, by adding cation vacancies, *i.e.,* by removing exchange interactions.

Although the increase in the negative shift with Cr content is consistent with that observed in the thin films, the typical constriction of the cycle for $x > 0.7$ was not observed. This outcome indicates that this feature is rather related to the microstructure of the film and not strictly a surface or interface effect. According to Wasilewski *et al.* [11] the constricted loops observed for the bulk are associated to a system containing mixture of hard and soft components. For thin films, the structural characterization showed the presence of only single phase $Fe_{3-x}Cr_xO_4$. However, the crystalline structure is not perfect. One observed for these films point defects and planar defects, especially for

samples with higher Cr content. Therefore, it would be interesting to investigate the influence of each of these structural defects on the M-H curves. Notably, the APBs, which are often cited [7] as responsible for anomalous magnetic behaviors observed in different nanostructures. Because APBs are defects created by fractional displacement of the lattice constant between atomic planes, both the atomic distances and the M-O-M angles (M = Cr, Fe) changes across their interface. Hence, extra exchange interactions arising from the APB interfaces should be taken into account [22], which dramatically increases the complexity of the simulations. Since a detailed study of the microstructure of the films is beyond the scope of this thesis, these calculations were not carried out. However, they are indeed part of the prospects of this work.

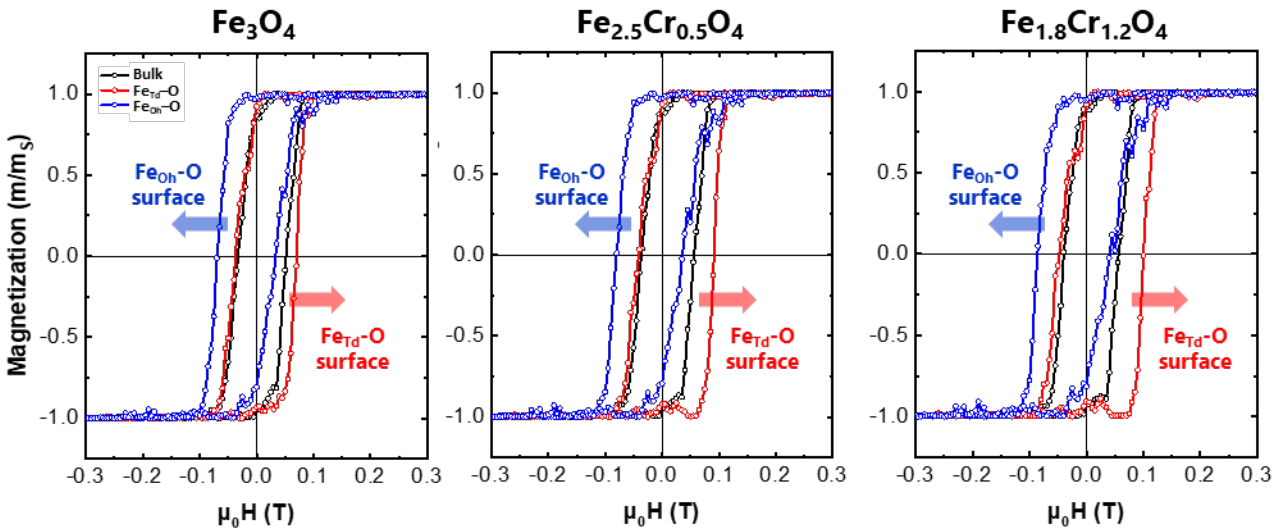


**Figure 5.10.** Simulated magnetic hysteresis cycle for bulk (black circles) and thin films in the $Fe_{3-x}Cr_xO_4$ (111) series. The simulations were performed for both $Fe_{Td}$–O terminated surface (red circles) and $Fe_{Oh}$–O terminated surface (blue circles).

**Highlights on the magnetic properties of $Fe_{3-x}Cr_xO_4$ thin films:**

- Increasing Cr content decreases the magnetic moment and the magnetic hardness of the $Fe_{3-x}Cr_xO_4$ thin films. Except for $x$ around 0.5, which shows high values of $M_R$ and $\mu_0H_C$.
- For $x < 1.2$, the thin films show lower magnetic moments than the bulk due to the presence of anti-phase boundaries (APBs).
- For $x \geq 1.2$, the thin films show higher magnetic moments than the bulk due to the increase in the inversion ratio.
- At low temperatures (T = 10 K), the M-H curves are shifted to negative field values. Ripples are observed in the curves for $0.2 \leq x \leq 0.5$, while loop constriction is observed for $x \geq 0.7$. These features are related to surface and interface effects, point defects and microstructure of the films.

# 5.3 Electronic transport and band gap control

## 5.3.1 Resistivity measurements

Another effect of substitutional Cr in the $Fe_3O_4$-$FeCr_2O_4$ system is the modification of the conduction mechanism, since the former is a known half-metal material while the latter is an insulator at room temperature. In ferrites, the electron conductivity is associated to the easy electron transfer in Oh-sites and requires two critical steps to occur: (*i*) the presence of charge carrier donor/acceptor pairs ($M^{n+}/M^{(n+1)+}$) and (*ii*) enough energy to overcome the activation barrier between hopping pairs [26]. Assuming that the charge transport occurs predominantly between like-cation pairs, only $Fe^{2+}/Fe^{3+}$ pairs should participate in electron hopping in this system as Cr assumes only one oxidation state. Hence, on replacing a $Fe^{3+}$ cation with a $Cr^{3+}$ cation in Oh-sites, one expects those charge-conducting sites to be blocked and the charge transport to be affected by the increase in hopping barriers. In addition, if $Fe^{2+}$ cations are displaced to Td-sites, as suggested by XMCD results, a new conduction mechanism involving hopping between Td and Oh-sites should also be considered [27], [28].

**Figure 5.11** shows the resistivity ($\rho$) of $Fe_{3-x}Cr_xO_4$ thin films as function of the temperature ($T$) measured using a standard four-probe dc-method in a quantum design physical properties measurement system (PPMS). For all compositions, the expected semiconducting behavior with increasing resistivity for decreasing temperature is clearly observed. To a first approximation, the curves of $\ln \rho$ against $1/T$ are straight lines with a slope continually increasing as $x$ increases. Therefore, there is a general increase in the resistivity of spinel solid solution with higher $x$ content, consistent with the decrease in the total number of conducting $Fe^{2+}/Fe^{3+}$ pairs. For instance, the resistivity of the films at room temperature ranged from $7\times10^{-4}$ Ω.m for $Fe_3O_4$ to $1\times10^{-1}$ Ω.m for $Fe_{1.8}Cr_{1.2}O_4$, increasing gradually with the Cr content. For $x > 1.2$, the resistivity attained values beyond the experimental limits of the PPMS system and is not shown here.

Besides increasing the resistivity, introducing Cr into the magnetite structure also inhibits the Verwey transition (see **Section 1.3.2.3**). As shown by Wright *et al.* [29], long-range ordered $Fe^{2+}{}_{Oh}$-$Fe^{3+}{}_{Oh}$ is necessary for the transition to occur. Since $Cr^{3+}$ ions disrupt the electron hopping along Oh-sites, no abrut drop of conductivity (typical of the Verwey transition) was observed upon cooling for the iron chromites. It should be noted that even for $Fe_3O_4$ the change in the conduction behaviour was attenuated or even inhexistent for some samples. However, the reason behind this behavior lies not in the chemical composition of the $Fe_3O_4$ epitaxial films, but in their microstructures. In fact, in very thin films, the density of antiphase boundaries is large. As shown in the litterature [6], [30], the thinner the $Fe_3O_4$ film, the larger the APBs density and the lower the Verwey temperature ($T_V$). For instance, 15-nm-thick $Fe_3O_4$ films show $T_V$ around 105 K, while no transition is observed for 8-nm-thick films. It has been suggested that for very high APBs density, the domain size is so small that the long-range order required for the Verwey transition is inhibited. Another consequence of the large density of APBs is the increase of the overall resistivity. Note that the resistivity measured for $Fe_3O_4$ in **Figure 5.11** ($7\times10^{-4}$ Ω.m) is considerably higher than the bulk value of $4\times10^{-5}$ Ω.m. This

because APBs act as scattering centers hindering the electron transport across the films [30], [31]. Moreover, the magnetic coupling across an APB is rather antiferromagnetic [9] while the charge transfer in $Fe_3O_4$ requires ferromagnetic alignment between neighboring donor/acceptor pairs. The presence of APBs thus affects the conductivity of all iron chromite thin films.

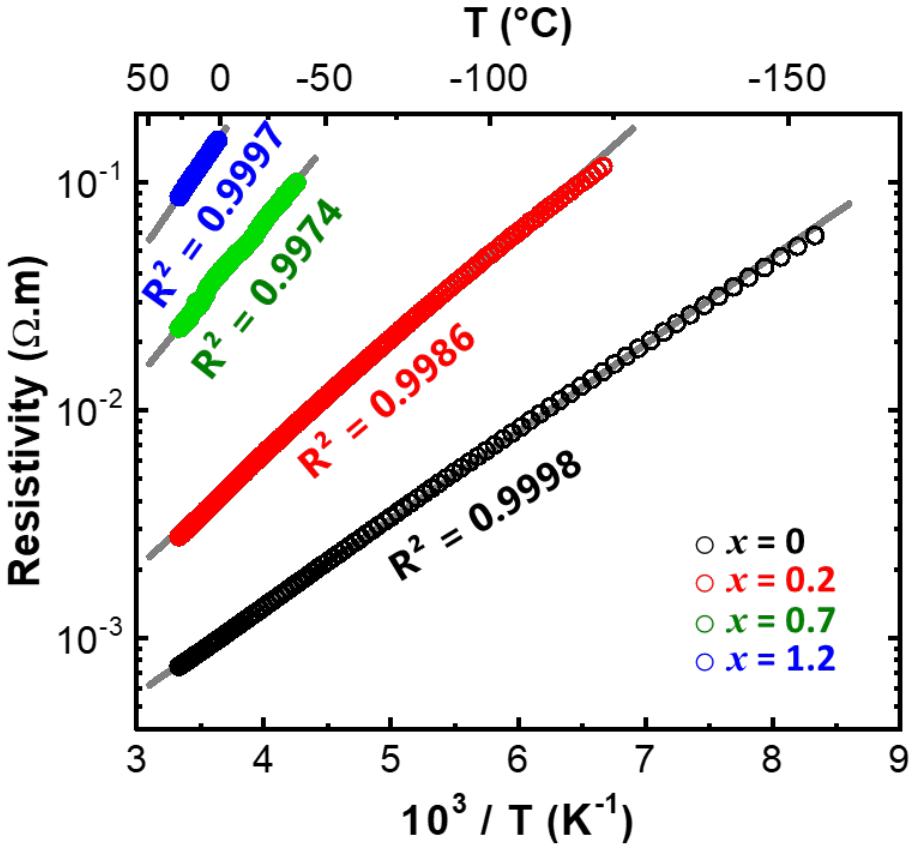


**Figure 5.11.** Electronic transport behavior in $Fe_{3-x}Cr_xO_4$ thin films. Herein, the temperature-dependent resistivity (ρ) is plotted as Arrhenius curves. According to the coefficient of determination ($R^2$), reasonably good linear fit (gray straight lines) is found for ln ρ against 1/T. Color code: $x$ = 0 (black), $x$ = 0.2 (red), $x$ = 0.7 (green) and $x$ = 1.2 (blue).

As discussed in **Section 1.3.2.3**, the theory for the electronic conductivity of these oxides, especially for $Fe_3O_4$, is still not very satisfactory. To give insight into the conduction mechanism, the general charge transport equation for semiconductors [32] is considered:

$$\rho(T) = \rho_0 \times e^{(E_a/k_B T)^p} \tag{5.3}$$

where pre-factor $\rho_0$ is the resistivity at $T \rightarrow \infty$ and $E_a$ is the activation energy. The power-law dependence ($p$) gives the type of charge hopping, *e.g.* $p$ = 1 corresponds to nearest-neighbor hopping (NNH) and $p$ = 0.25 (or 0.5) to variable range hopping (VRH) [33]. To determine accurately the $p$ value, ln(ρ) *vs.* $T^p$ data was linear fitted varying the exponent $p$ from 0.1 to 1 with steps of 0.05. Because magnetite may change its conduction behavior across Verwey transition, all fits were made for temperatures above 120 K. **Figure 5.12** depicts the residual sum of squares (RSS) from this

procedure. The optimal $p$ values (*i.e.,* the one that minimizes the RSS) were extracted from parabola fits and are indicated by arrows. Overall, the $p$ value decreases as $x$ increases. According to the optimal $p$ values, $Fe_3O_4$ follows a NNH mechanism ($p \cong 1$), while $Fe_{2.8}Cr_{0.2}O_4$ is best fitted in the Efros-Shklovskii (ES) VRH mechanism[35] ($p \cong 0.5$) for this temperature range. The change from NNH to VRH mechanism indicates that Cr introduces disorder in the cation arrangement and that short-range hops are now favored. The same behavior is to be found for the other iron chromites ($x > 0.2$). However, the difference in fit quality for these samples is negligible due to the smaller number of points. Thus, no minimum value was found for $p$ and nothing can be concluded with certainty about their conduction mechanism.

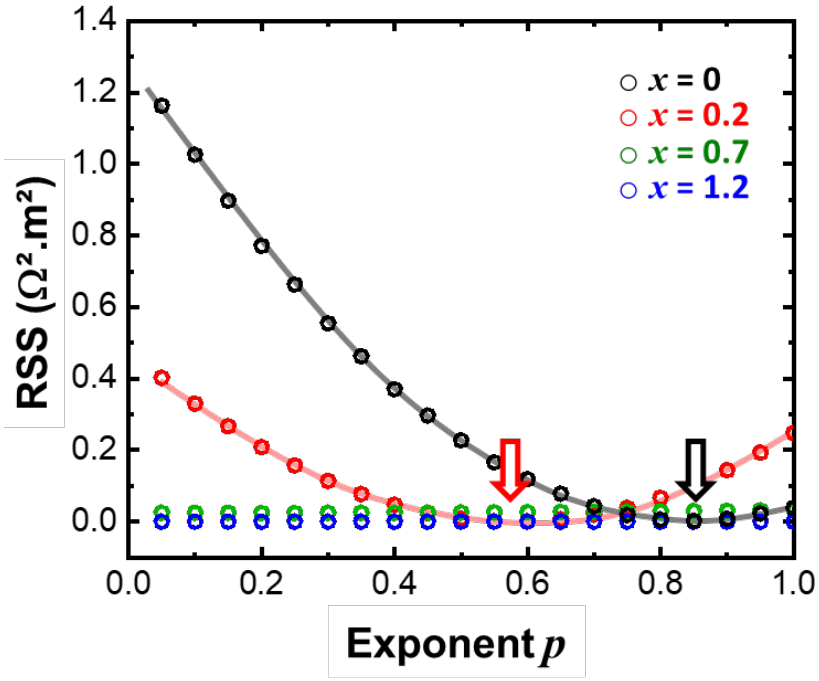


**Figure 5.12.** Plot of the residual sum of squares (RSS) against the exponent $p$ from the fit of Equation 5.3. The arrows depict the minimum of the parabola fit, indicating which conduction mechanism governs the iron chromites in such temperature range. Color code: $x$ = 0 (black), $x$ = 0.2 (red), $x$ = 0.7 (green) and $x$ = 1.2 (blue).

### 5.3.2 Electronic transport vs. cationic site distribution

In order to analyze the activation energy and the pre-factor value ($\rho_0$) obtained from fitting the resistivity curves, the same model has to be used. As a first approximation, the simplest form of the thermal activation process was considered ($p$ = 1), since reasonably good fit of resistivity curves

[35] Similar to the Mott VRH mechanism (see **Section 1.3.2.3**), the VRH mechanism proposed by Efros and Shklovskii (ES) [34] also considers disordered system whose electronic states are localized close to the Fermi level. Whereas the Mott mechanism assumes that the density of states near the Fermi level is constant, the ES mechanism considers that Coulomb interactions between localized electrons create a 'soft' gap in the density of states near the Fermi level. These different assumptions result in a different power-law dependence ($p$) to Equation 5.3: $\ln(\rho) \propto T^{0.25}$ for Mott-VRH and $\ln(\rho) \propto T^{0.5}$ for ES-VRH.

(**Figure 5.11a**) is possible assuming this mechanism. **Figure 5.13** shows the values of $\rho_0$ and $E_a$ obtained from the least-squares fitting of the Arrhenius curves, which are clearly affected by the increase of Cr content. The pre-factor $\rho_0$ steadily increases from $4.0\times10^{-5}$ Ω.m ($x$ = 0) to $1.7\times10^{-4}$ Ω.m ($x$ = 1.2), while the activation energy $E_a$ increases from 76 meV ($x$ = 0) to 161 meV ($x$ = 1.2). Considering the NNH hopping model [35], $\rho_0$ can be related to $Fe^{2+}/Fe^{3+}$ pair concentration and the possibility of this pair to form a conductive pathway. Therefore, in order to understand the evolution of the conduction mechanism with Cr content, it is imperative to consider the cation site-occupation. Another interesting point is that the material shows a more insulator-like behavior with increasing Cr content. The monotonic increase of activation energy with composition confirms that Cr is not active in the transport process for $x < 1.2$, which is in good agreement with the conduction mechanism proposed for iron chromite bulk samples [36] (see **Section 1.3.2.3**).

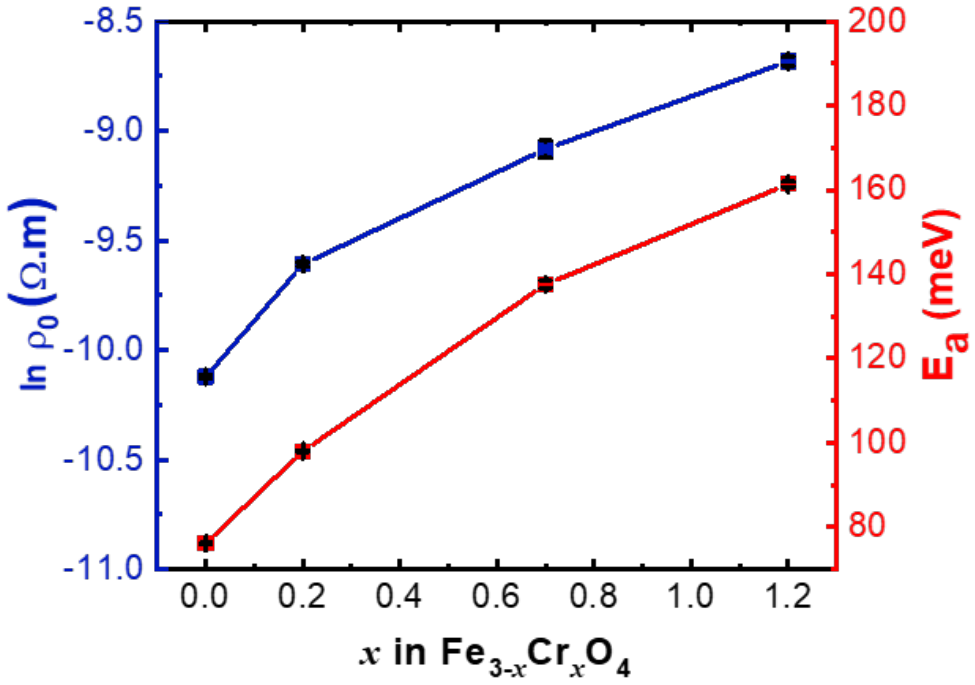


**Figure 5.13.** The pre-factor $\rho_0$ (left y-axis) and the activation energy $E_a$ (right y-axis) extracted from the fit of the resistivity curves. The error bars included in the plot are calculated based on the least-squared minimization linear fitting, which were consistently smaller than 1% for all samples.

Three types of pathways for electron hopping can be considered if $Fe^{2+}$ populates both sublattices, as described by the general formula: $Fe_a^{2+} + Fe_b^{3+} \rightarrow Fe_a^{3+} + Fe_b^{2+}$. The first one is Oh-to-Oh site hopping (**Figure 5.14a**), which is the favored mechanism in the spinel structure since the Oh-sites form infinite edge-sharing networks with one another. The other ones are Td-to-Td (**Figure 5.14b**) and Td-to-Oh (**Figure 5.14c**) transfer. These mechanisms are usually rejected for spinel ferrites since they are unfavorable over the Oh-to-Oh transfer. In the spinel structure, the Td-sites share corners with Oh-sites, but are isolated from one another. The existence of a large number of pairs of close neighbor states is indispensable for the NNH conduction to occur. Moreover, contrary to the case of $Fe^{2+}$ and $Fe^{3+}$ octahedra sharing edge, the $t_{2g}$ atomic orbitals of the two ions overlap

poorly for $Fe^{2+}$ and $Fe^{3+}$ sharing corners thereby hindering electron transfer between Td and Oh-sites. Although octahedral hopping appears to dominate in spinels, it may become invalid if the system is disordered or non-stoichiometric [27].

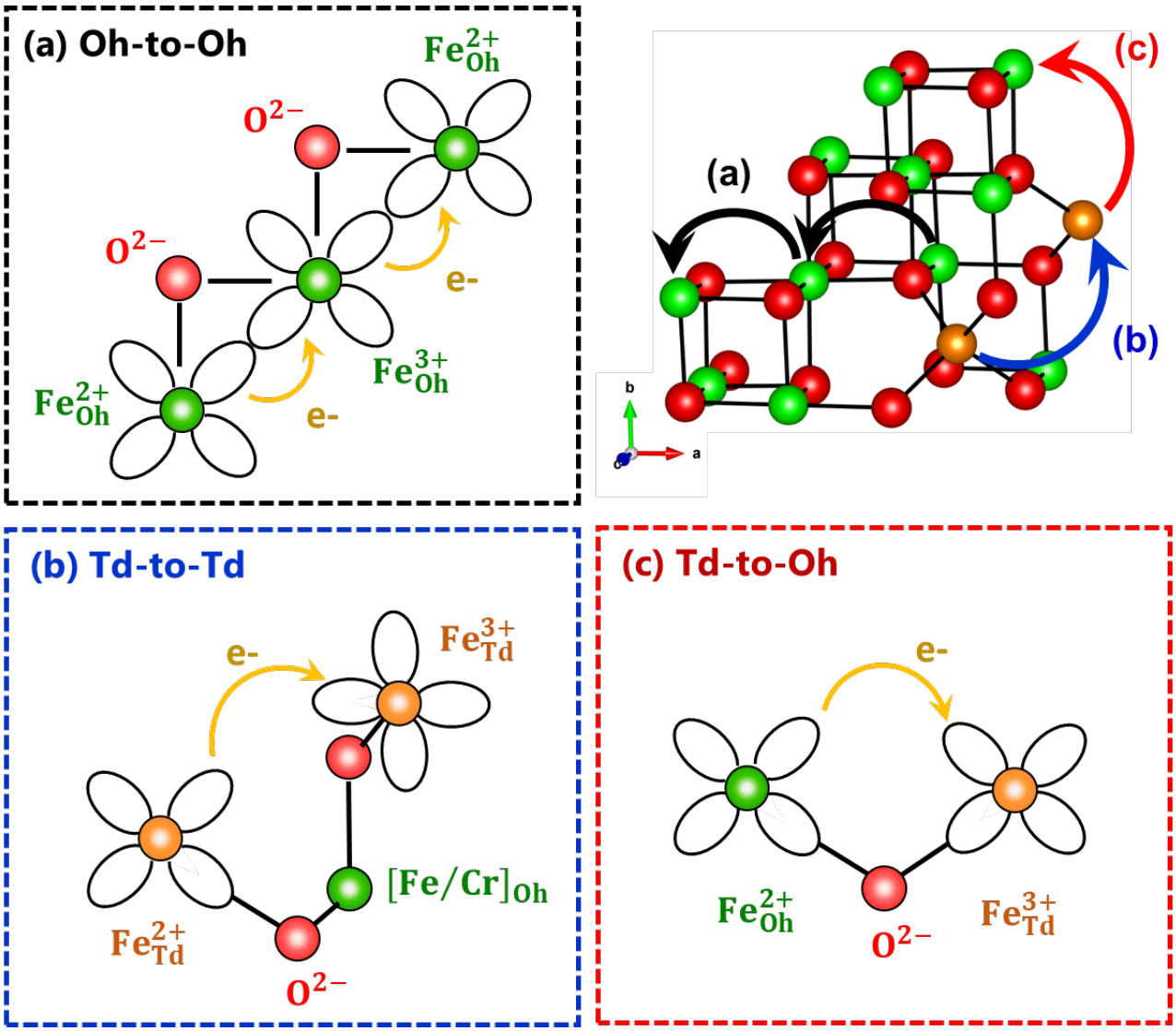


**Figure 5.14.** Schematic representation of possible charge transfer pathways in the spinel structure. (a) Generally, the electron hopping in ferrites occurs through the octahedra sites (Oh-to-Oh), where an alternate arrangement of $Fe^{2+}/Fe^{3+}$ cations lead to charge flow. Hopping through (b) tetrahedral sites (Td-to-Td) or (c) between Td and Oh-sites (Td-to-Oh) is more energetic due to the greater distance between these (in $Fe_3O_4$, $d_{Oh\text{-}Oh}$ = 0.3017 nm, $d_{Td\text{-}Oh}$ = 0.3538 nm and $d_{Td\text{-}Td}$ = 0.3695 nm) and the lack of effective orbital overlap. Color code: Td-site (orange), Oh-site (green) and oxygen (red).

As discussed in **Section 1.3.2.3**, if small polaron approximation is considered, the electrical conductivity (σ), which is the inverse of resistivity (ρ), should be proportional to the probability that there are enough $M^{n+}/M^{(n+1)+}$ components aligned in a contiguous pathway for percolation to occur:

$$\sigma \propto Nc'(1-c') \tag{5.4}$$

where N is the density of conducting sites, c' is the fraction of conducting sites occupied by charge carriers, $(1-c')$ is the fraction of potential jump sites. The behavior of electrical conductivity can be then predicted from the knowledge of the content and distribution of $Fe^{2+}$ cations amongst Oh and Td occupied sites (*i.e.,* the inversion ratio $y$). For instance, considering Oh-to-Oh transfer, c' = $Fe^{2+}{}_{Oh}$ / ($Fe^{2+}{}_{Oh}$ + $Fe^{3+}{}_{Oh}$), $(1-c')$ = $Fe^{3+}{}_{Oh}$ / ($Fe^{2+}{}_{Oh}$ + $Fe^{3+}{}_{Oh}$), and N becomes the total concentration $Fe^{2+}{}_{Oh}$ + $Fe^{3+}{}_{Oh}$. Hence, $Nc'(1-c')$ is written as ($Fe^{2+}{}_{Oh} \times Fe^{3+}{}_{Oh}$)/($Fe^{2+}{}_{Oh}$ + $Fe^{3+}{}_{Oh}$). Likewise, $Nc'(1-c')$ is equal to ($Fe^{2+}{}_{Td} \times Fe^{3+}{}_{Oh}$)/($Fe^{2+}{}_{Td}$ + $Fe^{3+}{}_{Oh}$) for Td-to-Oh transfer and $Nc'(1-c')$ is equal to ($Fe^{2+}{}_{Td} \times Fe^{3+}{}_{Td}$)/($Fe^{2+}{}_{Td}$ + $Fe^{3+}{}_{Td}$) for Td-to-Td transfer.

**Figure 5.15a** shows the evolution of concentration of hopping pairs, $Nc'(1-c')$, as function of $x$ considering the bulk cation distribution [1], [2] (dotted lines) and the XMCD results for the iron chromite thin films (squares). For bulk samples, the probability of $Fe^{2+}{}_{Oh}$/$Fe^{3+}{}_{Oh}$ to form a contiguous pathway is maximum at the equivalence point $Fe^{2+}{}_{Oh}$ = $Fe^{3+}{}_{Oh}$ ($x$ = 0 and $y$ = 1) and then decreases steadily as the $Fe_{Oh}$ percolation pathways are broken by Cr cations and they become inactive. Herein, I assumed that Cr cations do not act as an electron donor or acceptor and are not involved in conduction. For $x > 0.8$, the amount of $Fe^{2+}{}_{Oh}$/$Fe^{3+}{}_{Oh}$ pairs diminish sharply due to the decrease of the inversion ratio until the critical value of $x$ = 1.3 ($y$ = 0) where there is no possible $Fe^{2+}{}_{Oh}$/$Fe^{3+}{}_{Oh}$ pathway since all $Fe^{2+}$ cations have been displaced to Td-sites. On the other hand, the number of $Fe^{2+}{}_{Td}$/$Fe^{3+}{}_{Oh}$ pathways steadily increase in the $0 < x < 1.3$ range with the decrease of inversion ratio, being maximum at $x$ = 1.3 ($y$ = 0) where all Td-sites are occupied by $Fe^{2+}$ cations and only 65% of the Oh-sites are blocked by Cr. For $x > 1.3$, the amount of $Fe^{2+}{}_{Td}$/$Fe^{3+}{}_{Oh}$ contiguous pathways drops significantly as they are progressively broken by Cr. Likewise, the concentration of hopping $Fe^{2+}{}_{Td}$/$Fe^{3+}{}_{Td}$ pairs increases until $x$ = 0.8 (where $Fe^{2+}{}_{Td}$ = $Fe^{3+}{}_{Td}$ = 0.5) and then decreases sharply due to the decrease of inversion ratio. However, the amount of those pairs is never greater than $Fe^{2+}{}_{Oh}$/$Fe^{3+}{}_{Oh}$ or $Fe^{2+}{}_{Td}$/$Fe^{3+}{}_{Oh}$ hopping pairs. Therefore, for bulk samples, the conduction mechanism will go through Oh-to-Oh site hopping until $x$ = 1.2, whereas the more Cr-rich compositions may exhibit Td-to-Oh hopping or mixed $Fe^{2+}$-$Fe^{3+}$-$Cr^{3+}$ electron transfer, as suggested by Nell and Wood [36]. The transition from the Oh-to-Oh to the less favorable mechanism requires an appreciable amount of added energy. Consequently, Nell and Wood observed a rapid increase of the activation energy in the $1.2 < x < 1.5$ region.

For the $Fe_{3-x}Cr_xO_4$ (111) thin films, the dominant mechanism in the compositional range studied is Oh-to-Oh site hopping, as they remained intermediate spinel for $x$ up to 1.2 (**Figure 5.**). As shown in **Figure 5.15a**, the amount of the $Fe^{2+}{}_{Oh}$/$Fe^{3+}{}_{Oh}$ is greater than $Fe^{2+}{}_{Td}$/$Fe^{3+}{}_{Oh}$ or $Fe^{2+}{}_{Td}$/$Fe^{3+}{}_{Td}$ hopping pairs for all considered compositions. As demonstrated in **Section 1.3.2.3**, the pre-factor $\rho_{0,exp.}$ determined from the fit of the resistivity curves (**Figure 5.13**) can be related to the probability of finding a $Fe^{2+}$:$Fe^{3+}$ pair in neighbor Oh-sites. In **Figure 5.15b**, good correlation was found between the calculated $\rho_0$ ($\rho_0 \propto [Nc'(1-c')]^{-1}$) to the experimentally determined pre-factor ($\rho_{0,exp.}$), confirming that the polaron hopping model describes well the electron transport in this ternary system.

Although the electron hopping along the favored Oh-to-Oh site is still possible for $x$ up to 1.2, the probability of hopping along this path is effectively affected by Cr-concentration. As the distance between neighboring $Fe^{2+}$ and $Fe^{3+}$ in Oh-sites increases by the presence of $Cr^{3+}{}_{Oh}$, the

electrons are forced to follow narrow and complicated channels to an extent as high as the Cr content. Indeed, ρ(300 K) (**Figure 5.11**) increased from $7\times10^{-4}$ Ω.m ($x$ = 0) to $3\times10^{-3}$ Ω.m ($x$ = 0.2) since 10% of the Oh-sites were blocked by $Cr^{3+}$ cations. Moreover, a monotonic increase of activation energy (**Figure 5.13**) was observed for the thin films. As discussed above for bulk samples [36], the absence of sharp increase of activation energy confirms that the octahedral hopping between $Fe^{2+}$ and $Fe^{3+}$ is the sole pathway for the films. Interestingly, compared to these bulk samples, smaller activation energies were found for higher Cr content films considering the same NNH hopping model. For instance, for $x$ = 1.2, Nell and Wood [36] found $E_a$ = 250 meV, while for thin films[36] $E_a$ = 161 meV. This is due to the greater amount of $Fe^{2+}_{Oh}/Fe^{3+}_{Oh}$ hopping pairs for the thin films, as they have greater inversion ratio (**Figure 5.1**). Moreover, this composition shows slight deviation from stoichiometry (see Fe K-XANES results in **Section 4.4.2**), which also contributes to the improvement in the transport properties.

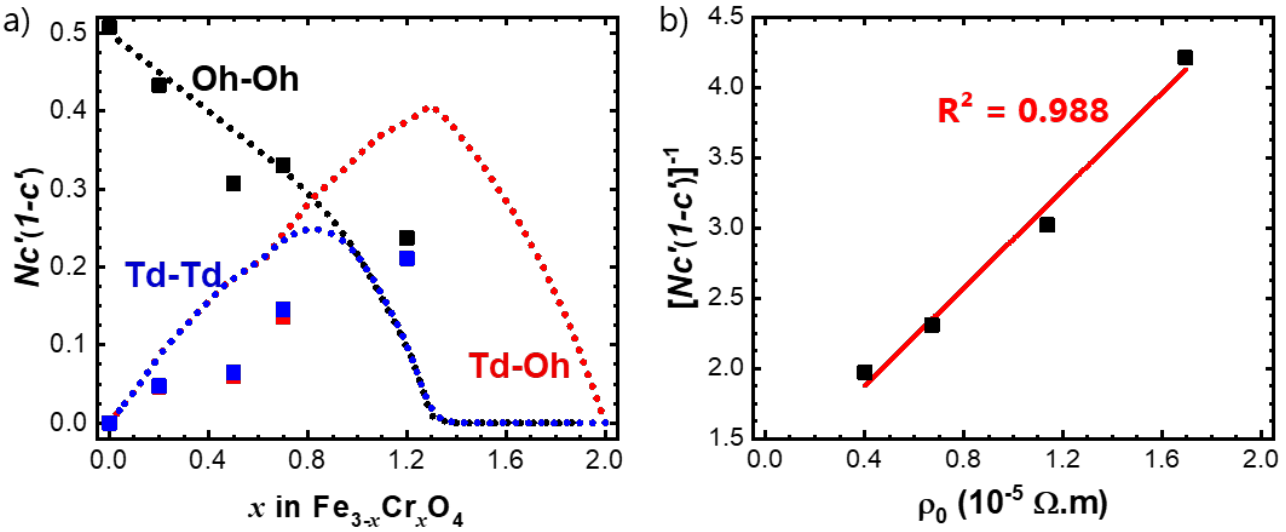


**Figure 5.15.** (a) Concentration of hopping pairs Nc'(1-c') (where c' is the fraction of conducting sites and N is the density of conducting sites) for different electron hopping pathways: Oh-to-Oh (black), Td-to-Oh (red) and Td-to-Td (blue). Dotted lines represent the values deduced from the bulk cationic site distribution [1] and the squares are the values for the thin films. (b) Comparison of the experimental pre-exponential term of the resistivity measurements ($\rho_0$) and concentration of hopping pairs considering Oh-to-Oh site hopping. The coefficient of determination ($R^2$) shows the quality of the linear fit.

### 5.3.3 Electronic and optical band gap control

The effect of Cr substitution in the band gap is also visible in the valence band (VB) spectra. **Figure 5.16** shows VB spectra for the different iron chromite samples, reflecting the specific contributions of Fe and Cr cations to the band structure. The higher the Fe content, the greater the band between 0 and 1 eV, typically assigned to the $t_{2g}$ subset of Fe 3$d$ band [37]. Meanwhile, the

[36] Similar activation energy ($E_a$ = 150 meV) was found for 120 nm thick $Fe_{1.8}Cr_{1.2}O_4$ films grown on MgO (001) [3], which also presented preference for inverse configuration at higher Cr content.

higher the Cr content, the greater the band around 2-3 eV, assigned to the $t_{2g}$ subset of Cr $3d$ band. Expanded view of VB spectra revealed that the leading edge of the $Fe_3O_4$ completely overlaps the Fermi level, whereas $Fe_{2.3}Cr_{0.7}O_4$ to $Fe_{1.8}Cr_{1.2}O_4$ compositions barely overtop it. These results confirm that doping magnetite with Cr is very effective to control the electronic transport and thus convert a correlated half metal to a semiconductor.

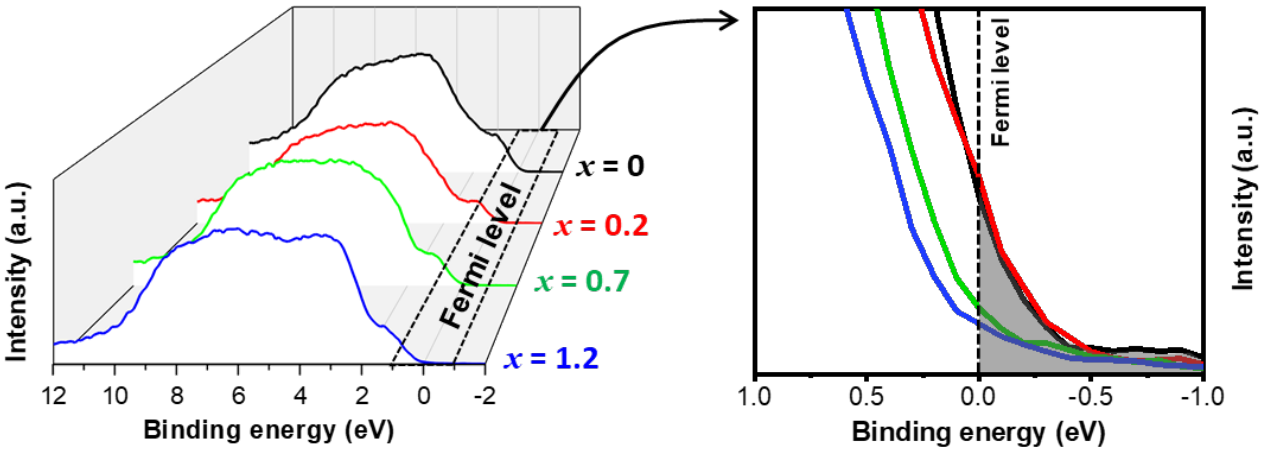


**Figure 5.16.** The valence band of $Fe_{3-x}Cr_xO_4$ thin films with expanded view of the Fermi level. Color code: $x$ = 0 (black), $x$ = 0.2 (red), $x$ = 0.7 (green) and $x$ = 1.2 (blue).

Interesting trends were also observed for the optical band gap. **Figure 5.17a** compares the UV-vis absorbance spectra of $Fe_3O_4$ and $Fe_{2.3}Cr_{0.7}O_4$ recorded in transmission mode in the spectral range of 400–800 nm. These spectra were obtained by dividing the spectra of the thin films by a bare substrate reference. The transmitted light was collected by a large numerical aperture (0.8) microscope objective to limit the impact of scattering on the measured transmittance. For comparison's sake, they are plotted as absorption coefficient ($\alpha$), which was calculated via the Beer-Lambert law. For thin films, $\alpha$ is defined by the absorbance ($A_{abs}$) over the film thickness ($t$): $\alpha = 2.303A_{abs}/t$. As shown in **Figure 5.17a**, the absorbance measured for the iron chromite is lower (80% of maximum $\alpha$) than for the magnetite. This is due to the absorbing nature of the iron element, since the films have similar roughness ($\sigma \cong 0.7$ nm) and therefore promote even amounts of scattered and reflected light. Moreover, the absorption peak is shifted towards the higher wavelength region (red shift): from 486 nm ($x$ = 0) to 530 nm ($x$ = 0.7). The fundamental absorption edge probes electronic transitions between the top of the valence band and the bottom of the conduction band, which is related to the nature and value of band gap. Thus, the red shift indicates the decreasing of the optical band gap ($E_g$) with increasing $x$.

The optical band gap ($E_g$) in semiconductors can be determined using Tauc's equation [38]. In crystallized semiconductors, the optical absorption for the inter band transitions close to $E_g$ varies as:

$$(\alpha h\nu)^{1/n} = B(h\nu - E_g) \quad (5.5)$$

where $h\nu$ is the photon energy, $\alpha$ the absorption coefficient and B a proportionality constant. The value of the exponent ($n$) denotes the nature of the electronic transition. Basic absorption processes are usually dominated for allowed direct ($n$ = 0.5) and indirect ($n$ = 2) transitions. Other possible transitions are forbidden direct and indirect with $n$ equals to 1.5 and 3, respectively. In the energy range 1.5 eV < $h\nu$ < 3.0 eV, **Figure 5.17b** shows the Tauc plots of $Fe_3O_4$ and $Fe_{2.3}Cr_{0.7}O_4$ for a direct allowed transition. At low photon energy, the absorption approaches zero and the material is transparent. Near the band gap value, the absorption increases considerably. This exponential behavior can be associated with defect absorption states. Then, a region of linearity is observed until the absorption processes saturate. At higher energies, the saturation of available transition states is responsible for a leveling out of absorption strength and the curve deviates again from the linear behavior.

According to Tauc *et al.* [38], the optical band gap can be obtained by extrapolating the linear region to the abscissa. For $Fe_3O_4$, the intercept of the plot $(\alpha h\nu)^2$ with the $h\nu$–axis yielded a value of $E_g$ of 2.14 eV, while $E_g$ for $Fe_{2.3}Cr_{0.7}O_4$ was equal to 1.96 eV. These values are consistent with optical spectroscopic measurements in the literature, where a band gap of 2.2 eV [39], [40] and 1.3 eV [41] were found for the parent compounds $Fe_3O_4$ and $FeCr_2O_4$, respectively. The increase of the Cr element on expense of the Fe element increases the disorder and defect states in the film texture resulting in the decrease of $E_g$ values in the $Fe_{3-x}Cr_xO_4$ series. The steady decrease in the optical band gap when replacing Fe with Cr was also observed for other spinel series. For instance, in $ZnCr_{2-x}Fe_xO_4$ nanocrystals [42], the band gap also decreases gradually from 2.18 eV ($ZnFe_2O_4$) to 1.81 eV ($ZnCr_2O_4$).

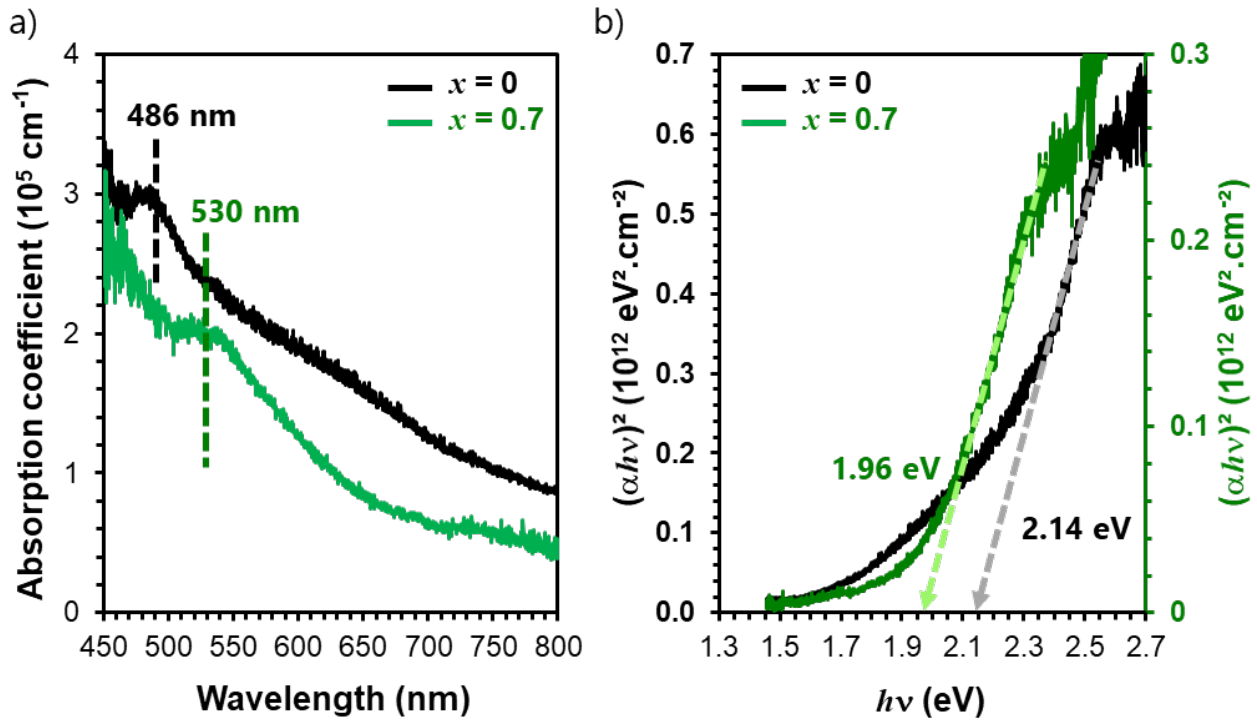


**Figure 5.17.** (a) UV-Vis absorbance spectra and (b) Tauc plot of the direct band gap transition of $Fe_3O_4$ (black line, left axis) in comparison with $Fe_{2.3}Cr_{0.7}O_4$ (green line, right axis).

**Highlights on the electronic transport in $Fe_{3-x}Cr_xO_4$ thin films:**

- Increasing Cr content increases the resistivity of the $Fe_{3-x}Cr_xO_4$ thin films.
- For $x < 1.2$, the thin films show higher resistivity than the bulk due to the presence of anti-phase boundaries (APBs).
- For $x \geq 1.2$, the thin films show lower resistivity than the bulk due to the increase in the inversion ratio.

## 5.4 Summary of results

Tuning the physical properties of the $Fe_{3-x}Cr_xO_4$ series can be achieved through the composition and size modulation. Herein, not only doping magnetite thin films with Cr was very effective to control their magnetic and electronic properties, but also the films showed different behavior than the bulk within the same composition range.

Like bulk materials, the total magnetization and the magnetic anisotropy of $Fe_{3-x}Cr_xO_4$ thin films decreased as the Cr content increased. Except for $x \cong 0.5$, which showed an exceptional higher magnetic anisotropy. Unlike bulk materials, thin films with high Cr content ($1.2 \leq x \leq 1.4$) still showed magnetization at room temperature, *i.e.,* near (or above) the Curie temperature of bulk samples. These features were interpreted in the light of the cationic site distribution obtained from XMCD measurements. For both bulk and thin films, the inversion ratio ($y$) steadily evolves with composition, ranging from an inverse arrangement (*i.e.,* $Fe_3O_4$) to normal ordering (*i.e.,* $FeCr_2O_4$). However, the transition from one spinel configuration to another is less abrupt in the films than in the bulk. Because thin films with high Cr content are still intermediate spinels, while bulk samples are normal spinels, the Curie temperature ($T_C$) of these films were increased. These relation between $y$ and $T_C$ was proven by means of atomistic spin dynamics. Herein, one confirmed the ability of the ASM model to relate microscopic structure to the macroscopic magnetic properties.

Besides changing the magnetic properties of the material, the cation distribution also plays a key hole in the conduction behavior. The electron pathways in $Fe_{3-x}Cr_xO_4$ (111) thin films were found to be the same as the nearest-neighbor Oh-site hopping in magnetite. Considering the small polaron model, the electrical conductivity in the $Fe_{3-x}Cr_xO_4$ series was written as the probability that a given cationic site will contain an extra charge carrier, *i.e.,* that an electron from $Fe^{2+}_{Oh}$ performs a successful hop to $Fe^{3+}_{Oh}$. Like bulk materials, the thin films depicted a general increase in the resistivity with higher $x$ content, consistent with the decrease in the total number of conducting $Fe^{2+}/Fe^{3+}$ pairs. Unlike bulk materials, smaller activation energies were found for higher Cr content films ($x$ = 1.2). These differences were also related to the cationic site distribution. In fact, the films have greater inversion ratio and the favored Oh-to-Oh hopping pathway is still available for them, which results in smaller activation energy.

The cationic site distribution was therefore essential to comprehend thoroughly the evolution of the physical and chemical properties the $Fe_{3-x}Cr_xO_4$ thin films.

## 5.5 References

[1] M. Robbins, G. K. Wertheim, R. C. Sherwood, and D. N. E. Buchanan, "Magnetic properties and site distributions in the system $FeCr_2O_4$-$Fe_3O_4$($Fe^{2+}Cr_{2-x}Fe_x^{3+}O_4$)," *Journal of Physics and Chemistry of Solids*, vol. 32, no. 3, pp. 717–729, Jan. 1971.

[2] H. N. Ok, L. S. Pan, and B. J. Evans, "$Fe^{57}$ Mössbauer study of chromium-doped magnetite, $Fe_{3-x}Cr_xO_4$ ($0 \leq x \leq 0.5$) above the Verwey transition," *Physical Review B*, vol. 17, no. 1, pp. 85–90, Jan. 1978.

[3] D. S. Lee and G. Chern, "Electrical transport properties of $Fe_{3-x}Cr_xO_4$ ferrite films on MgO (001) grown by molecular beam epitaxy," *Physica B: Condensed Matter*, vol. 407, no. 3, pp. 297–301, Feb. 2012.

[4] C.-L. Chen, C.-L. Dong, K. Asokan, G. Chern, and C. L. Chang, "Electronic structure of Cr doped $Fe_3O_4$ thin films by X-ray absorption near-edge structure spectroscopy," *Solid State Communications*, vol. 272, pp. 48–52, Apr. 2018.

[5] S. A. Chambers *et al.*, "Electronic and Optical Properties of a Semiconducting Spinel ($Fe_2CrO_4$)," *Advanced Functional Materials*, vol. 27, no. 9, p. 1605040, Mar. 2017.

[6] J.-B. Moussy *et al.*, "Thickness dependence of anomalous magnetic behavior in epitaxial $Fe_3O_4$(111) thin films: Effect of density of antiphase boundaries," *Physical Review B*, vol. 70, no. 17, p. 174448, Nov. 2004.

[7] D. T. Margulies *et al.*, "Anomalous moment and anisotropy behavior in $Fe_3O_4$," *Physical Review B*, vol. 53, no. 14, pp. 9175–9187, Apr. 1996.

[8] A. Punya, P. Laoratanakul, R. Yimnirun, and Y. Laosiritaworn, "Thickness Dependence of Magnetic Hysteresis of Ising Films in Nano-thickness Range," *J.Nat.Sci. Special Issue on Nanotechnology*, vol. 7, no. 1, pp. 203–211.

[9] S. Celotto, W. Eerenstein, and T. Hibma, "Characterization of anti-phase boundaries in epitaxial magnetite films," *The European Physical Journal B - Condensed Matter*, vol. 36, no. 2, pp. 271–279, Nov. 2003.

[10] D. T. Margulies *et al.*, "Origin of the Anomalous Magnetic Behavior in Single Crystal $Fe_3O_4$ Films," *Physical Review Letters*, vol. 79, no. 25, pp. 5162–5165, Dec. 1997.

[11] P. Wasilewski, D. Virgo, G. C. Ulmer, and F. C. Schwerer, "Magnetochemical characterization of $Fe(Fe_xCr_{2-x})O_4$ spinels," *Geochimica et Cosmochimica Acta*, vol. 39, pp. 889–902, 1975.

[12] Q. Li, J. Xu, J. Liu, H. Du, and B. Ye, "Rise and fall of ferromagnetism in O-irradiated $Al_2O_3$ single crystals," *Journal of Applied Physics*, vol. 117, no. 23, p. 233904, Jun. 2015.

[13] P. K. Baltzer, P. J. Wojtowicz, M. Robbins, and E. Lopatin, "Exchange Interactions in Ferromagnetic Chromium Chalcogenide Spinels," p. 11.

[14] M. Robbins, "Magnetic properties of chromium chalcogenide spinels," *Geochimica et Cosmochimica Acta*, vol. 39, pp. 883–888, 1975.

[15] J. Ma *et al.*, "Magnetic and structural phase transitions in the spinel compound $Fe_{1+x}Cr_{2-x}O_4$," *Physical Review B*, vol. 89, no. 13, Apr. 2014.

[16] C. T. Chen *et al.*, "Experimental Confirmation of the X-Ray Magnetic Circular Dichroism Sum Rules for Iron and Cobalt," *Physical Review Letters*, vol. 75, no. 1, pp. 152–155, Jul. 1995.

[17] D. Caruntu, G. Caruntu, and C. J. O'Connor, "Magnetic properties of variable-sized $Fe_3O_4$ nanoparticles synthesized from non-aqueous homogeneous solutions of polyols," *Journal of Physics D: Applied Physics*, vol. 40, no. 19, pp. 5801–5809, Oct. 2007.

[18] E. Schmidbauer, "$^{57}$Fe Miissbauer Spectroscopy and Magnetization of Cation Deficient $Fe_2TiO_4$ and $FeCr_2O_4$. Part II: Magnetization Data," *Physics and Chemistry of Minerals*, vol. 15, pp. 201–207, 1987.

[19] Néel, M. Louis, "Propriétés magnétiques des ferrites: ferrimagnétisme et antiferromagnétisme," *Annales de Physique*, vol. 12, no. 3, pp. 137–198, 1948.

[20] M. Uhl and B. Siberchicot, "A first-principles study of exchange integrals in magnetite," *Journal of Physics: Condensed Matter*, vol. 7, no. 22, pp. 4227–4237, May 1995.

[21] D. Das and S. Ghosh, "Density functional theory based comparative study of electronic structures and magnetic properties of spinel $ACr_2O_4$ (A = Mn, Fe, Co, Ni) compounds," *Journal of Physics D: Applied Physics*, vol. 48, no. 42, p. 425001, Oct. 2015.

[22] R. Moreno, S. Jenkins, V. K. Lazarov, and R. F. L. Evans, "Role of anti-phase boundaries in the formation of magnetic domains in magnetite thin films," *Journal of Physics: Condensed Matter*, vol. 33, no. 17, p. 175802, Apr. 2021.

[23] R. F. L. Evans, U. Atxitia, and R. W. Chantrell, "Quantitative simulation of temperature-dependent magnetization dynamics and equilibrium properties of elemental ferromagnets," *Physical Review B*, vol. 91, no. 14, p. 144425, Apr. 2015.

[24] M. H. Francombe, "Lattice changes in spinel-type iron chromites," *Journal of Physics and Chemistry of Solids*, vol. 3, pp. 37–43, 1957.

[25] S. Jenkins, R. W. Chantrell, and R. F. L. Evans, "Exchange bias in multigranular noncollinear $IrMn_3$ / CoFe thin films," *Physical Review B*, vol. 103, no. 1, p. 014424, Jan. 2021.

[26] A. Bhargava *et al.*, "Breakdown of the Small-Polaron Hopping Model in Higher-Order Spinels," *Advanced Materials*, vol. 32, no. 49, p. 2004490, Dec. 2020.

[27] B. Gillot, F. Jemmali, and A. Rousset, "Kinetics and mechanism of ferrous spinel oxidation studied by electrical conductivity and thermogravimetry," *Journal of Materials Science*, vol. 21, no. 12, pp. 4436–4442, Dec. 1986.

[28] R. Dieckmann, C. A. Witt, and T. O. Mason, "Defects and Cation Diffusion in Magnetite (V): Electrical Conduction, Cation Distribution and Point Defects in $Fe_{3-\delta}O_4$," *Berichte der Bunsengesellschaft für physikalische Chemie*, vol. 87, no. 6, pp. 495–503, Jun. 1983.

[29] J. P. Wright, J. P. Attfield, and P. G. Radaelli, "Long Range Charge Ordering in Magnetite Below the Verwey Transition," *Physical Review Letters*, vol. 87, no. 26, p. 266401, Dec. 2001.

[30] A. V. Ramos *et al.*, "Magnetotransport properties of $Fe_3O_4$ epitaxial thin films: Thickness effects driven by antiphase boundaries," *Journal of Applied Physics*, vol. 100, no. 10, p. 103902, Nov. 2006.

[31] W. Eerenstein, T. T. M. Palstra, T. Hibma, and S. Celotto, "Diffusive motion of antiphase domain boundaries in $Fe_3O_4$ films," *Physical Review B*, vol. 68, no. 1, p. 014428, Jul. 2003.

[32] R. R. Heikes, R. W. Ure, S. J. Angello, and J. E. Bauerle, *Thermoelectricity: Science and Engineering*. Interscience Publishers, 1961.

[33] I. G. Austin and N. F. Mott, "Polarons in crystalline and non-crystalline materials," *Advances in Physics*, vol. 18, no. 71, pp. 41–102, Jan. 1969.

[34] A. L. Efros and B. I. Shklovskii, "Coulomb gap and low temperature conductivity of disordered systems," *Journal of Physics C: Solid State Physics*, vol. 8, no. 4, pp. L49–L51, Feb. 1975.

[35] J. M. Honig, "Electrical properties of metal oxides which have 'hopping' charge carriers," *Journal of Chemical Education*, vol. 43, no. 2, p. 76, Feb. 1966.

[36] J. Nell and B. Wood, "High temperature electrical measurements and thermodynamic properties of $Fe_3O_4$-$FeCr_2O_4$-$MgCr_2O_4$-$FeAl_2O_4$ spinels," *American Mineralogist*, vol. 76, pp. 405–426, 1991.

[37] E. Vescovo, H.-J. Kim, J. M. Ablett, and S. A. Chambers, "Spin-polarized conduction in localized ferromagnetic materials: The case of $Fe_3O_4$ on MgO(100)," *Journal of Applied Physics*, vol. 98, no. 8, p. 084507, Oct. 2005.

[38] J. Tauc, R. Grigorovici, and A. Vancu, "Optical Properties and Electronic Structure of Amorphous Germanium," *physica status solidi (b)*, vol. 15, no. 2, pp. 627–637, 1966.

[39] H. K. Mao and P. M. Bell, "Crystal-fiels effects in spinel: oxidation states of iron and chromium," *Geochimica et Cosmochimica Acta*, vol. 39, pp. 865–874, 1975.

[40] M. E. Sadat *et al.*, "Photoluminescence and photothermal effect of Fe3O4 nanoparticles for medical imaging and therapy," *Applied Physics Letters*, p. 6, 2014.

[41] A. Boudjemaa, R. Bouarab, S. Saadi, A. Bouguelia, and M. Trari, "Photoelectrochemical $H_2$-generation over Spinel $FeCr_2O_4$ in $X^{-2}$ solutions ($X^{-2}$ = $S^{-2}$ and $SO_3^{-2}$)," *Applied Energy*, vol. 86, no. 7, pp. 1080–1086, Jul. 2009.

[42] R. M. Sebastian, M. S., P. Radhakrishnan, and E. M. Mohammed, "Effect of iron substitution on structural, magnetic and nonlinear optical properties of zinc chromite nanoparticles," *Optik*, vol. 127, no. 19, pp. 7967–7972, Oct. 2016.

[43] M. D. Scafetta, T. C. Kaspar, M. E. Bowden, S. R. Spurgeon, B. Matthews, and S. A. Chambers, "Reversible Oxidation Quantified by Optical Properties in Epitaxial $Fe_2CrO_4^{+\delta}$ Films on (001) $MgAl_2O_4$," *ACS Omega*, vol. 5, no. 7, pp. 3240–3249, Feb. 2020.

# Chapter 6:

# Conclusions and perspectives

This PhD thesis was divided into two studies on thin films of the Fe-Cr-O system: **α-$Cr_2O_3$** and **$Fe_{3-x}Cr_xO_4$**. In the first part, a bridge was built between the **epitaxial strain** and the **electronic structure** of $Cr_2O_3$ thin films. In the second part, the **macroscopic behavior** of $Fe_{3-x}Cr_xO_4$ thin films has been unveiled in the light of their **composition**, **cationic disorder** and **microstructure**. These apparently unrelated studies converged in two aspects: (*i*) the **experimental** and **theoretical** methods applied to their development and (*ii*) their potential applications in **corrosion**, modern **electronics** and **photocatalysis**. This final chapter briefly summarizes the main conclusions drawn from each study and outlines the perspectives opened up by this work.

The main purpose of this thesis was to analyze the macroscopic behavior of $Cr_2O_3$ and $Fe_{3-x}Cr_xO_4$ thin films in the light of their microscopic properties. To do so, I carried out a comprehensive study coupling several characterization methods (*e.g.,* spectroscopy, diffraction and physical property measurements) with theoretical calculations. To de-convolute the effect of the fine structure from other types of defects and fully understand the macroscopic behavior of $Cr_2O_3$ and $Fe_{3-x}Cr_xO_4$ thin films, the investigation was performed in high-purity, epitaxial thin films. The main idea is to use these "model" systems (*i.e.,* well-defined composition and structure) to aid the understanding of complex systems. It should be noted that this thesis is a transdisciplinary research work, so the results obtained for each studied compound of the Fe-Cr-O system are placed in two different contexts: (*i*) as key elements in the corrosion mechanism of Fe-Cr based alloys and (*ii*) as promising materials for spintronic and photocatalysis applications.

First, the main results regarding the study of $\alpha$-$Cr_2O_3$ thin films were highlighted.

In **Chapter 3**, the effects of lattice strain in the electronic structure of growing $\alpha$-$Cr_2O_3$(0001) thin films were investigated by combining X-ray photoemission spectroscopy (XPS) and crystal field multiplet (CFM) calculations. Herein, epitaxial thin films of high crystalline quality were successfully synthetized by molecular beam epitaxy (MBE). Three model strain scenarios (*i.e.,* completely relaxed, under compression or under tensile in-plane strain) were designed by lattice mismatch using monocrystalline $\alpha$-$Al_2O_3$(0001) substrate or $\alpha$-$Fe_2O_3$(0001) buffer layer. The residual strain was determined *in situ* using electron diffraction (RHEED). *Ex situ* Cr 2*p* XPS spectra were recorded for each one of these scenarios, which yielded slightly different lines-shape. In the light of CFM calculations, the effect of epitaxial strain on the spectroscopic signatures was assessed through the crystal field parameters: Dq, D$\sigma$ and D$\tau$, described in the $C_{3v}$ point group symmetry. In fact, the induced distortions in the Cr local environment broke the degeneracy of the *3d* orbital triplet $t_{2g}$ into $a_1 + e$ orbitals, whose energy gap ($\delta$) is related to the crystal field parameters through the relationship: $\delta = 3D\sigma + 20/3D\tau$. For relaxed thin films, the lines-shape of the Cr 2*p* core levels were well reproduced when the $t_{2g}$ subset is fully degenerated ($\delta = 0$). In-plane tensile strain stabilized $a_1$ with respect to $e$ orbitals ($\delta < 0$), whereas compressive strain destabilized $a_1$ orbitals ($\delta > 0$). Hence, a quantitative relation was established between the crystal field splitting energy ($\delta$) extracted from the fit of the experimental XPS spectra and the residual strain determined using electron diffraction. Furthermore, this study explained the multi-peak envelope that constitute the Cr 2*p* core levels, whose complex shape has given conflicting interpretations in the literature.

### ❖ Study limitations and alternatives

Before discussing the prospects for future works, it is important to acknowledge the limitations encountered in this study of $\alpha$-$Cr_2O_3$ thin films due to methodological and time constrains. As discussed below, these factors do indeed influence our findings, but they do not undermine the value of the research.

1. ***Ex situ* XPS measurements.** The spectra were recorded *ex situ*. Once exposed to air, the extreme surface of thin films is contaminated with carbon oxides and can eventually evolve.

Thus, it would be more convenient to perform such a study using *in situ* XPS. However, the spectrometer attached to our MBE setup does not have a monochromatic X-ray source. Therefore, the recorded spectra in this apparatus lack the resolution necessary to distinguish the subtle changes in the spectroscopic signatures of $\alpha$-$Cr_2O_3$ from one stress state to another. High-resolution spectra are mandatory for the methodology (XPS+CFM) to be applicable.

2. **RHEED analysis.** The amount of strain in each model scenario was probed using electron diffraction (RHEED) during the film growth, which is a rather local technique. Thus, it would be interesting to analyze the extent of strain relaxation using alternative techniques, such as reciprocal space mapping [1] and geometric phase analysis [2]. It should be noted that most of the films here are very thin (less than 10 nm); therefore, they may not produce enough signal for X-ray diffraction measurements in laboratory apparatuses, even when very long acquisition times are considered.

3. **Parametric simulations.** CFM is a multi-electronic semi-empirical method, which has both advantages and drawbacks. The major advantage is the low-computational cost of this method. The major drawback is the parametric character. Ten parameters (7 to describe the multi-electronic state and 3 to describe the $C_{3v}$ symmetry) had to be set in order to simulate the Cr $2p$ core levels. With so many parameters, countless curves can be produced and approximations had to be made. After careful evaluation of the parameters, one showed that all curves in different strain scenarios can be fitted by changing only one parameter: D$\tau$. This outcome brought robustness to the method proposed. For future works, it is envisioned to use ligand field multiplet (LFM) calculations to describe the satellite peaks assigned to charge transfer excitations. In $\alpha$-$Cr_2O_3$, these peaks sit close to the Cr $2p_{1/2}$ signal, that is, in a zone of the spectrum that did not evolve with strain. For simplicity, the additional parameters needed to describe ligand charge transfer were neglected in this work. However, for a more faithful description of the entire Cr $2p$ core levels, these parameters have to be considered.

## ❖ Perspectives

Despite the abovementioned limitations and suggestions, the dual methodology (XPS + CFM) proposed in this thesis is very convenient. It provides a structural tool for understanding the influence of strain on the electronic structure of complex oxides. It is particularly useful when the thinness of the systems hampers laboratory diffraction analysis. Moreover, it calls only for XPS measurements (*i.e.,* a laboratory instrument) and requires calculations with low computational cost. Due to its accessibility, the study on $\alpha$-$Cr_2O_3$ thin films has exciting prospects as detailed below:

1. **Future works in corrosion.** Accounting for strain evolution during oxide growth is of utmost importance for understanding the breakdown of the oxide scales in the corrosion context. In this work, the proposed methodology (XPS + CFM) was applied to revisit the microstructure of polycrystalline $\alpha$-$Cr_2O_3$ layers grown during the oxidation of a commercial chromia-forming alloy. Even if the model could not fully describe the spectrum at the very beginning

of the alloy-to-oxide transformation, geometry statements could indeed be done. It was shown that the Cr local environment is significantly distorted with respect to their $C_{3v}$ site symmetry at the beginning of the oxidation, and then gently relaxes as the oxidation proceeds. Under the growth conditions used in this thesis, completely relaxed $\alpha$-$Cr_2O_3$ was found after growing 15.5 nm of the oxide scale. Therefore, the proposed methodology is able to identify successfully the stress state on ultrathin films of complicated microstructure and can be used broadly in the study of chromia oxide scales.

2. **Future works in spintronics.** Determining the crystal field splitting ($\delta$) parameter of $\alpha$-$Cr_2O_3$ epitaxial films is of utmost importance for tuning their physical properties in the spintronic context. In fact, the literature [3] shows that even small changes of 30 meV in $\delta$ are enough to make positive the magnetocrystalline anisotropy of $\alpha$-$Cr_2O_3$ and, therefore, potentially increase the operating temperature of $Cr_2O_3$-based devices. Therefore, the proposed methodology can assist the design of multilayered systems strained by lattice mismatch (*i.e.,* strain engineering approach).

The second part of this work was to understand the effects of composition, cation disorder and microstructure on the physical properties of $Fe_{3-x}Cr_xO_4$ thin films.

In **Chapter 4**, one showed that it is possible to growth epitaxial $Fe_{3-x}Cr_xO_4(111)$ thin films (~15 nm thick) on $\alpha$-$Al_2O_3(0001)$ substrate despite the large lattice mismatch between the two materials (~8% between the oxygen sublattices). For $x < 1.2$, these thin films were stoichiometric; they had high crystalline quality and low surface roughness. For $1.2 \leq x \leq 1.7$, the films were slightly under oxidized; they had lower crystalline quality (*i.e.,* more planar defects) and rougher surface than films with $x < 1.2$. For $x > 1.7$, it was not possible to achieve bidimensional growth in our MBE setup. The $Fe_{3-x}Cr_xO_4(111)$ thin films were composed by $Cr^{3+}$ ions sitting at octahedral interstices and $Fe^{2+}$ and $Fe^{3+}$ ions distributed at octahedral and tetrahedral interstices of the spinel structure. The cationic site distribution of these thin films was obtained by exploring their X-ray absorption (XAS) and X-ray magnetic circular dichroism (XMCD) spectra via CFM calculations. The careful study of different calculation parameters (crystal field and Racah parameters) on these core level spectra describes the evolution of both chromium and iron fine structures as a function of the film composition. These simulations showed that the series gradually evolves from inverse to normal spinel configuration. For $x \leq 0.5$, $Fe^{2+}$ ions sit mainly at Oh-sites while $Fe^{3+}$ ions are distributed between Td and Oh-sites (*i.e.,* inverse spinel configuration). For $0.5 \leq x \leq 1.2$, $Fe^{2+}$ and $Fe^{3+}$ ions are found in both Td and Oh-sites (*i.e.,* intermediate spinel configuration) and the inversion ratio decreases as $x$ increases. The inclusion of $Fe^{2+}$ in adjacent Td-sites as $x$ increases caused distortions in the $CrO_6$ local environment.

In **Chapter 5**, the cation distribution and the microstructure of the thin films were taken into account to understand the effect of chromium substitution on the electronic transport and magnetic properties of $Fe_{3-x}Cr_xO_4$ thin films. Special attention was given on comparing the films with reference bulk samples. For $x < 1.2$, the thin films showed lower magnetic moments and higher resistivity than the bulk due to the presence of stacking defects, such as anti-phase boundaries (APBs). For $x \geq 1.2$,

despite the presence of many planar defects, the thin films showed higher magnetic moments and lower resistivity than the bulk due to the increase in the inversion ratio. Therefore, the cation distribution appeared as a key point in the comprehension of thin film properties. Indeed, magnetic moment, Curie temperature, electronic and optical band gap significantly changed as the compound assumed an inverse or normal spinel structure, that is, whether the $Fe^{2+}$ cations populate Oh or Td-sites.

In **Section 5.2**, atomistic spin model (ASM) was proposed to understand the evolution of magnetic moment with cation disorder. Here one proved that the inversion ratio was directly related to Curie temperature of the material. Furthermore, one aimed to comprehend the "anomalous" magnetic behavior of these films at low temperatures. At low temperatures (T = 10 K), one observed that the M-H curves are shifted to negative field values. For $x \geq 0.7$, loop constriction was also present. According to preliminary results of the ASM simulations, these features were related to surface and interface effects, point defects and microstructure of the films. However, a detailed study of the microstructure of the films (*e.g.,* simulation of APBs) is required to further comprehension of the observed phenomena and constitutes prospects for this work.

### ❖ Study limitations and alternatives

As in the study of $\alpha$-$Cr_2O_3$ thin films, some limitations were also encountered during the synthesis, characterization and modeling of $Fe_{3-x}Cr_xO_4$ thin films. They are due to the lack of previous research studies on the topic, as well as methodological and time constraints. Some of the study limitations and alternatives are discussed below:

1. **The substrate.** Because of the large lattice mismatch between the spinel $Fe_{3-x}Cr_xO_4$ phase and the corundum $\alpha$-$Al_2O_3$ substrate, heteroepitaxy is difficult especially for increasing Cr content. Indeed, it was not possible to grow in our MBE setup high crystalline quality films with $x > 1.4$. As discussed in **Section 4.6**, a way to overcome this issue is to find another substrate, which is far from an easy task. According to Scafetta *et al.* [4], $MgAl_2O_4$(001) substrates could be a suitable option. A more expensive alternative is Pt(111), on which ferrite thin films are known [5, pp. 92–94] to grow very well. A metallic substrate is an interesting alternative as it can also overcome "charge effects". These artifacts appeared during XPS and XAS/XMCD (in total electron yield mode) measurements of insulating samples, *i.e.,* high Cr content ($x \geq 1.4$) or low temperature (T = 4 K). These artifacts are very troublesome as they distort the spectroscopic signal features, especially for XAS/XMCD measurements. In fact, spectra recorded for $x$ = 1.4 had to be discarded from further analysis due to charge effects.

2. **Strain relaxation.** The $\theta$-$2\theta$ X-ray diffraction patterns showed that the out-of-plane parameters of all films are slightly smaller than bulk samples, indicating a small remaining out-of-plane compressive strain of 1%. According to RHEED patterns and high-resolution transmission electron micrographs (HRTEM), in-plane compressive strains also persisted in these samples after the growth of 15 nm films. An overall reduction of bond distances was even confirmed in the fitting of K-shell extended X-ray absorption fine structure (EXAFS)

spectra. Precisely accounting for these residual strains is of upmost importance, since they also influence the macroscopic properties of thin films (*e.g.,* magnetic crystalline anisotropy). As mentioned in the study of $\alpha$-$Cr_2O_3$ films, the RHEED is a rather local technique. Moreover, despite giving good insights into the microstructure of the films, the HRTEM images recorded in this work are not accurate enough to analyze lattice spacing. In order to assess the extent of strain relaxation in the various films (especially of in-plane strains), complementary analyses are required, such as reciprocal space mapping or geometric phase analysis.

3. **Parametric simulations**. Both theoretical methodologies (CFM e ASM) used in the study of $Fe_{3-x}Cr_xO_4$(111) thin films depend on parameters, which can be determined experimentally or by *ab initio* simulations.

    a. **CFM simulations**. Brice-Profeta [6, pp. 166–168] showed that the lines-shape of the $Fe_3O_4$ XMCD signal is better described by the LFM approach. For simplicity's sake, this approach was not used in this study, since it increases the number of parameters to be adjusted. For future works, however, it is envisioned to perform LFM simulations of $Fe_{3-x}Cr_xO_4$ XAS and XMCD spectra.

    b. **ASM simulations.** Due to the lack of *ab-initio* investigations on the intermediate compositions of the $Fe_{3-x}Cr_xO_4$ series, both the anisotropy constant and the exchange interaction between atomic sites had to be roughly approximated. For future works, *ab-initio* investigations on these intermediate compositions are envisioned in order to feed this model.

## ❖ Perspectives

The ability of tuning the physical properties of the $Fe_{3-x}Cr_xO_4$ series by composition and size modulation offers good prospects for these compounds:

1. **Future works in corrosion.** Fe-Cr spinel oxides are common compounds in corrosion layers of Fe-Cr based alloys. Because these continuum oxide scales govern the electronic and cationic transport between the alloy and the aqueous medium, they have a key role in the corrosion process (*e.g.,* in the development and maintenance of protective scale). However, not much is known about the transport properties of spinel oxides in corrosion layers because of their variable composition, poor crystallinity, complex microstructure and nanometer thickness. Although this work did not go as far as comparing the model systems and real corrosion layers, the experimental data collected here will ultimately help in the development of microscopic models and the improvement of mesoscopic models applied to corrosion. Indeed, the results obtained from electronic resistivity measurements can be used as input to modelling oxidation of Fe-Cr based alloys. For instance, in diffusion Poisson coupled model (DPCM) [7], for which solid-state transport of charge carriers (*i.e.* point defects, ions, electrons or holes) in the oxide layer is considered, so the physical mechanism for transport has to be known (which is not always the case, especially for intermediate compositions).

**Furthermore,** due to flexibility of the MBE setup, countless samples of different compositions of interest can be synthesized and data on them can be acquired. In parallel to the study of the $Fe_{3-x}Cr_xO_4$ series, I initiated the optimization of the MBE growth conditions for $Fe_{3-x}Ni_xO_4$ series ($0 \leq x \leq 1$) and $(Fe,Cr,Ni)_3O_4$ series on sapphire substrates. Likewise, these systems have a key role in the corrosion process of Ni-based alloys and stainless steel. Therefore, a similar study of their structural, chemical and physical properties is envisaged for these samples.

2. **Future works in spintronics and photocatalysis.** The ability of tuning the magnetic properties, the electronic transport and the optical band gap by changing the amount of Cr in the $Fe_{3-x}Cr_xO_4$ thin films confirms the potential interest of these materials for spintronics and photocatalysis. For instance, Chambers *et al.* [8] showed that $Fe_2CrO_4$ is photoconductive across the visible portion of the electromagnetic spectrum, which makes this composition a good candidate for photo-electrochemical processes such as water splitting. Later, this same research group [9] also showed that over oxidized $Fe_2CrO_{4+\delta}$ exhibits minimal absorption below ~1.2 eV and may be useful for applications requiring a tunable infrared absorption coefficient. They stated that higher oxidation states may lead to potentially favorable optical properties for solar energy conversion, marked by weaker infrared and stronger UV-visible light absorption with increasing $\delta$.

In addition to corrosion and electronics, both $Cr_2O_3$ and $Fe_{3-x}Cr_xO_4$ series intervene in many others research fields, such as geology, metallurgy and heterogeneous catalysis, for which a comprehensive description of their macroscopic behavior from the microscopic perspective is certainly profitable.

## 6.1 References

[1] P. F. Fewster, "Reciprocal space mapping," *Critical Reviews in Solid State and Materials Sciences*, vol. 22, no. 2, pp. 69–110, 1997.

[2] M. J. Hÿtch, "Measurement of displacement and strain by high-resolution transmission electron microscopy," in *Stress and Strain in Epitaxy*, M. Hanbücken and J.-P. Deville, Eds. Amsterdam: Elsevier, 2001, pp. 201–219.

[3] S. Mu and K. D. Belashchenko, "Influence of strain and chemical substitution on the magnetic anisotropy of antiferromagnetic $Cr_2O_3$: An *ab-initio* study," *Physical Review Materials*, vol. 3, no. 3, Mar. 2019.

[4] M. D. Scafetta *et al.*, "Epitaxial growth and atomic arrangement in $Fe_2CrO_4$ on crystal symmetry matched (001) $MgAl_2O_4$," *Journal of Vacuum Science & Technology A*, vol. 37, no. 3, p. 031511, May 2019.

[5] A. V. Ramos, "Epitaxial Cobalt-Ferrite Thin Films for Room Temperature Spin Filtering," Theses, Université Pierre et Marie Curie - Paris VI, 2008. [Online]. Available: https://tel.archives-ouvertes.fr/tel-00394398

[6] S. Brice-Profeta, "Etude de l'ordre chimique et magnétique d'oxydes spinelles de taille nanométrique par dichroïsme magnétique circulaire des rayons X," 2004.

[7] C. Bataillon *et al.*, "Corrosion modelling of iron based alloy in nuclear waste repository," *Electrochimica Acta*, vol. 55, no. 15, pp. 4451–4467, Jun. 2010.

[8] S. A. Chambers *et al.*, "Electronic and Optical Properties of a Semiconducting Spinel ($Fe_2CrO_4$)," *Advanced Functional Materials*, vol. 27, no. 9, p. 1605040, Mar. 2017.

[9] M. D. Scafetta, T. C. Kaspar, M. E. Bowden, S. R. Spurgeon, B. Matthews, and S. A. Chambers, "Reversible Oxidation Quantified by Optical Properties in Epitaxial $Fe_2CrO_4{}^{+\delta}$ Films on (001) $MgAl_2O_4$," *ACS Omega*, vol. 5, no. 7, pp. 3240–3249, Feb. 2020.

# Étude expérimentale et théorique des films minces de composition Fe-Cr-O : de la structure fine aux propriétés macroscopiques

Résumé de la thèse en français

La chromine ($\alpha$-$Cr_2O_3$) et les spinelles de Fe-Cr ($Fe_{3-x}Cr_xO_4$) sont des composés du système ternaire Fe-Cr-O qui font l'objet de nombreuses études car ils interviennent dans des domaines très variés. Ces oxydes apparaissent notamment lors des processus de corrosion à la surface des aciers inoxydables et sont responsable de leur plus ou moins grande durabilité. Ces mêmes composés présentent des propriétés physiques d'intérêt dans le domaine de la spintronique car ils offrent une large gamme de propriétés magnétiques (ferrimagnétique, antiferromagnétique) et électroniques (semi-métallique, semi-conducteur, isolant).

Les principaux enjeux de cette thèse sont (*i*) de synthétiser des films minces épitaxiés de $\alpha$-$Cr_2O_3$(0001) et de $Fe_{3-x}Cr_xO_4$(111) de haute qualité structurale et de composition chimique maîtrisées et (*ii*) de relier leurs données microscopiques (état d'oxydation, ordre cationique, structure électronique) à des grandeurs physiques macroscopiques comme la résistance électrique ou l'aimantation. Les résultats obtenus sur ces oxydes modèles cristallins, permettront ensuite d'enrichir les connaissances sur les propriétés structurales et de transport de ces couches minces pour la corrosion. Cette étude permettra également de mieux comprendre les propriétés magnétiques et électroniques de ces oxydes et d'envisager leur intégration dans des dispositifs de la spintronique.

La thèse est divisée en deux grandes parties associées à chaque oxyde ($\alpha$-$Cr_2O_3$ et $Fe_{3-x}Cr_xO_4$). Chaque partie traite des problématiques spécifiques à chacun de ces deux matériaux.

## ❖ Étude de l'effet de la contrainte sur le champ cristallin des films minces de $Cr_2O_3$

La première partie de la thèse est donc dédiée à l'étude de l'effet de la déformation de films minces de chromine ($\alpha$-$Cr_2O_3$) sur l'environnement local du chrome. Cette étude s'inscrit dans les deux contextes mentionnés (corrosion et spintronique) que nous détaillons maintenant. Dans le cadre de la corrosion, $\alpha$-$Cr_2O_3$ apparaît comme une couche protectrice lors de la corrosion des alliages chromino-formeurs : elle ralentit la cinétique d'oxydation et prolonge ainsi la durée de vie du matériau. Analyser la contrainte au cours de la croissance de cet oxyde est primordiale pour comprendre les mécanismes de relaxation qui aident à maintenir l'intégrité de cette couche protectrice. Dans le cadre de la spintronique, la chromine $\alpha$-$Cr_2O_3$ est un oxyde antiferromagnétique et magnétoélectrique qui peut donc être envisagé pour différentes applications comme les mémoires magnétiques (MRAMs) constituées à partir d'une matrice de jonctions tunnels magnétiques. Dans ce cadre, l'ingénierie de contrainte peut être utilisée pour manipuler les propriétés physiques de la chromine, telle que l'anisotropie magnétocristalline ou la température de Néel. L'ajustement de ces deux grandeurs est crucial pour augmenter la température de fonctionnement des systèmes à base de $\alpha$-$Cr_2O_3$, point clé pour les applications dans des dispositifs de la spintronique.

L'étude de cet oxyde sous forme de couche mince cristalline comporte trois étapes : la synthèse, la caractérisation et la modélisation. Les couches minces de $\alpha$-$Cr_2O_3$(0001) sont d'abord synthétisées par épitaxie par jets moléculaires assistée par plasma d'oxygène atomique (O-MBE), **Figure A1**, en fonction de l'état de contrainte épitaxiale : tension, compression dans le plan ou parfaitement relaxé. Pour chaque cas, les spectres des niveaux de cœur $2p$ du chrome sont mesurés par spectroscopie de photoémission de rayons X (XPS) et analysés à l'aide de calculs multiplets (méthode CFM) qui ont été développés au cours de ce travail.

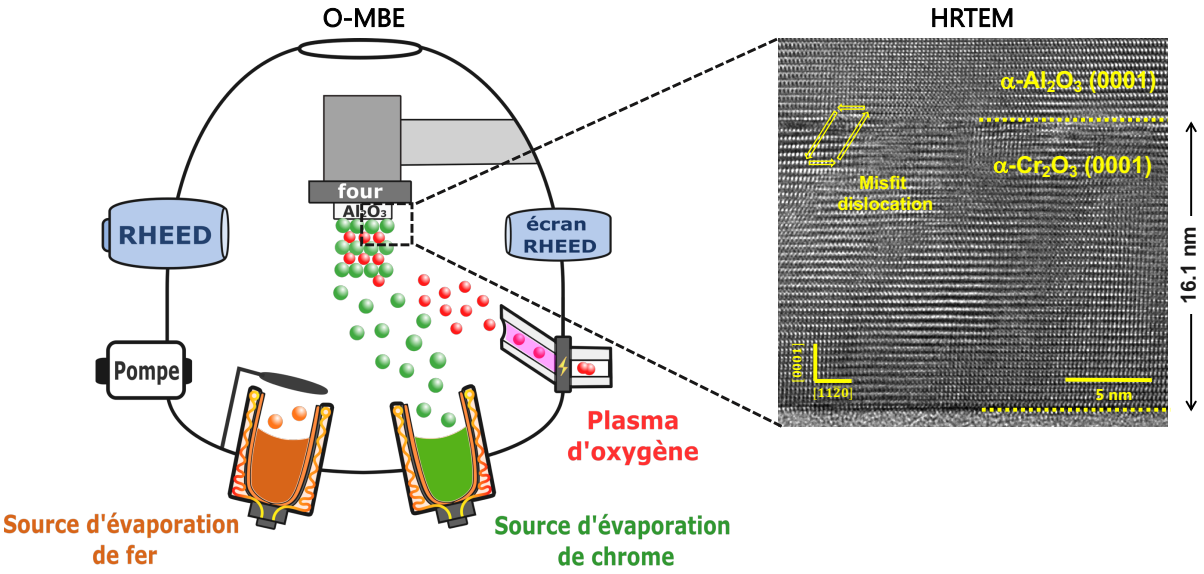


**Figure A1.** À gauche, schéma de principe de la croissance par O-MBE. À droite, image HRTEM montrant l'épitaxie de $\alpha$-$Cr_2O_3$(0001) sur substrat de $\alpha$-$Al_2O_3$(0001).

La **Figure A2** résume l'évolution de l'état de contrainte obtenue au cours de la croissance cristalline de $\alpha$-$Cr_2O_3$ par diffraction des électrons de haute énergie en incidence rasante (RHEED). L'oxyde $\alpha$-$Cr_2O_3$ étant déposé en épitaxie sur un substrat monocristallin de saphir $\alpha$-$Al_2O_3$(0001), l'énergie de contrainte s'accumule rapidement avec l'épaisseur du film déposé en raison du désaccord du paramètre de maille de +3,36 %. La relaxation des contraintes se fait en partie par l'apparition de dislocations (**Figure A1** à droite) et le système est complètement relaxé au-delà d'une dizaine de nanomètres. Trois couches minces de $\alpha$-$Cr_2O_3$(0001) d'épaisseur : 1.1 nm ; 5.3 nm et 16.4 nm ont ainsi été sélectionnées pour étudier les spectres XPS sous une contrainte en compression latérale élevée (+2,8 ± 0,5 %), modérée (+1,5 ± 0,5 %) et parfaitement relaxé (~0 %), respectivement. Des couches minces de $\alpha$-$Cr_2O_3$ contraintes en tension ont également été déposées à l'aide d'une couche tampon de $\alpha$-$Fe_2O_3$(0001). En effet, le désaccord du paramètre de maille entre ces deux oxydes est de -2,19 %. Dans ce système, $\alpha$-$Cr_2O_3$(0001) reste contraint en tension dans le plan jusqu'à

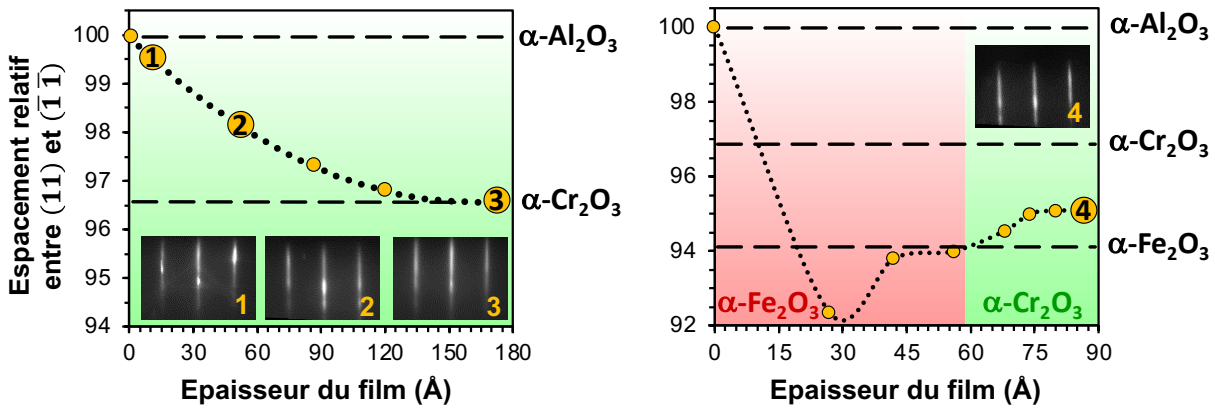


**Figure A2.** Évolution de l'espacement relatif des tiges de diffraction RHEED pendant la croissance épitaxiale de $\alpha$-$Cr_2O_3$(0001) pour différents états de contrainte dans le plan en compression : $\alpha$-$Cr_2O_3$ sur substrat de $\alpha$-$Al_2O_3$ (image à gauche) ou en tension : $\alpha$-$Cr_2O_3$ sur une couche tampon de $\alpha$-$Fe_2O_3$ (image à droite).

plusieurs angströms (**Figure A2** à droite). Ainsi un film de $\alpha$-$Cr_2O_3$ de 3 nm d'épaisseur déposé sur cette couche tampon de $\alpha$-$Fe_2O_3$(0001), correspondant à une contrainte en tension de -1,6 ± 0,5 %, a été sélectionné pour analyser le spectre XPS du niveau de cœur $2p$ du chrome.

Pour chaque état de contrainte, les spectres de photoémission X des niveaux de cœur $2p_{3/2}$ du chrome (**Figure A3**) montrent des changements dans leur forme dont l'origine n'a jamais été clarifiée dans la littérature. A l'aide des calculs CFM, nous avons pu établir que les différentes formes spectrales des niveaux $2p$ du chrome sont la signature de la distorsion locale de l'octaèdre $CrO_6$ dans la structure cristalline de $\alpha$-$Cr_2O_3$ et de la réorganisation des orbitales $3d$. La **Figure A3** montre comment les distorsions de l'environnement local du chrome liées à la déformation lèvent la dégénérescence du triplet $t_{2g}$ des orbitales $3d$ en une orbitale et deux orbitales dégénérées $a_1 + e$. Ainsi nous pouvons comprendre que signature XPS de la chromine complètement relaxée correspond à une dégénérescence des orbitales $t_{2g}$. Un état de contrainte en tension (ou en compression) dans le plan induit quant-à-lui une stabilisation (ou déstabilisation) de l'orbitale $a_1$ par rapport aux orbitales $e$. L'analyse des spectres XPS des niveaux $2p$ du chrome permet dès lors d'identifier l'état de contrainte de la chromine. Au-delà du cas des couches minces épitaxiées utilisées pour mettre au point la démarche, il a été ensuite possible de suivre l'évolution de l'état de contrainte de la couche de $\alpha$-$Cr_2O_3$ polycristalline obtenue durant l'oxydation *in situ* d'un alliage commercial nickel-chrome.

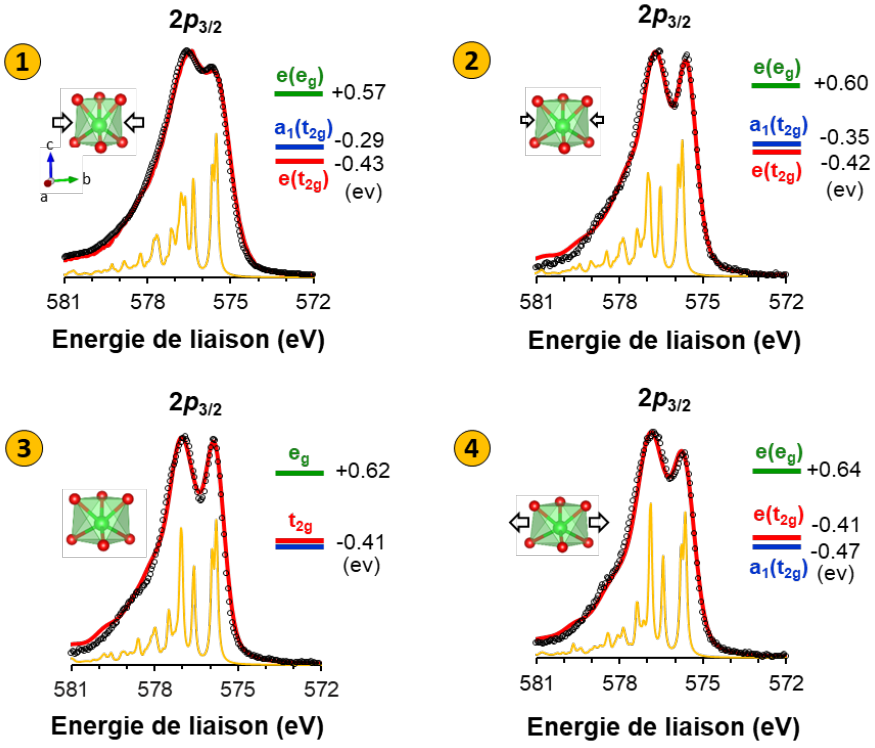


**Figure A3.** XPS Cr-$2p_{3/2}$ (cercles noirs évidés) et calculs réalisés par CFM (ligne rouge) pour des films minces de $\alpha$-$Cr_2O_3$(0001) soumis à une contrainte dans le plan : (1) compression élevée, (2) compression modérée, (3) relaxation complète et (4) tension. Pour chaque spectre, les raies calculées (FWHM = 0,1 eV) sont montrées (ligne jaune), qui ont été convoluées avec une fonction Lorentzienne (FWHM = 0,3 eV) et une fonction Gaussienne (FWHM = 0,7 eV) pour reproduire l'élargissement des raies expérimentales. En regard, la dégénérescence des niveaux $3d$ est montrée pour chaque cas. Une représentation schématique des distorsions de l'octaèdre $CrO_6$ est également indiquée.

Cette première étude nous a donc permis d'élaborer des films minces de $\alpha$-$Cr_2O_3$(0001) de haute qualité cristalline et de comprendre la signature XPS des raies $2p$ du chrome à partir d'une analyse de l'état de contrainte dans les films. Ensuite ces résultats ont été appliqués avec succès à des couches polycristallines obtenues à partir de l'oxydation d'un alliage Ni-Cr. Cette étude illustre bien comment les films modèles monocristallins peuvent être utilisés pour interpréter les données obtenues sur des échantillons polycristallins issus d'un processus de corrosion. Ce travail a également permis de mettre en place des outils (croissance d'oxydes par MBE, analyses RHEED, XPS, calculs multiplets) pouvant être utilisés pour étudier d'autres oxydes complexes. C'est l'objet de la seconde partie de cette thèse où nous avons étudié les chromites de fer de type $Fe_{3-x}Cr_xO_4$ avec $0 \leq x \leq 1,7$. En effet, cet oxyde à base de fer et de chrome est le système, qui apparait dans les couches de corrosion et qui peut également présenter un fort potentiel dans le domaine de la spintronique.

## ❖ Étude des propriétés physiques des films minces de $Fe_{3-x}Cr_xO_4$ à partir de sa structure fine

La seconde partie de cette thèse est donc consacrée aux effets de composition/désordre et à l'impact de la microstructure sur les propriétés physiques de films minces de structure spinelle (**Figure A4**) du type $Fe_{3-x}Cr_xO_4$. Dans le domaine de la corrosion, la présence d'une couche continue formée par ces oxydes de structure spinelle est souvent observée à la surface des aciers à base fer lors du processus de corrosion. Cette phase spinelle est assez mal connue du fait de sa composition variable, sa faible cristallinité, sa microstructure complexe et sa faible épaisseur. Dans ce contexte, l'objectif est ici de construire une base de données sur ces oxydes à l'aide de couches minces modèles de composition contrôlée, élaborées une nouvelle fois par O-MBE. L'analyse approfondie des propriétés structurales et physico-chimiques permettra de développer des modèles microscopiques et d'améliorer le cas échéant les modèles mésoscopiques utilisés en corrosion. En parallèle, ces films minces de haute cristallinité sont intéressants dans la recherche sur les matériaux car des nouvelles fonctionnalités peuvent être trouvées en fonction de la nature et de l'organisation locale des cations. À cet égard, la famille de type $Fe_{3-x}Cr_xO_4$ présente un grand intérêt au vu des propriétés magnétiques, électriques ou optiques très différentes selon la concentration en chrome. L'objectif est donc ici d'étudier l'effet de la composition ($x$) en chrome sur les propriétés structurales et physico-chimiques des films minces de $Fe_{3-x}Cr_xO_4$.

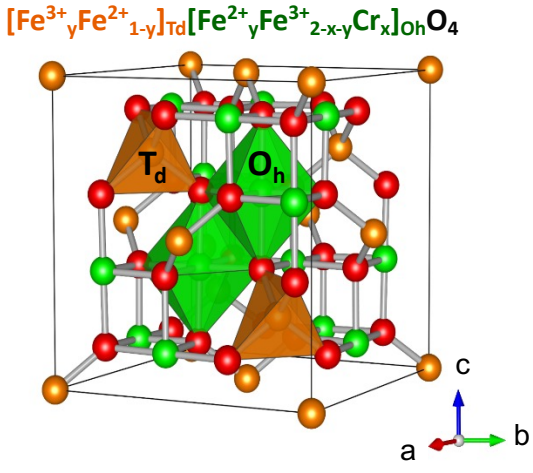


**Figure A4.** Représentation de la structure spinelle $[Fe^{3+}_yFe^{2+}_{1-y}]_{Td}[Fe^{2+}_yFe^{3+}_{2-x-y}Cr^{3+}_x]_{Oh}O_4$ avec les sites tétraédriques (Td) et octaédriques (Oh).

La première étape de cette étude a donc consisté à synthétiser par O-MBE des films minces épitaxiés de $Fe_{3-x}Cr_xO_4$(111) (15 nm d'épaisseur) de haute cristallinité sur un substrat monocristallin de $\alpha$-$Al_2O_3$(0001) avec une composition chimique contrôlée ($0 \leq x \leq 1,7$). Une caractérisation

structurale, chimique et physique complète de chaque échantillon a été réalisée. Plusieurs techniques sont utilisées dans cette étape du travail, comme des méthodes spectroscopiques (XPS, XANES, EXAFS…), des techniques de diffraction d'électrons ou de rayons X, de magnétométrie et de transport électronique. Grace à des partenariats (CEMES-CNRS et Synchrotron SOLEIL), nous avons aussi pu analyser la microstructure et la composition chimique locale des films par microscopie électronique en transmission (TEM) et spectroscopie de perte d'énergie des électrons (EELS) respectivement, et sonder l'arrangement des cations dans la structure cristallographique par absorption X (XAS/XMCD). Ainsi la composition chimique et plus particulièrement la quantification des éléments Fe et Cr a pu être effectuée avec précision par différentes méthodes spectroscopiques (EELS, EDX, XPS et XAS). Les résultats obtenus par ces différentes techniques sont cohérents et nous ont donc permis de définir avec certitude la concentration en chrome. Pour $x < 1{,}2$, les films sont stœchiométriques et homogènes, tandis que les films de composition $x \geq 1{,}2$ sont légèrement sous-oxydés. On observe aussi que la qualité cristalline (TEM, RHEED, XRD) des films diminue avec l'augmentation de la teneur en Cr. Les films de composition $x < 1{,}2$ ont en effet une qualité cristalline supérieure et une rugosité de surface plus faible que les films de composition $x \geq 1{,}2$.

L'analyse des spectres d'absorption X (XAS) et dichroïsme magnétique circulaire (XMCD) couplés à des calculs multiplets (CFM) a aussi permis d'extraire l'environnement local (*i.e.* valence et occupation des sites cationiques) du fer et du chrome en fonction de la teneur en chrome, comme illustré à la **Figure A5**. Les principaux résultats (**Figure A6**) montrent (*i*) que le chrome est uniquement dans l'état de valence $Cr^{3+}$ et se substitue au fer en position octaédrique (Oh) exclusivement, (*ii*) que les cations $Fe^{2+}$ et $Fe^{3+}$ sont redistribués dans les deux sites tétraédrique (Td) et octaédrique (Oh) et enfin (*iii*) que l'évolution du taux d'inversion ($y$), *i.e.* le passage d'une structure spinelle inverse à spinelle normale, dans les films est plus faible que pour les composés massifs à mesure que la concentration en chrome augmente. En effet, la distribution des cations Fe varie en fonction de la teneur en chrome : pour $x \leq 0{,}5$ les ions $Fe^{2+}$ siègent exclusivement sur les sites Oh et la distribution correspond à une structure spinelle inverse, au-delà les ions $Fe^{2+}$ et $Fe^{3+}$ se trouvent à la fois dans les sites Oh et Td (structure spinelle intermédiaire).

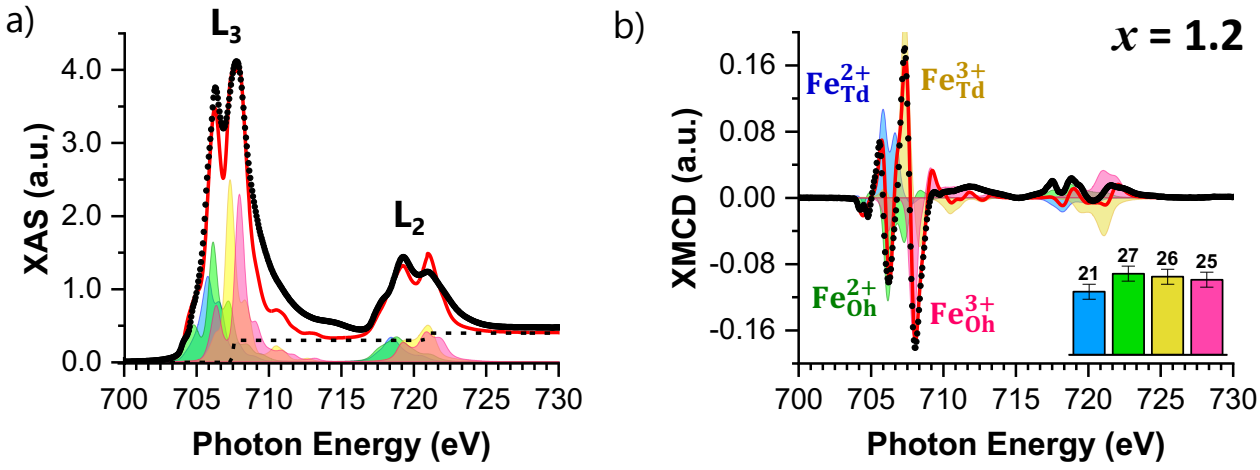


**Figure A5.** (a) Spectres d'absorption X (XAS) et (b) de dichroïsme magnétique circulaire (XMCD) au seuil $L_{2,3}$ du fer (points noirs) couplé à des calculs multiplets (spectres de fonds colorés).

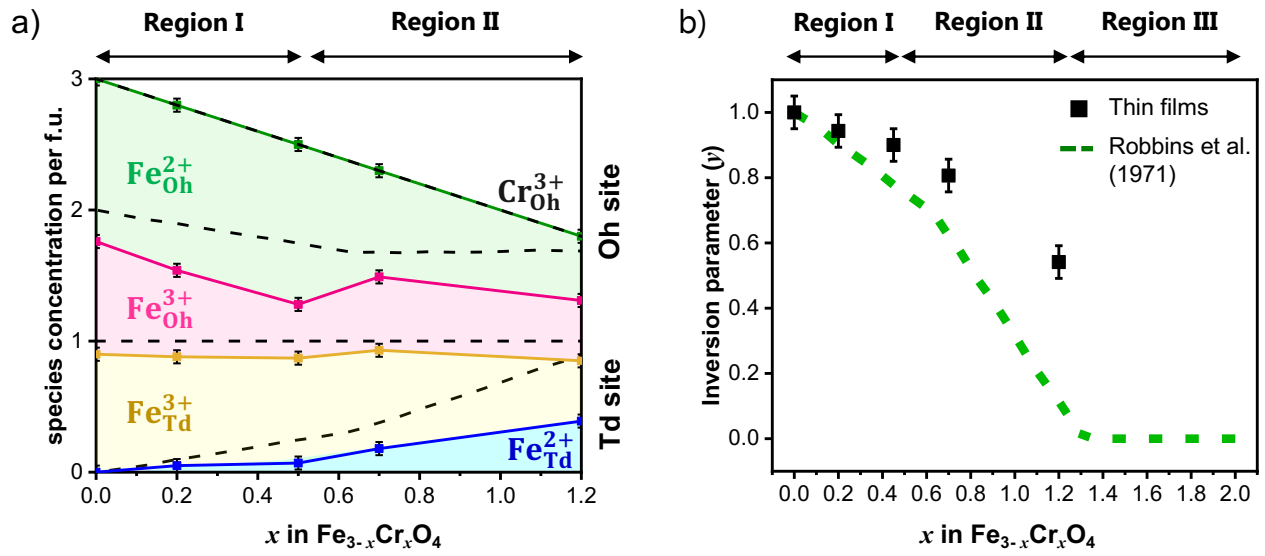


**Figure A6.** (a) Diagramme de distribution d'espèces par site cationique provenant des mesures XMCD (lignes solides), en comparaison avec les valeurs pour les composés massifs [Robbins *et al.* 1971] (lignes noires pointillées). (b) L'évolution du paramètre d'inversion ($y$) avec la composition ($x$) pour les films minces (carrés noirs) et les composés massifs (ligne verte pointillée).

La quantification de la distribution cationique s'est révélée cruciale pour interpréter les propriétés macroscopiques (transport, magnétisme…) des films minces de $Fe_{3-x}Cr_xO_4$. On observe en effet que l'augmentation de la teneur en Cr est associée à une diminution de l'aimantation (**Figure A7a**) et une augmentation de la résistivité électrique (**Figure A8a**). Pour interpréter cela, l'évolution du moment magnétique ($\mu_{total}$) en fonction de la concentration en chrome ($x$) a tout d'abord été relié au taux d'inversion ($y$) déduit des résultats XMCD : $\mu_{total} = 2(3-x-y)\ \mu_B$ par formule unité. La **Figure A7b** montre ainsi que le moment magnétique local déduit de la distribution des sites cationiques diminue progressivement avec la teneur en Cr. Notons que bien que le moment magnétique extrait de ces données XMCD évolue avec la composition de manière similaire aux mesures magnétométriques (VSM), un décalage est observé, probablement en raison de la présence des parois d'antiphase, défauts non pris en compte à partir des mesures d'absorption X. Notons également que les films à haute teneur en Cr ($x \geq 1{,}2$) présentent des moments magnétiques plus élevés que les composés massifs. Ceci est dû à des variations dans le taux d'inversion entre ces deux systèmes (**Figure A6b**), que nous avons pu mettre en évidence à partir de simulations atomistiques en dynamique de spin.

Une analyse approfondie des propriétés de transport a également été effectuée. L'augmentation de la résistivité avec la teneur en chrome a pu être associée à la disponibilité des chemins de sauts d'électrons Oh–Oh (**Figure A8b**), c'est-à-dire à la concentration en fer dans les sites octaédriques. Bien que le saut d'électrons Oh–Oh soit toujours possible pour $x < 1{,}2$ (car $y > 0$), la probabilité du saut le long de ce chemin est effectivement affectée par la concentration en Cr, comme illustré à la **Figure A8c**. Comme la distance entre les $Fe^{2+}$ et $Fe^{3+}$ voisins dans les sites Oh augmente par la présence de $Cr^{3+}$ en site Oh, les électrons sont forcés de suivre des chemins étroits et compliqués dans une mesure aussi élevée que la teneur en Cr. En effet, la résistivité à 300 K passe de $7\times10^{-4}$ Ω.m ($x = 0$) à $3\times10^{-3}$ Ω.m ($x = 0{,}2$) car 10 % des sites Oh sont bloqués par des cations $Cr^{3+}$.

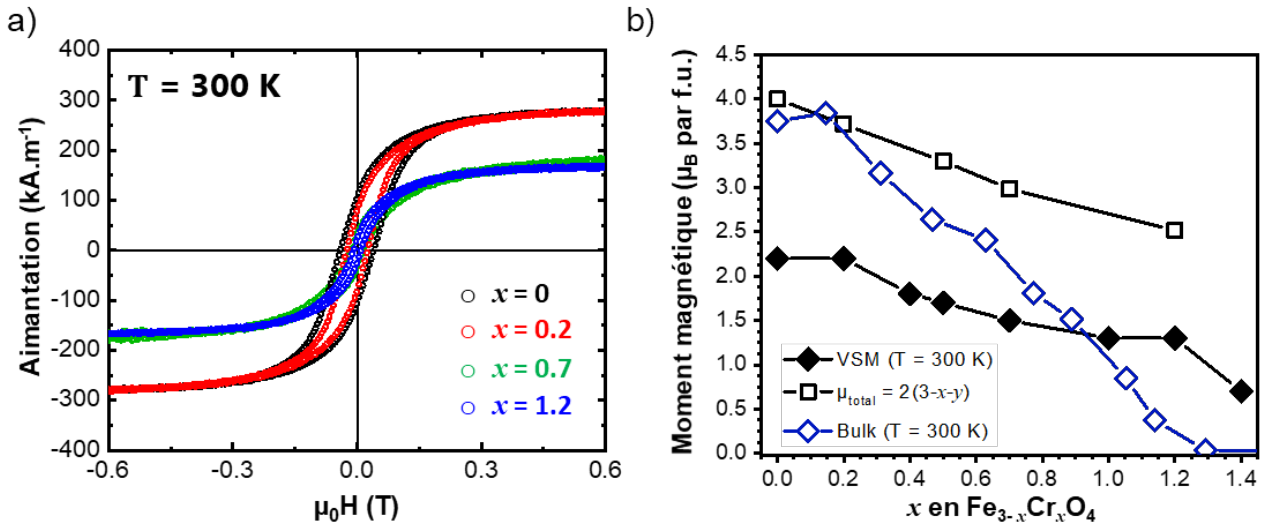


**Figure A7.** Magnétisme dans les films minces de $Fe_{3-x}Cr_xO_4$. (a) Cycles d'hystérésis dans le plan, mesurés par VSM à T = 300 K. (b) Évolution du moment magnétique local en fonction de la composition pour les films minces à T = 300 K en comparaison avec les échantillons massifs (losanges bleus, P. Wasilewski et *al.* 1975). Les résultats VSM sont représentés par des losanges noirs, tandis que les valeurs déduites de la distribution des sites cationiques (XMCD) sont représentées par des carrés noirs ouverts.

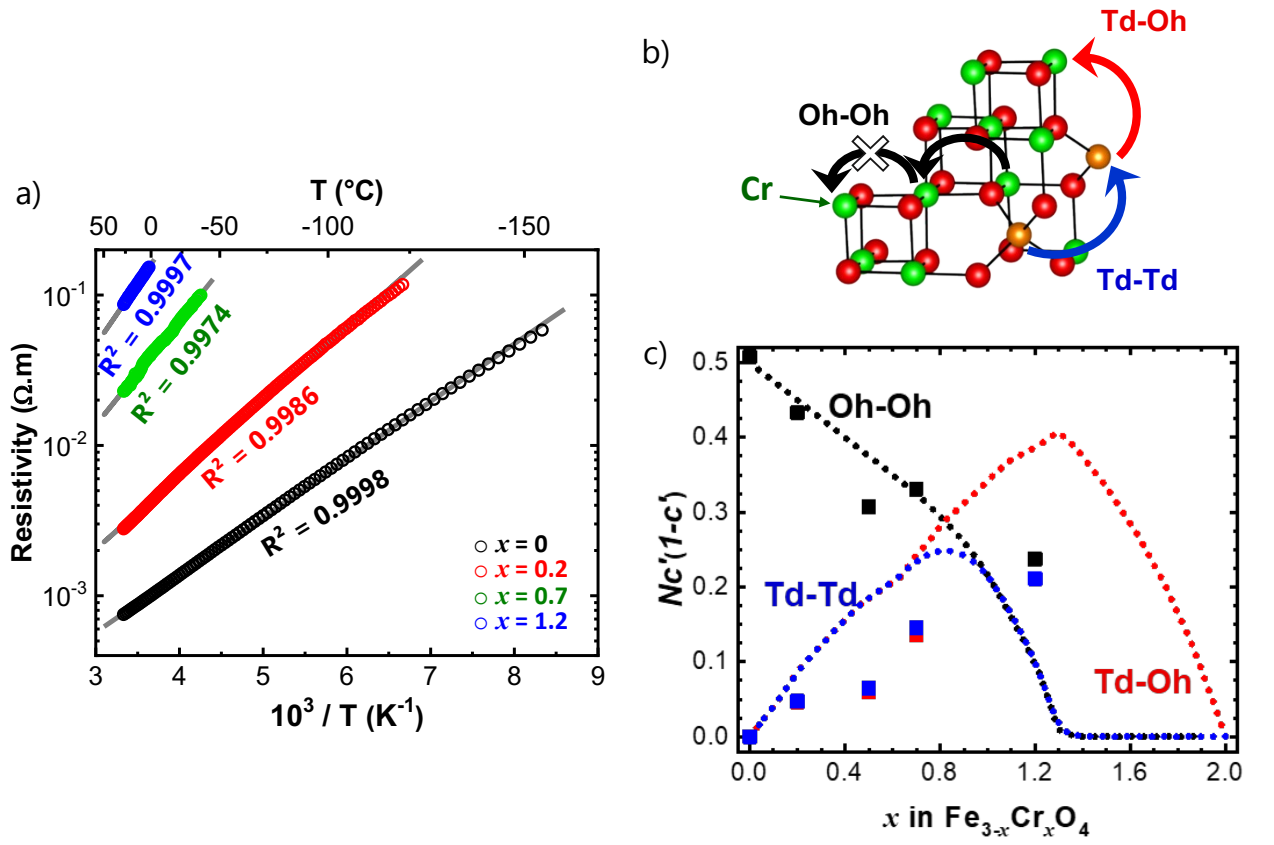


**Figure A8.** Transport électronique dc dans les films minces de $Fe_{3-x}Cr_xO_4$. (a) Résistivité en fonction de la température (cercles) pour différentes compositions ($x$) en chrome et ajustements réalisés par des lois de type Arrhenius (lignes grises). (b) Modèle de conduction électrique permettant de définir les différents chemins de conduction pour les électrons entre les sites Oh et Td. (c) Disponibilité des chemins de sauts d'électrons Oh-Oh (noir), Td-Oh (rouge) et Td-Td (bleu) en fonction de la composition pour les films minces (carrés) en comparaison avec les échantillons massifs (lignes pointillées).

Ce travail de thèse a donc permis d'élaborer des films minces de $Cr_2O_3$ et $Fe_{3-x}Cr_xO_4$ de haute qualité structurale et chimique et de relier le comportement macroscopique (état de contrainte, magnétisme, transport électronique…) de ces oxydes aux propriétés microscopiques. En particulier, l'étude de l'état de contrainte dans $Cr_2O_3$ ou l'analyse de l'organisation cationique en fonction de la teneur en chrome dans $Fe_{3-x}Cr_xO_4$ a permis d'interpréter la plupart des propriétés observées dans ces films. Les résultats obtenus, tant du point de vue expérimental que théorique, devraient permettre de mieux comprendre les processus de corrosion dans le système Fe-Cr-O et d'envisager différentes applications dans le domaine de la spintronique, l'optoélectronique ou encore la photocatalyse.